DISS. ETH NO. 28086

RF Control and Coherence Spectroscopy of THz Quantum Cascade Laser Frequency Combs

A thesis submitted to attain the degree of

DOCTOR OF SCIENCES of ETH ZURICH

(Dr. sc. ETH Zurich)

presented by

Andres Forrer

MSc ETH Physics, ETH Zurich

BSc ETH Physics, ETH Zurich

born on 19.04.1991

citizen of Alt St. Johann, SG - Switzerland

accepted on the recommendation of

Prof. Dr. Jérôme Faist, examiner
Prof. Dr. Giacomo Scalari, co-examiner
Prof. Dr. David Burghoff, co-examiner
Dr. Stefano Barbieri, co-examiner

2021

"Und das ist mein Geheimnis. Es ist sehr einfach: Man sieht nur mit dem Herzen gut. Das Wichtigste ist für die Augen unsichtbar."

Der kleine Prinz
von Antoine de Saint-Exupéry

–

"And now here is my secret, a very simple secret: It is only with the heart that one can see rightly; what is essential is invisible to the eye."

The Little Prince
from Antoine de Saint-Exupéry

Contents

List of Acronyms

Acronyms

AM	amplitude modulated
AOM	accousto-optical modulator
APM	additive pulse mode-locking
AR	active region
BWO	backward wave oscillator
CW	continuous wave
DFB	distributed feedback
DFG	difference-frequency generation
DFG	sum-frequency generation
DFT	Discrete Fourier Transform
DTGS	deuterated triglycine sulfate detector
EO sampling	electro-optical sampling
FEL	free-electron-laser
FM	frequency modulated
FROG	Frequency-Resolved Optical Gating
FT	Fourier Transform
FTIR	Fourier-Transform Infrared Spectrometer
FWHM	full-width half maximum
FWM	four-wave-mixing
GCPW	grounded coplanar waveguide
GTI	Gires-Tournois interferometer
GVD	group velocity dispersion
HBT	heterojunction bipolar transistor
HEB	hot-electron bolometer
HEMT	high electron mobility transistor
HeNe laser	helium-neon laser
HF	hydrofluoric acid
IAC	Interferometric Autocorrelation
IBS	intermode beatnote spectroscopy

ICL	interband cascade laser
ICP	inductively coupled plasma etching
IFG	interferogram
KLM	Kerr lens mode-locking
laser	Light Amplification by Stimulated Emission of Radiation
LEF	linewidth enhancement factor
LIV	light-current-voltage
LO	local oscillator
maser	Microwave Amplification by Stimulated Emission of Radiation
MBE	molecular beam epitaxy
mid-IR	mid-infrared
MOVCD	metalorganic chemical vapour deposition
NA	Numerical aperture
near-IR	near-infrared
NEGF	Non-Equilibrium Green's Function
PCB	printed circuit board
PECVD	plasma enhanced chemical vapor deposition
PLL	phase-locked loop
QCL	Quantum Cascade Laser
QD	quantum dot
QW	quantum well
QWIP	Quantum Well Infrared Photoconductor
RIE	reactive ion etching
RNGH	Risken-Nummedal-Graham-Haken
RTD	resonant tunneling diode
SA	Spectrum Analyzer
SEM	scanning electron microscopy
SESAM	semiconductor saturable absorber mirror
SHB	spatial-hole-burning
SHG	second-harmonic generation
SMIBS	self-mixing intermode beatnote spectroscopy
SNR	signal-to-noise ratio
SPIDER	Spectral Phase Interferometry for Direct Electric-field Reconstruction

SWIFT	Shifted Wave Interference Fourier Transform
THz	terahertz
THz-TDS	THz Time-Domain Spectroscopy
Ti:Sa	Ti:sapphire
TPA	two-photon absorption
VNA	vector network analyzer
ZPD	Zero Path Delay

Publications

Journal Papers

- Andres Forrer, Yongrui Wang, Mattias Beck, Alexey Belyanin, Jérôme Faist, and Giacomo Scalari, "Self-starting harmonic comb emission in THz quantum cascade lasers", *Appl. Phys. Lett.* **118**, 131112 (2021)
  https://doi.org/10.1063/5.0041339
- Andres Forrer, Lorenzo Bosco, Mattias Beck, Jérôme Faist, and Giacomo Scalari, "RF Injection of THz QCL Combs at 80 K Emitting over 700 GHz Spectral Bandwidth" *Photonics* **7**, no. 1: 9 (2020)
  https://doi.org/10.3390/photonics7010009
- Andres Forrer, Martin Franckié, David Stark, Tudor Olariu, Mattias Beck, Jérôme Faist, and Giacomo Scalari, "Photon-Driven Broadband Emission and Frequency Comb RF Injection Locking in THz Quantum Cascade Lasers." *ACS Photonics* **7** (3), 784-791 (2020)
  https://doi.org/10.1021/acsphotonics.9b01629
- Andres Forrer, Markus Rösch, Matthew Singleton, Mattias Beck, Jérôme Faist, and Giacomo Scalari, "Coexisting frequency combs spaced by an octave in a monolithic quantum cascade laser," *Opt. Express* **26**, 23167-23177 (2018)
  https://doi.org/10.1364/OE.26.023167
- Urban Senica, Elena Mavrona, Tudor Olariu, Andres Forrer, Mehran Shahmohammadi, Mattias Beck, Jérôme Faist, and Giacomo Scalari, "An antipodal Vivaldi antenna for im-

proved far-field properties and polarization manipulation of broadband terahertz quantum cascade lasers", *Appl. Phys. Lett.* **116**, 161105 (2020)
https://doi.org/10.1063/5.0004038

Contributions to international conferences - first author

- "Shifted Wave Interference Fourier Transform Spectroscopy of Harmonic and Fundamental RF Injection-Locked THz Quantum Cascade Laser Frequency Combs", *International Semiconductor Laser Conference (ISCL 2021)*, Potsdam, Germany, October 10-14, 2021, **Poster**
- "Shifted Wave Interference Fourier Transform Spectroscopy Of RF Injection-Locked THz Quantum Cascade Laser Frequency Combs", *International Conference on Infrared, Millimeter and Terahertz Waves (IRMMW-THz 2021)*, online, August 30 - September 3, 2021, **Talk**
- "Pure and Self-starting Harmonic Combs in THz Quantum Cascade Lasers: Theory and Experiments", *Conference on Lasers and Electro-Optics Europe (CLEO EUROPE)*, online, June 21-25, 2021, **Talk**
- "Shifted Wave Interference Fourier Transform Spectroscopy of THz Quantum Cascade Laser Frequency Combs operating above 70 K", *Conference on Lasers and Electro-Optics Europe (CLEO EUROPE)*, online, June 21-25, 2021, **Poster**
- "Self-Starting Harmonic Combs in THz Quantum Cascade Lasers", *Conference on Lasers and Electro-Optics (CLEO)*, online, May 9-14, 2021, **Talk**
- "Harmonic Combs in THz Quantum Cascade Lasers", *Photonics Online Meeting (POM)*, online, January 13-14, 2021, **Poster**
- "Self-Started Harmonic Frequency Combs in THz Quantum Cascade Lasers", *International Quantum Cascade Lasers School*

& Workshop (IQCLSW 2020), online, September 7-10, 2020, **Poster**

- "High-performance THz QCL frequency combs", *SPIE Photonics West*, San Francisco, California, US, February 1-6, 2020, **Talk**
- "Injection locking and bi-stable operation of a homogeneous bound-to-continuum THz Quantum Cascade Laser spanning up to 1.65 THz", *Infrared Terahertz Quantum Workshop (ITQW 2019)*, Ojai, CA, USA, September 15-20 , 2019, **Talk**
- "1.65 THz Spanning Homogeneous THz Quantum Cascade Laser: Comb Operation and Injection Locking", *International Conference on Infrared, Millimeter, and Terahertz Waves (IRMMW-THz)*, Paris, France, September 1-6, 2019, **Talk**
- "Homogeneous, bound-to-continuum THz Quantum Cascade Laser: 1.65 THz spectral bandwidth and RF injection locking", *Joint Annual Meeting of Swiss Physical Society Austrian Physical Society (SPS)*, Zürich, Switzerland, August 26-30, 2019, **Poster**
- "Homogeneous, Bound-to-Continuum THz QCL Active Region Design Featuring 1.65 THz Emission Bandwidth in CW", *Conference on Lasers and Electro-Optics Europe (CLEO EUROPE)*, Munich, Germany, June 23-27, 2019, **Talk**
- "Homogeneous, metal-metal THz QCLs emitting up to 1.65 THz bandwidth in CW and its frequency comb injection locking", *French-German THz Conference (FGTC)*, Kaiserslautern, Germany, April 2-5, 2019, **Talk**
- "Dual-Color, Octave Spaced THz Frequency Combs in a Monolithic Quantum Cascade Laser", *International Quantum Cascade Laser School and Workshop (IQCLSW)*, Cassis, France, September 2-7, 2018, **Talk**
- "Octave-spaced, monolithic dual-frequency comb quantum cascade laser source", *EOS Topical Meeting on Terahertz Science & Technology*, Berlin, Germany, May 6-9, 2018, **Talk**

- "Octave-Spaced, Dual-Frequency Comb Quantum Cascade Laser Source in a Single Monolithic Waveguide", *OSA Advanced Photonics Congress*, Zürich, Switzerland, May 2-7, 2018, **Talk**
- "Octave-spaced on-chip THz frequency combs", *Conference on Lasers and Electro-Optics (CLEO)*, San Jose, CA, US, May 13-18, 2018, **Talk**
- "Octave-spaced dual frequency comb in a single monolithic quantum cascade laser source", *International Symposium on Physics and Applications of Laser Dynamics (IS-PALD)*, Paris, November 15-17, 2017, **Talk**

Abstract

Frequency combs generated by mode-locked lasers revolutionized the field of high precision metrology in 1999. They quickly found applications in other research and industrial fields such as astronomy, spectroscopy, atomic clocks or security, as they act as optical rulers with a direct link to the RF domain. Therefore, the concept of the frequency comb is explored in many laser systems. One of these systems is the Quantum Cascade Laser (QCL). QCLs were theoretically predicted in 1971 and rely heavily on quantum well engineering in electrically pumped semiconductor intersubband heterostructures. They were experimentally demonstrated for the first time in 1994 in the mid-IR. They rapidly developed, being able to cover nearly the whole mid-IR range and work nowadays at room temperature. Due to their engineering capability, QCLs also showed in 2002 the emission in the terahertz (THz) region, which are up to today mainly bound to cryogenic temperatures. The high nonlinearities that arise in QCLs allow the formation of frequency combs due to four-wave-mixing (FWM) and spatial-hole-burning (SHB), induced by the Fabry-Pérot cavities.

In this thesis, we will in detail investigate frequency combs emitted by THz QCLs. In chapter 1, we will therefore look into the THz spectral region and the available sources. It will cover briefly the working principle of QCLs followed by a mathematical definition of a frequency comb and a historical review on the developments of them in mode-locked lasers which led to the Nobel Prize. Further, we will show the key developments towards frequency comb emission in THz and mid-IR QCLs.

Chapter 2 will treat the fabrication of THz double-metal ridge waveguide QCLs. We will investigate group velocity dispersion (GVD) effects, induced by the active region (AR), and their influence on the cold cavity modes. We will show how to suppress higher order transverse modes by means of side absorbers and see their effect on the cold cavity mode response. Since the following

chapters will rely on RF measurements, we will briefly discuss RF compatible mounting of our devices and characterize the cryostat setup.

In chapter 3, we will go in detail into the mathematical analysis of Fourier-Transform Infrared Spectrometer (FTIR) measurements. We will explain well-known methods for data analysis of standard FTIR data and discuss in detail effects of finite measurements, i.e. the Discrete Fourier Transform (DFT), which lead to spectral leakage. In addition, we will discuss how these spectral leakage effects can be suppressed using window functions. We then extend and adopt these methods for multi-mode and frequency comb laser sources. We will see that accurate data analysis can increase the nominal resolution of 2.25 GHz of our FTIR down to roughly 10 MHz for the frequency comb case. Therefore, we will show that standard FTIR measurements can already give significant insides of the equidistant spacing of optical modes.

Chapter 4 will discuss the broadband emission of homogeneous THz QCLs, which originates from domain formation within the structure. The results are supported by numerical and experimental data. We will also see that such structures emit frequency combs and that we can RF injection lock these states. By increasing the RF modulation, we will observe that the lasing spectrum can be significantly changed.

In chapter 5, we will embed the same active region as in chapter 4 into a lower loss Cu–Cu waveguide. We will see increased performance compared to Au–Au waveguides and that broadband comb formation can be observed up to 80 K. We will then further test the RF injection capabilities of these devices and show broadening of spectra up to 700 GHz at 80 K.

Besides observing frequency combs defined by the fundamental round trip time, we could also observe harmonic combs in the previous mentioned Cu–Cu devices. We will therefore investigate experimentally and theoretically their presence in THz QCLs in chapter 6. We will show that pure and self-starting harmonic combs can be explained by an asymmetric gain due to two optical transitions with different oscillator strengths.

In chapter 7, we will briefly look into a special designed two stack laser which emits two frequency combs spaced by an octave in pulsed operation. The results will reflect the large GVD present in THz QCL devices and we will verify the spectral origin of each comb

by means of self-mixing intermode beatnote spectroscopy (SMIBS) and intermode beatnote spectroscopy (IBS) with a Schottky diode mixer.

In chapter 8, we will briefly explore different techniques which allow to measure the coherence or temporal profile of comb emitting laser sources. It will be followed by a detailed overview of Shifted Wave Interference Fourier Transform (SWIFT), which will be mainly used in chapter 9 and will allow us to access the coherence and temporal profile of our THz QCLs.

In the final chapter 9, we will use a fast antenna coupled, superconducting NbN hot-electron bolometer (HEB) to perform SWIFT measurements on free running and strongly RF modulated homogeneous and heterogeneous THz QCLs. We will analyze fundamental and harmonic frequency combs, and will show clearly for the first time that strong RF injection, resonant and off-resonant, will mainly lead to sub-comb formation in the investigated THz QCLs.

Zusammenfassung

Frequenzkämme, die von gepulsten, modengekoppelten Lasern emittiert wurden, revolutionierten 1999 den Bereich der Hochpräzisionsmetrologie. Sie fanden schnell Anwendung in anderen Forschungs- und Industriebereichen wie Astronomie, Atomuhren, Spektroskopie, oder im Sicherheitssektor, da sie als optische Lineale mit einer direkten Verbindung zum HF-Bereich operieren. Das Konzept des Frequenzkamms wird daher in vielen Lasersystemen erforscht. Eines dieser Systeme ist der Quanten Kaskaden Laser (QCL). Diese wurden 1971 theoretisch studiert und beruhen in hohem Masse auf dem Design von Quantentöpfen in elektrisch gepumpten Halbleiter-Intersubband-Heterostrukturen und wurden 1994 zum ersten Mal experimentell im mittleren IR-Bereich realisiert. Sie haben sich schnell entwickelt, können fast den gesamten mittleren IR-Bereich abdecken und funktionieren heute bei Raumtemperatur. Da die grundlegenden Quantentöpfe angepasst und gestalltet werden können zeigten QCLs im Jahr 2002 auch die Emission im THz-Bereich, wobei diese bis heute hauptsächlich an kryogene Temperaturen gebunden sind. Die in diesen Lasern auftretenden hohen nichtlinearen Effekte ermöglichen die Bildung von Frequenzkämmen aufgrund von Vier-Wellen-Mischung (FWM) und Räumlichem Lochbrennen (SHB), welches durch die Fabry-Pérot-Kavitäten induziert wird.

In dieser Arbeit werden wir die von THz QCLs emittierten Frequenzkämme im Detail untersuchen. In Kapitel 1 werden wir uns daher mit dem THz-Spektralbereich und den verfügbaren Quellen befassen. Es wird kurz auf das Funktionsprinzip von QCLs eingegangen, gefolgt von einer mathematischen Definition eines Frequenzkamms und einem historischen Rückblick auf die Entwicklungen in gepulsten, modengekoppelten Lasern, die zum Nobelpreis führten. Des Weiteren werden wir die wichtigsten Entwicklungen zur Frequenzkammemission im THz- und mittleren IR-Bereich aufzeigen.

Kapitel 2 wird die Herstellung von THz Doppelmetall Wellenleiter QCLs behandeln. Wir werden die Gruppengeschwindigkeits-

dispersions-Effekte (GVD) untersuchen, die durch die Aktive Region (AR) induziert werden, und deren Einflüsse auf die kalten Hohlraummoden. Wir werden zeigen, wie transversale Moden höherer Ordnung mit Hilfe von Seitenabsorbern unterdrückt werden können und wie sich dies auf das Verhalten der kalten Hohlraummoden auswirken. Da sich die folgenden Kapitel auf HF-Messungen stützen werden, werden wir kurz die HF-kompatible Montage unserer Geräte diskutieren und den Kryostataufbau charakterisieren.

In Kapitel 3 werden wir auf die mathematische Analyse von Fourier-Transform-Infrarotspektrometer (FTIR) Messungen eingehen. Wir werden bekannte Methoden für die Datenanalyse von standardmässigen FTIR Messungen erklären und untersuchen ausführlich die Auswirkungen endlicher Messungen, d.h. der Diskrete Fourier-Transformation (DFT), welche zu spektralen Leck-Effekten führen. Wir werden zeigen wie diese spektralen Leck-Effekte durch Fensterfunktionen unterdrückt werden können. Anschliessend werden wir diese Methoden auf Multimoden- und Frequenzkamm-Laserquellen ausweiten und anwenden. Wir werden sehen, dass eine genaue Datenanalyse die nominale Auflösung von 2.25 GHz unseres FTIRs auf etwa 10 MHz für den Frequenzkammfall erhöht werden kann. Daher können standardmässige FTIR Messungen bereits signifikante Einblicke in die äquidistanten Abstände der optischen Moden geben.

In Kapitel 4 wird die breitbandige Emission eines homogenen THz QCL diskutiert, die ihren Ursprung in Domänenbildung innerhalb der Struktur hat. Die Ergebnisse werden durch numerische und experimentelle Daten gestützt. Wir werden sehen, dass solche Strukturen auch Frequenzkämme emittieren und dass wir diese Zustände durch HF-Injektion stabilisieren können. Weiter kann durch Erhöhung der HF-Modulationsstärke das Laserspektrum erheblich verändert werden.

In Kapitel 5 werden wir die gleiche Aktive Region wie in Kapitel 4 in einen Cu–Cu Wellenleiter mit geringerem Verlust einbetten. Wir werden sehen, dass die Leistung im Vergleich zu Au–Au Wellenleitern erhöht ist und dass eine breitbandige Kammbildung bis zu 80 K beobachtet werden kann. Anschliessend testen wir die HF-Injektionsfähigkeiten dieser Geräte und zeigen eine Verbreiterung der Spektren auf bis zu 700 GHz bei 80 K.

Neben der Beobachtung von Frequenzkämmen, die durch die Umlaufzeit definiert sind, wurden in den bisherig untersuchten Cu–

Cu-Geräten auch harmonische Kämme beobachtet. Wir untersuchen daher in Kapitel 6 experimentell und theoretisch ihr Vorhandensein in THz QCLs. Wir werden zeigen, dass die reinen und selbststartenden harmonischen Kämme durch eine asymmetrische Laserverstärkung aufgrund von zwei optischen Übergängen mit unterschiedlichen Oszillatorstärken erklärt werden können.

In Kapitel 7 werden wir uns kurz mit einem speziell entwickelten Zweistapel-Laser beschäftigen, der im gepulsten Betrieb zwei Frequenzkämme im Abstand von einer Oktave aussendet. Die Ergebnisse spiegeln die grossen GVD-Effekte wider, die in THz QCL-Geräten vorhanden sind, und werden den spektralen Ursprung jedes Frequenzkamms mittels einer selbst mischenden Intermoden Schwebung (SMIBS) Technik und einer Intermoden Schwebung Spektroskopie (IBS) mit einem Schottky-Diodenmischer nachweisen.

In Kapitel 8 werden wir uns kurz mit verschiedenen Techniken befassen, die es ermöglichen die Kohärenz oder das zeitliche Profil von Frequenzkamm emittierenden Laserquellen zu messen. Es folgt ein detaillierter Überblick über SWIFT, die hauptsächlich in Kapitel 9 verwendet wird und uns ermöglicht die Kohärenz und das zeitliche Profil unserer THz QCLs zu messen.

Im letzten Kapitel 9 werden wir einen schnellen, antennengekoppelten, supraleitenden NbN Heissen-Elektronen-Bolometer (HEB) verwenden, um SWIFT Messungen an freilaufenden und stark RF-modulierten homogenen und heterogenen THz QCLs durchzuführen. Wir werden fundamentale und harmonische Kämme analysieren und werden zum ersten Mal klar nachweisen, dass die starke HF-Injektion, resonant und nicht-resonant, hauptsächlich zur Bildung von Unterkämmen in den untersuchten THz QCLs führt.

Acknowledgments

You have to walk every path yourself, but what makes the journey successful are the people who accompany you. Many fantastic people joined me during my last few years and I would like to thank all of them.

A big thanks goes to my parents, Monika and Ueli, and their new partners, who supported me during my childhood. And still do so now. They enabled to each of us in our family to find its way, without pressure but full support. Thank you! Of course, I also thank my brothers, sisters and all my friends for all the moments during and beside my working life. You have always grounded and balanced me.

My biggest support was Salome, and certainly the person who sacrificed the most for my work life. You were always by my side and supported me during times when I was running from one event to the next. You allowed me to move forward in my work life without complaining too much, telling me to slow down at the right moments and reminding me that there is more to life than work. I am so grateful and love you for all the things you do and mean to me!

There are many people who are in the background making all the experiments we do at ETH Zürich possible. Here I would like to give special thanks to the cleanroom FIRST team, the engineering office and the mechanical workshop. There are also many other people outside ETH Zürich with whom I have had the pleasure to discuss and share great ideas at many conferences or collaborations. A direct thanks goes to Yongrui Wang and Alexey Belyanin for their theoretical support in our work on harmonic combs. Further, all SWIFT measurements performed in this work would not have been possible without the HEB provided by Sara Cibella. Thank you for this great device.

During my time in the Faist group, I had and still have the pleasure of working with many brilliant researchers. Everyone in

the group has always been supportive and I have been able to learn and have a friendly relationship with everyone. Thank you all for the great discussions, whether in research or simple about our life. And of course for all the time outside of work that we spent together and for all the moments that made you not only a coworker but also a friend.

In the early years, I had the pleasure of being "table neighbor" to Janine Keller, with whom I always started my day with coffee and tea. Even if we did not work on the same project, or maybe because of that, I really liked talking with you, enjoyed our breaks and I am very grateful that you were kind of mentor for me in my early days.

And what would my thesis be without a QCL! I thank Mattias Beck for the growth of all the layers used in this thesis. It is always a pleasure to have a chat with you and learn from your experience. I look forward to many layers to come and shine.

There are many more people I would like to mention here, but this would basically end up in listing all persons who are and have been in the group during my time. Therefore, again a big thank to all my friends from the Faist group.

While writing this thesis, I also had the direct feedback from my colleagues. They kept giving me suggestions, critical questions and improved my final work in many ways. Therefore, I thank David Stark, Mathieu Bertrand, Johannes Hillbrand, Sergej Markmann, Paolo Micheletti, Philipp Täschler, and Urban Senica.

Further, I thank Prof. David Burghoff and Dr. Stefano Barbieri for examining my thesis. It is an honor to have two great scientists of our field inspecting my work. I enjoyed the discussions we were able to have in person during several conferences and to read the papers of you two, which significantly influenced this thesis and our community.

Last but not least, I would like to thank Jérôme Faist and Giacomo Scalari. You both are brilliant scientists with many great ideas and enthusiasm. You never wait for the future, you try to create it! I appreciate the freedom and trust you gave me during my PhD. And at the right moments you both have pushed me in the right direction with many insights and suggestions, challenging me to go one step further. Above all, Giacomo was my close mentor who believed in me from the beginning and encouraged me to do my

doctorate. I was able to learn directly from you in the lab and we had fruitful discussions about new ideas and projects. Because of Giacomo, every week that I started on Monday, I did not think "Oh no, let it be weekend again!" or "What does he wants me to do this week?" but rather "What can we do next?", "Let's find out more!" or "What will we explore this week?". In the end, the passion you two have for physics is contagious and has made me think outside the box. Thank you, Giacomo and Jérôme, for that!

1

Introduction

Optical frequency combs had a tremendous influence on high precision metrology as they act as absolute rulers in the optical domain with a direct link to the RF domain [1–5]. Their impact rapidly extended into research fields of spectroscopy, astronomy, and optical clocks, to name a few [6]. The emission of fully stabilized, equally-spaced and phase-locked optical modes was first shown in mode-locked Ti:sapphire (Ti:Sa) lasers [5] in the near-infrared (near-IR) spectral region. In fact, mode-locked lasers naturally emitted free running frequency combs without active absolute frequency referencing and stabilization, which has already many advantages due to the optical mode coherences, used as, for example, in dual-comb experiments [6–9]. The concept of frequency comb emission is nowadays extended to many other laser systems [10–14]. These systems showed that not only mode-locked lasers, i.e. equal intermodal difference phases, but also phase-locked lasers, i.e. arbitrary but fixed optical mode phases, can lead to frequency comb emission. One of these laser systems is the Quantum Cascade Laser (QCL) [11, 12, 15–17].

This thesis investigates the direct generation of frequency combs by terahertz (THz) QCLs and their characterization. In this chapter, we will first describe in section 1.1 different sources available to generate THz radiation. In section 1.2, we will discuss the conceptual description and the working principle of QCLs. Further, we will mathematically describe frequency combs in section 1.3 and give a historical background of their developments which led to frequency combs and the Nobel Prize. The final section 1.4 will provide the milestones in the development, characterization and control of QCL based frequency combs, both in the THz and mid-infrared (mid-IR) region.

1.1 Terahertz radiation

THz emission bridges the gap between the microwave radiation generated by electronic devices and the high frequency radiation emitted by lasers. The THz region is located between 300 GHz and 10 THz [18] (100 GHz to 30 THz [19]) and finds many applications in imaging, spectroscopy, astronomy, security or communication [18–23]. The low frequency range, i.e. 300 GHz to ∼1.5 THz, can be reached by room temperature, semiconductor based, electronic devices like Gunn diodes, resonant tunneling diodes (RTDs), heterojunction bipolar transistors (HBTs) or high electron mobility transistors (HEMTs) [18, 19]. For all of these sources, the radiated power drops significantly above 1 THz [18]. To reach higher frequencies, often the tabletop approach of THz Time-Domain Spectroscopy (THz-TDS) can be exploited to generate and detect THz radiation from a photoconducting antenna or switch, irradiated by a mode-locked fs mode-locked laser at 1550 nm [19, 24, 25]. For higher powers one also explores THz emission from (physically large and bulky) free-electron-lasers (FELs), gyrotrons, synchrotrons or backward wave oscillators (BWOs) [26]. Historically, there are also optically pumped far-IR gas lasers available [18, 26].

The direct generation of coherent THz radiation above 1 THz emitted by optoelectronic semiconductor devices can be achieved by p-type germanium (p-Ge) lasers [27] or QCLs [15, 16, 19, 28]. P-Ge lasers were shown in 1982 and are still bound to cryogenic temperatures around 20 K and rely on magnetic fields, since their working principle is based on Landau levels [18, 26]. In contrary, electrically pumped THz QCLs are able to cover roughly the range between 1 to 5 THz. The emitted power is typically in the mW range in continuous wave (CW) but also reaching Watt-levels in pulsed operation [29, 30]. Most THz QCLs operate at cryogenic temperatures but significant progress was achieved for the maximum pulsed temperature operation [31–33] reaching up to 250 K [34]. The THz emission by means of difference-frequency generation (DFG) in mid-IR QCLs [35–37] at room temperature is also possible but only generates reduced output power. Additionally, THz QCLs are able to emit over more than one octave in bandwidth [38, 39] and can operate in a frequency comb state [40–42].

As we will see in the next section, QCLs are by themselves fascinating devices since the artificial heterostructure engineering of

intersubband energy levels allows the growth of many different gain media covering the THz and mid-IR spectral region.

1.2 Quantum Cascade Lasers

In 1970, L. Esaki and R. Tsu proposed in Ref. [43] the concept of creating an artificial crystal by means of a semiconductor heterostructure, also called superlattice, which features *intersubband* transitions, rather than interband transitions. One year later, R. Kazarinov and R. Suris pointed out in Ref. [44] that such a heterostructure could lead to population inversion and therewith optical amplification if a field is applied to the superlattice [43]. The concept of the QCL is now based on an active region design consisting of a sequence/period of quantum wells which form the laser levels, by means of *intersubband* transitions, as it is schematically shown in Fig. 1.1 (a). The key point is that such a quantum well sequence is connected to a next quantum well sequence, which is usually identical, via an injector region and because of the biasing of the structure one electron will cascade through many quantum well periods. This *cascaded* design allows one electron to emit multiple photons and is also reflected in the name Quantum *Cascade* Laser. In Fig. 1.1 (b) and (c) we sketch the optical transitions present in interband and intersubband structures. For both cases, the energy dispersion is represented as well. Due to the similar energy dispersion, which is called band structure, in intersubband quantum wells, the final joint density of states will be delta-like as for atomic transitions. An interband laser will provide a step-like density of states with gain but also losses at higher frequencies [28]. In 1994, J. Faist et al. showed for the first time experimental lasing of a QCL in the mid-IR [15]. QCLs then rapidly developed and reached CW room temperature operation in 2002 [45]. In the same year, the same heterostructure concept allowed direct THz emission from a QCL at cryogenic temperatures [16]. QCLs have nowadays many application in research and industry [28, 46]. Not only does the principle of a QCL allow to achieve gain and therefore lasing, but it is also a very non-linear artificial material which shows four-wave-mixing (FWM) [47]. As we will discuss later, the FWM combined with spatial-hole-burning (SHB) induced by the standing waves [1] in the laser cavity can lead

1. It should be mentioned that frequency comb operation in the absence of standing waves was observed in ring QCLs as well [48, 49].

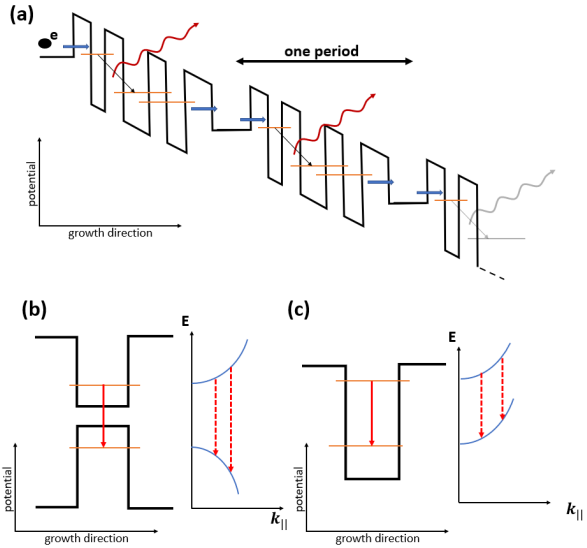

Figure 1.1 – Schematic of QCL operation principle. (a) Simplified representation of an active region design. The heterostructure is biased, which allows alignment of energy levels and transport in the structure. By engineering the individual energy levels and their coupling, population inversion and gain can be achieved. After emitting one photon in one period, an electron will cascade through the following periods. (b) Schematic of an interband transition and the energy dispersion relation. (c) Schematics of an intersubband transition and its energy dispersion relation that results in an atomic-like joint density of states. Figure inspired by Ref. [28]

to frequency comb formation in QCLs.

In the following, we will therefore first mathematically describe what a frequency comb is followed by an historical recap of their developments from mode-locked lasers.

1.3 The frequency comb

Frequency combs emitted by mode-locked lasers have revolutionized the field of high-resolution and absolute frequency spectroscopy and led to the Nobel Prize in 2005 in Physics for John Hall and Theodor W. Hänsch [2, 5, 50–52]. Around the same time, researchers in the field of QCLs went also into the direction of mode-locking hoping to achieve frequency comb emission and high peak pulse en-

ergies. More than 20 years later, frequency comb emission in mid-IR and THz QCLs has been demonstrated [11, 12, 17] even though not only due to mode-locking, i.e. pulsed emission. In this section, we will therefore define the frequency comb in subsection 1.3.1, go briefly through the history of *traditional* frequency combs emitted by mode-locked lasers in subsection 1.3.2 followed by the less known frequency modulated (FM) lasers in subsection 1.3.3. In the follow-up section 1.4, the milestones on the way towards QCL frequency combs will be discussed.

1.3.1 The power of frequency combs

What makes frequency combs so special? The short answer is that they are *simple*. Not the generation of frequency combs and their understanding, but how a frequency comb is represented in frequency and time domain. In words, one would describe a frequency comb as a set of equally-spaced and phase-locked modes. Mathematically, each mode frequency f_n is therefore defined in the following way:

$$f_n = f_{ceo} + n \cdot f_{rep} \tag{1.1}$$

where f_n is the n-th mode frequency, n being an integer number, f_{ceo} the carrier envelope offset frequency and f_{rep} the repetition frequency. f_{rep} and f_{ceo} are located in the RF domain and provide a direct link to the optical modes through Eq. 1.1. The definition of the repetition frequency is clear in the picture of mode-locked lasers, which emit pulses with exactly this repetition rate. $2\pi \cdot f_{ceo} t_{rep}$ corresponds to the phase change of the carrier wave with respect to the envelope per round trip t_{rep}.

From Eq. 1.1 it becomes evident what *simple* means: Each mode can be described by two frequencies f_{ceo} and f_{rep}, and with an index n. If one stabilizes f_{ceo} and f_{rep} to a reference clock, one has stabilized all modes. To give an example what this means, we consider the frequency comb published in Ref. [53]: The modes span from 510 nm to 1125 nm, an optical bandwidth of 330 THz, and with a repetition rate of 90 MHz the whole comb consists of $3.6 \cdot 10^6$ modes which are coherently locked by *simply* stabilizing two frequencies. Moreover, Udem et al. showed in Ref. [51] that the

modes of a 20 THz wide comb spectrum are equidistantly spaced within 3 parts in 10^{17}.

In the time domain the electric field $E(t)$ of a frequency comb reads as

$$E(t) = Re\left(\sum_n A_n \cdot e^{-i2\pi(n\cdot f_{rep}+f_{ceo})\cdot t}\right) \tag{1.2}$$

$$= Re\left(\sum_n |A_n| e^{i\phi_n} \cdot e^{-i2\pi(n\cdot f_{rep}+f_{ceo})\cdot t}\right) \tag{1.3}$$

where n the index of n-th mode, $A_n = |A_n|e^{i\phi_n}$ the complex mode amplitude with ϕ_n it's (temporal constant) phase.

The most straightforward picture of a frequency comb in the time domain is the emission of pulses from a mode-locked laser [2]. Fig. 1.2 (a) shows an artificial comb amplitude spectrum as a function of the frequency normalized to the repetition rate with a Gaussian distribution of 20 modes. The spacing is given by the normalized f_{rep} and the first mode has the index n=30. The normalized f_{ceo} corresponds to the mode frequency modulo the repetition frequency in this normalized picture.

Fig. 1.2 (b) shows the E-field in time domain of the comb with all modes having equal and fixed phases. It can be seen that there is a phase shift $\Delta\phi_{ceo}$ of the carrier and the envelope between successive pulses. This phase shift is related to the dispersion in the laser cavity and is related to f_{ceo} by $f_{ceo} = \frac{1}{2\pi}\Delta\phi_{ceo} f_{rep}$. Therefore, the envelope travels with the group velocity ν_g whereas the carrier wave travels with the phase velocity ν_p. The phase shift per round trip can also be expressed as $\Delta\phi_{ceo} = (1/\nu_g - 1/\nu_p) l_c \omega_c$ where l_c the cavity round-trip length and ω_c the carrier frequency.

Fig. 1.2 (c) shows the E-field in time domain of the same amplitude spectrum but with randomly spaced and fixed phases distributed over 2π. Due to the random (fixed) phase relation between the modes, there is not a single point in time where all modes are exactly in-phase with each other and will therefore produce in general a quasi-CW output instead of a pulsed one. With respect to the

2. The pulse nature is NOT necessary for comb operation.

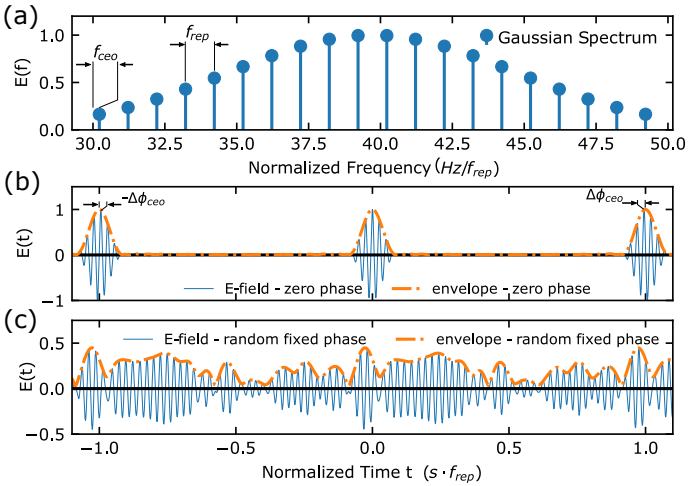

Figure 1.2 – Frequency comb. (a) Amplitude spectrum of a numerically generated comb. (b) Time domain representation of the E-field for the spectrum shown in (a) with constant and equal phases for all modes. This situation leads in general to pulsed emission. (c) Time domain representation of the E-field for the spectrum shown in (a) with random, but fixed phase for each mode. The resulting temporal profile is periodic and in general quasi-CW.

mode-locked laser, which produces a so-called amplitude modulated (AM) comb, the situation of quasi-CW is often referred to as FM comb. However, the temporal field envelope of the FM comb is perfectly periodic in time reflecting the comb nature. The fundamental difference comes only in the peak intensity. It is of course significantly higher in pulsed operation which provides advantages when used in nonlinear processes or when the time profile for sampling is relevant as for example in a THz-TDS system.

According to A. E. Siegman [54], any *periodic* signal in time, regardless of relative amplitude and phase relation, can be considered as *mode-coupling*. In addition, he stated "*As a somewhat arbitrary distinction, we might then reserve the term mode-locked for only those situations in which the sidebands are arrayed all in phase, or nearly so, regardless of their amplitudes; since only these situations lead to the kind of short-pulse output that has become associated with the term "mode-locking" in lasers.*". In that sense, the term mode-locked comb, as well as AM comb, will be used for all situations where all comb mode phases are nearly identical to each other. On the other hand, instead of mode-coupling we prefer the term

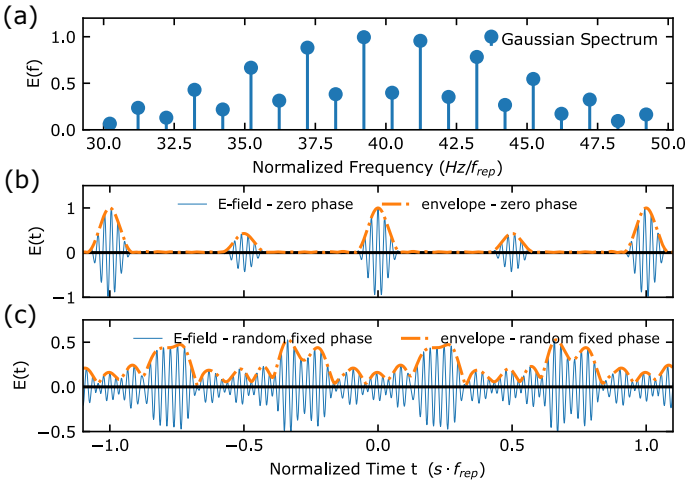

Figure 1.3 – Frequency comb. (a) Amplitude spectrum of a numerically generated comb for which every second mode is attenuated. (b) Time domain representation of the E-field for the spectrum shown in (a) with constant and equal phases for all modes. This situation leads, in general, to a double pulse emission. (c) Time domain representation of the E-field for the spectrum shown in (a) with random, but fixed phase for each mode. The resulting temporal profile is periodic and quasi-CW.

phase-locking for the general terminology for fixed phase relation which seems to be established in the QCL community. The term FM comb is used for comb generation, where the phase relation between modes minimizes the AM modulation in the laser emission. As we will see later, QCLs generally tend to operate naturally close to an FM comb state.

Additionally, it should be mentioned that the equal phase relation of all modes in a mode-locked laser does not necessarily lead to one single pulse. Multiple pulses in time domain can occur due to special spectral shapes. One situation, where every second mode is attenuated compared to its neighbors leads for example to a double pulsed output emission and is shown in Fig. 1.3 (a) and (b), and was also experimentally observed in THz QCLs [55]. For completeness, the time domain profile of an FM comb state is presented in Fig. 1.3 (c). Therefore, one should keep in mind that equal mode phases do not necessarily lead to a single pulse.

In the following section we will discuss briefly the developments of mode-locked lasers and how they led to high resolution frequency

comb spectroscopy and with it the Nobel Prize.

1.3.2 Excursion on lasers and mode-locked laser frequency combs

The stimulated emission in the microwave domain led to the development and demonstration of the Microwave Amplification by Stimulated Emission of Radiation (maser) by J.P. Gordon, H.J. Zeiger and C.H. Townes in 1954 [56]. In 1958, A.L. Schawlow and C.H. Townes theoretically proposed, along with A.M. Prokhorov and N.G. Basov, the infrared and optical maser [57] which was realized in 1960 by T.H. Maiman [58]. The optical maser is now known as Light Amplification by Stimulated Emission of Radiation (laser) [3].

In the following years, the field split into two branches [4]: frequency stabilized CW lasers for high precision spectroscopy and pulsed or mode-locked lasers for nonlinear and ultra-fast phenomena. Here, we will follow the branch of mode-locked lasers.

The paper of H. A. Haus [60] in 2000 provides an overview on experiments and theory which are summarized in the following. It will be extended by an additional view on FM lasers studied in the early 1960s which was summarized by the book of A.E. Siegman [54]. Additionally, the review paper of U. Keller [61] provides an intuitive view on the different techniques for mode-locking. Fig. 1.4 shows the timeline of the generation of shorter and shorter pulses in dye and Ti:sapphire lasers.

The indication of short pulses, due to active modulation of the laser losses, was first found in HeNe [62, 63] and ruby lasers [64]. Clear identification of pulses, produced by active modulation induced Q-switching, was reported roughly one year later [62, 65, 66]. Q-switching itself is a technique where the laser cavity quality factor is modulated at a frequency normally significantly lower than the round-trip time of the cavity. This is for example achieved by an electro-optic or acousto-optic modulator and allows the gain medium to store energy before emitting another pulse. Passive Q-switching can also be obtained [67].

Active mode-locking induced by a fast amplitude or frequency modulator at the cavity round-trip frequency was also possible and

3. Gordon Gould is associated in the creation of the word laser. He had notes and patent claims from 1957 and the patent field in 1959. In 1977 the US court decided in favor of G. Gould [59].

4. According to T. Hänschs Nobel Lecture [1].

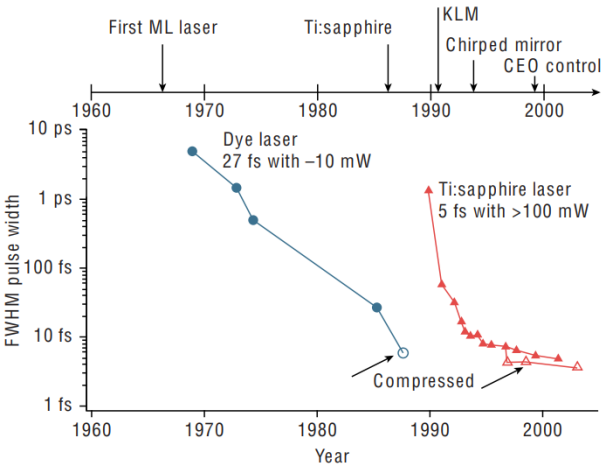

Figure 1.4 – Evolution of pulse duration in Dye and Ti:Sa lasers. The top axis highlights key developments. Reprinted by permission from Springer Nature Customer Service Centre GmbH: Springer Nature, Nature, Ref. [61], © 2003 Nature Publishing Group.

led to short pulses. The generation of short pulses from an amplitude modulator seems to be more intuitive, but both, AM and FM, led to so-called AM and FM mode-locking which was theoretically summarized for example in Ref. [54, 68]. Here, FM mode-locking is associated with the mechanism to generate short pulses, not to be mistaken for an FM laser which has a quasi-CW emission with an underlying comb spectrum.

The next breakthrough in generating even shorter pulses was made by DeMaria et al. [69] in 1966 by replacing the active modulator in the cavity with a passive saturable absorber. It led to the emission of very short, mode-locked pulses but with an additional passive Q-switching of the laser. Fig. 1.5 (a) shows the intensity as a function of time with the slow Q-switched induced envelope. The underlying pulses are shown in detail in Fig. 1.5 (b).

It was then shown by E. P. Ippen, C. V. Shank, and A. Dienes in Ref. [70] in 1972 that passive mode-locking of a CW dye laser could be achieved, which emitted stable and continuous picosecond pulses. Interferometric Autocorrelation (IAC) measurements indicated pulse widths on the order of 1.5 ps. Shortly afterwards subpicosecond pulses were realized [71]. The theoretical background

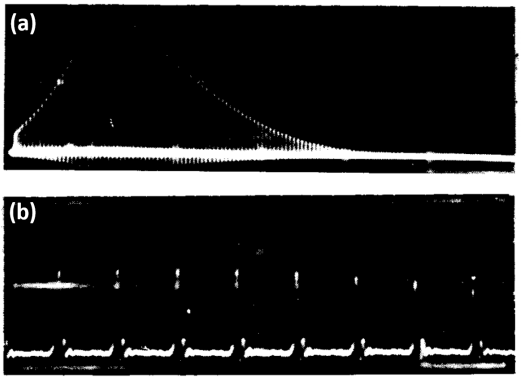

Figure 1.5 – Observation of short pulses with an overlapping Q-switching in a dye laser. (a) Q-switched induced envelope with (b) zoomed in. Reprinted and adapted from Ref. [69], with the permission of AIP Publishing.

was provided by Haus in Ref. [72] in the case of a *fast* saturable absorber, i.e. faster than the gain recovery time. The pulse width is therefore on the order of the absorber recovery time, i.e. in the ps range. Due to the shorter pulse width and therefore larger frequency bandwidth, dispersion effects started to play a significant role. By dispersion compensation, a pulse duration of 6 fs was finally achieved in dye lasers [73].

Further, the first soliton laser was shown in 1984 [74] by additive pulse mode-locking (APM) in a two resonator laser which led to 21 fs short pulses. The saturable absorber was here mimicked by a birefringent element and two polarizers.

So far, the dye laser has been the workhorse until the end of the 1980s. With the discovery of a new broadband solid-state gain medium, the Ti:sapphire laser was born. 50 fs short pulses where generated by a passively mode-locked Ti:sapphire laser [75], but the main breakthrough was the generation of 60 fs long pulses in a single resonator which had no obvious saturable absorber [76] [5]. The mechanism behind it was identified as Kerr lens mode-locking (KLM) [77] where the high pulse intensity leads to self-focusing of the pulse onto an aperture whereas the low intensity light is unfocused and therefore experiences higher losses. Unfortunately, these lasers needed to

5. Fun Fact: Sibbett referred to it as "magic mode-locking" since a bump on the optical table could initialize the mode-locking.

be initialized to emit pulses and operated closer to their instability edge [61].

The development of the semiconductor saturable absorber mirror (SESAM) [78, 79] allowed finally stable and self-starting mode-locking and prevented Q-switching instabilities. The ability to design the SESAM allowed the generation of all kind of pulse widths from the nanosecond range down to sub-10 fs pulses, from slow to fast saturable absorbers, all in an intra-cavity fashion [79]. Additionally, techniques based on self RF modulated accousto-optical modulators (AOMs) allowed the generation of stable and short pulses as well. Therefore, the Ti:sapphire also became commercially available and found more and more applications outside the mode-locked laser community.

The Nobel Prize

By now we saw that the community of mode-locked lasers managed to produce stable and short pulses. But up to then mode-locked lasers were not associated with frequency combs in the sense of a precise reference source. In the community of high precision spectroscopy, researchers tried to link the optical domain with the RF domain, where reference clocks (cesium atomic clock) are available, by means of PLL frequency chains [80, 81] or frequency interval divider chains [82, 83]. These chains tried to connect the optical and RF domain. It was argued that they cannot bridge the RF to the optical domain in a single step with a frequency multiplier since the phase noise would drastically increase, even of the best quartz oscillator [1]. Therefore, each element in the frequency chain acted like a phase noise filter to prevent an increase in phase noise.

Even though Hänsch worked already with a mode-locked frequency comb to perform spectroscopy in 1978 [84], it was only in 1999 when Hänsch realized that besides the accurate stabilization of f_{rep} the additional locking of f_{ceo} to a reference clock would lead to an absolute stabilization of the comb [51, 52]. In their situation f_{ceo} was stabilized via an optical frequency interval divider. Telle et al. proposed in Ref. [85] additional self-referencing techniques. It was in 2000 that the group of J. Hall demonstrated the first self-referenced frequency comb by using a photonic crystal fibre [4, 53]. This was further pushed by octave spanning purely intra-cavity fre-

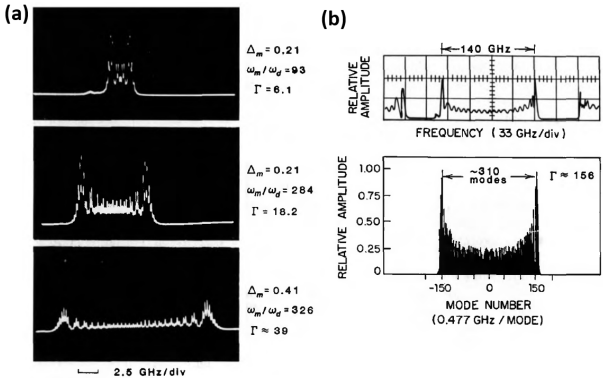

Figure 1.6 – (a) FM laser emission from Nd:YAG laser for different values of phase modulation index Γ, modulation frequency detuning ω_d, modulation frequency ω_m and single pass modulation index Δm. (b) Neodymium-pentaphosphate FM laser. Details in Ref. [54]. Reprint from Ref. [54]. Reprinted with permission from University Science Books, all rights reserved.

quency combs [86], as well as erbium-doped fiber frequency combs [87].

As mentioned in the section 1.3.1 the group of T. Hänsch showed that all modes in their frequency comb are phase stable in 3 parts in 10^{17} [51] and therefore the optical frequency comb acts like a precise ruler linked to the RF domain via f_{rep} and f_{ceo}.

1.3.3 FM laser

Before we move on to QCLs, in the next section we will have a short historical overview of FM lasers since they show some similarities to the observations in QCLs, especially similar spectral shapes as some mid-IR QCL combs [88, 89]. With the development of AM and FM mode-locking in the early 1960s it was found that a slight detuning of the FM modulation frequency from the axial cavity mode frequency spacing will lead to a quasi-CW output where the emission frequency is swept in time. It was experimentally observed, for example, in a HeNe laser [90] and theoretically described in Refs. [91, 92] and [63], mainly pioneered by S. Harris. An experimental result from a Nd:YAG laser is shown in Fig. 1.6.

Detuning of the FM modulation from axial mode spacing led to transition from FM mode-locking to frequency swept operation,

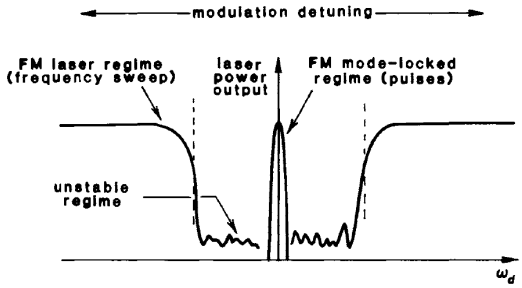

Figure 1.7 – Schematic of the transition from FM laser or frequency-swept operation to FM mode-locked, i.e. pulsed, state as a function of FM infection frequency detuning. Reprint from [54]. Reprinted with permission from University Science Books, all rights reserved.

i.e. FM laser operation. A schematic of the locking regions for FM mode-locked (pulses) and FM lasing (quasi-CW with frequency sweep) is presented in Fig. 1.7. A theoretical framework is provided for example in Ref. [66, 68, 91]. Siegman theoretically described the FM injection of a laser resulting in an FM state and found that the solutions are described by the Bessel functions $J_n(\Gamma)$, see Eq. 1.4.

$$\mathcal{E}(t) = E_0 e^{j\omega_0 t} \sum_{n=-\infty}^{\infty} J_n(\Gamma) e^{(j+n\omega_m)t} \tag{1.4}$$

$$= E_0 e^{j\omega_0 t + j\Gamma sin(\omega_m t)} \tag{1.5}$$

Here, ω_m is the modulation frequency, Γ is the phase modulation index related to Δm the single-pass modulation index by $\Gamma = \Delta m/(\omega_d T)$ with ω_d the detuning frequency of ω_m to the axial mode spacing frequency and T the round trip time.

A simple linear theory of this operation mode predicts [54], that the laser bandwidth is proportional to the inverse of the detuning between the driving frequency and the passive mode spacing. When the bandwidth approaches the linewidth of the gain medium the modes re-phase and the laser exhibits pulsed operation. In this case the pulse repetition rate is equal to the driving frequency.

In the following years, only a few papers went into further examination of FM lasers [93, 94] and even T. Hänsch used an FM laser for spectroscopy applications [95].

1.4 Milestones towards QCL frequency combs

In this section we will go through the history of frequency comb generation in QCLs. The results are mostly reported chronologically with selected intersection with the developments in microresonator frequency combs. The chronological order might jump between different developments, especially from mid-IR to THz QCLs, but therefore reveals the rich physics found in QCL frequency combs over two decades. Further, this section will not cover all papers like for example harmonic combs, results in interband cascade lasers (ICLs) or quantum dot (QD) lasers nor any dual-comb applications.

With the enormous success of mode-locked lasers emitting frequency combs and high intense and short pulses, the QCL community also tried to achieve mode-locking in QCLs. At the same time, it was clear that the in general fast gain recovery time of QCLs on the sub-picosecond to picosecond scale [96] works against passive mode-locking with fast saturable absorbers. First attempts in 2000 by active RF modulation of mid-IR QCLs were published by Paiella et al. in Ref. [97] at 10 K. The optically detected beatnote was partially due to RF pickup [97] and consisted of a large pedestal with high phase noise, actually not consistent with coherent locking. In the same year, the same group reported (falsely) self-mode-locking of a mid-IR QCL while observing an optical beatnote with a full-width half maximum (FWHM) below 100 kHz at the round trip frequency of 13 GHz [98]. Nevertheless, this already showed that some modes are to a certain extent coherently locked. From the comparison of the optical power of the beatnote RF power it was assumed that roughly 20% of the modes must be locked. At that time it was believed that the detected beatnote arises from pulses, i.e. all modes have equal phases, and it was not realized that an FM state with *randomly* spaced but fixed phases could also produce a frequency comb. The results in Ref. [98] were later reinterpreted as multi-mode operation from Risken-Nummedal-Graham-Haken (RNGH) instabilities and SHB [99] [6]. The typical splitting of the optical spectrum into two lobes was well explained by the Rabi splitting and IAC measurements of that state showed only *partial* mode-locking, i.e. not the typical 8:1 ratio in the IAC trace. Additionally, in 2001, it was demonstrated that mid-IR QCLs are indeed inherently fast

6. At that time mode-locking and frequency combs were used nearly as a synonym which was later shown to be not the case.

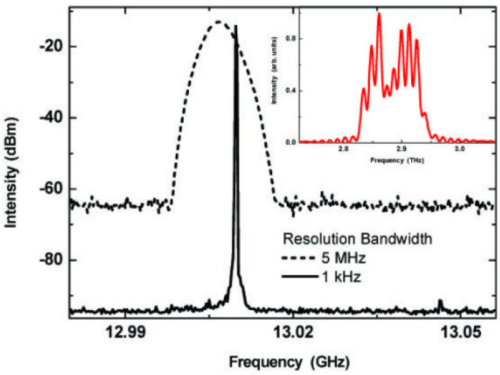

Figure 1.8 – Optically detected beating signal from a THz QCL in a Schottky mixer. The kHz linewidth indicates phase-locking of the optical modes. Reprinted with permission from Ref. [101]© The Optical Society.

and that the gain can follow GHz modulation [100] working against mode-locking.

The first narrow beatnote linewidth, indicating comb operation, with a free running FWHM of roughly 10 kHz, i.e. suitable for a potential phase-locked loops (PLLs), was reported by Barbieri et al. in Ref. [101] in the THz in 2005. The THz QCL was used in a heterodyne imaging experiment that was not related to any mode-locking experiment and the beatnote was detected with a Schottky mixer. The beatnote was used as a link of the optical domain to the RF domain but is was already mentioned that the narrow linewidth could indicate self-induced mode-locking. The recorded narrow beatnote and the corresponding spectrum are shown in Fig. 1.8. In the same year Betz et al. [102] showed that a single mode THz QCL can be stabilized by a PLL on the electrical signal in a heterodyne experiment with a far-infrared (FIR) laser, a general mechanism often used later.

In 2007 it was shown that THz QCLs are also very prone to fast RF modulation additionally favored by their double-metal waveguide geometry [103] supporting GHz modulation. In the same publication it was shown that very strong RF modulation, even far off the nominal round trip frequency, leads to optical sideband generation spaced by the injected frequency.

It was in the same year that the field of optical microresonators had their breakthrough by showing the generation of a monolith-

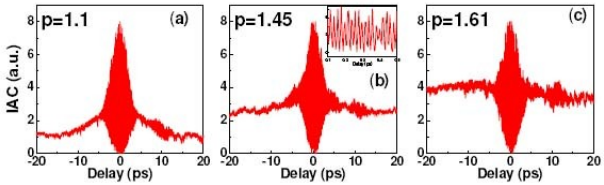

Figure 1.9 – IAC measurements of a strongly RF driven mid-IR QCL, where p indicates the current (in times the laser threshold). At low pumping currents the IAC trace in (a) shows a 8:1 ratio between peak and background indicating pulsed emission. IAC in (b) and (c) indicate emission different from mode-locking. Reprinted with permission from Ref. [105], © The Optical Society.

ically integrated frequency comb [104]. In contrast to traditional mode-locked lasers, the comb structure is generated by pumping a high-Q resonator in which the Kerr nonlinearities create the combs. Therefore, they were often called Kerr combs. The uniform spacing of the modes was shown to be $7.3 \cdot 10^{-18}$. The underlying phase relation was at that time not yet investigated nor the time profile.

As mentioned before, Gordon et al. investigated the multi-mode regime of mid-IR QCLs in 2008 in Ref. [99]. The traditional IAC methods from mode-locked laser community showed that the signal was repeating after the round-trip frequency but did not support the emission of pulses and therefore mode-locking. Although the periodicity appeared in the measurements, it was not related to an FM state yet.

The same group worked with an RF optimized laser cavity that allowed in 2009 to show an 8:1 peak-to-background ratio in the IAC measurement presented in Ref. [105]. Although the results looked very promising, the IAC measurement did not provide exact information on the phase relation of the modes nor on the time profile. Also the shape of the IAC trace differed from that of a perfect pulse and indicated some amount of dispersion. Some selected IAC traces are shown in Fig. 1.9. It was also well known in the mode-locked community that more sophisticated methods like Frequency-Resolved Optical Gating (FROG) [106] or Spectral Phase Interferometry for Direct Electric-field Reconstruction (SPIDER) [107] were needed to reveal the precise pulse nature and its phase. Due to the lack of these methods this paper did not find broad attention outside the QCL community.

In the meantime, significant understanding on RF modulating

THz QCLs [108] and the on-chip beatnote detection by an integrated Schottky detector [7] [109] was gained. It was shown that a THz QCL can be locked to an erbium doped fiber laser [110] and that the beatnote frequency can be RF injection locked [111].

The first measurement in the time domain of an active RF mode-locked QCL was performed in 2011 by Barbieri et al. in Ref. [12]. By electro-optical sampling with a femtosecond pulse laser, they measured the electrical field in time and could reconstruct the corresponding temporal intensity. The naturally single mode THz QCL was strongly RF modulated, roughly +10 dBm at the device, to generate an active mode-locked comb. Besides the RF injection, f_{ceo} was stabilized with an electronic servo loop from the electro-optical sampled signal with the locked reference comb. Therefore, it was also the first fully stabilized frequency comb emitted by QCLs. An excellent overview on this topic was given in Ref. [112]. Fig. 1.10 (a) shows the heterodyne signal from the electro-optical sampling, (b) the measured E-field in time and the red dotted line indicates the fit with equal phase assumption of the modes. Fig. 1.10 (c) shows the reconstructed intensity and (d) the fitted phases from the E-field measurement which where extracted later in a review paper [113]. A clear equal phase relation of all strong central modes is observed. It should be noted that the roughly one to two orders of magnitude longer gain recovery time of THz QCLs [114–116] makes active mode-locking more favorable in THz QCLs compared to mid-IR QCLs. Additionally to the modulation of losses, as done in actively mode-locked lasers, the RF modulation is assumed to also generate sidebands due to FWM in the optical domain, which pull and lock potential free running cavity modes.

In the same year, microresonator based combs revealed randomly spaced but fixed phase relation between comb modes [118]. In their experiment, the authors reshaped the emission, to achieve the shortest pulse possible, to inversely determine the phase relation of the modes. It also showed the existence of FM frequency combs [8] in microresonators. The different states and their generation mechanisms observed in microresonators are summarized in Ref. [119] and [120]. Microresonator frequency combs eventually showed soliton operation, i.e. stable pulses, in 2014 [121].

7. Around 2013 it was realized that even without special integration of a Schottky contact one can extract the electrical beatnote on the bias line.

8. Not to be mixed up with FM mode-locking.

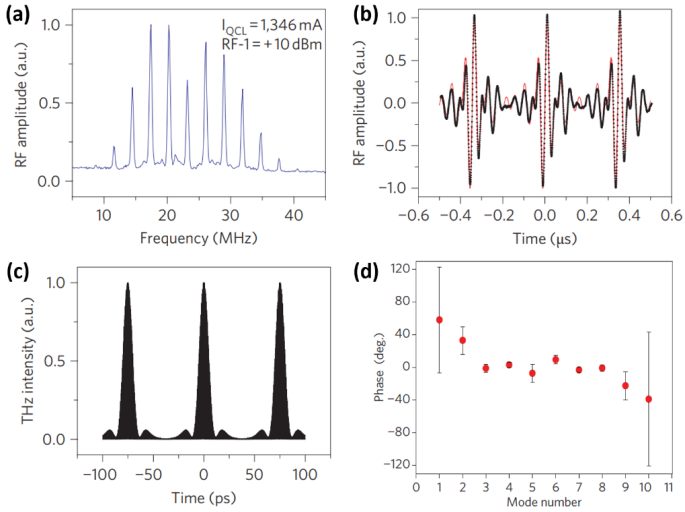

Figure 1.10 – Electro-optical sampling of a fully stabilized and RF injected THz QCL. (a) Heterodyne signal from the electro-optical sampling showing the down-mixed modes. (b) Measured temporal E-field (black) with assumed zero-phase fit (red). (c) Extracted temporal intensity from (b). (d) Extracted mode phases from (b) showing the nearly equal phase relation of the mode phases. (a-c) Reprinted and adopted by permission from Springer Nature Customer Service Centre GmbH: Springer Nature, Nature Photonics, Ref. [12] © 2011 Macmillan Publishers Limited and (d) reprinted/adopted by permission from Springer Nature Customer Service Centre GmbH: Springer Nature, Nature Photonics, Ref. [117] © 2013 Macmillan Publishers Limited.

The next milestone was then achieved in mid-IR QCLs in 2012 by Hugi et al. presented in Ref. [11]. The authors showed that the emission of a mid-IR QCL produces an optical beatnote with a linewidth below 10 Hz detected by a fast Quantum Well Infrared Photoconductor (QWIP) detector, indicating phase-locking of the optical modes. To show the FM nature of the device the authors placed a sheet of polyethylene with a wavelength dependent absorption into the optical path between the QCL and the detector. The lasing spectrum overlapped with one side of the absorption resonance and therefore the sheet acted as an optical discriminator which converted frequency modulation to amplitude modulation. The authors observed a 10 to 18 time increase of the optical beatnote power indicating an FM emission from this mid-IR QCL. If the QCL would have had an AM emission they would have expected to see a decrease in the beating signal strength due to absorption.

The authors also developed the so-called intermode beatnote spectroscopy (IBS). In such an experiment, the emitted light is passed through an Fourier-Transform Infrared Spectrometer (FTIR). Additionally to the slow intensity detector, the light is also focused onto a fast QWIP detector which detects the optical beatnote. It can be shown that the interferogram of the optical beatnote reveals the spectral content of the modes which produce exactly this beatnote [11]. Therefore, the spectral coverage of the frequency comb modes can be measured. At the same time, the proposed method does not reveal any direct mode phase nor temporal information of the comb. Nevertheless, the recorded interferograms exhibit certain symmetry properties around the Zero Path Delay (ZPD): if the QCL emits pulses, i.e. it is mode-locked, the intermode beatnote interferogram will have a peak at the ZPD. If the phases of the comb modes are unequal but distributed fixed around 2π, the intermode beatnote interferogram will exhibit a minimum in the intermode beatnote interferogram at the ZPD. Exactly such a minimum was found in the free running experiments as shown in Fig. 1.11 (b) together with the intermode beatnote spectrum in (a). This further confirmed the FM nature of the comb. In the supplement they also showed a high-resolution spectrum (0.0026 cm^{-1}) which supports the equidistant mode spacing and showed that RF injection of 26.6 dBm led to a collapse of the comb state in this laser. Further, in a heterodyne experiment with a distributed feedback (DFB) laser they showed that by current tuning this heterodyne signal is shifting in frequency. At the same time, f_{rep} also shifted slightly as a function of current, but the total shift of the heterodyne signal could not only come from the slight f_{rep} shift and therefore resulted mainly from f_{ceo} tuning.

In the following years, additional experiments on RF modulation and injection of mid-IR QCLs as well as on their nonlinear properties were performed [47, 122–124].

The next milestone was achieved in 2014 by Burghoff et al. in THz QCLs by presenting a phase sensitive measurement of a comb state [17]: Shifted Wave Interference Fourier Transform (SWIFT). SWIFT is an extension of the intermode beatnote spectroscopy in which the optically detected beatnote is additionally IQ demodulated by the electrically extracted beatnote. Therefore, one can show [17] that SWIFT provides information about the phase differences of adjacent modes and the coherence of the optical spectrum. This was possible since the authors exploited the fact that the electrical beatnote can easily be extracted from the bias-line via a bias-tee. The

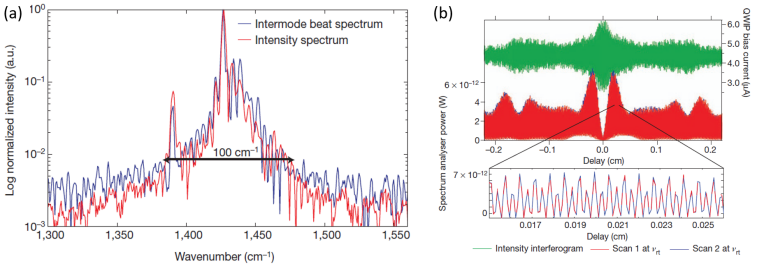

Figure 1.11 – (a) Intensity spectrum and IBS spectrum showing the spectral overlap and therefore the mode coherence. (b) Intensity and IBS interferograms. The minimum at the ZPD in the IBS interferogram indicates FM emission. Reprinted and adopted by permission from Springer Nature Customer Service Centre GmbH: Springer Nature, Nature, Ref. [11], © 2012 Nature Publishing Group.

details of SWIFT are discussed in chapter 8. The recorded intensity interferogram, the I and Q interferograms of the demodulation, and the correlation of the modes, are shown in Fig. 1.12. Additionally, the QCL in [17] had an integrated corrugated structure for dispersion compensation. Contrary to electro-optical sampling, SWIFT did not rely on an optical reference comb but needed a fast detector. The repetition rate was actively stabilized by an electrical feedback loop from the fast detector signal and f_{ceo} was left free running. Later, it was shown that with the intensity spectrum and the phase difference of adjacent modes, the time domain signal can be reconstructed [125]. For the temporal reconstruction one needed to verify that the modes are coherently locked (SWIFT spectrum compared to spectrum product) and note that the mode phases could only be accurately determined from cumulative summing of the phase differences, i.e. assuming no-gaps in the spectrum. In the case of a spectral gap, as it was the case in Ref. [125], the temporal intensity could still be evaluated statistically by introducing a random phase at the spectral gap and evaluate the temporal intensity multiple times to get an uncertainty range. In the case of the particular THz QCL in [125], it was seen that the different spectral lobes produce significant AM output at different times, i.e. sign of temporal hole burning, whereas the total output is rather flat. One lobe exhibits a saw-tooth like instantaneous frequency (FM operation) whereas the other showed even clear pulses, i.e. AM operation [125]. The results qualitatively agreed with the theory provided in Ref. [126] and were later, for this specific active region, reproduced by full

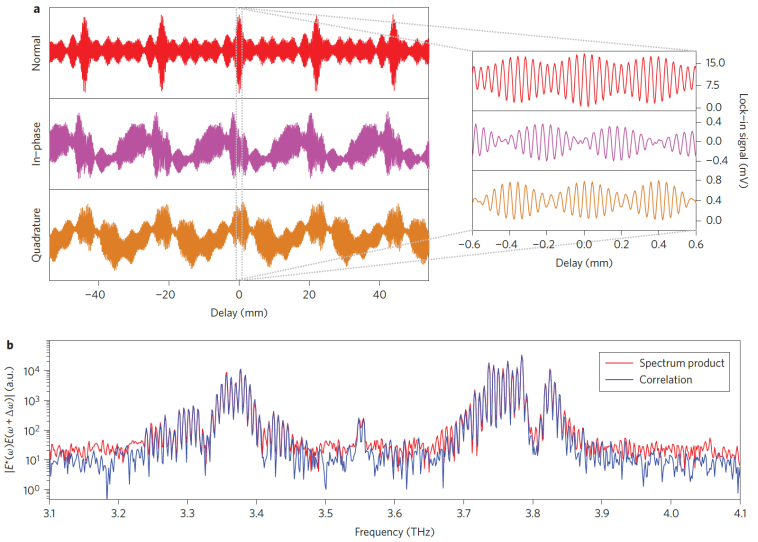

Figure 1.12 – SWIFT measurement of a THz QCL. (a) Intensity interferogram and I and Q traces from a SWIFT measurement. (b) Coherence of the spectrum product and the SWIFT spectrum. Reprinted by permission from Springer Nature Customer Service Centre GmbH: Springer Nature, Nature Photonics, Ref. [17], © 2014 Nature Publishing Group.

Maxwell-Bloch simulation [127].

In the same year, Villares et al. proved the equidistant mode spacing of mid-IR QCLs in a dual-comb experiment to a fractional accuracy of $7.5 \cdot 10^{-16}$ [128]. Therefore, the frequency comb nature of the emission spectrum was fully proven in free running QCLs. Further, Wienold et al. [41] showed indication of comb operation in broadband THz QCLs by means of a self-mixing experiment, i.e. self-mixing intermode beatnote spectroscopy (SMIBS), which does not require any fast detectors.

The next step went into broadband emission in THz QCLs where the monolithically integrated self-referenced, i.e. octave spanning, frequency comb seemed feasible. That THz QCLs are capable of emitting over more than one octave in a multi-mode regime was finally shown by Rösch et al. in 2015 [38]. At the same time the comb operation, indicated by a narrow beatnote, was limited to 624 GHz bandwidth. The comb bandwidth is limited mainly by group velocity dispersion (GVD) effects. At the same time it was

shown that mode control by introducing lossy side absorbers cleans up the spectral modes [129, 130]. By optical injection seeding, short pulses of 2.5 ps length were achieved in such a structure [130]. The same broadband active region was investigated in Ref. [131] in an electro-optical sampling experiment. The experiment did not reveal a clear picture as the free running operation indicated the generation of sub-combs and strong RF injection seemed to only partially lock the modes. Therefore, no clear comb operation could be identified.

In 2017 Mottaghizadeh et al. [132] presented 5 ps short pulses emitted by an active mode-locked THz QCL on a bandwidth of 250 GHz. As in their previous work [133], the modes showed a phase difference close to zero corresponding to mode-locking. The surprising result was actually the appearance of a double pulse in the E-filed time domain measurement. The reason for the double pulse nature was not identified by the authors but it was induced by the special spectral shape very close to that of a second harmonic comb state described as well in Fig. 1.3.

Simultaneously, it was shown that strong RF injection in single plasmon THz QCLs led to significant spectral broadening [134]. But at the same time, the coherence was not shown, and the extracted mode spacing from the spectrum indicated only partial locking of the modes even though stated differently by the authors. Nevertheless, the clear eye-diagram of the beatnote showed its stable free running operation on a narrower bandwidth.

There were also different results on dispersion, RF injection or broadband comb operation [39, 135–137], but the next significant result towards understanding frequency comb formation in QCLs was made by Singleton et al. in 2018 [88]. The authors showed by means of SWIFT on a free running device that for mid-IR QCLs the phase differences between adjacent modes were linearly swept from $-\pi$ to π, shown in Fig. 1.13. This finally led to a linear chirp of the instantaneous frequency of this FM mid-IR QCLs. These results were in contrast to the FM combs in microresonators where no clear phase relationship was found [118].

One year later, Hillbrand et al. showed in Ref. [138] by means of SWIFT that a mid-IR QCL in a multi-mode regime can be RF injection locked to be fully coherent over the whole spectrum while preserving the FM nature, i.e. linear phase difference and linear chirp, of the emitted frequency comb. The result seemed first unintuitive since from strong (15 dBm) RF injection one might expect

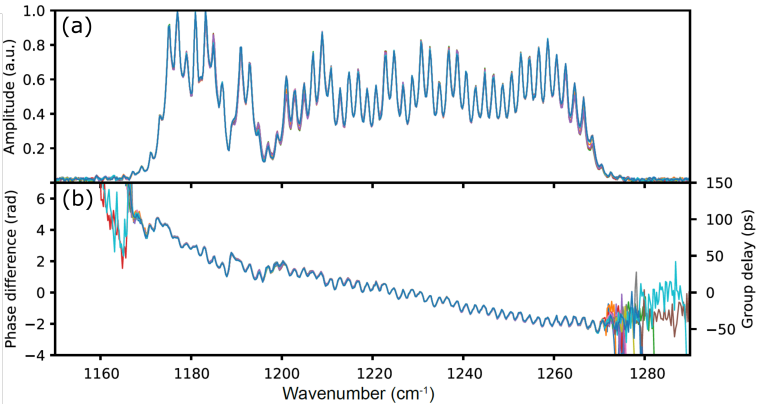

Figure 1.13 – Multiple SWIFT measurements of a mid-IR QCL. (a) Amplitude spectra from twelve SWIFT measurements showing the reproducibility of SWIFT. (b) The extracted phases differences indicate a linear chirp of the free running mid-IR QCL. The phase difference is directly related to the group delay. Reprinted with permission from Ref. [88] © The Optical Society.

equal phase locking of the modes [9]. In the mean time, Singleton et al. showed that the linear dispersion could be compensated for by an external grating compressor resulting in 12 ps short pulses [139].

In the THz, Consolino et al. recreated and realized in Ref. [140] a fully stabilized THz QCL similar to Ref. [133]. Instead of electro-optical sampling they produced a reference optical rectified comb in the THz which led to a dual-comb setup. Although the RF power was not stated for this experiment, it seemed to be a *mild* RF injection since the resulting E-field represented an FM and not a mode-locked comb. Due to the supposed mild injection locking this state was most probably closer to the free running case. In a later experiment [141], the same authors repeated the experiment, but locked the repetition rate with an electrical PLL and software corrected for the f_{ceo} fluctuations. It showed that this free running f_{ceo} was stable on the order of seconds but slow drifts over multiple minutes were clearly observed, leading to a slightly changed intensity profile.

Other groups also worked on heterogeneous broadband THz QCLs towards octave spanning frequency combs by implementing a Gires-Tournois interferometer (GTI) for dispersion compensation [142]

9. This is currently investigated and most probably arises from the linewidth enhancement factor (LEF) resp. the polarizability of the active region.

reaching similar comb bandwidths as in uncompensated structures [39]. We showed in Ref. [143] that also homogeneous structures were able to emit over a bandwidth of more than 1.8 THz in a self-oscillating bias state. In Ref. [144] the same structure showed broad comb operation up to 800 GHz under RF injection up to 80 K due to the embedding of the active region (AR) into a double-metal copper device adopted from our high-temperature THz QCL fabrication process [32].

In 2020, Hillbrand et al. showed in Ref. [145] that a special designed homogeneous active region and the resulting mid-IR QCL could be active mode-locked. This result completed the previous reported indications of mode-locking capabilities of mid-IR QCLs [146]. The pulse length was measured to be 6.5 ps long by SWIFT and IAC [145].

Further, Opačak et al. from the same group eventually provided a theoretical model which numerical results reflected the observed linear chirp in free running mid-IR QCL frequency combs [89]. At the same time, the effective semiconductor Maxwell-Bloch equation approach for a Fabry-Pérot multi-mode QCLs by Silvestri et al. [147], originally predicting Quantum Dot laser states, also recovered the temporal behavior of mid-IR QCLs. The work by D. Burghoff in Ref. [148] [10] came up with a nonlinear Schrödinger Equation which provided an analytical solution, as well as numerical one, which accurately covered the physics in mid-IR and THz QCLs by means of an active cavity mean-field theory. The results were related to Turing rolls and were referred as *extendons* in analogy to solitons. The analytical and experimental results are presented in Fig. 1.14.

Schneider et al. then further experimentally investigated the RF injection of heterogeneous active regions under strong RF injection which did led to significant broadening of the intensity spectrum, still in an FM state rather then a mode-locked state [149]. Täschler et al. further showed that such an RF injected QCLs had a nearly linear chirp which could be compensated by an external grating leading for the first time to sub-picosecond pulses [150]. The pulsed nature was confirmed by SWIFT, IAC measurement and by a sum-frequency generation (DFG) upsampling technique developed by Täschler et al.. The latest results on strongly injected broadband THz QCLs are provided in chapter 9.

10. This work is recently further extended and a draft was published on arXiv: http://arxiv.org/abs/2110.04356

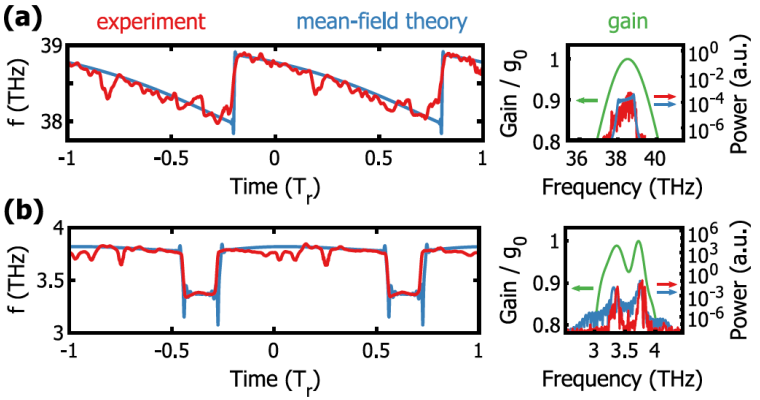

Figure 1.14 – Results from Nonlinear Schrödinger Equations predicting analytically and numerically the comb formation in QCLs. (a) Experimental and theoretical results for a mid-IR device. (b) Experimental and theoretical results for a THz device. Reprinted with permission from [148] © The Optical Society.

So far, Fabry-Pérot type of cavities were investigated. But lately, theoretical predictions of solitons in an active medium ring resonator [151, 152] led to fabrication of ring QCLs in the mid-IR [48] and THz [49]. Nevertheless, these results did not yet show soliton formation in QCLs. It was only recently that Meng et al. could show the formation of dispersive Kerr solitons in ring QCLs [153]. The main results are shown in Fig. 1.15.

We also want to mention the approach of DFG of THz radiation by mid-IR QCLs [37]. The developments showed that these devices could also produce a THz comb at room temperature, but with significantly lower output power compared to direct frequency combs emitted by THz QCLs [154].

1.5 Conclusion

In this chapter we first look at the different sources able to emit THz radiation, followed by a short description of the QCL working principle. Secondly, we mathematically defined the frequency comb and summarized the different terminologies like mode- and phase-locking, FM comb and so on. In a historical review we saw that since the first demonstration of a laser, researchers went quite soon into the generation of pulsed emission first by means of active mode-

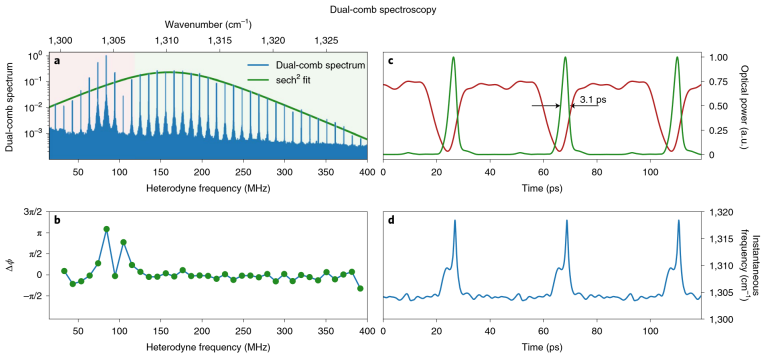

Figure 1.15 – Soliton formation in ring mid-IR QCLs. (a) Measured intensity spectrum from a dual-comb experiment with a reference mid-IR QCL. The sinc^2 square fit indicates the soliton nature. (b) Extracted phase differences from the dual-comb experiment. (c) Reconstructed waveform of the soltion portion of the spectrum (green) and the background (red). (d) Instantaneous frequency of the waveform in (c). Reprinted and adopted by permission from Springer Nature Customer Service Centre GmbH: Springer Nature, Nature Photonics, Ref. [153], © 2021 Nature Publishing Group.

locking and Q-switching. It was then shown that placing a saturable absorber into the laser cavity led to even shorter pulses. Until 1990, the workhorse for generating short pulses was the dye laser.

With the developments of the Ti:sapphire laser a new type of an effective saturable absorber based on Kerr lensing was discovered, which led to the emission of femtosecond pulses for the first time in a single resonator. With KLM laser and further developments of the SESAM as well as integrated dispersion compensation, very stable pulses were generated.

T. Hänsch realized that stable and short pulses lead to a spectrum consisting of equally spaced modes well defined by a repetition frequency and a carrier envelope offset frequency, which lie in the RF domain. By locking the repetition and carrier envelope offset frequency to a reference source, they showed the first fully and absolute stabilized frequency comb which linked the optical with RF domain. Therefore, the very complex frequency chains, previously used, became redundant. The group of J. Hall then showed that by producing an octave-spanning spectrum in a nonlinear fiber the comb can be self-referenced and the f_{rep} and f_{ceo} locking was achieved in one single step.

Since comb emission is not only restricted to mode-locked lasers

we shortly looked into the history of FM lasers which also produce comb spectra but with quasi-constant emission. FM lasers were demonstrated in the 60s by means of active modulation and have an underlying frequency sweep.

The absence of any passive FM laser and the enormous success of mode-locked laser probably pushed first experiments in QCLs towards mode-locking. First attempts showed comb-like spectra, but mode-locking could not be verified. It was then in THz QCLs, exhibiting a longer gain recovery time than mid-IR QCLs, which due to active modulation led to pulsed emission shown by electro-optical sampling. The breakthrough on the understanding of free running frequency combs emitted mid-IR QCLs was the experimental verification of an FM relation of the laser modes. The FM nature could then be further verified by SWIFT, a newly developed method for measuring the phase relation and the coherence between comb modes. With the experimental observation of the underlying linear chirp in mid-IR QCLs there came a series of numerical and theoretical models which predicted exactly this type of frequency comb generation in QCLs.

In a series of measurements, it was then shown that RF injection led to significant broadening of QCLs in the FM and AM states and that by GVD compensation the emission from a FM state could be compressed to sub-picosecond pulses for the first time.

Due to the large understanding gained in the last years, the QCL community also went into the direction of generating solitons in ring cavities which were experimentally measured in a mid-IR ring QCL.

In the following chapters, we will now go into specific examples of comb operation in homogeneous and heterogeneous THz QCLs.

2

Broadband THz Quantum Cascade Laser Waveguides

The basis for frequency comb operation in THz Quantum Cascade Lasers (QCLs) is given by the design and growth of broadband active regions, embedded in a cavity which allows multi-mode operation. The range for comb formation further depends on the four-wave-mixing (FWM) and coupling of the cavity modes, the dispersion of the cavity and the gain, and on the suppression of undesired higher order transverse cavity modes. When it comes to extraction of beating signals (or the RF modulation of devices), one further has to optimize the laser mounting and the cryostat. As this list could be extended even more we will try to focus on the essential ingredients here. Therefore, in the following we will briefly go through the topic of active region (AR) growth and simulation in section 2.1. In section 2.2 we will discuss the cleanroom fabrication and the numerical modeling of the THz waveguide. In the last section 2.3 we will briefly go through the physical mounting of THz QCLs on an RF optimized flow cryostat.

2.1 Quantum Cascade Laser active regions

The basis of every THz QCL frequency comb is a broadband AR. To achieve a broad gain medium we rely on two things: accurate simulation of AR designs and a high-quality growth of the heterostructure. Therefore, we briefly go into different THz QCLs designs and their simulation followed by different growth techniques.

Active Region designs and simulation

In chapter 1, Fig. 1.1 we briefly saw the basic working principle of QCLs. In actual realizations, there are different designs which rely on various transitions and scattering processes observed in quantum well (QW) structures. Designing a QW structure allows to engineer for example the upper-state lifetime or the extraction efficiency. Further, optimized designs allow to reduce non-radiative transitions into other states. Detailed information can also be found in the book of J. Faist [28] or Ref. [155] especially for THz QCLs. In the following, we present in a schematic manner in Fig. 2.1 the most common AR design approaches. Fig. 2.1 (a) shows the chirped superlattice (SL) approach which consists of several QWs. The transition happens between minibands, i.e. from a lower state of a miniband to a top state of the next lower miniband. The bound-to-continuum (BtC) design is shown in Fig. 2.1 (b) and (c) for a 7 QW and 4 QW design. The lasing transition is here from a single upper lasing state to a miniband. This leads in general to a more diagonal transition in real space, slightly decreasing the oscillator strength, but increasing the upper state lifetime [156]. The depletion of the lower level can additionally be enhanced by phonon scattering. Fig. 2.1 (d)-(f) present designs which consist of a lower number of QWs per period, resulting in more isolated states rather than minibands and rely on fast scattering mechanism to deplete the lower lasing level. The designs are therefore the so-called Scattered Assisted (SA), Resonant Phonon (RP) and Direct Phonon (DP) design and are especially employed in high temperature devices [31, 32].

By now we have seen some building blocks and initial designs which are still oversimplified [1]. They provide us an intuitive picture on how different QCLs work, but for accurate predictions one needs more sophisticated methods. We will briefly mention different approaches here and refer the reader to detailed papers on this topic [157–161]. The total Hamiltonian consists of terms describing the heterostructure, the photons as well as the scattering mechanisms and their interactions. Different models solve certain aspects of this Hamiltonian exactly, whereas others are simplified or disregarded. Therefore, the simplest approach is to solve the Schrödinger + Poisson Equation for one or two periods of the heterostructure to find the wavefunctions and static electron distribution and work with a *rate equation* model [28]. Additional terms in the Hamilto-

1. For examples we did not show higher energy states.

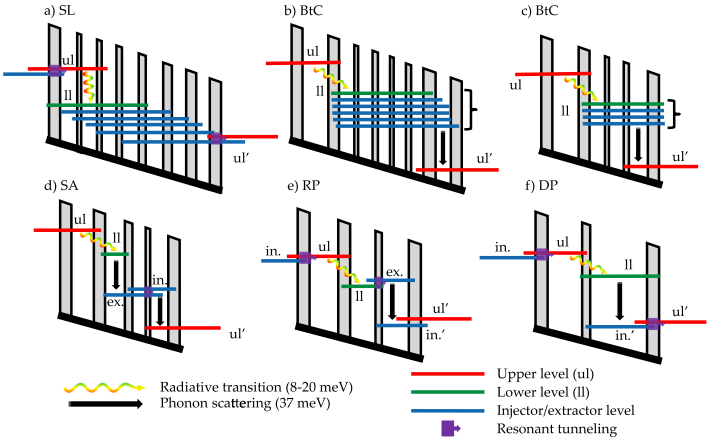

Figure 2.1 – Schematic of several THz QCL designs (a) Chirped Superlattice (SL). (b) Bound-to-Continuum (BtC) realized with 7 quantum wells. (c) Bound-to-Continuum (BtC) realized with 4 quantum wells. (d) Scattering Assisted (SA). e) Resonant Phonon (RP). (f) Direct Phonon (DP). At the bottom, a legend shows the meaning of each used symbol. Figure adapted from Ref. [23].

nian can be entered from empirically extracted values. Further, the rate equation approach cannot include the light-matter interaction and the coherence between states. Therefore, a density-matrix approach [162] can solve this problem, as it includes the carrier-light interaction. This can be done on a subset of states or by a full density-matrix formalism. The full quantum transport can be described by Non-Equilibrium Green's Function (NEGF) [2] approach. This method consists in solving the whole Hamiltonian, which on the contrary is very complex and numerically heavy.

Due to scattering processes and the energy of the optical phonon, the simple rate-equation approach cannot accurately predict the gain in THz QCLs. Therefore, one needs to exploit the density-matrix or better the NEGF approach to accurately model THz ARs.

Active Region growth

One step is to design and predict a working AR, the other step is to actually grow the final structure. This can be done by metalorganic chemical vapour deposition (MOVCD) or molecular beam

2. Special thanks here to Martin Franckié.

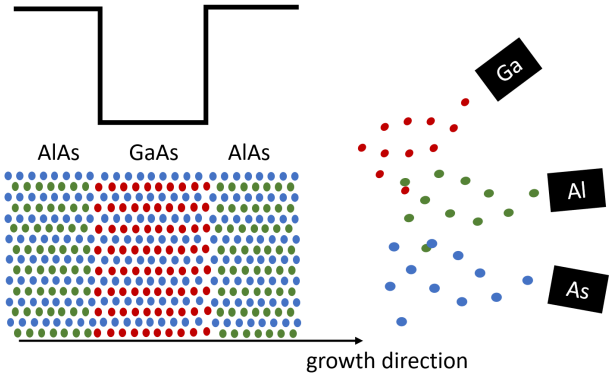

Figure 2.2 – Schematic of QW growth by means of MBE. By alternating between AlAs and GaAs, one defines the QWs. On top is the illustration of the resulting potential. Figure inspired by Ref. [28]. Today's QCL ARs are generally latticed matched InGaAs/$Al_xIn_{1-x}As$ or GaAs/$Al_xGa_{1-x}As$ growths.

epitaxy (MBE). Both techniques need to grow with high spatial coherence, low defect density, high purity and well calibrated doping. At the same time, a QCL consists of many QWs which need to be grown. This leads in general to several µm thick depositions. A schematics of MBE growth of a AlAs/GaAs QW is shown in Fig. 2.2. It is based on thermal evaporation in an ultra-high vacuum environment and allows growth accuracy at the Å level. The growth can also contain other components like In and Al to grow lattice matched InGaAs/$Al_xIn_{1-x}As$ or GaAs/$Al_xGa_{1-x}As$ ARs. The latter is often used to grow THz QCLs. On the contrary, MOVCD works with vaporized chemicals, which contain the desired atoms, which are transported into the reactor together with other gases. There, a critical chemical reaction takes place, which turns the chemicals into the desired crystal. The ARs grown in this work have been grown by MBE [3].

2.2 Double-metal waveguide

After the heterostructure growth, the AR needs to be processed into a laser or any other desired structure. In the demonstration of the first THz QCL [16], the authors used a so-called single-plasmon waveduide. It consisted of a metal top contact and a highly-doped

3. Special thanks here to Mattias Beck.

GaAs bottom layer to confine the mode inside the AR which also acted as a grounding plane. In general, these waveguides lead to an efficient outcoupling of the lasing mode with good far field properties [155, 163]. But due to the plasmonic nature at the doped layer interface the mode is only partially overlapped with the AR and the overlap factor is strongly wavelength dependent. Therefore, the single plasmon waveguide does not allow tight confinement of the mode with the AR over a broad bandwidth, especially at longer wavelengths. In the case of broadband THz QCLs, one can exploit the double-metal waveguide [164, 165]. This type of waveguide extends the wavelength range to lower frequencies and increases the overlap factor to nearly unity. Additionally, the threshold gain is significantly lowered compared to the single-plasmon waveguide [166]. They allow broad comb emission in the THz as shown in Ref. [17, 38] even though single-plasmon waveguide can also emit frequency combs [41]. One major drawback of the double-metal waveguide is the sub-wavelength confinement, which leads to an intrinsic impedance mismatch at the facets creating a highly divergent far field [167].

The fabricated devices in this thesis are all based on the double-metal waveguide and we will therefore go through the main fabrication aspects in detail in the next subsection.

2.2.1 Fabrication

The general process for double-metal waveguide was already developed in the previous years [164, 166] and here we focus on the essential cleanroom fabrication steps of a dry-etched, double-metal waveguide.

Fig. 2.3 provides a sketch of these essential steps. A Ti/Au or a Ta/Cu layer is evaporated by an electron-beam evaporator on the active region and a highly doped carrier substrate. The latter is used for heat extraction as well as for additional electrical grounding of the structure. The Ti and Ta act as an adhesion layer for Au and Cu, respectively. The AR is then thermo-compressive wafer-bonded during 15 min at 320°C and 4.5 MPa to the carrier substrate, followed by mechanical and chemical removal of the MBE carrier substrate. By photolithography the waveguide structure is printed onto the AR and the top contact, a Ti/Au or Ta/Cu/Ti/Au, is evaporated. The additional Au layer on the Cu prevents oxidation

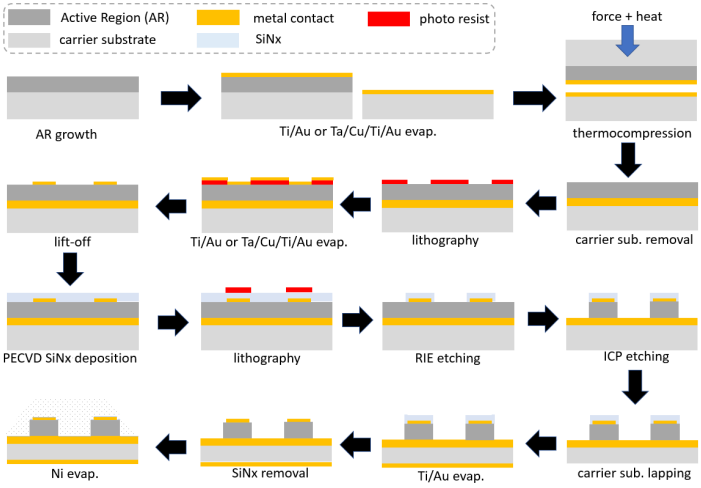

Figure 2.3 – Cross-section view of essential cleanroom fabrication steps as described in the text and in detail in Ref. [23, 38, 168]. (Sketch does not scale.)

of the top contact and favors wire bonding of the device. After lift-off of the residual Au, a 3 µm tick SiNx layer is deposited by plasma enhanced chemical vapor deposition (PECVD) for further dry etching. By an additional photolithography step and reactive ion etching (RIE) of the SiNx, a hardmask for the dry-etching step is created. Here, the hardmask allows the implementation of a set-back for side absorbers which are discussed later in detail. The AR is then etched by inductively coupled plasma etching (ICP) which creates the final waveguide. To increase the thermal behavior of the device, the carrier substrate is mechanically lapped down and a Ti/Au layer for indium soldering is evaporated on the back. By wet etching in a 1:5 hydrofluoric acid (HF), the remaining hardmask is removed and a thin layer of 5-10 nm of Ni for the lossy side absorbers is optionally evaporated on top of the device [4]. The final cleavage of the sample then defines the cavity and leads to nearly perfect facets due to the crystalline nature of AR. The cleaved devices are indium soldered to a copper mount and electrically contacted via wires bonds. Different mounting schemata are presented in section 2.3.

4. The Ni evaporation can also be performed in a post-process on already mounted devices.

2.2.2 Fabry-Pérot cavity modes

In the previous subsection we saw how to fabricate a double-metal THz QCL. By cleaving the processed structures, we form a Fabry-Pérot cavity, whose modes we would like to describe. To do so we first have to describe the refractive index of our cavity, which will be frequency dependent as we will see now.

Most THz QCLs grown nowadays, and all those used in this thesis, are based on a GasAs/AlGaAs heterostructure. Although GasAs/AlGaAs allows to grow high quality active regions, the TO and LO phonon of GaAs are centered close to 8.03 THz and 8.75 THz forming the so-called Reststrahlenband [169]. Due to the close location of the GaAs phonon to the target emission frequencies, the real refractive index n is frequency dependent, leading to a relatively large group velocity dispersion (GVD). Therefore, we first investigate bulk GaAs, the main contribution of GVD, followed by 2D simulation of the cavity modes.

Bulk GaAs

In this subsection we use the following definition of the complex refractive index $\tilde{n}$

$$\tilde{n} = n + ik \tag{2.1}$$

and

$$\varepsilon_r = \varepsilon_1 + i\varepsilon_2 \tag{2.2}$$

for the complex dielectric function ε_r. $\tilde{n}$ and ε_r are related by

$$\begin{aligned} \varepsilon_1 &= n^2 - k^2 \\ \varepsilon_2 &= 2nk. \end{aligned} \tag{2.3}$$

The real part n of $\tilde{n}$ corresponds to the refractive index, while the imaginary part k is related to the losses α as

$$\alpha = \frac{4\pi}{\lambda} k \tag{2.4}$$

with λ being the wavelength.

Therefore, the refractive index n is a function of the complex dielectric function and reads as

$$n = \frac{1}{\sqrt{2}} \left(\varepsilon_1 + \sqrt{\varepsilon_1^2 + \varepsilon_2^2} \right)^{1/2} . \tag{2.5}$$

ε_1, ε_2 are the real and imaginary parts of the dielectric function. ε_r is well described in textbooks [170, 171] by a Lorentz oscillator model, which is then eventually written as [169]

$$\varepsilon_r(\omega) = \varepsilon_\infty + (\varepsilon_{st} - \varepsilon_\infty) \frac{\Omega_{TO}^2}{\Omega_{TO}^2 - \omega^2 - i\Gamma_{TO}\omega} \tag{2.6}$$

where ε_∞ is the *high frequency dielectric function*, ε_{st} the *static dielectric function*[5], Ω_{TO} the TO phonon frequency and Γ_{TO} accounts for the intrinsic losses. These values are determined experimentally and found to be $\varepsilon_\infty = 10.89$, $\varepsilon_{st} = 12.90$, $\Omega_{TO} = 2\pi \cdot 8.034$ THz and $\Gamma \approx \frac{1}{100\ fs}$, where Γ is temperature dependent [172]. From Eq. 2.6 we see that $\varepsilon_r(\omega = 0) = \varepsilon_{st}$ corresponds to the low frequency and $\varepsilon_r(\omega \to \infty) \approx \varepsilon_\infty$ to the high frequency limit.

By inserting Eq. 2.6 into Eq. 2.5 we can determine the refractive index n of GaAs as well as its group refractive index n_g defined as $n_g = n + \omega \left(\frac{dn}{d\omega} \right)$. Fig. 2.4 (a) shows the calculated refractive and group index of GaAs in the range of 1.5 THz to 4.5 THz. It becomes evident that the refractive index significantly changes over this frequency range.

In addition, the group velocity is defined as

$$v_g = \left(\frac{d\omega}{dk} \right) = \frac{c}{n + \omega \left(\frac{dn}{d\omega} \right)} \tag{2.7}$$

and the GVD as

$$GVD = \frac{d}{d\omega} \left(\frac{1}{v_g} \right) . \tag{2.8}$$

5. Some authors might use $\boldsymbol{\varepsilon_{st}\varepsilon_0 = \varepsilon_0}$, where ε_0 the "static dielectric constant of the crystal" and ε_0 the "static dielectric constant of the vacuum".

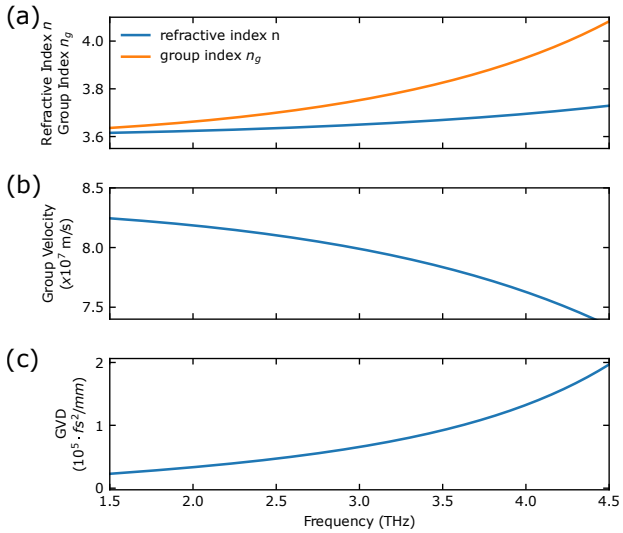

Figure 2.4 – (a) Refractive index and group refractive index, (b) group velocity and (c) GVD for bulk GaAs based on Eq. 2.6.

The corresponding curves for v_g and GVD are presented in Fig. 2.4 (b) and (c), respectively. Therefore, the bulk GaAs refractive index n and therefore its GVD is non-constant due to the proximity of the Reststrahlenband.

2D Simulation: Losses and Mode-Control

Even though the description of bulk GaAs provides already many insights about the general GVD effects, it does not really cover the effective refractive indexes of different normal (cold) cavity modes of THz QCLs and their losses. To cover the geometrical effects, we perform 2D Comsol simulations on typical double-metal waveguides similar to Ref. [172, 173].

A general device is modeled by bulk GaAs as described by Eq. 2.6, includes the doping layers at the top and bottom contact and as well as the metal contacts themselves. In the latter, we simply assume Au or Cu contacts, leaving out the thin Ti or Ta layer. For the top contact we include lossy Ni on the side absorbers for transverse mode control, as shown and discussed in Ref. [129, 130]. The purpose of these side absorbers, also referred to as setbacks, is to in-

crease losses of higher order transverse modes while only marginally increasing the losses for the fundamental transverse mode. The higher order transverse modes naturally have a higher overlap factor with the side absorbers and therefore experience higher losses than the fundamental transverse mode. For waveguide widths around 80 µm suitable side absorber widths of 3 to 4 µm are found experimentally and their effect can be further tuned by selecting the thickness of Ni. The typical Ni thickness is 5 nm, which can also be evaporated or increased in a postprocess.

Since the doping in the AR is relevant for the transport of the electrons during operation, i.e. electrons are coherently coupled to the light, we set $\Gamma = 0$ in Eq. 2.6 for GaAs and the absorption of the AR will be calculated separately for example with a Schrödinger+Poisson solver, which simulates the AR design. Other approaches [172, 173] used an average doping value of the AR.

Further, we model the temperature dependence of the top and bottom doping layer of the AR by the Drude-Lorentz model:

$$\varepsilon_{r,doped} = \varepsilon_r(\omega)\left(1 - \frac{\omega_p^2}{\omega - i\gamma\omega}\right) \tag{2.9}$$

with ω_p the plasma frequency and $\gamma = 1/\tau$ the scattering rate with γ temperature dependent. The scattering time τ is further related to the mobility μ as

$$\mu = e\tau/m^* \tag{2.10}$$

with e the electronic charge and $m^* = 0.067m_0$ the effective electron mass of GaAs. For the simulations we take now the temperature dependent mobility model and values from Ref. [174] to determine μ and therewith γ in Eq. 2.9. In addition, the plasma frequency is defined by the electron density n_s as $\omega_p = \sqrt{\frac{n_s e^2}{\varepsilon_0 \varepsilon_r m^*}}$. This leads especially at low frequencies to free-carrier absorption.

Similar, we describe the temperature dependent top and bottom contact, i.e. metals, of our waveguide by the Drude model which reads as

$$\varepsilon_{r,metal}(\omega) = 1 - \frac{\omega_p^2}{\omega^2 + i\omega\tau^{-1}} \tag{2.11}$$

where again the temperature dependence is included in the scattering time τ.

Empirical values can be found in Ref. [175, 176]. The temperature dependent scattering time τ is also related to the DC conductivity σ_{DC} and DC resistivity ρ_{DC} as

$$\tau^{-1} = \varepsilon_0 \omega_p^2 \rho_{DC} = \varepsilon_0 \omega_p^2 \frac{1}{\sigma_{DC}} \tag{2.12}$$

and values are taken from Refs. [177], [178] and [179]. The extracted data for different metals and temperatures are interpolated and provided to the 2D Comsol simulations.

In the following we consider a double-metal waveguide with a width of 80 µm and a height of 13 µm. The height is given by the AR growth and is generally on the order of 10 to 15 µm for THz QCLs. The width is defined by the lithography step and varies typically from 40 µm to 150 µm, although there is no strict upper or lower limit. Most of the ridges investigated in this thesis are about 80 µ m wide. For narrower and wider widths the optimal side absorber width needs to be adjusted. Further, we vary in these simulations the side absorber width on each side from 1 µm to 5 µm and the AR temperature takes values T = 60 K, 150 K, 220 K and 293 K. The upper absorber width limit of 5 µm is found experimentally to effectively suppress higher order transverse modes but also noticeably reduces the lasing performance. Side absorber widths around 3.5 µm seem to provide an optimal compromise of enough higher order transverse mode suppression and maintaining the lasing performance for 80 µm wide waveguides. The mode solutions considered are the fundamental TM00 mode and the next two higher order modes TM01 and TM02. All modes at 2.75 THz as well as the waveguide geometry are shown in Fig. 2.5.

By running the eigenmode solver (COMSOL®) for frequencies from 1.5 to 4.5 THz we find the effective refractive index n and the corresponding effective group index n_g for each mode, which are presented in Fig. 2.6 together with the bulk GaAs refractive index. First, the effective refractive index as function of frequency of each mode, and therefore the corresponding GVD, keeps nearly unchanged for varying setback values and different temperatures (not shown). Second, it becomes evident that the refractive index at lower frequencies as well as for higher order modes is lower than

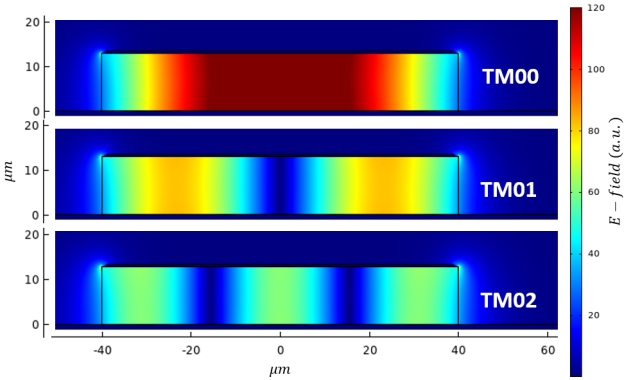

Figure 2.5 – 2D simulation of the TM_{00}, TM_{01} and TM_{02} mode (norm of E-field, |E|) at 2.75 THz for a 80 μm wide ridge.

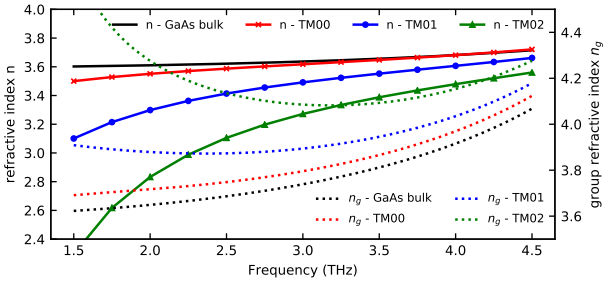

Figure 2.6 – Refractive index n (solid) and group index n_g (dashed) for bulk GaAs and 2D simulated TM_{00}, TM_{01} and TM_{02} modes at 60 K.

for bulk GaAs. This is expected since the lower frequencies and higher order modes are less confined to the double-metal waveguide and have field components traveling in vacuum.

In Fig. 2.7 we calculate the waveguide losses from the imaginary part of the effective refractive index for the TM00 mode of a Au and a Cu waveguide at various temperatures. We want to mention here that this is the lattice/AR temperature which is in general significantly different to the experimentally measured heat sink temperature [6]. As can be seen from Fig. 2.7, the Cu based waveguide leads to lower losses for the same AR temperature. This result agrees with the simulations and experimentally determined

6. Simulations of the heat dissipation are not performed in this work.

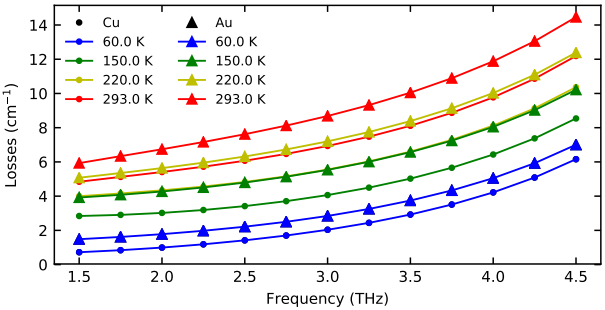

Figure 2.7 – Calculated losses of a Au and Cu based, 80 µm wide waveguide with fixed side absorber width of 1 µm. The Cu based waveguide leads to lower losses at higher temperatures compared to the Au based waveguide.

temperature performances of THz QCLs in Ref. [180].

In Fig. 2.8 (a) and (b) we investigate the effect of the side absorbers on the losses of all considered modes at 60 K and 150 K, respectively. For a lattice temperature of 60 K, the induced losses due to the doping layer and the metals are highly suppressed and the effect of the side absorber is marginal, see Fig. 2.8 (a). At this point it should be highlighted that the waveguide roughness or any contamination of the walls are not included whereas these definitely increase the losses in real devices, especially for the higher order modes. Furthermore, the experimental results presented in chapter 5 at lower temperatures mainly show multi-mode lasing rather than comb operation, whereas at higher temperatures larger regions of comb operation are observed. This could experimentally indicated that the effect of the side absorbers are indeed reduced at lower temperatures as predicted here for 60 K lattice temperature.

The situation drastically changes for 150 K lattice temperature as shown in Fig. 2.8 (b). In the studied case, the side absorbers have relatively small effect on the TM00 mode, whereas the losses for the TM01 and TM02 are significantly increased for increasing side absorber widths. Only in the high frequency region we see a reduced effect which comes from the tighter confinement of the mode below the metal, i.e. lower intensities at lossy interfaces. Also here, the simulations confirm the experimental results on THz QCLs where the higher order modes are suppressed [130].

Additionally, the total loss α is the sum of the mirror losses α_m,

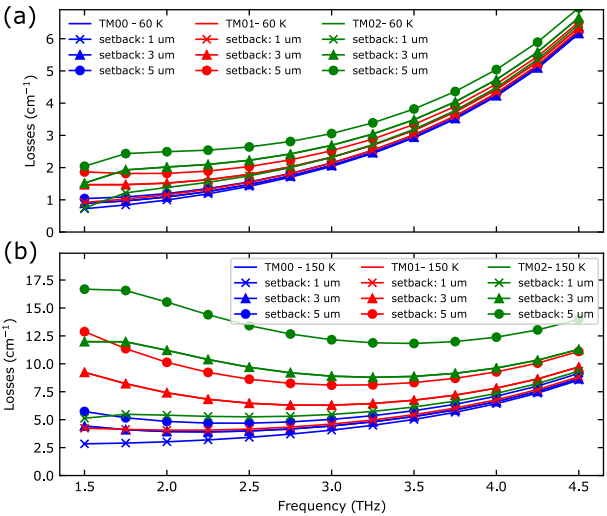

Figure 2.8 – Simulated losses for the investigated cavity modes for different side absorber widths at a lattice temperature of (a) 60 K and (b) 150 K.

the already calculated waveguide losses α_w and the absorption losses from the active region, calculated with a Schrödinger+Poisson solver [28], α_{AR}

$$\alpha = \alpha_w + \alpha_m + \alpha_{AR}. \tag{2.13}$$

The waveguide losses α_w and absorption losses from the AR α_{AR} are temperature dependent, whereas the mirror losses α_m are temperature independent.

The mirror losses can be written as

$$\alpha_m = \frac{1}{2l}\ln\left(\frac{1}{R_1 R_2}\right) \tag{2.14}$$

with l the cavity length and $R_{1,2}$ the mirror reflectivity on each side. Numerically, one finds that $R_{1,2} \approx 0.7 - 0.8$ [172, 181] for our double-metal waveguides. For the fundamental transverse mode in a 4 mm long device presented in chapter 6 we estimate $\alpha_{AR} \approx 5\ cm^{-1}$, $\alpha_m \approx 1\ cm^{-1}$ and $\alpha_w \approx 6\ \mathrm{cm}^{-1}$ around 3 THz and therefore we find for the total loss $\alpha \approx 12\ \mathrm{cm}^{-1}$ at 150 K lattice temperature.

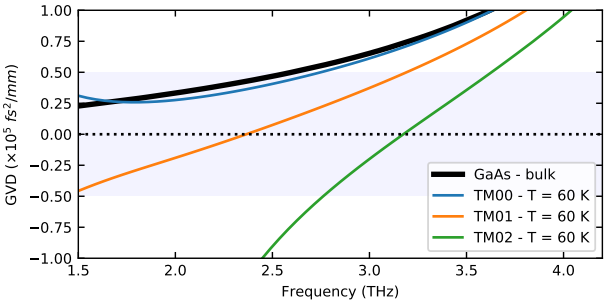

Figure 2.9 – Calculated GVD for the TM00, TM01 and TM02 modes from the 2D numerically extracted effective refractive index for a 80 µm wide ridge. Shaded area indicates region for which comb formation can be observed according to Ref. [182].

Of course, this provides kind of a lower limit for the losses since any sidewall roughness, contamination and thin Ti or Ta layers are not included. Additionally, depending on the active region design higher values of α_{AR} on the order of 20 cm^{-1} are found [38, 156] and are also highly temperature dependent.

Furthermore, the lasing threshold gain g_{th} is given by

$$g_{th} = \alpha/\Gamma \tag{2.15}$$

with Γ the overlap factor of the mode with the AR. Due to the close unity value of Γ and the high reflecting facets, the double-metal waveguide generally leads to lower thresholds compared to single-plasmon waveguide devices even though the pure single-plasmon waveguide losses are lower [172].

Finally, we investigate the GVD of the effective refractive index. As shown in Fig. 2.9 we find that the waveguide lowers the GVD compared to the bulk GaAs. From Ref. [182] it was found that roughly a GVD between -500 and 500 fs^2/mm can lead to comb formation, but this should also depend on the gain of each individual AR.

Gain induced GVD

Before moving on to the longitudinal cavity modes we briefly discuss the contributions to the total GVD which read as

$$GVD = GVD_w + GVD_{mat} + GVD_{AR} \tag{2.16}$$

where GVD_w is the waveguide GVD, GVD_{mat} the material GVD and GVD_{AR} the gain GVD.

At this point it should be noted that the total GVD is not simply the sum of the individual contributions of each single GVD calculated by itself. One should start from the total susceptibility $\chi_{tot} = \chi'_{tot} + i\chi''_{tot}$, which includes the gain and the material contribution, insert it into a 2D or even 3D numerical simulation of the mode to obtain the effective refractive index. The GVD is then calculated from this total effective refractive index.

To make some qualitative and analytical statements on the effect of the gain on the GVD we neglect the waveguide effect since we saw in Fig. 2.9 that the GVD of the TM00 mode differs only slightly from bulk GaAs. We can then assume that the host medium has a refractive index n_h and assume weak absorption ($\chi'' << 1+\chi$) [183] and can therefore relate the gain (= -loss) to the imaginary part of χ by

$$\chi'' \approx -\frac{\alpha c n_h}{2\pi\nu}. \tag{2.17}$$

α is the gain, written as negative loss, and ν the frequency.

Using the Kramers-Kronig relation [7] we calculate the real part of the susceptibility from the gain [8]. Finally, one finds that the refractive index is

$$n = \mathbf{Re}\left(\sqrt{1 + \chi_h + \chi' + \chi''}\right) \tag{2.18}$$

where χ_h is the susceptibility of the host material, that is, GaAs.

If one inserts a flat gain medium, as sketched in Fig. 2.10 in blue, and performs the described procedure, we find the effect of the gain induced GVD is quite large, as shown in Fig. 2.11. Similar results are found in the analytical analysis in Ref. [54] for a wave traveling through a gain medium close to an absorption resonance for which the longitudinal modes are pulled towards the gain center.

7. Numerically it corresponds to the Hilbert transform, which provides in general stable solutions.

8. The gain is obtained from AR simulations.

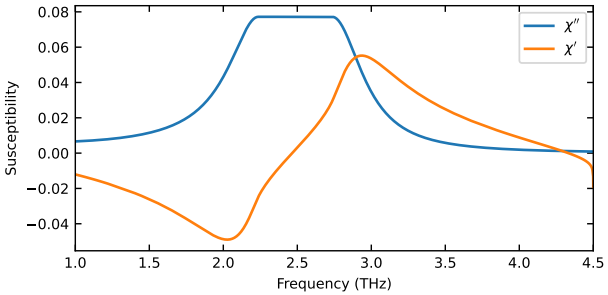

Figure 2.10 – Representative real (orange) and imaginary (blue) susceptibility for broad and flat gain medium.

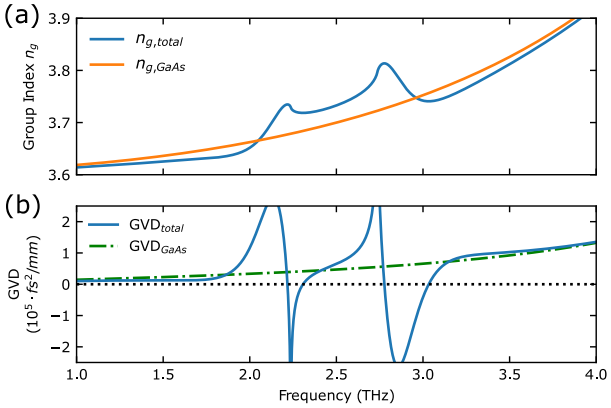

Figure 2.11 – Gain induced change of group index in (a) and corresponding GVD in (b) for the artificial gain medium in Fig. 2.10.

Rather surprisingly one found experimentally that the mode spacing of multi-mode spectra [184] [9] follows more closely to the GVD when neglecting the gain induced GVD effects, i.e. the mode spacing follows the *cold* cavity modes when not in a comb state. This discrepancy of the expected gain induced mode spacing to the experiments might be caused by the simple approach in the above theoretical analysis. For the gain induced GVD we simply assumed a fixed gain, but did not include any dynamics, spatial hole burning effects (inhomogeneous gain saturation), pulling or nonlinear effects nor did we consider that the effective refractive index of the waveg-

9. Similar results are also found in our THz QCLs but were not published.

uide will be influenced as well. Further discussion on this topic would go beyond the scope of this work, so we restrict ourselves in the following to the GVD description, excluding gain effects.

Cavity Modes

In the previous subsections we saw that the effective refractive index is dominated by the material, that side absorbers mainly influence the losses of higher order modes and that the gain should influence the total GVD. Since the latter seems not to reflect the experimental findings we consider in the following section only the cold cavity modes by means of Fabry-Pérot resonances in a double-metal waveguide with bulk GaAs.

To do so we first derive that the longitudinal mode spacing is given by the group index $n_g(\omega)$ rather than the refractive index $n(\omega)$. The longitudinal modes are defined to be phase-matched after one cavity round trip. In other terms, the corresponding wavevector of a longitudinal cavity mode times the cavity round trip length $2L$ has to be an integer multiple p of 2π, i.e. $2L \cdot n(\omega_p)\omega_p/c = p \cdot 2\pi$ with $n(\omega)$ the frequency dependent refractive index. In addition, we expand $n(\omega)$ around the mode frequency ω_p and approximate the refractive index of the next longitudinal mode by $n(\omega_{p+1}) \approx n(\omega_p)+dn/d\omega\cdot\Delta\omega$ with $\Delta\omega$ the mode spacing. Also, two neighboring longitudinal modes have a spatial phase difference of 2π. We can therefore solve for the mode spacing:

$$
\begin{aligned}
& 2\pi = 2L \cdot \frac{n(\omega_{p+1})\omega_{p+1}}{c} - 2L \cdot \frac{n(\omega_p)\omega_p}{c} \\
\leftrightarrow \quad & \frac{2\pi c}{2L} = n(\omega_{p+1})\omega_{p+1} - n(\omega_p)\omega_p \\
\leftrightarrow \quad & \frac{2\pi c}{2L} \approx (n(\omega_p) + dn/d\omega \cdot \Delta\omega) \cdot (\omega_p + \Delta\omega) - n(\omega_p)\omega_p \\
\leftrightarrow \quad & \frac{2\pi c}{2L} = \Delta\omega \left(n(\omega_p) + \omega_p \cdot dn/d\omega + dn/dw \cdot \Delta\omega\right) \\
\leftrightarrow \quad & \frac{2\pi c}{2L} \approx \Delta\omega \left(n(\omega_p) + \omega_p \cdot dn/d\omega\right) \\
\leftrightarrow \quad & \Delta\omega = \frac{2\pi c}{2(n(\omega_p) + \omega_p \cdot dn/d\omega)L} = \frac{2\pi c}{2n_g(\omega_p)L}
\end{aligned}
$$

Here, we assume $dn/d\omega \cdot \Delta\omega$ to be small and negligible. Further, we define the group refractive index n_g as $n_g(\omega) = n(\omega) + \omega\frac{\mathrm{d}n}{\mathrm{d}\omega}$. Therefore, we find for the mode spacing:

$$\Delta\nu = \frac{c}{2n_g L} \tag{2.19}$$

To illustrate that the dispersion of THz QCLs seems to disfavor equidistant spaced cold cavity modes we make a simple calculation of modes spaced by an octave as observed in Ref. [38]. The group refractive index is 3.643 at 1.65 THz and 3.801 at 3.35 THz taken from Fig. 2.6 and excludes gain induced GVD effects. Computing now the mode spacing we find:

$$\Delta\nu(1.65THz) = 13.679\ GHz$$
$$\Delta\nu(3.35THz) = 13.110\ GHz$$

which is a 570 MHz difference in the mode spacing at each side of the spectrum.

Even tough unequally spaced cavity modes due to the high GVD are expected, Bachmann et al. showed in Ref. [130] that the implementation of lossy side absorbers [129] enhances the spontaneous formation of THz QCL frequency combs and seems to *clean up* the emission spectra, i.e suppress higher order transverse modes, over a broad range. From the previous analysis it becomes clear that the side absorbers suppress the higher order transverse modes but not yet why comb formation is also enhanced [130].

As briefly mentioned above, the gain can pull the cold cavity modes to a different frequency. This effect is also related to the quality factor Q_c of each cold cavity mode at ω_c and the gain quality factor Q_a with its center at ω_a, i.e. $\omega_c' = \frac{Q_c\omega_c + Q_a\omega_a}{Q_c+Q_a}$ with ω_c' the pulled cavity mode frequency [54]. Furthermore, parametric gain also induces pulling effects and can lead to comb formation, compare, for example, with numerical simulations in Ref. [89, 126, 147]. Pulling effects were also experimentally confirmed in Kerr combs in microring resonators showing self optical injection locking of laser modes due to FWM [120]. Intuitively, this simply means that a sharp resonance does not get pulled far from its resonance frequency, whereas a low quality factor of the cavity mode allows for wider frequency pulling. This corresponds to the well-known weak injection

locking theory which predicts a locking range inversely proportional to the quality factor [54].

Taking now textbook solutions to describe the Fabry-Pérot resonances ([183] p. 317) one finds that the intensity I as a function of frequency ν reads as

$$I = \frac{I_{max}}{1 + (2\mathcal{F}/\pi)^2 \sin^2(\pi\nu/\nu_{rep})} \tag{2.20}$$

with $\mathcal{F} = \frac{\pi r^{1/2}}{1-r}$ the finesse, r the amplitude attenuation factor, and $\nu_{rep} = \frac{c}{2n_g l}$ the frequency dependent standing wave frequency spacing where n_g the group refractive index and l the cavity length. I_{max} is related to the initial intensity I_0 as $I_{max} = I_0/(1-r)^2$. Further, the amplitude attenuation factor is related to the losses α_r by $r^2 = exp(-2\alpha_r \cdot l)$, where r^2 is the intensity attenuation factor. Including the waveguide losses α_wg and the mirror reflectances R_1 and R_2 [10] one finds [183] that the finesse reads as

$$\mathcal{F} = \frac{\pi e^{-\alpha_r l/2}}{1 - e^{-\alpha_r l}} \tag{2.21}$$

with $\alpha_r = \alpha_{wg} + \alpha_\mathrm{m}$ and $\alpha_\mathrm{m} = \frac{1}{2l}\ln(1/(R_1 R_2))$. We now quantitatively investigate the Fabry-Pérot resonances for different scenarios. In Fig. 2.12 (a) we keep the reflection coefficient $r = 0.8$, assume a constant group index n_g and compare to the case of 8 and 12 cm^{-1} total losses. In this case, we normalize each curve to the response function with lowest losses. Considering the effect of the cavity quality factor on the frequency pulling effect as described in Ref. [54], the higher quality factor modes would get less pulled.

In Fig. 2.12 (b) the effect of GVD for the TM00 mode according to Fig. 2.9 is now introduced and a clear shift of the peak frequencies can be observed. Due to the low quality factor of the lossy modes, further pulling should be possible according to Ref. [54]. From this picture it becomes clear that a certain amount of loss can increase the frequency locking range of the FWM as, for example, also described in [185]. At the same time one needs to find the optimal compromise of the additional losses due to the side absorbers to

10. The complex mirror *amplitude* reflectance r_i, also called *reflection coefficient*, is related to the mirror *intensity* reflectance R_i by $R_i = r_i^2$, also called *reflectance*, *reflectivity* or *power reflection coefficient*.

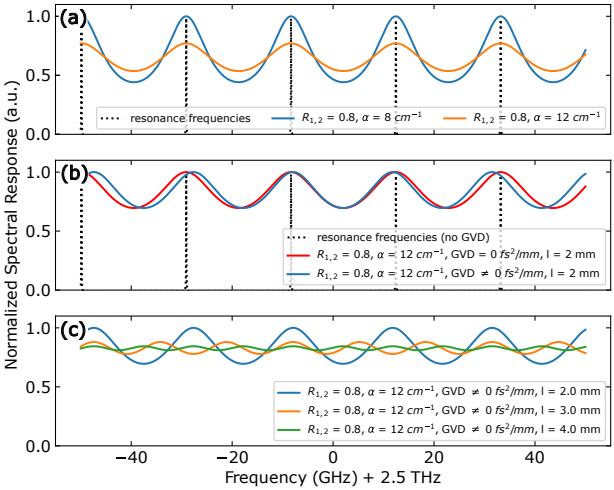

Figure 2.12 – Cold Fabry-Pérot mode responses for different scenarios. For each panel the responses are normalized to the highest frequency response curve. (a) Constant reflectivity $R_{1,2} = 0.8$, GVD = 0 fs^2/mm, 8 and 12 cm^{-1} total losses and a 2 mm cavity length. (b) Constant reflectivity but zero and non-zero GVD for the TM00 mode according to Fig. 2.9 for 12 cm^{-1} total losses and a 2 mm cavity length. Numerical values from Fig. 2.6 for the fundamental transverse mode are inserted in Eq. 2.20 for non-zero GVD. (c) Constant reflectivity and nonzero GVD for increasing cavity length. It becomes clear that the quality factor decreases for increasing losses and cavity lengths.

lower the quality factor of the cavity modes and increase frequency pulling effects but preserve lasing of the device over a broad bandwidth. Furthermore, this description of the cold cavity modes might explain certain findings in the off-resonant injection which will be discussed in chapter 9.

In Fig. 2.12 (c) the spectral responses for different cavity lengths are compared. Due to the length dependence of the finesse, one observes further *damping* of the cavity mode response function. This could indicate that longer devices favor comb formation but this claim needs to be verified as well.

In the previous consideration of the cold cavity mode response we only analyzed the TM00 mode. As we saw before, the side absorbers play a key role in the suppression of the higher order transverse modes and we might also consider their cold cavity mode responses. Therefore, we illustrate in Fig. 2.13 the cold cavity mode responses

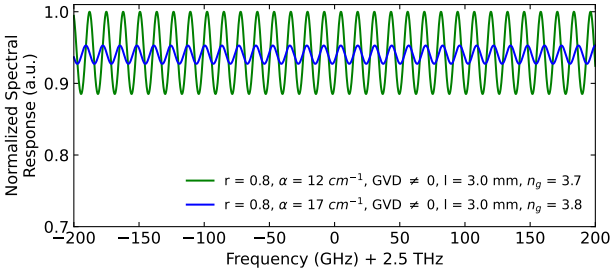

Figure 2.13 – Fabry-Pérot modes of the fundamental (green) and first higher order (blue) mode which have different group index and losses. The response is normalized to the fundamental mode response. By inducing losses, due to side absorbers, to the higher order mode we observe the suppression of the mode response (blue).

including GVD for the TM00 and TM01 mode with a group index $n_g = 3.7$ and $n_g = 3.8$ as well as 12 and 17 cm^{-1} loss, respectively. The side absorbers lead here to an additional loss of 5 cm^{-1} for the TM01 mode compared to the TM00 mode, see also Fig. 2.8, and one finds that the cavity mode is suppressed compared to the fundamental mode as expected. This explains the cleaning of the spectra due to the side absorbers as observed in Ref. [130]. At the same time, there are spectral regions for which the TM01 response is higher than the TM00 due to the different GVD of the two modes. In these regions lasing on the TM01 mode could be possible.

2.2.3 Waveguide RF impedance

The final point on the cavity concerns the RF properties. Due to the ultrafast nature of QCL gain media and population grating effects [186] inside the device, the QCL itself acts as a fast heterodyne detector, allowing one to directly observe intermode beatings up to multiple GHz on the laser bias line [28, 101, 109].

By construction, the double-metal waveguide is similar to a microwave microstrip line and therefore supports the propagation of RF signals. Depending on the application, one is interested in matching the surrounding circuit to the impedance of the QCL. For simplicity the QCL is treated in the following as an insulator ignoring its real finite conductance. In a first step we take the textbook formula of a microwave strip line [187] and will find that for

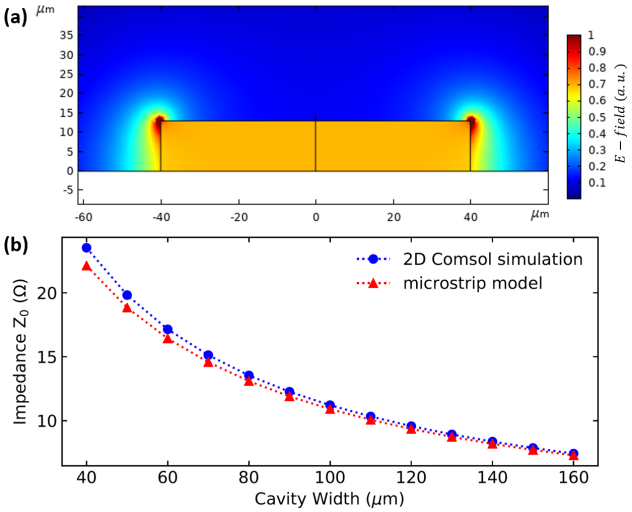

Figure 2.14 – (a) 2D simulation of an RF mode at 10 GHz supported by a THz QCL waveguide. Tight confinement is observed. The simulation assumes room temperature of the waveguide, perfect electrical conductors as contacts, and insulating bulk GaAs as AR. (b) Simulated impedance (blue) compared to the approximate microstrip model (red) showing good agreement.

an 80 µm wide and 13 µm thick cavity the impedance Z_0 is roughly 13 Ω. To confirm this simplified model we perform an idealized 2D simulation, i.e. assuming perfect electrical conductors and constant material properties, and we find similar Z_0 for varying cavity widths as shown in Fig. 2.14. Fig. 2.14 (a) presents the waveguide cross-section showing that the RF mode is also well confined in the waveguide, like the THz modes. Fig. 2.14 (b) compares the 2D numerically extracted Z_0 to the simple microstrip line model showing good agreement of both. We note here that the doping in THz QCLs is significantly lower than in mid-IR QCLs. This higher doping in mid-IR devices will increase the RF losses.

2.3 RF mounting

In the last section of this chapter, we investigated the RF mounting of double-metal waveguides used in THz QCLs. In general one is interested in extracting the internally detected intermode beating signals which provide first indications for comb operation. As we

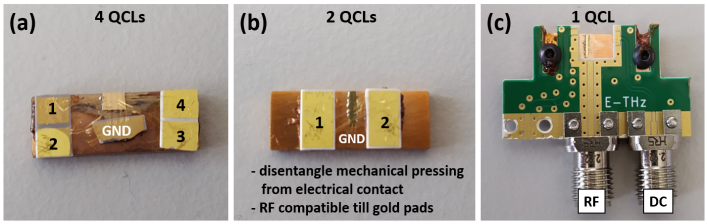

Figure 2.15 – (a) Mounting of THz QCLs on a copper submount with ceramic gold pads. It allows mounting of four devices simultaneously, but is not RF optimized due to the long wire bonds and ceramic pads. Electrical contact provides mechanical pressing to the cryostat and are not RF optimized. (b) Adopted mounting with decoupled electrical and mechanical contact. Shorter wire bonds result in improved RF performance. Cryostat is RF compatible until ceramic pads, see also Fig. 2.16 (a). (c) PCB optimized mounting of a single device. DC and RF line are decoupled and an additional monitor port is optionally available. Mechanical pressing is as well decoupled.

saw in the last section, the cavity impedance is on the order of 15 Ω. This impedance is further modified since the lasers are additionally indium soldered to a copper mount and wire bonded for electrical contact. Here, Fig. 2.15 shows all the different versions of mounted devices used in this thesis.

The first version as shown in Fig. 2.15 (a) arises from historical reasons. The electrical contact pads are at the same time used to clamp the device to the cryostat. Therefore, these clamps are the electrical contacts and are suitable only for DC and low frequencies. The placement of the gold ceramic pads allows to mount 4 QCLs at the same time but also requires relatively long wire bonds. These wire bonds have a high induction and reduce the high frequency performance.

In the second version shown in Fig. 2.15 (b), the mechanical clamping is decoupled from the electrical contact. This reduces the number of mounted lasers to two. The ceramic gold pads are now located close to the QCLs and are connected via a slidable SMA connector (SMA straight flange receptacle jack, HUBER+SUHNER, 23_SMA-50-0-11/111_NE) as shown in Fig. 2.16 (a). In this configuration we provide an RF compatible cryostat up to the ceramic gold pads. Both, RF and the DC signal pass through the same gold pad. RF losses from the cryostat input to the device can be estimated from RF injection measurements of a QCL. When injecting once directly the QCL and once over the neighboring device act-

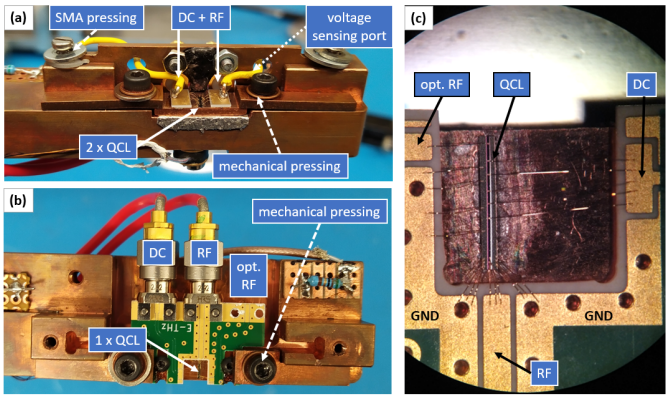

Figure 2.16 – (a) Mounting of semi-RF optimized devices on the cryostat. Mechanical and electrical contacts are separate, and RF cables are installed until ceramic pads. (b) Mounting of a PCB device. (c) Zoom in on the wire bonded PCB mounted device.

ing as an antenna, one finds different injection locking ranges. By comparing the injection powers for similar injection locking ranges and due to the symmetric mounting of the two devices one can then estimate that the total RF loss from the cryostat input till the QCL is roughly 25 dBm at 35 GHz. The cables have marginal losses and the main contributions come therefore from the ceramic gold pad and the wire bonds.

In the final version shown in Fig. 2.16 (c) the ceramic gold pads are replaced by a printed circuit board (PCB). This allows to decouple the DC bias line from the RF line. Further, the RF line is 50 Ω impedance matched and allows short wire bonding of the device at the back of the waveguide. This configuration is favorable since the fundamental beatnote signal is maximal when extracted at the end of the waveguide, as shown in Ref. [186]. The DC line is intentionally not RF optimized and consists of long wire bonds evenly spaced over the laser ridge. Additionally, the PCB offers a monitoring port that can be connected to the front of the device.

Fig. 2.16 (b) and (c) show the cryostat mounting and a zoomed version of the wire bonding configuration. The major drawback of this configuration is that it only allows to mount a single device at a time.

For the last mounting version we perform additional vector network analyzer (VNA) experiments to calibrate the losses up to the

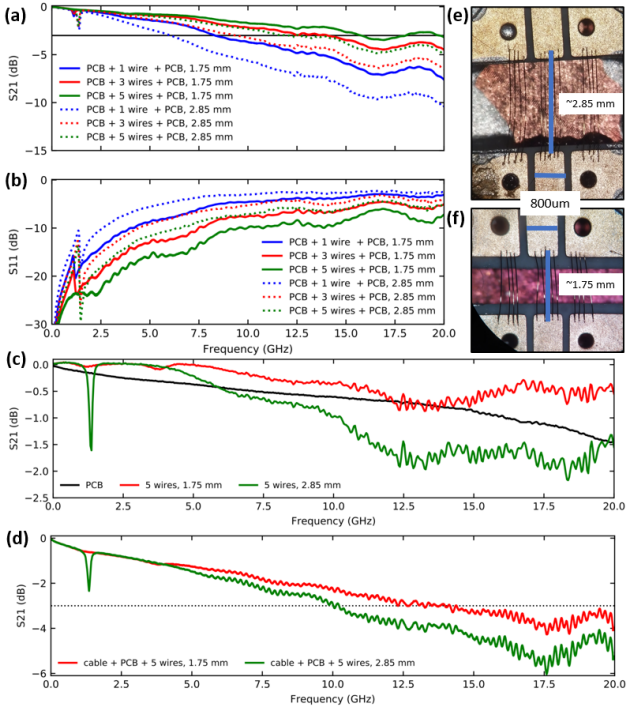

Figure 2.17 – VNA measurements. (a) & (b) Two straight PCB connected by different amount of wire bonds for 1.75 mm and 2.85 mm wire length as shown in (e) and (f). (c) Single PCB S-Parameters and deduced wire bond S-parameters. (d) S-Parameter from the input of the cryostat up to the top contact of a laser (assumed 50 Ω matching). The dip around 1.5 GHz arises from an unwanted resonance which corresponds to roughly 2.5 cm, on the order of the PCB geometry.

QCL. Here, we consider the SMA feed through at the cryostat input, the RF cable inside the cryostat, the SMA-PCB connector and PCB itself plus the wire bonds. Since we cannot directly measure from the cryostat input till the device, we first perform a dummy measurement for different wire bonds connecting two PCBs and then combine the results with the remaining components. Fig. 2.17 shows the corresponding results stepwise. In Fig. 2.17 (a), (b) we plot the S21 and S11 parameters of two PCBs connected with different numbers of wire bonds with lengths of 1.75 mm and 2.85 mm. A picture of each case is shown in Figs. 2.17 (e) and (f). As expected, the losses due to the inductance of the wire bonds reduce by adding

multiple flat and parallel wires, and shows that shorter wires are preferred. We further measure a single reference PCB board to extract its S21 parameter which is shown in Fig. 2.17 (c) in black. The S-parameters [11] now allow to remove the effect of the two PCBs revealing the S21 parameters of the wire bonds only as shown in green and red in the same figure. It shows that five short wires provide low RF losses up to 20 GHz.

In Fig. 2.17 (d) we now present the combined S21 values for the cryostat SMA feed through, RF cable, SMA-PCB connector, the PCB and the wire bonds. It shows that in this implementation the losses up to 12.5 GHz are below -3 dB for the five short wire configuration and below -4 dB up to 20 GHz, assuming a 50 Ω matched device.

At this stage we ignored the fact that in the final device we have a low impedance laser with a finite length and an open end. Therefore, by default, this will lead to reflections from the front facet, as well as resonances given by the cavity length [12]. Detailed experiments on RF mounted devices were performed, for example, in Refs. [103, 108, 111].

2.4 Conclusion

In conclusion, we discussed in this chapter briefly the different designs for THz ARs, the AR simulation techniques and growths followed by their fabrication into double-metal waveguides which are used in this thesis. In the following, we went through the main contribution of the GVD of bulk GaAs followed by 2D simulation of the TM00, TM01 and TM02 modes and their effective GVDs. We also saw that the side absorbers provide significant losses to suppress higher order transverse modes for sufficiently high AR temperature and showed qualitatively that the gain induced GVD could in principle significantly modify the total GVD. By investigating the Fabry-Pérot spectral response of the cold cavity modes, we understood further the higher order transverse mode suppression and that a lower quality factor of the cold cavity response should allow larger frequency pulling effects. In 2D simulations, we also briefly

11. Actually, one has to convert it first to the T-matrices.
12. The refractive index is slightly different at RF frequencies compared to the THz and leads to a phase mismatch.

investigated the RF mode in double-metal waveguides and found its impedance on the order of 15 Ω. In the last section we went through different laser mounting techniques and examined in detail an optimized PCB mounting of RF compatible THz QCLs.

3

Fourier-Transform Infrared Spectroscopy of Lasers

3.1 Introduction

Fourier-Transform Infrared Spectrometers (FTIRs) are commonly used to measure the optical absorbance or transmittance of different samples [188]. Traditionally, they are based on a Michelson Interferometer combined with a broad and incoherent source and a spectrometer itself is often referred as an FTIR. Despite being traditional exploited with an incoherent light source it can as well be combined with any coherent source to determine the emission spectrum or be used for spectroscopy. FTIRs as interferometers are well understood [188] but concerning the signal processing of laser sources and especially frequency comb sources there are some fundamental differences to the well studied incoherent light source case. In this chapter, we want to address the fundamental properties of an FTIR, without probing any sample, and the consequences when analyzing frequency comb sources and multi-mode lasers. First, we will discuss the symmetry of the recorded interferograms (IFGs) followed by an excursion to phase correction. Second, some fundamental aspects of signal processing and the effect of finite measurements will be reviewed also regarding spectral leakage and the use of window functions. And third, the fact of equidistantly spaced comb modes will be exploited in the part of signal processing and we will show how it can enhance the resolution of the FTIR.

3.2 Michelson Interferometer

An ideal FTIRs is based on a Michelson Interferometer consisting of a 50-50 beam splitter (BS), one fixed and one variable mirror as well as a detector. The setup is sketched in Fig. 3.1 and leads to an interferometric effect at the detector. For different retardation of the variable mirror, the light will constructively or deconstructively interfere on the detector. The simplest case of one single frequency is discussed first. Therefore, the intensity as a function of optical delay leads to a wavelength dependent interference pattern. The retardation dependent intensity $I(\delta)$ produced by light at a wavelength λ measured at the detector is therefore written as:

$$I(\delta) = \frac{1}{2} \cdot I(\lambda) \cdot \left(1 + cos(2\pi \frac{\delta}{\lambda})\right). \tag{3.1}$$

$I(\delta)$ is referred as interferogram, field autocorrelation or also as second-order coherence function. In this thesis we will use the term interferogram. The factor 1/2 arises from the beam splitter, which will reflect half of the light intensity onto the detector and half back towards the source. The static contribution is normally discarded in the spectral analysis due to the wavelength independence. Nevertheless, it's often used to examine the contrast of the interferogram and gives information about the alignment and if the two arms in the FTIR are balanced or not [188]. The retardation or simply delay δ is twice the mirror displacement Δd and $\delta = 0$ is called Zero Path Delay (ZPD) where both mirrors have the same distance to the beam splitter.

Reducing Eq. 3.1 to the interferometric term leads to

$$S(\delta) = B(\lambda) \cdot cos(2\pi \frac{\delta}{\lambda}) \tag{3.2}$$

where $S(\delta)$ the recorded detector signal and $B(\lambda)$ is the intensity of a light source at wavelength λ modified by the instrumental characteristics. We note here that due to the FTIR symmetry, $S(\delta)$ is an even function in theory.

For the generalization to a continuum we rewrite $\frac{1}{\lambda} = \tilde{\nu}$ where $\tilde{\nu}$ the wavenumber and we obtain

$$S_{tot}(\delta) = \int_{-\infty}^{\infty} B_{tot}(\tilde{\nu}) \cdot cos(2\pi\delta\tilde{\nu}) d\tilde{\nu} \tag{3.3}$$

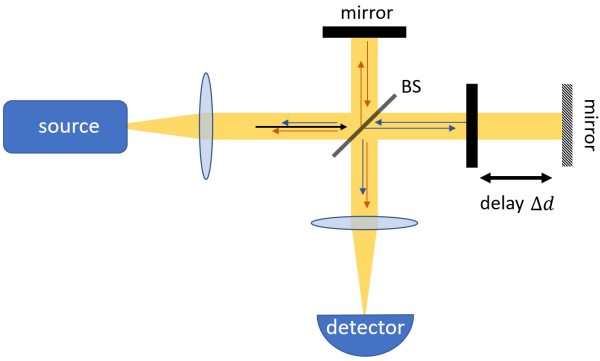

Figure 3.1 – Sketch of an FTIR based on a Michelson Interferometer.

representing the *Fourier Cosine Transformation* [1] and it's inverse as

$$B_{tot}(\tilde{\nu}) = \int_{-\infty}^{\infty} S_{tot}(\delta) \cdot cos(2\pi\tilde{\nu}\delta)d\delta. \tag{3.4}$$

$S_{tot}(\delta)$ is called *IFG* and $B_{tot}(\nu)$ *intensity spectrum* (SPC).

We note here that due to the 2π factor inside the cosine there is no prefactor present in the definition of the Fourier Cosine Transform.

The FT exhibits two important symmetries exploited in FTIRs:

— if f(t) real and even then $\mathcal{F}[f(t)]$ is pure real and even
— if f(t) real and odd then $\mathcal{F}[f(t)]$ is pure imaginary and odd

As a consequence the FT of any real signal contains all phase and amplitude information on the positive frequency domain axis and Eq. 3.4 is rewritten as:

$$B(\tilde{\nu}) = 2 \cdot \int_{0}^{\infty} S(\delta) \cdot cos(2\pi\tilde{\nu}\delta)d\delta. \tag{3.5}$$

1. We define the forward and inverse complex Fourier Transform (FT) as $F(\nu) = \int_{-\infty}^{\infty} f(t)e^{-i2\pi\nu t}dt$ and $f(t) = \int_{-\infty}^{\infty} F(\nu)e^{+i2\pi\nu t}d\nu$ where in general t the time and ν the frequency. Due to the presence of the 2π in the exponents, we have no prefactors in this definition. Using the Euler Formula $e^{\pm i\phi} = cos(\phi) \pm isin(\phi)$ we relate the real and the imaginary part of the complex FT to the Fourier Cosine and Fourier Sine Transform.

With Eq. 3.5 it is in theory possible to reconstruct any signal by measuring from the ZPD to infinity ($\delta = 0$ to $+\infty$). In practice, one is limited to a finite mirror displacement and by the imperfections of any FTIR which leads to real but not strictly speaking even detector signals around the ZPD. The former case together with the discretization of the recorded FTIR signal is discussed later. The latter is addressed in the next section and is often referred as Phase Error Correction or simply Phase Correction.

3.3 Phase Correction

In the previous section we saw that for the idealized FTIR the recorded signal is real and even around the ZPD. In real life FTIRs optical, electronic and sampling effects will lead to a real but not necessary even signal [188]. Therefore, the resulting complex FT will not only be purely real but will also have an imaginary part. In other words: the resulting spectrum has a non-zero frequency dependent phase.

For simplicity, we continue to work with the complex FT given by

$$B(\tilde{\nu}) = \int_{-\infty}^{\infty} S(\delta) e^{-i2\pi\tilde{\nu}\delta} d\delta \tag{3.6}$$

$$S(\delta) = \int_{-\infty}^{\infty} B(\tilde{\nu}) e^{+i2\pi\tilde{\nu}\delta} d\tilde{\nu} \tag{3.7}$$

and recall that for the ideal FTIR $S(\delta)$ and $B(\tilde{\nu})$ are real and even functions and the expression is equivalent to Eq. 3.4 and 3.5 [2].

According to Ref. [188] the two most common errors arise from sampling effects of the IFG and from electronic filter induced frequency dependent phase lags. Optical elements like the beam splitter can also induce a frequency dependent phase lag due to their dispersion. By sampling effects, we mean that the IFG is generally sampled before the ZPD, i.e. $\delta_{start} = -\varepsilon$, and that the exact ZPD is not contained in the discrete samples of the IFG. This simply leads

2. If the recorded IFG is real valued, it leads to symmetric absolute amplitudes and antisymmetric phases around the zero frequency. Therefore, integration form 0 to $+\infty$ and multiplying by a factor of 2 provides the same information and modern FTIRs scan manly along one side of the ZPD.

to the assumption of a wrong ZPD which is a delay shift of the IFG. This can be expressed as

$$\begin{aligned} S(\delta) &= \int_{-\infty}^{\infty} B(\tilde{\nu}) e^{+i2\pi\tilde{\nu}(\delta-\varepsilon)} d\tilde{\nu} \\ &= \int_{-\infty}^{\infty} B(\tilde{\nu}) e^{-i2\pi\tilde{\nu}\varepsilon} e^{+i2\pi\tilde{\nu}\delta} d\tilde{\nu} \end{aligned} \tag{3.8}$$

This corresponds to a linear phase change $\Theta_1(\tilde{\nu}) = -2\pi\varepsilon\tilde{\nu}$ in the frequency domain. For the Discrete Fourier Transform (DFT), discussed further in the next section, the first point of the sampling data set should correspond to the ZPD position. Due to the finite sampling spacing the exact ZPD is in general missed and one should select the closest sampling point to the expected ZPD position. This then leads to a maximal phase error of $\Theta_1(\tilde{\nu}) = -2\pi\frac{\Delta\delta}{2}\tilde{\nu}$ where $\Delta\delta$ is the sampling spacing. Since this error occurs simply because of the discrete sampling the underlying IFG is still an even function with respect to the real ZPD and the complex spectrum can be simply rotated back to the real axis by the phase error.

For electronic filter effects [3] and optical dispersion effects we can assume that they lead to a fixed frequency dependent phase lag $\Theta_2(\tilde{\nu})$ of the IFG and Eq. 3.5 will be written as:

$$\begin{aligned} S(\delta) &= \int_{-\infty}^{\infty} B(\tilde{\nu}) e^{+i2\pi\tilde{\nu}\delta - \Theta_2(\tilde{\nu})} d\tilde{\nu} \\ &= \int_{-\infty}^{\infty} B(\tilde{\nu}) e^{-i2\pi\Theta_2(\tilde{\nu})} e^{+i2\pi\tilde{\nu}\delta} d\tilde{\nu} \end{aligned} \tag{3.9}$$

One could write, at least locally, $\Theta_2(\tilde{\nu}) = A + B\tilde{\nu} + C\tilde{\nu}^2 + ...$ where A, B, C and so on are constant prefactors. The previous effect of a wrong ZPD can be included in the linear term here.

Experimentally one observes that this phase change is slowly varying as a function of frequency. Therefore, modern FTIRs record a long single-side IFG which actually includes a very short double-side part in the beginning. Such a double-sided part of a single-side

3. In rapid scan, the recorded signal as a function of time sees in general not a perfect flat response of all electronic elements.

IFG is shown in Fig. 3.2 (a). By recording this short double-sided IFG around the ZPD the slowly varying phase can be resolved and corrected. The most common methods therefore are known as Forman and Mertz method [189, 190]. Both methods use the fact that the double-side IFG should be symmetric around the ZPD and use the slowly varying phase to correct the single-sided IFG or directly the spectrum. Mathematically, the two methods are in principle equivalent but lead numerically to slightly different results. The Mertz method interpolates the phase of the double-sided IFG spectrum, $e^{-i2\pi\Theta(\tilde{\nu})}$ and multiplies the complex FT of the full IFG by the inverse of this phase, $e^{+i2\pi\Theta(\tilde{\nu})}$, to rotate the spectrum back onto the real axis. The Forman method also takes the phase of the double-sided IFG spectrum but takes the inverse FT of the opposite phase, i.e. $\mathcal{F}^{-1}[e^{i2\pi\Theta(\tilde{\nu})}]$, and convolutes it with the fully IFG. The convolution in time domain is mathematically identical to the rotation in the frequency domain. In practice, the Forman method leads to symmetrization of the IFG and can, compared to the Mertz method, be repeated several times and is therefore numerically superior to the Mertz method. By taking the real part of the corrected spectrum one omits half of the (complex) noise with it and gets the correct phase relation if the FTIR performs a phase sensitive measurement. An example of the double-sided IFG phase as well as the Forman corrected IFG is presented in Fig. 3.2 for a broadband source. It becomes obvious that the extracted slowly varying phase is well defined in the spectral regions with high intensity and that any computer will assign arbitrary phases, related to the noise, where no signal is observed. Therefore, the phases in Fig. 3.2 (c) are color weighted by the intensity spectrum shown in Fig. 3.2 (b). Details on the phase correction implementation can be found for example in Ref. [189, 190] and [191].

If it comes to laser based IFGs we have to address one main issue which is more pronounced in the phase correction procedure than for broadband sources: the double-sided IFG will only lead to meaningful phase information where the signal is present and everywhere else the phase is actually random and has to be discarded or assumed to have a certain shape from previous reference measurements. This will lead to slight phase errors in low intensity spectral regions. A double-sided IFG, intensity spectrum and it's phase are plotted in Fig. 3.3 for a broadband THz Quantum Cascade Laser (QCL).

In general we assume in good approximation that the phase

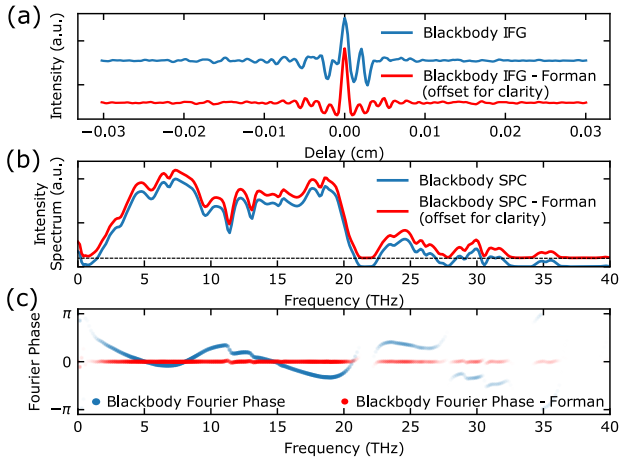

Figure 3.2 – **(a)** Uncorrected IFG (blue) and Forman phase-corrected IFG (red) of blackbody source (Globar). **(b)** Absolute value of the intensity spectrum of IFGs shown in (a). **(c)** Fourier phases of the complex Fourier intensity spectrum show in (b). The phase of the uncorrected spectrum is slowly changing as a function of frequency whereas the Forman corrected phases are by construction nearly zero. The color of each phase point is weighted by the corresponding intensity amplitude from (b).

change is locally linear and extrapolate for the regions of weak intensity. The other possibility would be to use a reference broadband source phase for the correction. Besides taking a reference phase, the correction method, Mertz or Forman, stays the same.

Some reader could argue now that by measuring the spectrum of a QCL, where we have some laser modes and between only noise, it is sufficient to take the power spectrum (absolute value of the complex FT) and not going through the pain of implementing one of these very sensitive phase correction methods. As long as we are interested in the intensity spectrum of a laser and not the phase, and having modes separate by more than the nominal resolution of the FTIR, including the mode broadening due to apodization, the approach of the power spectrum is sufficient. But actually one would not only sacrifice a noise increase by a factor of two [4] but would also increase the resolution bandwidth, see also section 3.4.2. Therefore, in phase sensitive measurements like Shifted Wave Interference

4. Since we include not only the noise from the real part but also from the imaginary part of the spectrum.

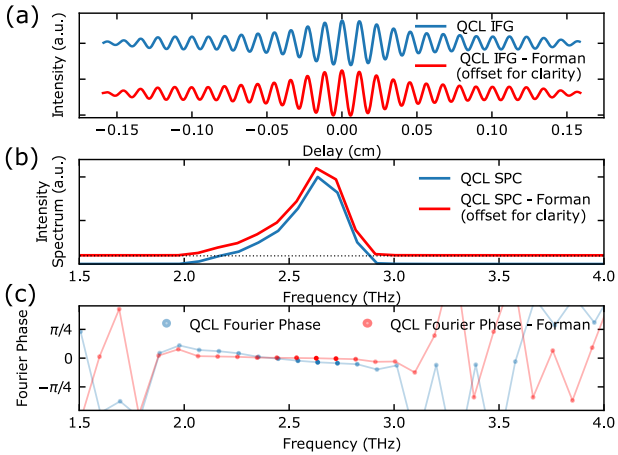

Figure 3.3 – **(a)** Uncorrected IFG (blue) and Forman phase-corrected IFG (red) of a broad THz QCL. **(b)** Absolute value of the intensity spectrum of IFGs shown in (a). **(c)** Fourier phases of the complex Fourier intensity spectrum show in (b). Compared to the broad incoherent source in Fig. 3.2 (c) here we cover a short range where the Fourier phases are approximately changing linearly (blue curve). Due to the absence of any light outside the lasing spectrum we find a random phase there. The phase can be corrected by the extracted points or by a linear fit through them. The red curve shows the Forman corrected phases close to zero in the lasing spectrum region. The color of each phase point is weighted by the corresponding intensity amplitude from (b).

Fourier Transform (SWIFT) or in the case of closely spaced modes, the phase correction methods give us an advantage over the simple approach. The knowledge of phase correction is further discussed in section 3.5 when applied to multi-mode laser spectra.

But before discussing the special case of FTIR measurements of laser intensity spectra, the effect of finite IFGs and discrete sampling are treated in the following section.

3.4 Discrete Fourier Transform

In the previous section we treated the IFG as a continuous function from 0 to $+\infty$. Real IFGs are sampled discrete and have a finite length. Therefore, the DFT is used, leading to a finite resolution and high frequency limit. The resolution is given by the length of the IFG and leads to a nominal frequency resolution $\Delta\nu$:

$$\Delta\nu = \frac{1}{N \cdot \Delta t} \tag{3.10}$$

where N is the number of sampling points and Δt the sampling delay time spacing. Δt relates to the mirror delay spacing Δd as $\Delta t = 2 \cdot \Delta d/c$ with c the speed of light and $2 \cdot \Delta d$ the optical path delay spacing. The IFG is generally presented as a function of the optical path delay (in cm) for historical reasons. Commercial FTIRs exhibit a resolution down to 0.075 cm^{-1}/ 2.25 GHz (Vertex 80v, Bruker) or down to roughly 0.017 cm^{-1}/ 510 MHz for high resolution FTIRs (Bomem, ABB).

The high frequency limit is given by the Nyquist limit, which is half the sampling rate of the IFG given by $f_s = 1/\Delta t = c/(2 \cdot \Delta d)$.

$$f_{Nyquist} = \frac{1}{2} \cdot \frac{1}{\Delta t} \tag{3.11}$$

In general, the sampling rate of the IFG is not a limiting factor, and therefore $f_{Nyquist}$ can be set sufficiently higher than the maximal expected frequency component. Additionally, it has the advantage of having a better estimate for the ZPD position, which reduces phase errors.

Depending on the bandwidth of the FTIR, a too low Nyquist frequency could lead to aliasing effects where frequency components above the Nyquist frequency are mirrored down to lower frequencies. By optical or digital filtering this can be avoided as well.

The finite and discrete nature of the IFG does not only limit the resolution and the high frequency limit, but also leads to a reduced orthogonal basis compared to the complex FT from 0 to $+\infty$. Mathematically the complex FT is replaced by the DFT and reads as:

$$a_k = \sum_{n=0}^{N-1} a_n \cdot e^{-2\pi i \frac{nk}{N}} \qquad k = 0, 1, 2, ..., N-1. \tag{3.12}$$

Eq. 3.12 uses the indexes in arrays used in computers. The sum in Eq. 3.12 can be seen as a projection of each point a_n onto a

basis vector [5] $e^{-2\pi i \frac{nk}{N}}$. $1/N$ represents the spacing between sample points and n/N is the current position. Multiplying the exponent by $1 = \frac{\Delta t}{\Delta t}$ we receive:

$$\begin{aligned} a_{\nu_k} &= \sum_{n=0}^{N-1} a_n \cdot e^{-2\pi i (\frac{k}{N \cdot \Delta t})(n \cdot \Delta t)} \\ &= \sum_{n=0}^{N-1} a_n \cdot e^{-2\pi i (k \Delta \nu)(n \cdot \Delta t)} \\ &= \sum_{n=0}^{N-1} a_n \cdot e^{-2\pi i \nu_k t_n} \qquad k = 0, 1, 2, ..., N-1 \end{aligned} \tag{3.13}$$

where t_n are the sampling times and ν_k the frequencies. This corresponds to a mapping of the time signals to each frequency. The DFT frequencies themselves are orthogonal to each other and therefore any signal which is periodically repeated after N samples, and resolved by the Nyquist limit, is orthogonal and mapped perfectly to these frequencies. Therefore, the DFT frequencies can be seen as a reduced orthogonal basis for all $1/N$ periodic functions, and we could also call them basis vectors, eigenvectors or eigenfrequencies.

An alternative view on the DFT is that it represents a kind of a lock-in measurement for each eigenfrequency with the reference being fixed in phase and frequency.

The reduction from the complete orthogonal basis of the FT to a reduced orthogonal basis of the DFT leads to an unwanted effect called *spectral leakage* for signal which are not periodic within the recording length and is discussed in the following subsection.

3.4.1 Spectral Leakage

There are many different ways to describe spectral leakage which is induced by the finite length of the IFG. An intuitive picture in the time domain is presented in Fig. 3.4. Fig. 3.4 (a) shows in blue an infinite signal and in black the recording range of the FTIR. This is often referred as boxcar function or kernel of the complex FT. In

5. As we will also discuss later, there is only a subset of periodic functions for which the given basis vectors of the DFT act as an orthogonal basis.

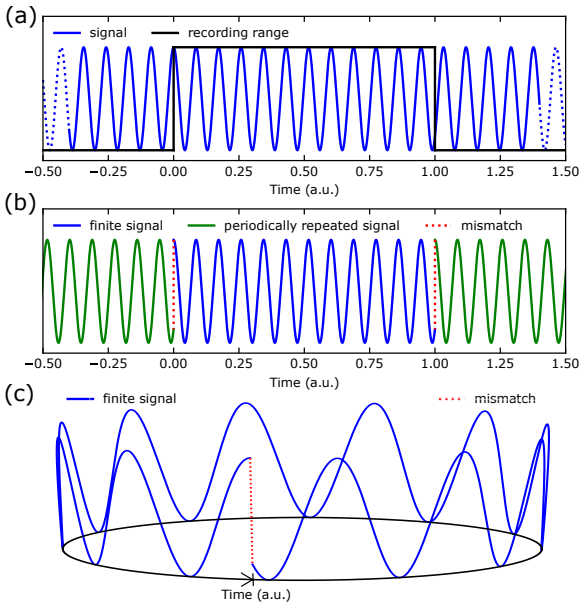

Figure 3.4 – Spectral leakage. (a) A continuous signal is measured in a finite time indicated by the black boxcar function. (b) The DFT interprets the finite signal as a periodically repeated one, presented in green. (c) Visualization of DFT periodicity on a circle. The mismatch depends on the investigated signal frequency and is the source of spectral leakage.

Fig. 3.4 (b), the recorded signal is presented again in blue. The FT assumes now that the signal is periodically repeated after the recording length, which generally leads to a mismatch of the real signal after each period, indicated in red in Fig. 3.4 (b). This mismatch leads to a discontinuity which leaks into other modes. The same picture is presented in Fig. 3.4 (c) where the time signal is wrapped around a circle given by the recording length. In this picture one does immediately see that no leakage occurs if the recording length is a multiple of the underlying signal period. This can be achieved in special cases and is further discussed in section 3.5.

This also means that only a discrete set of functions fulfill the periodicity condition for a given finite recording length. Therefore, the frequencies of this specific set of periodic functions can be seen as an eigenbasis for a given recording length [6]. The discrete sampled IFG

6. For the infinite signal the complex FT is a complete and infinite orthogonal basis where each frequency represents a basis vector.

length defines the fundamental periodicity, whereas the sampling rate defines an upper frequency limit. Frequencies above this upper limit are undersampled and will be assigned to a lower frequency components, an effect referred as aliasing. Therefore, the finite length and the discrete sampling results in a finite set of functions, fulfilling the periodic boundary condition, which form a reduced orthogonal basis. Any signal with frequency components matching the basis frequencies (eigenfrequencies) can be fully represented in that basis. Any frequency different from the eigenfrequencies cannot be correctly mapped to the reduced basis and its projection on the reduced basis vectors corresponds to spectral leakage.

For a better picture we switch to the frequency domain. The finite IFG can be seen as an infinite signal with a boxcar/ rectangular kernel given by the recording length. The complex FT of this boxcar function is a Sinc and is referred as the *line shape* of the FTIR. Each signal frequency component, not necessary the DFT eigenfrequencies, is then convoluted by this line shape. In Fig. 3.5 we will now consider three scenarios to illustrated spectral leakage: single frequency signal matching one eigenfrequency, single frequency signal not matching any eigenfrequency and two single frequency signals not matching any eigenfrequencies.

Fig. 3.5 (a) sketches the single frequency signal (green arrow behind red line) matching a DFT eigenfrequency (black arrow). The signal convoluted with the line shape (green dotted Sinc function) will have its zero crossing on all the other eigenfrequencies which shows the orthogonality of the basis. Therefore, the red dots correspond to the final DFT points and no spectral leakage is observed.

In general, the recorded signal (green arrow) does not overlap with the DFT basis, as shown in Fig. 3.5 (b). But the signal convoluted with the line shape (green dotted line) does overlap with the DFT eigenfrequencies. The red dots are the spectral points seen by the DFT. The single frequency signal is therefore spread in frequency, called spectral leakage, and arises from non-orthogonal mapping of the signal.

The orthogonality of the DFT eigenfrequencies is actually reflected in the zero-crossings of the Sinc line shape and is given by the recorded length. But since in general the recorded signal does not lie on the DFT eigenfrequencies anyway, and therefore the zero-crossings of the Sinc line shape, one can also use a denser, non-orthogonal DFT basis. This would mean that the new DFT basis is

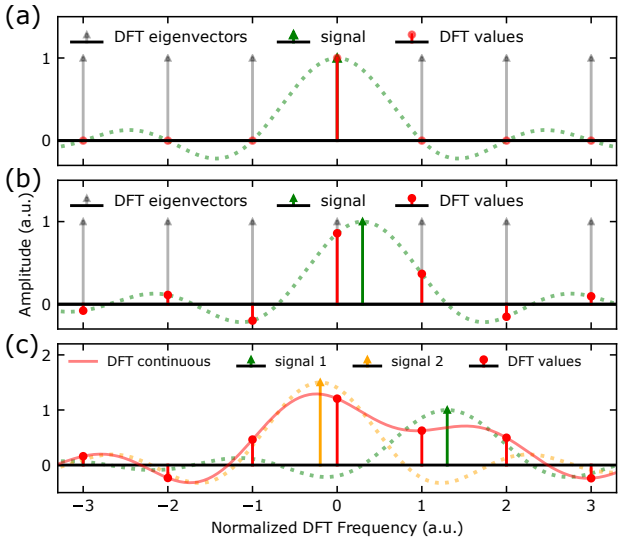

Figure 3.5 – Spectral leakage and DFT basis. (a) The frequency component of the recorded signal (green, behind red) is equal to a DFT eigenvector (black). The signal is therefore perfectly mapped by this eigenvector, and the line shape has its zero-crossing at all other eigenfrequencies. (b) The signal frequency (green) does not coincide with any basis vector from the DFT. Therefore, the final spectral points of DFT correspond to the mapping of the signal line shape to all eigenvectors and are presented in red. Therefore, the intensity is *leaked* from the original frequency to other frequency components. (c) Situation for two signals (green and orange) where each has a Sinc line shape weighted by its amplitude. The total signal (red curve) is the sum of the linshapes. The DFT points are then again the mapping of the total signal to the eigenfrequencies (red dots). The total signal (red) can be as well obtained by zero-padding. Close by modes can therefore influence significantly the amplitude and peak frequency of each other.

sampling more densely the signal convoluted by initial instrumental line shape [7]. Numerically, the DFT basis can be changed by appending zeros at the end of the recorded data, often called zero-padding. This will change the DFT eigenfrequencies as intended, but not the instrumental line shape (Sinc function), which is defined by the number of recorded data points. This actually allows to better estimate the underlying amplitude and frequency of a signal [8]. Since we consider here a single frequency signal, the resulting

7. Loosely speaking one could say it 'draws' the underlying signal convoluted by the line shape (green dotted line).

8. In general it is observed that the resolution on the mode frequency can

peak reflects the signal amplitude very accurately.

To recap we saw that the single frequency signal is convoluted by the instrumental line shape (Sinc), which is by itself defined by the finite recording length (boxcar). The discrete basis of the DFT will then sample the convoluted signal, and the sampling can be increased by zero-padding. The zero-crossings of the Sinc line shape correspond to orthogonal frequencies with respect to the Sinc peak and do not induce any spectral leakage. All other points different from the peak and zero-crossings correspond to spectral leakage induced signal components.

Before we saw that a single frequency signal leakages into "signal free" frequencies. If we now have close-by signals, spectral leakage of each will influence in general the single signal convoluted peak of the other signal. This situation is sketched in Fig. 3.5 (c) for two modes (orange and green arrow) in the spectrum where we omit the eigenfrequency vector for visibility. Each signal is convoluted with the instrumental line shape (orange and green Sinc functions). The total signal in the frequency domain is then the sum of these individual convoluted signals (red curve). The presented solid red curve also represents the DFT spectrum of a largely zero-padded IFG and the red dots the points of the unpadded DFT. Additionally, we see that spectral leakage cannot only change the amplitude of the underlying signal, but also shifts its peak position as clearly visible in Fig. 3.5 (c), solid red curve.

In the special case of a two mode signal where one mode coincidences with a DFT eigenfrequency and a the other one not, the amplitude of the first mode is in principle perfectly measured but the spectral leakage of the other mode leads to a corruption of the first mode amplitude. Therefore, one can only in very special configurations avoid spectral leakage.

As a brief summary, spectral leakage comes from the FTIR line shape and the non-complete basis of the DFT. To reduce spectral leakage effects one can now try to change the kernel function from the boxcar window to other windows function which is discussed in the next subsection.

be increased by roughly a factor of 10 by zero-padding, see also Ref. [38].

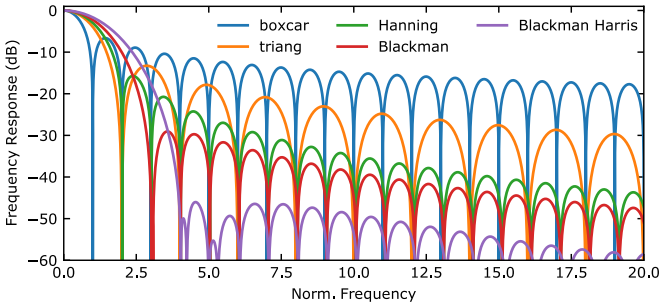

Figure 3.6 – Frequency response of several window functions. Lower side lobes reduce leakage into further modes, but come with the cost of increased main lobe width, i.e. decreasing the resolution.

3.4.2 Window Functions

The instrumental line shape of the FTIR can by changed by apodizing the IFG after being recorded [9]. The functions to apodize the IFG are called window functions like the boxcar, triangular, Blackman or Hanning window to name a few. Their frequency responses consist of a main lobe and side lobes. They are all designed to reduce spectral leakage into the side lobes which comes with the cost of increasing the main lobe width. Therefore, the selection of the window function varies for each situation.

Fig. 3.6 presents the frequency response of some selected window functions. For symmetry reasons, only the positive frequency axis is plotted. We also note that compared to traditional signal processing the intensity, and not a voltage, is measured in FTIRs and that therefore the dB-scale is multiplied by a factor 2.

From Fig. 3.6 it becomes clear that a higher side lobe suppression comes with an increase of the main lobe width. Defining the FTIR resolution by the FWHM of the main lobe it becomes evident that for close modes spacings not every window function can be used and therefore introduces higher leakage in even further spaced modes. Often it is also important how fast the side lobes decay (sidelobe fall off in dB/decade). Table 3.1 presents the 3 dB bandwidth (BW),

9. At the same time by changing the instrumental lineshape the eigenfrequencies can loose their orthogonality.

Table 3.1 – Main lobe BW, first sidelobe height and siedlobe fall off for selected window functions for fields. i.e. 6 dB BW corresponds to the 3 dB BW for an intensity spectrum. Values extracted from Ref. [192, 193].

window	3 dB BW (norm. frequency)	6 dB BW (norm. frequency)	highest sidelobe (dBc)	sidelobe fall off (dB/decade)
Rectangular	0.89	1.21	-12	-6
Triangular	1.28	1.78	-27	-12
Hanning	1.54	2.14	-32	-18
Blackman	1.73	2.35	-58	-18
minimum 4-term Blackman Harris	1.90	2.72	-92	-6

6 dB BW, the highest sidelobe and the sidelobe fall-off for some common window functions [10].

We therefore understand now the effects of a finite signal, that it induces spectral leakage and that this can be suppressed by window functions at the coast of reduced resolution, i.e. an increased main lobe width of the FTIR line shape. In the next section, we combine the collected knowledge from the previous sections and apply it to laser sources.

3.5 Spectral analysis of laser sources

The application of phase correction and spectral analysis with FTIRs does differ when used for lasers and for each situation an optimal approach can be found. In the special case of a frequency comb, one can even achieve in theory a situation where no spectral leakage into other modes will happen. As soon as accurate mode position as well as the resolving of individual modes becomes relevant,

10. Window function are normally used for fields and not intensities. In the case of an FTIR where the intensity is measured, the values in Tab.3.1 have to be divided by 2 resp. the 6 dB BW becomes the 3 dB BW.

like estimation of f_{ceo} of each mode, one needs to understand the consequences of the different approaches for the spectral analysis. These situations will be discussed in the following subsections.

3.5.1 Multi-mode Laser

Compared to broadband incoherent sources, multi-mode lasers emit fairly coherent on the scale of the FTIR resolution. Therefore, the assumption of delta-like modes can be made which is not the case for broadband incoherent sources. Each lasing mode represents under this assumption a cosine function with constant amplitude in the time domain. This simplifies the spectral analysis by simply apodizing the IFG symmetrically (ZPD at the edge of IFG) and then the intensity spectrum is the absolute value of the DFT. By this, the noise is increased by a factor 2 compared to the phase corrected approach, which is in most cases irrelevant. We now discuss the limits of this simple approach and explain in which situations phase correction methods should be applied for increased resolution.

Looking at standard FTIRs like the Bruker Vertex 80v they exhibit a resolution of 0.075 cm^{-1} (2.25 GHz). The dynamic range of an FTIR detector in the THz (deuterated triglycine sulfate detector (DTGS)) is on the order of roughly 40 dB. By comparing to Fig. 3.6 we see that for the Blackman Harris window function all sidelobes are below this -40 dB limit given by the DTGS detector and would be the window function of choice. At the same time, it comes with an increased main lobe width of 2.72 times the nominal resolution at 3 dBm or $2.72 \cdot 2.25\ GHz = 6.1\ GHz$. The main lobe reaches -40 dB at 3.86 times the nominal resolution (8.7 GHz).

The consequence for the analysis of multi-mode lasers is that for clear separation of two peaks by a 3 dB dip and to avoid any visible effect induced spectral leakage the modes should be spaced by at least ∼8.3 GHz. For clear separation of the modes by the noise floor, the spacing must be larger than ∼17.5 GHz for the Blackman Harris window. The latter is more for aesthetic purposes. Other windows will help to distinguish close modes from each others but will lead to visible sidelobes which can influence the peak position and the amplitude of close by modes.

If the modes are even closer to the window BW, spectral leakage leads to a significant distortion of the intensity spectrum. To solve this problem, we can exploit the symmetry of the IFG described

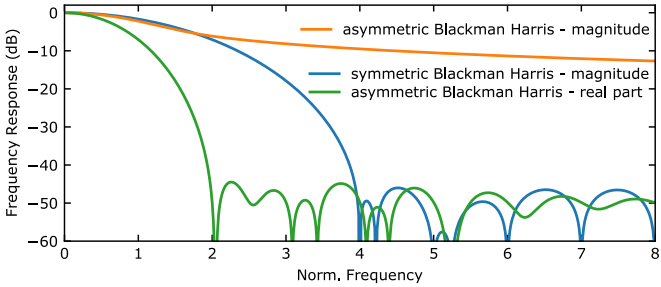

Figure 3.7 – Frequency response of symmetric Blackman Harris window function (blue) and asymmetric Blackman Harris windows function (orange). The asymmetric window function does in principle lead to an increase in spectral leakage for the magnitude. Exploiting the fact that the IFG corresponds to a Cosine one can take the real part of the spectrum, i.e. the real part of the response function as shown in green. This reduces the main lobe width by roughly a factor 2.

in section 3.3 of phase correction to increase our resolution. In the phase correction approaches, the window function is centered at the ZPD and the short double-sided part of the IFG is additionally apodized with a ramp function from 0 to 1. In such a case we end up with an asymmetric or partial window function. This means that from the ZPD on we see half of a the selected window function. In Fig. 3.7 we plot the response function of an asymmetric Blackman Harris window function in orange used in the Forman algorithm [11]. The response function leads to extremely large spectral leakage since the window function is not periodic. By simply taking the absolute value of the DFT, the intensity spectrum would not improve at all.

But since we applied the phase correction to our IFG the signal should only be in the real part of the DFT. Therefore, Fig. 3.7 shows in green the real part of the response function of the asymmetric Blackman Harris window function. Compared with the standard Blackman Harris window function in blue, we see that the main lobe BW is reduced by approximately a factor 2 [12]. The real part appears to be a squeezed version of the symmetric window, but it is not totally identical due to the ramped function of the double sided section and numerical induced effects due to discontinuity at

11. The exact shape does as well depend on the relative length of the double-sided IFG to the full length.

12. This is expected since the asymmetric window function has an underlying periodic window function of double the length of the IFG.

the ends [13].

Therefore, phase correction methods lead to an increased resolution on the intensity spectrum and allow to resolve even modes spaced by roughly 3 GHz for the Bruker Vertex 80v. At the same time, this approach should be taken with care when absolute amplitudes and frequencies are required. The validity of taking the real part holds as long as the phase correction works. Also, the short double-sided signal for phase correction has a higher noise density per normalized frequency than for the entire IFG, resulting in a slightly larger phase error. Therefore, the phases of strong modes can be approximated accurately, whereas weak modes rely on extrapolation of the phase.

Fig. 3.8 (a) compares the phase corrected spectrum (Forman algorithm) in blue with the uncorrected approach in red of a broad, multi-mode THz QCL operating in CW. The device is a copper based double-metal laser with a length of 3 mm and a width of 64 µm operated at a bias of 1.03 A/13.07 V at 42 K and is based on the AR published in Ref. [39]. It becomes evident that the modes are mostly better resolved in the phase corrected spectrum, i.e. lower noise between modes, but at the same time we see some significant differences for example around 2.6 THz and 3.5 THz. If we zoom in at 2.38 THz, shown in Fig. 3.8 (b), it becomes clear that the phase corrected spectrum in blue with a linear extrapolation of the phase does not fully correct the phases and therefore a larger leakage into these modes is observed. By extending the extrapolation to higher order, here a polynomial of order 7, the phase error of the FTIR is better approximated, see orange curve. The situation shown at the edge of the spectrum in Fig. 3.8 (c) could not be improved by higher order phase extrapolation. These modes seem to be enhanced compared to the uncorrected spectrum. This can be attributed to low coherent or diverging modes since in the phase corrected spectrum the window function is centered at the ZPD, i.e. no damping of the signal, whereas in the uncorrected spectrum the ZPD is close to the edge of the window function, i.e. the modes are damped by the window function. Even if the modes could experience an amplitude

13. This discontinuity leads surprisingly to a sampling rate dependent real part of the response function. For example, the number of sampling points for the Blackman Harris should be greater than $2^{15} = 32768$ to reach spectral leakage lower than -40 dB. This can be seen as the sampling rate affects the slope of the discontinuity.

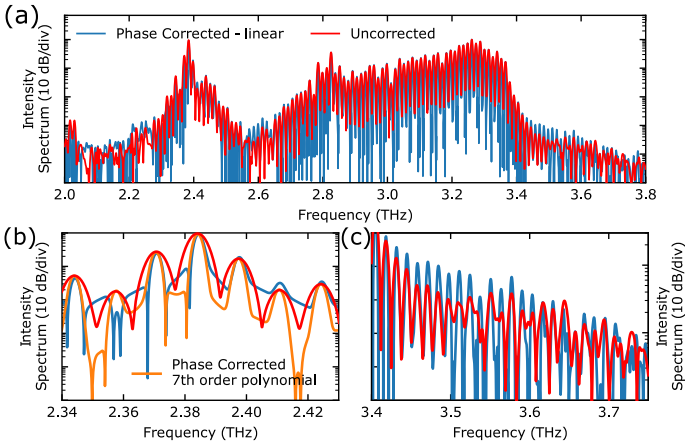

Figure 3.8 – Multi-mode laser spectrum. (a) Uncorrected intensity spectrum (red) and Forman phase corrected intensity spectrum (blue). (b) The increased resolution of phase correction method is visible but with induced errors due the linear phase error assumption, see modes at 2.36 and 2.42 THz. Improved phase correction (orange) due to higher order polynomial fit of the phase error. (c) The uncorrected spectrum has the window function centered to the IFG whereas the phases corrected spectrum has the window function aligned with the ZPD. Therefore, the increased amplitude at 2.6 THz and 3.5 THz in the corrected spectrum indicates incoherent or diverging modes which are weighted stronger in the phase corrected case.

change due to leakage, the increased resolution can be beneficial to resolve closely spaced modes.

As a brief summary, we saw that phase correction can help to increase the resolution by a factor of two but at the same time relies on good phase error extrapolation. The optimal window function in the described case is the Blackman Harris with and without phase correction but comes with 2.72 lower resolution compared to the instrumental lineshape. Other windows can as well be used to resolve even closer spaced modes, but the sidelobes must be distinguished from real optical modes. In the next subsection we treat the special case of frequency combs and will see that in theory spectral leakage free spectra can be obtained.

3.5.2 Frequency Comb Lasers

In the last section we saw that for resolving all modes, we need a certain minimum spacing of the modes or a long enough IFG to

avoid significant spectral leakage. And also then it becomes difficult to distinguish very close modes. At the same time, frequency combs consist of equally spaced and phase-locked modes, which is a special case of multi-mode lasing. Therefore, frequency combs exhibit some periodicity properties in the time and frequency domains, which we want to exploit.

The analysis in the time domain, i.e. the IFG, relies on the symmetry of the IFG induced by the comb nature and is easily and fast inspected visually and less on a mathematical level. Therefore, the symmetry arguments which indicates comb operation is further discussed in the context of harmonic combs in chapter 6 and the appendix C.

In section 3.4 we saw that the natural instrumental lineshape of the boxcar function is a Sinc function in the frequency domain which makes the DFT eigenfrequencies orthogonal to each other. Since in general the the lasing modes do not overlap with the eigenfrequencies one suffers from high leakage effects which was solved by windowing the IFG at the cost of frequency resolution. If all laser modes would now fall onto the DFT eigenfrequencies one would in principle not experience any spectral leakage. This situation can be produced while measuring a frequency comb.

Each mode n can be described by the repetition frequency f_{rep} and the carrier envelope frequency f_{ceo} as $f_n = f_{ceo} + n \cdot f_{rep}$. For the situation that $f_{ceo} = 0$ it becomes evident that by measuring or cutting the IFG to an integer multiple of f_{rep} the comb modes fall onto the DFT frequencies and are orthogonal [14]. By that each amplitude is measured correctly without the need of zero-padding or windowing. f_{rep} is in general known very precisely, since it can be measured electrically on the bias line and the periodicity of the IFG also allows a very precise determination of f_{rep} [15]. It should be noted here that even though the nominal resolution of the FTIR is generally in the GHz range, the mode frequency is resolved on the

14. The IFG is in all cases already a resampled version of the ADC recorded signal. Therefore, it can be resampled again to be precisely matched to a multiple of f_{rep}.

15. The uncertainty of the exact HeNe frequency compared to the high precision RF measurements of the beatnote leads to a slight difference when f_{rep} is extracted from the IFG compared to the measured value. This difference has to be attributed when cutting and leads to some uncertainties in the frequency on the order of a few MHz.

order of a few MHz due to the HeNe accuracy exploited in standard FTIRs.

In general THz QCLs do not have a $f_{ceo} = 0$, which would lead to a shifted version of the laser modes compared to the eigenfrequencies of the DFT. The naive approach would be to zero-pad by many multiples of the f_{rep} length. With that many more DFT frequencies will be generated which form subgroups of orthogonal subbases shifted to each others [16]. Therefore, one could achieve having the comb modes on such an orthogonal subbasis. At the same time, one would experience huge spectral leakage into all other subbases and the calculation is computational heavy due to the large zero-padding needed.

A more efficient approach is to estimate f_{ceo} and go into the moving frame of it. This approach was already applied to frequency combs in Ref. [194] and [195] where f_{ceo} was measured and stabilized. The drawback in the method shown in Ref. [195] is that the IFG was not resampled to be an exact multiple of f_{rep} but instead they shift by an additional frequency to locally overlap the DFT frequencies with the comb frequencies or add zero-padding to change the DFT frequencies. But therewith they did not change the underlying lineshape and induced slight spectral leakage. The error induced was tolerated due to the very high number of 10^6 sampling points and the recording length, which barely leads to spectral leakage in their case.

The previous mentioned paper used a stabilized frequency comb to perform high precision spectroscopy, whereas in our situation we apply a similar approach to measure laser spectra of free running THz QCL combs. The procedure, calling it CombFFT, is therefore the following:

1. measure the IFG (optional: the electrical beatnote)
2. optional: perform Forman phase correction
3. apply zero-phase bandpass filter around spectral components
4. perform the Hilbert transform of the IFG
5. generate analytical function from interpolated complex IFG
6. extract the satellite positions from the IFG envelope to estimate f_{rep}. if electrical beatnote is measured, one can rescale the delay

16. The eigenfrequencies which are orthogonal have a spacing given by the IFG length cutted by f_{rep} and not to the zero-padded frequencies.

7. select ZPD peak as first point of IFG and determine from the interpolated function f_{ceo} at the last satellite (should be a peak as well if f_{ceo} was found correctly).
8. rotate the complex IFG by $e^{-i2\pi f_{ceo} \cdot t}$
9. optional: optimize f_{rep} and f_{ceo} by minimizing the noise of the DFT (at least $2 \times f_{rep}$ IFG length needed)
10. resample IFG to extracted f_{rep} with a power of 2 number of sampling points
11. perform DFT on resampled IFG
12. shift DFT frequency by the offset frequency f_{ceo}

We note here that this algorithm is applied to free running THz QCLs. Therefore, f_{ceo} and f_{rep} will drift during the time of the FTIR measurement. The shift could be on the order of MHz which is not addressed in this approach. Additionally, the reference laser used in an FTIR should be stable and the frequency known to a high precision to reduce uncertainties in the IFG measurements [17]. For the investigated IFG of a THZ QCL where the beatnote was measured, the extracted beatnote frequency from the CombFFT algorithm agreed within 5 MHz of the electrically measured frequency. This would be on the order of the FWHM of the HeNe reference laser used in the FTIR. For simplicity the described method will be referred as CombFFT in the following.

In Fig. 3.9 (a) we compare the standard Forman corrected spectrum with the CombFFT spectrum for a homogeneous THz QCL showing a narrow beatnote detected on the bias-line indicating comb operation. It is clearly visible that the modes are well resolved and that the noise between modes is reduced when using the CombFFT. At the same time the noise does not fully go down to the noise floor. It is most likely due to the free running nature of the THz QCL comb and the uncertainties of the reference HeNe which introduces this noise.

In comparison, Fig. 3.9 (b) shows the ComFFT applied to a multi-mode state of the same device. The non-equidistant spacing

17. For example Nicolet FTIRs state accuracy of HeNe reference laser of 0.01 cm^{-1} = 300 MHz or less, see also discussion in Ref. [188], chapter 5.1.4. Beam divergence of the finite source size and misalignments of the source can also lead to accuracy errors, see Ref. [188] in chapter 2.6, but in the case of QCLs and good alignment, i.e. non-decaying IFG envelope, seem not to be a limiting factor.

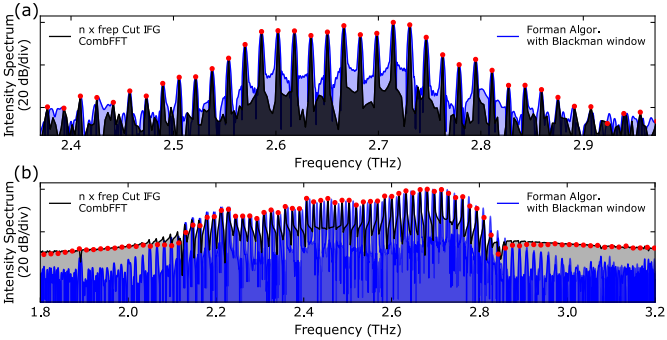

Figure 3.9 – Forman corrected intensity spectrum vs CombFFT. (a) Intensity spectrum of free running THz QCL with a narrow, single beatnote indicating comb operation. The CombFFT method (black) shows sharp modes and a decreased noise floor between mode pairs compared to the Forman phase corrected spectrum. (b) CombFFT applied to a multi-mode lasing THz QCL showing that the non-equidistant mode spacing leads to the expected high spectral leakage. Therefore, the CombFFT provides a clear sign for non-comb states.

of this multi-mode regime leads to high spectral leakage between and outside the spectral region of the lasing modes. Therefore, the CombFFT can clearly distinguish comb from multi-mode operation.

As discussed before, if it comes to the precision of the CombFFT, one relies on the precision of the reference laser and that the free running laser is not drifting over multiple of MHz during a scan. Since this accuracy depends on the alignment of the QCL and as well on the in general unknown performance of the HeNe laser, it is hard to derive an equation for the CombFFT precision. Nevertheless, for each measurement one can compare the extracted f_{rep} from the IFG with a slightly changed f_{rep} and with an optimized one. This is done in Fig. 3.10 where the unoptimized and optimized CombFFT of the same spectrum as in Fig. 3.9 (a) is compared to a ± 7.5 MHz changed f_{rep} CombFFT. For this specific case, as well as similar ones, it is observed that changes on the MHz level already introduce clear spectral leakage of all modes into the others. It is therefore evident that the CombFFT is about two orders of magnitudes more sensitive on the mode frequencies of a frequency comb states than, for example, the zero-padded Forman algorithm, which is roughly 200 MHz. At the same time, the CombFFT should in principle be able to even detect two very close modes, i.e. below the FTIR resolution down to roughly 10 MHz, since one mode would lead to

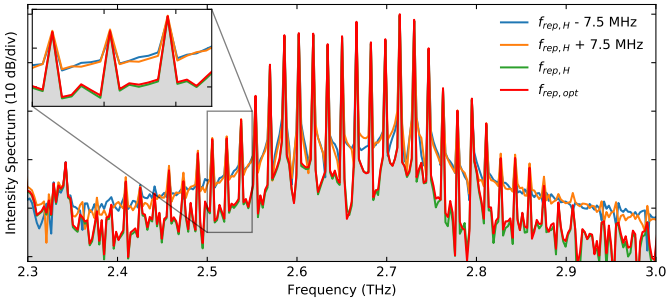

Figure 3.10 – CombFFT applied to the same state as in Fig. 3.9 (a). The CombFFT uses once the IFG extracted $f_{rep,H}$, a noise between modes optimized $f_{rep,opt}$ and a ±7.5 MHz offset of $f_{rep,opt}$. Clear spectral leakage is observed for the ±7.5 MHz offset and shows that the CombFFT is sensitive on the MHz level in this example.

high leakage [18].

The reason for this high performance of the CombFFT becomes clear when inspecting the response function of the boxcar function as shown in Fig. 3.6. The boxcar function has sharp singularities at the eigenfrequencies of the DFT. Since the CombFFT shifts the comb modes into this singularities, the noise between modes should fall to the noise floor for a fully stabilized comb. For the free running comb and due to the stability of the HeNe laser, this cannot be fully achieved. Nevertheless, the modes are fairly well located on the DFT eigenfrequencies. The high spectral leakage of the rectangular window is here actually beneficial in two ways: First, the first sidelobe is already -6 dB below the main lobe. Secondly, the sidelobe fall off is -3 dB/decade. Together with the sharp singularity, this makes the rectangular window the ideal window to verify equidistant modes on the MHz level.

Once the equidistant spacing of the comb modes is verified on the level of the CombFFT, or by other means, it enables in principle to perform spectroscopy at the MHz level and sweeping of the QCL comb could allow interleaving of multiple spectra to record narrow absorption lines [196, 197]. If the CombFFT results in a low leakage spectrum, one has determined f_{rep} and f_{ceo} on the MHz level and the comb mode frequencies are well defined. To further reduce the noise,

18. This might not be fully true if one mode amplitude is very small compared to the other.

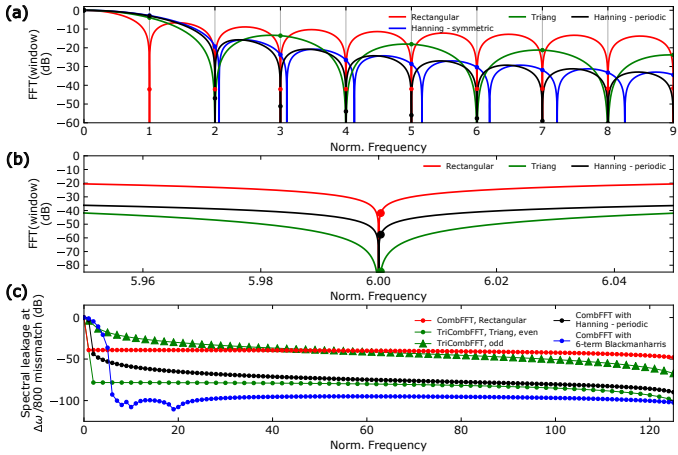

Figure 3.11 – Singularity of window functions. (a) Frequency response of different window function. The rectangular window has its singularities for each integer frequency, i.e. overlapping with the DFT eigenfrequencies. Other periodic window function have their singularities overlap with a subset of eigenfrequencies. Symmetric window functions have in general no overlap of the singularities and the DFT eigenfrequencies.(b) Zoom on the 6th eigenfrequency showing that different window functions have a sharper singularity than others. The dots indicate the leakage for each window function if f_{rep} is mismatched by 1.6 MHz with respect to the IFG length for the case shown in Fig. 3.10. (c) Theoretical spectral leakage for different window functions with an assumed f_{rep} to DFT spacing mismatch of $\Delta\omega/800$. Depending on the available IFG length one can chose the optimal window to reduce spectral leakage even in presence of non-perfect spacing resp. sampling errors.

effects of measurement uncertainties of the HeNe, the free running nature of the QCL and numerical artifacts on the absolute mode amplitude one can apply a periodic window function [19] to step 10 of the CombFFT procedure. Many window functions [192, 198, 199] are defined periodically and produce a reduced orthogonal basis with eigenfrequencies spaced further than the main lobe width. Fig. 3.11 (a) plots the response function for the rectangular, triangular, symmetric and periodic Hanning window function. As stated before, the rectangular window overlaps with the complete orthogonal basis of the DFT, i.e. its eigenfrequencies. The presented triangular window function forms a reduced basis over every second eigenfrequency

19. In Python for example, all window functions are by default defined symmetric. Only the periodic definition keeps a reduced orthogonal basis for other window functions, normally after the width of the main lobe.

and the periodic Hanning a reduced orthogonal basis after the first neighboring eigenfrequency. The symmetric Hanning does not form a reduced orthogonal basis with respect to the DFT eigenfrequencies and is not suited for the windowed CombFFT. Therefore, the use of suited periodic window functions in the CombFFT procedure before performing the DFT leads to an improved amplitude accuracy and reduction of remaining leakage errors on the cost of frequency accuracy and sensitivity on non-equidistant modes. Since the frequency accuracy was only needed in a previous step with the rectangular CombFFT, where we can also store the frequencies, we can now sacrifice on the frequency resolution since we know them already and gain in amplitude accuracy. The dots in Fig. 3.11 (a) represent the spectral leakage induced by a f_{rep} mismatch of 1.6 MHz.

As shown in Fig. 3.11 (b), where we zoom in on the 6th eigenfrequency, the singularities of each window function has a different steepness. Here, the 6th eigenfrequency was chosen according to the spectra presented in Fig. 3.9 (a) and Fig. 3.10 to match the number of satellites in the IFG. Each dot represents the spectral leakage we would induce by a mismatch of the f_{rep} of 1.6 MHz. The spectral leakage of the rectangular window from one mode is around -40 dB into the neighboring mode reps. into the other DFT frequencies. This is on the order of the dynamical range of the THz DTGS detector in the Bruker 80v. The total leakage is then the sum of all leakage from all spectral modes.

The periodic Hanning window has its singularities after the first neighboring DFT frequency, which all have a lower steepness than the rectangular window singularities. The same mismatch of 1.6 MHz of f_{rep} leads to a reduced leakage of -57 dB. By using the triangular window function on IFG consisting of an even multiple of f_{rep}, the leakage effect can even further be reduced. Since it's the by far best choice for short IFG of even f_{rep} lengths, i.e. of 2 or 4 f_{rep}, we call it TriCombFFT. For the TriCombFFT the spectral leakage is as low as -84 dB for the example of 1.6 MHz mismatch and the high spectral leakage in all odd DFT frequencies can be omitted since no comb mode lies on them [20].

Fig. 3.11 (c) reports the spectral leakage into other modes when the DFT spacing is missed by a factor $\Delta\omega/800$ where $\Delta\omega$ is the nominal frequency resolution. It shows again that the rectangular CombFFT has highest leakage, therefore suited to verify equidistant

20. This should of course be verified before applying the TriCombFFT.

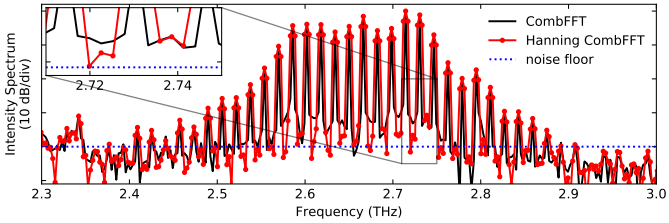

Figure 3.12 – CombFFT with Rectangular and Hanning window. As was suggested in Fig. 3.11, the CombFFT with the Hanning window does further reduce the leakage between modes close to the noise floor. Inset: zoom in on an unchanged spectral component. This could indicate that there is an actual weak mode at this frequency showing the sensitivity of the CombFFT.

modes, whereas the TriCombFFT leads to very low spectral leakage for any mismatch. For long IFGs consisting of more than six satellites the use of additional 6-term Blackman Harris or higher term windows with very high sidelobe suppression can be exploited.

In Fig. 3.12 we compare the rectangular CombFFT with the Hanning CombFFT. It shows that, as expected, the noise between modes is further suppressed as a result of spectral leakage minimization. At the same time, the Hanning window has its first singularity at the second DFT frequency, which leads to a triangular kind of peak of the mode. The symmetry of this triangular peak is also a very good indication for a correct determination of f_{rep}. These characteristic peaks lose their symmetry when the mode amplitude is very close to the noise floor (blue dotted). To highlight the sensitivity of the CombFFT method, we look at the inset of Fig. 3.12. It shows that at 2.74 THz a slight peak is observed in both cases. If it would be an artifact of the CombFFT it should have changed due to the different spectral leakage when the Hanning CombFFT was applied. Since the peak kept unchanged, this indicates that there is a weak mode present between the two strong modes.

3.6 f_{ceo} extraction

Even though the repetition frequency f_{rep} can be measured over the bias line of a QCL, the same does not apply for the carrier envelope frequency f_{ceo}. One possibility to measure f_{ceo} is a heterodyne measurement with a well known reference distributed feedback

(DFB) QCL as was shown in Ref. [11]. Furthermore, the so-called self-referencing f-2f technique [85], relying on an octave-spanning frequency comb, could also provide the measurement of f_{ceo}. Both techniques have their limitations and cannot be realized in a general fashion. Therefore, we discuss here how one can estimate the f_{ceo} from an FTIR measurement. If one has a single frequency comb, we can exploit the CombFFT. The algorithm by default extracts the repetition rate f_{rep} and the carrier envelope frequency f_{ceo}. Therefore, this provides an estimate of f_{ceo} on the order of some MHz for our FTIR. The situation is different if one observes for example sub-combs with different f_{ceo}'s since the CombFFT cannot be applied. Best practice here is to record an IFG as long as possible and use a suited window function to reduce spectral leakage [21]. Under this assumption, the delta-like comb mode is convoluted by the window function response with nearly zero spectral leakage. Even though the mode is broad due to the finite resolution bandwidth, the peak positions of all comb modes in such a case are therefore accurate on the tens of MHz. By extracting the peak position frequency of each mode and calculate the modulo with respect to the repetition rate, we can extract the f_{ceo} for each mode. The peak can be found via zero-padding or by cubic interpolation of the mode. If we apply this approach to a comb state, we find that the extracted f_{ceo} as a function of mode frequency are scattered around one line with a nearly zero slope. The residuals are on the order of tens to hundred MHz. If we apply the same technique but choose f_{rep} minus 10 MHz, we find that the extracted f_{ceo}'s as a function of mode frequency lie again on a line but this time with a clearly visible slope. Therefore, the mean value of f_{ceo}'s lying on a line with nearly zero slope provides a good estimate of f_{ceo}. This approach can now also be applied to sub-combs, as we will see in chapter 9.

3.7 Summary

In this chapter the basic concepts of an FTIR were introduced. We discussed the symmetry properties of the FT and the Michelson Interferometer. A short excursion on Forman and Mertz phase correction was given followed by the implications when using discrete

21. This can also be achieved with a shorter IFG and cutting it correctly to roughly match the minimums of the window function response to the mode spacing.

sampled IFGs. This included in detail the effect of spectral leakage and its reduction by apodization with window functions and that a complete orthogonal basis for periodic functions is given by the DFT. The last section applies this knowledge to the spectral analysis of multi-mode and comb spectra. For multi-mode operating THz QCLs it was demonstrated that appropriated windowing needs to be selected and that phase correction leads to a doubled resolution but relies on precise phase correction which is difficult to verify. When it came to comb states, the orthogonal basis of the DFT was exploited to determine f_{rep} and f_{ceo} on the MHz level of a free running THz QCL comb. Therefore, it should allow spectroscopy with MHz resolution when combined with interleaving technique.

4

Broadband, homogeneous THz Quantum Cascade Lasers

Rösch et al. showed in Ref. [38] and Ref. [39] that THz Quantum Cascade Lasers (QCLs) can emit over more than one octave in a single, monolithic and electrically pumped device and that comb formation over a bandwidth of 1.1 THz is possible. The devices were based on heterogeneous stacks consisting of three [38] or four similar active region designs [39]. Each single active region design was tailored to cover a part of the final spectrum and the gain shape was engineered to minimize chromatic dispersion. The current density from one stack to the other had to be matched for simultaneous lasing. In experiments, this leads in general to sequential switching on of each stack. In both papers, the comb formation was observed in regions where only a part of the stacks was lasing simultaneously. Lasing of all stacks always led to multi-mode operation with high phase noise of the beating signals clearly observed on the laser bias. Furthermore, threshold current densities of 275 A/cm^2 and 400 A/cm^2 are relatively large, leading to high currents and heating, and limit the mounting to narrow and short devices [1]. Attempts to RF injection lock such devices [131] resulted in limited success compared to their less broad counterparts [12, 103]. By returning from a heterogeneous to a homogeneous design, we will show that many of the previous mentioned drawbacks can be solved by maintaining a broad emission bandwidth.

Therefore, in this chapter we will present results on a broadband, *homogeneous* THz QCLs [2]. The active region design, the

1. Comparable bandwidths were only achieved later by a similar approach in Ref. [200] with an improved current density of roughly 170 A/cm^2 at 10 K.

2. Most of the content in this chapter appeared, in some parts *verbatim*, in A. Forrer et al. "Photon-Driven Broadband Emission and Frequency Comb RF

light-current-voltage (LIV) and the spectral evolution depending on the bias will be presented in section 4.1. The appearance of a bi-stable regime, originating from domain formations within the QCL, resulting in a up to 1.8 THz wide spectrum, will be observed. This domain formations will be theoretically investigated by means of Non-Equilibrium Green's Function (NEGF) simulations and will be temporally as well spectrally resolved experimentally in section 4.2. section 4.3 will present indications for comb formation as well as the RF injection of f_{rep}, in the comb, high-phase noise and bi-stable regime.

4.1 THz QCL design and operation characteristics

We present here a QCL design [3] which is derived from our previous 4 quantum well structure [201], optimized for wide bandwidth and low threshold operation. The design relies on a high degree of diagonality of the lasing transition. The lifetime of the upper state and the gain recovery time are also increased, as already experimentally verified for the previous, less diagonal structure showing a gain recovery time of ∼35 ps [116], significantly larger than the ∼10 ps found for a bound-to-continuum THz design under lasing operation in Ref. [202]. This long lifetime makes the transport above threshold significantly photon-driven, i.e. the upper state lifetime is largely reduced due to stimulated emission while keeping the lower state lifetime approximately constant [203]. As a consequence, the transport is drastically modified showing a characteristic discontinuity at threshold that accounts for the difference of lifetimes before and after entering the lasing regime. The increased lifetime does in fact also change the typically non-resonant optical response to modulation currents for QCLs towards a resonant one, making the design more prone to amplitude modulation up to tens of GHz [28].

The bandstructure of one period of the laser is reported in Fig. 4.1. The heterostructure was grown by molecular beam epitaxy (MBE) on a semi insulating GaAs substrate in the GaAs/$Al_{0.15}Ga_{0.85}As$ material system. Thermocompressive Au-Au (500/500 nm) wafer bonding on a receptor substrate was followed by dry-etching double-metal laser ridges with ICP and top metalization (Ti/Au, 10/200

Injection Locking in THz Quantum Cascade Lasers." ACS Photonics 7, no. 3, 784–91 (2020).

3. Active region design Nr. EV2244.

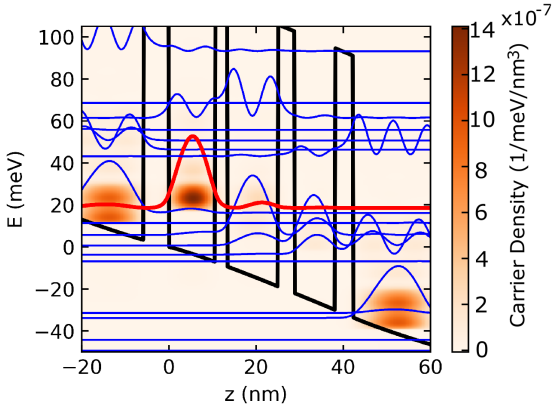

Figure 4.1 – Color scale display of the energetically and spatially resolved electron density computed in the non-equilibrium Green's function model for an applied bias of 50 mV per period and lattice temperature of $T_L = 150$ K. The Wannier-Stark wavefunctions and conduction band potential profile are overlaid. The layer sequence based on GaAs/$Al_{0.15}Ga_{0.85}As$ is 18.3/**5.8**/10.6/**2.9**/11.5/**3.9**/9.2/**4.1** in nm where barriers are in bold and the $2.3 \cdot 10^{16}$ cm^{-3} Si doped injection well is underlined. The sequence is repeated 151 times and grown by molecular beam epitaxy (MBE). Reprint from Ref. [143].

nm) following the fabrication procedure in chapter 2, section 2.2.1. The ridges feature setbacks on either side for transverse mode control as reported in Ref. [130] and discussed in chapter 2, section 2.2.2. In Fig. 4.2 we present the light-current-voltage (LIV) curve as a function of temperature for a 1.5 mm long and 70 µm wide device operated with a pulse length of 1 µs at 100 kHz. For low temperatures we observe an uncorrected single-facet peak output power of 1.6 mW and a threshold current density of 110 A/cm^2. The laser operates up to a maximum temperature of 100 K. As expected for strongly diagonal designs both in mid-IR [204] and THz QCLs [205] we observe a sharp kink in the IV curve at the laser threshold indicating a pronounced photon-driven transport at low temperatures.

In the following, we present a series of measurements which are performed simultaneously, i.e. applied voltage and current in Figs. 4.3, 4.4 and 4.8 represent the same measurement run to provide the best correlation of the data. The QCL device was mounted in a flow cryostat, aligned to an Fourier-Transform Infrared Spectrometer (FTIR) (Bruker, Vertex 80v), powered by a CW current/voltage source (Keithley 2000 with an additional RC filter) over a bias-tee (SHF BT 45D, 1-45 GHz) and connected as well to a spectrum

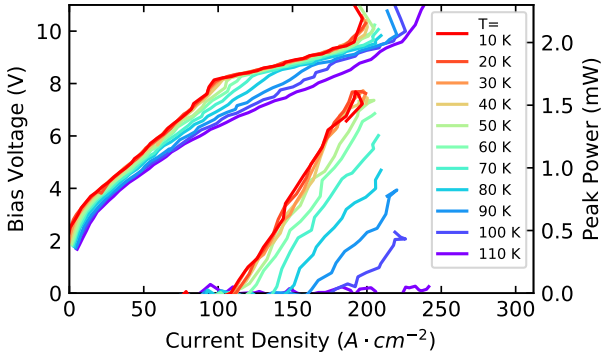

Figure 4.2 – Pulsed LIV curve of a 1.5 mm long, 70 μm wide QCL for increasing heat sink temperature. Emission peak power up to 1.6 mW from a single facet and lasing up to 100 K is observed for 1 μs long pulses at 100 kHz repetition rate. The output power is uncorrected to any detector size and window losses. Reprint from Ref. [143].

analyzer (SA) (Rohde&Schwarz, FSW 64) over the bias-tee. An additional bias connection allowed for observing the instantaneous voltage over the QCL with an oscilloscope (LeCroy, HDO6104). The SA and oscilloscope measurements were performed three times before spectrum acquisition and once afterwards for consistency check. In Fig. 4.3 (a) we plot a series of CW spectra as a function of applied bias to the laser. Here, the current source was switched to operate as a voltage source allowing to enter the normally inaccessible negative differential resistance (NDR) regime of the QCLs in CW (electronic circuit similar as in Ref. [206]). The device is a relatively short Fabry-Pérot cavity of 1.2 mm and 90 µm width.

At low currents in Fig. 4.3 (a), corresponding to the first part of the dashed L-I curve in Fig. 4.4 (a) in black, the laser is spontaneously operating on the so-called harmonic state, recently demonstrated and discussed in mid-IR QCLs [207, 208]. The harmonic states are further discussed in chapter 6 and 9. Such a lasing state is characterized by a spectrum displaying mode separations of several cavity round trip frequencies. Its origin lies in the interaction between population pulsations and population gratings in the laser cavity where a $\chi^{(3)}$ nonlinearity is present. We observe harmonic state signatures starting from a bias current of $I = 1.22\ I_{\mathrm{thresh}}$ and a harmonic mode spacing of $6 \times f_{\mathrm{rep}} = 210$ GHz. To fully prove the coherence of the modes a multi-heterodyne beat against another

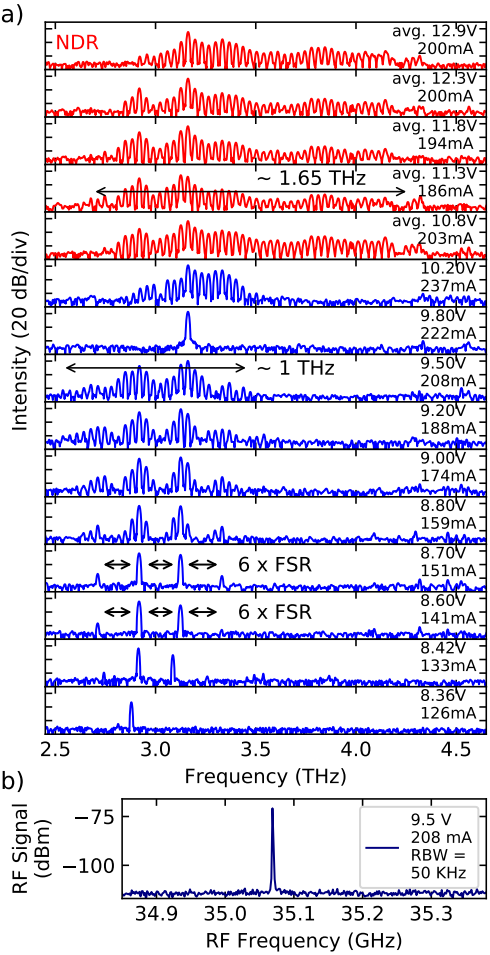

Figure 4.3 – (a) Evolution of the emission spectrum as a function of the CW applied bias for a 1.2 mm long and 90 µm wide device. For low currents we observe self-started harmonics spaced by 6 times the free spectral range (FSR). Increasing voltage leads to a dense spectrum spanning up to nearly 1 THz at 9.5 V, followed by a collapse into a single mode and recovery to dense mode before entering the NDR. The spectra in red are recorded only for voltage driven operation and features emission up to 1.65 THz from this homogeneous QCL. (b) Free-running single and narrow beatnote in the presence of feedback from the FTIR and a S/N of 43 dB at 9.5 V, indicating frequency comb operation. Reprint from Ref. [143].

QCL comb would be necessary. Shifted Wave Interference Fourier Transform (SWIFT) measurements like in chapter 9 are not realized since the repetition frequency of hundreds of GHz is too high for the detectors and RF electronics. In contrast to mid-IR QCL combs, where the harmonic state is built mostly symmetrically around one center mode [207, 208], the harmonic state of this particular THz QCL has its symmetry in between two lasing modes, which is also discussed in more detail in chapter 6. After this harmonic state the emission spectrum evolves into a dense multimode state, progressively broadening to span from 2.53 THz to 3.47 THz for $I = 208$ mA and 9.5 V. At the same time, a single narrow beatnote is observed, shown in Fig. 4.3 (b), indicating comb operation. With the results we present in chapter 9, it becomes clear that the spectrum most probably consists of subcombs, each with the same repetition rate but different f_{ceo}. At 215 mA the laser abruptly turns into single mode operation at 3.1 THz: in the IV curve in Fig. 4.4 (a) this is visible as a precursor to the strong NDR happening at $I = 240$ mA.

Inside the NDR region the instantaneous CW bias voltage is in fact pulsating at RF frequencies, which we have measured by acquiring the bias drop on the laser with an oscilloscope.

These intensity pulsations group into two different regimes which have main frequency components of 54 MHz and 40 MHz and occur for applied voltages of 10.9 V to 11.2 V and 11.3 to 12.9 V, respectively. For each regime, a typical time trace is presented in Fig. 4.4 (b) showing a stable intensity pulsation. Similar self-pulsations were already observed in a THz QCL under long current pulse driving close to the laser threshold, and was attributed to domain formation inside the device by Winge *et al.* [206] supported by a theoretical model (see also Ref. [43, 157, 206, 209–212]). A quantitative view with time resolved measurements is discussed in the next section. In this NDR regime, the spectral output of the laser spans an extensive frequency range from 2.6 to 4.3 THz, about 1.7 THz which corresponds to a fractional $\Delta f/f_0 = 0.5$ with respect to the central frequency $f_0 = 3.45$ THz. Further devices showed lasing spanning over 1.83 THz in this regime, see Fig. 4.6 (a). This represents the highest relative frequency span for a homogeneous quantum cascade laser structure so far.

If the laser structure is driven in current mode, we observe a radically different behavior; in Fig. 4.4 (a) we plot the overlap of 3

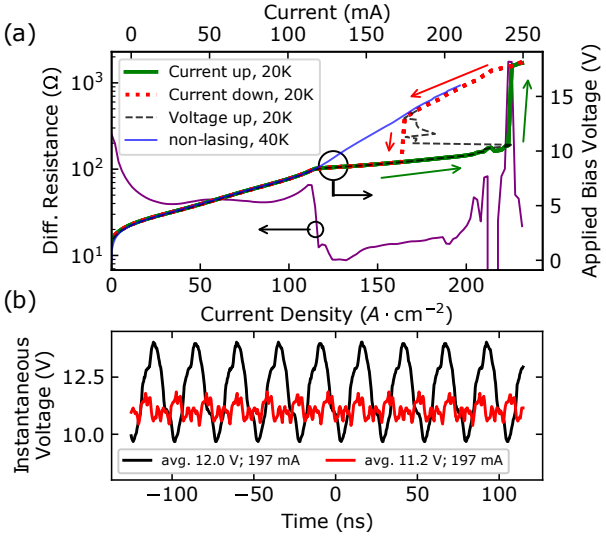

Figure 4.4 – (a): CW IV curve for increasing current (green), decreasing current (red) and voltage driven (black) operation of a 1.2 mm long and 90 µm wide device. For all lasing devices the pronounced kink in the IV occurs due to the photon driven transport. The current driven modes show a clear hysteresis behavior without lasing for voltages in the upper branch. The comparison with a 0.345 mm long and 70 µm wide non-lasing device (blue) shows that the IV of the lasing device recovers the one of the non-lasing after the NDR. The temperature difference is explained by the better heat extraction of the smaller non-lasing device. The purple curve shows the differential resistance (of the green curve). (b) Instantaneous voltage over the QCL for two bias points in the voltage driven NDR regime. The two main frequency components are 40 MHz (black) and 54 MHz (red) and are stable over longer time scales. Reprint from Ref. [143].

measurements each of the CW current driven IV of a lasing device for increasing (green) and decreasing (red) currents at 20 K together with one IV curve of a non-lasing structure (blue) at 40 K. The current is swept from zero to higher values in the lasing device up to 240 mA (223 A/ cm^2, same value as for the voltage driven NDR). At NDR the device shows a hysteresis on the curves of lasing and non-lasing devices.

By calculating the differential resistance from the voltage driven IV curve in Fig. 4.4 (a), we can estimate the ratio $\tau_{eff}/(\tau_{eff} + \tau_2)$ by [156, 203]

$$\frac{\tau_{eff}}{\tau_{eff}+\tau_2} = 1 - \frac{R_{d,S>0}}{R_{d,S=0}}, \tag{4.1}$$

where $R_{d,S>0}$ and $R_{d,S=0}$ are the differential resistance above and below threshold, respectively, τ_2 the lower state lifetime and $\tau_{eff} = \tau_3 \cdot (1 - \tau_2/\tau_{32})$ with τ_3 the upper state lifetime and τ_{32} the non-radiative lifetime. Entering the values from Fig. 4.4 (a) we find $\tau_{eff}/(\tau_{eff}+\tau_2) \approx 0.81$. This value is roughly twice that reported in Ref. [156] and indicates a long upper state lifetime. This result is also supported by the non-equilibrium Green's function (NEGF) simulations in the following section, where the corresponding scattering rates calculated in the Wannier basis provide a ratio of 0.83 at 50 mV/period and lattice temperature $T_L = 150$ K [4]. Additionally, we find that the diagonal transition has a relatively low computed maximum oscillator strength between the upper state and the lower states of $\sum_{low_j} f_{up,\ low_j} \approx 0.25 - 0.20$ from the lasing threshold to the NDR.

4.2 Non-Equilibrium Green's Function simulation and time-resolved spectrum

In order to explain the experimental observations of a pulsating laser in the NDR region, we now present NEGF [213] [5] simulations of the laser under operation, as well as time-resolved spectrum measurements, i.e. a spectrogram. In the NEGF formalism used here, the photo-induced current can be included by increasing the ac field strength in the simulations until the gain clamps at some assumed value for the total losses [214]. At a lattice temperature of $T_L = 150$ K [6] there is still enough gain for significant photo-driven transport, even for losses as high as 10 cm^{-1} and 20 cm^{-1}, as shown in Fig. 4.5. This performance is most likely overestimated since electron-electron scattering has been neglected in these simulations, which can significantly deteriorate the performance [215]. The simulations show that the laser turns on at the first alignment peak close to 6 V, and the strong photo-induced current allows the laser to operate into the bias region where the non-lasing device

4. Simulations for lower T_L result in numerical instabilities.

5. Original code written by the Group of A. Wacker and further developed M. Franckié in the Group of J. Faist.

6. Simulations for lower T_L result in numerical instabilities.

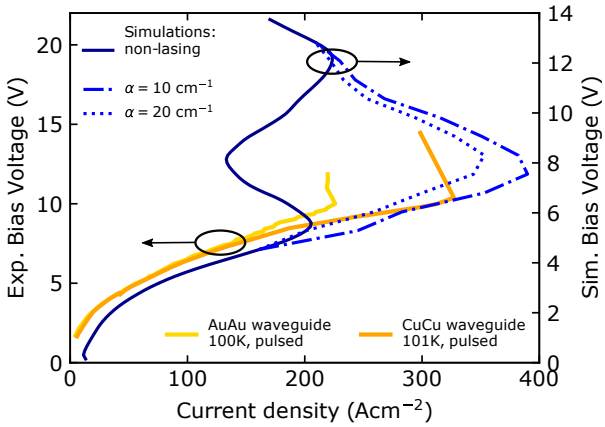

Figure 4.5 – NEGF simulated LIV at 150 K (lattice temperature, dark blue dashed), NEGF including photon-driven transport clamped to losses of 10 cm^{-1} resp. 20 cm^{-1}. Experimental LIV curves are presented for gold (1.5 mm x 90 µm) and copper (2.3 mm x 106 µm) devices at 100 K (heat sink temperature). The voltage difference of simulation to experiment is attributed to the Schottky contact and additional serial resistances in the real device. Reprint from Ref. [143].

shows NDR (indicated by the dark-blue line). Such a clear NDR feature is not seen in the experimental non-lasing device driven in voltage mode, most likely because of leakage currents through high lying parasitic states. At a bias around 8 V the gain begins to drop and as a result so does the photo-driven current, which creates an NDR region for the lasing device where in the absence of lasing the differential resistance returns to positive values. Above this bias, the laser operates with high optical power in an unstable electrical region. This can explain the broad spectra observed in this bias region for the experimental device in Fig. 4.3, as the laser can alternate between different bias points at a constant current density. In addition, electric field domains can be formed where separate sections of the laser are temporally biased with different voltages simultaneously.

Since the peak current density shows a strong temperature dependence, a quantitative comparison between the simulated currents at 150 K and the LIV at low temperatures for the device employing an Au-Au waveguide is not possible. Therefore, we also fabricated a device with a Cu-Cu waveguide which showed significant photo-

driven transport even at 100 K heat sink temperature, as seen by the orange solid line in Fig. 4.5. These Cu-Cu devices are further discussed in chapter 5. Just as in the simulations, at the alignment bias where the slope of the IV curve flattens out, the device starts to lase and pushes the operation opposite to the non-lasing NDR region. At a higher bias, the current starts to decrease again as the gain diminishes. The difference in bias between the experimental and simulated curves is explained by an estimated contact Schottky bias drop of 0.9 V for the Au-Au device and 0.6 V for the Cu-Cu device, and an additional series resistance providing lower slope in the IV curve.

The IV curve provides insights on the electrical origin of the self-pulsation, but additional gain simulations are necessary to explain the broadened spectrum. Also, more sophisticated models rely on accurate gain predictions as explained in Ref. [206]. Therefore, we now compare the evolution of the simulated and experimental emission spectrum in Fig. 4.6. Panel (a) presents the broadest spectrum spanning 1.83 THz of a 1.45 mm long and 65 µm wide device in the intensity pulsating regime with high phase noise. The spectrum is compared additionally to the electroluminescence measurement of a non-lasing device (short cavity of 0.345 mm) in Fig. 4.6 (b) and to the simulated gain in Fig. 4.6 (c). The bandwidths of the electroluminesence and the simulated gain agree reasonably with each other and as well with the minimal and maximal observed frequency in all measured devices indicated by the red dashed lines in (c). However, the bandwidth at a given bias point is significantly narrower than the spectrum in (a). In the simulation, the 20 cm^{-1} contour line is marked to represent the estimated value of the waveguide losses. The simulated gain curve reproduces well the trend of frequency vs. bias, although the simulations predict emission at frequencies below 2.5 THz. Actually, the waveguide losses are non-uniform and increase for lower frequencies due to the presence of lossy side-absorbers as we saw in chapter 2, Fig. 2.8. This can explain the absence of low frequency modes in the experiments. In the inset of Fig. 4.6 (b) we plot an electroluminescence spectrum taken at 10 V bias where a ∼1 THz broad signal is measured, agreeing with the ∼1 THz spectra observed in Fig. 4.3.

Connecting to the above discussion regarding laser operation in the photo-driven NDR region, combining the simulated spectra around 7 V with those around 10 V would reproduce a spectral width similar to that observed in Fig. 4.6 (a). A photo-driven domain for-

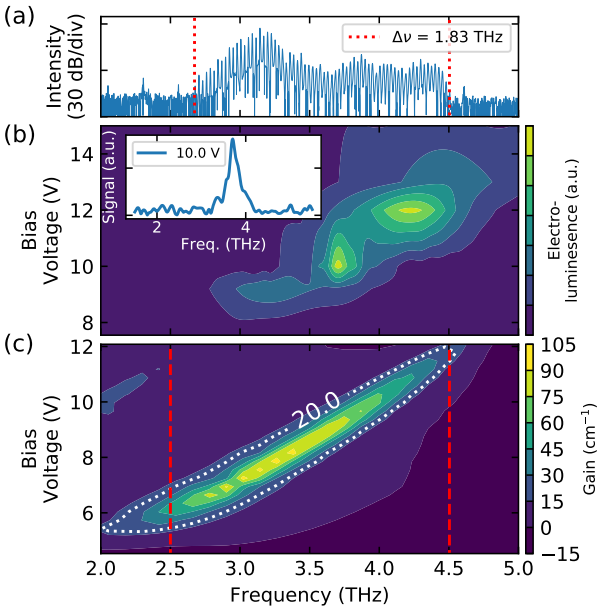

Figure 4.6 – (a) 1.83 THz broad spectrum of a 1.45 mm long and 65 µm wide device operating in CW. (b) Electroluminesence measurement of a 0.345 mm long and 70 µm wide non-lasing device with respect to the simulated gain by NEGF in (c). The lasing spectral region, taking the minimum and maximum frequency at all measured bias points, is indicated by the red dashed lines. The emission in (a) covers 90 % of NEGF predicated lasing frequencies. Differences in bias voltage are explained by additional serial resistance in the experiment like the Schottky contact of the laser. Reprint from Ref. [143].

mation could therefore explain the observed broad spectra in the high phase-noise regime. However, such a phenomenon would require a more sophisticated modeling as the different domains would affect the current-voltage relationship in an intricate manner.

Nevertheless, spectral pulsation of the device can be directly measured due to the self-sustained pulsation of the bias voltage. Therefore, we perform a step-scan FTIR measurement with a fast detector (Superconducting Hot-Electron Bolometer (HEB) by *Scontel*) and trigger on the FTIR step followed by a trigger on the self-sustained oscillation with a fast oscilloscope. A 2 µs long time trace of the detector and voltage signal is recorded and by post-processing sliced into the oscillation period length and averaged. A ∼20 ns time delay due to different traveling times for the voltage signal (cables)

and detector signal (optical path + cables) is measured (cables) or calculated (optical path) and accounted for in the analysis. In the end we can reconstruct an interferogram for each point on the voltage oscillation, i.e as a function of time which will present a spectrogram. Due to the detector's ∼200 MHz amplifier bandwidth limit and signal-to-noise consideration, the data are further averaged over 1.2 ns time intervals. The resulting spectrogram is shown in Fig. 4.7 together with the voltage signal (top) and the spectra from the total HEB signal and the reference measurement of the FTIR deuterated triglycine sulfate (deuterated triglycine sulfate detector (DTGS)) detector (right). The gray shaded area around the voltage oscillation indicates the uncertainty in the delay between voltage signal and spectrogram, whereas the red shaded region shows the 1.2 ns window for averaging. For visibility short interferograms are used for the spectrogram, whereas for the HEB spectrum (vertical side of Figure) the full interferogram length was taken. Therefore, the spectrogram shows the spectral regions which are present for each time step rather than the individual modes. An animation of the time resolved spectra, taking the hole interferogram, is provided in the supplementary material of Ref. [143]. From the spectrogram we deduce that there are clear periodic changes in the emission spectrum during one period of the voltage oscillation. These results suggest domain formation occurring inside the QCL, rather than the bias changing uniformly over the whole structure.

4.3 Injection locking and coherence properties

We now discuss the spectral coherence properties of the studied laser as a function of the different biasing regimes. In Fig. 4.8 we present a beatnote map recorded with a spectrum analyzer which extracts the signal with a bias-tee from the bias line of the laser. The beatnote map was recorded simultaneously to the spectra in Fig. 4.3 (a) and the data is binned along the RF frequency axis to make the beatnote clearly visible in the colormap. Below the NDR there are regions where one (label (1)) or several extremely narrow beatnotes (label (2), (3)) appear. In the regions labeled (2) and (3) the multi-mode appearance are actually sidebands of the main narrow beatnote [131] which are amplitude and frequency modulated, not related to the strong voltage oscillations in the NDR. When the laser enters the NDR region the beatnote broadens, showing that the laser is operating in a high phase noise regime labeled as (4).

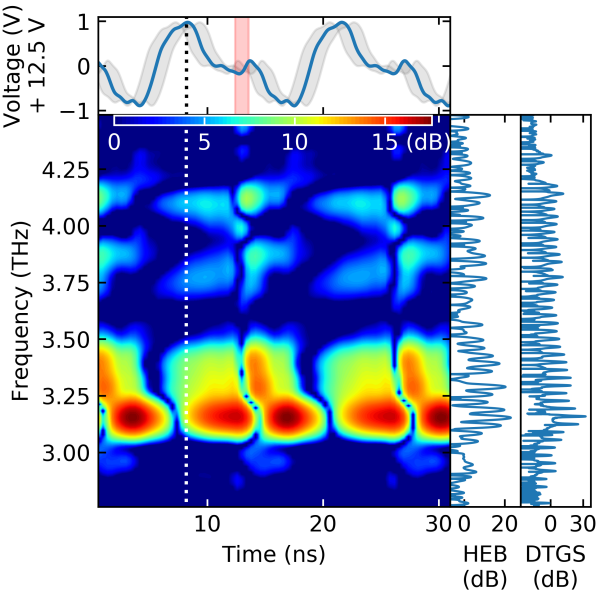

Figure 4.7 – Top: Stable voltage oscillation over the device bias (1.45 mm long, 65 µm wide). Red shaded indicates the time interval used for getting the mean interferogram point from the detector signal. Grey shaded indicates the delay uncertainty between voltage signal and spectrogram. Right: Spectra recorded by the internal DTGS and external, fast superconducting HEB detector. Colormap: Spectrogram of shortened interferograms for visibility reasons. An animation of the time-resolved data is provided in the supplementary of Ref. [143] using the full interferogram length. Clear changes between the different emission modes are observed and qualitatively support the argument of oscillating between multiple solutions for a constant current when entering the NDR regime. This could also be seen as an oscillation between the 7 V and 10 V bias point in the NEGF simulation as can be seen in Fig. 4.5 and 4.6. Reprint from Ref. [143].

Here, two broad signals can be observed around 34 GHz and 35 GHz, respectively. Each of these two signals have their corresponding narrow beatnote in the stable regimes (1) and (3) for the signal around 34 GHz, and regimes (1) and (2) for the signal around 35 GHz. This suggests that the broad spectrum observed in the NDR region is due to both, the low-bias and high-bias regimes, being present at the same time in the QCL.

Providing the bias line with another bias-tee and employing a microwave generator, we can investigate the frequency locking char-

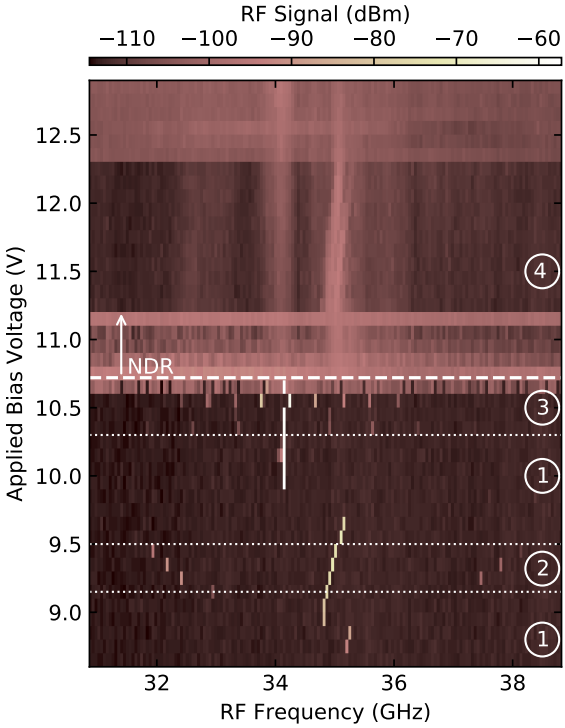

Figure 4.8 – Simultaneously recorded beatnote map to the spectra in Fig. 4.3 (a). The RF axis is binned of 30 values for better visibility. In regions (1) a single and narrow beatnote with a S/N up to 43 dB is observed. Regions (2) and (3) show a single narrow beatnote with sidebands. In region (4), in the NDR, a broad phase noise is observed. Still there are two clear regions corresponding to the stable beatnotes below NDR. Reprint from Ref. [143].

acteristics of the laser structures in the stable operating regime [111, 124, 216]. The cryostat is equipped with 40 GHz compatible RF cables and 18 GHz compatible SMA connectors at the cryo finger connected to gold pads followed by gold wires to the QCL. The total losses from cables, bias-tee, connectors, gold pads and wires are estimated to be 25 dB around 35 GHz, deduced from transmission measurements. A typical injection locking map is reported in Fig. 4.9 (a) for an estimated injected microwave power of -37 dBm at the QCL. It is evident that the laser beatnote is pulled towards the injected signal and successively locked. The sidebands, which are generated, are typical for this kind of experiments [124]. A max-

imum locking range of 4 MHz is achieved for an injected power of -33 dBm, where we injection lock more than 20 laser modes. The reported locking range as a function of the injected microwave power in the inset of Fig. 4.9 (a) shows a very good agreement with Adler's equation which describes the injection locking as a function of the injected power, the RF quality factor of the slave resonator and the injection frequency [54]. Our results compare well with the ones reported in Ref. [111] where a THz QCL operating in double metal waveguide with a beatnote at a very similar frequency was investigated. Our injection locking range is a factor of 10 smaller, and this could be ascribed to the non-optimal RF matching of our cryo head, which translates into an effectively higher quality factor for the RF cavity. In Fig. 4.9 (b) we measured the spectrum of the lasing device at 241 mA, 10.6 V at 20 K under injection locking with -26 dBm power at the laser. For these injection powers the emission spectra typically stayed unchanged.

Furthermore, we investigate injection locking in the high-phase noise regime, i.e. with a broad RF signal. Such a regime below the NDR is presented in Fig. 4.9 (c) in green, where the injection is still far from the high-phase noise RF signal. The injection power at the laser is estimated to be 2 dBm, and the signal is cut above -90 dBm and binned into groups of 5 along the RF frequency axis for visibility. The modulation of the injection sidebands along the RF frequency axis is due to the resonances of the circulator used. The abrupt kink at 27 GHz is an artifact of the spectrum analyzer. The high phase noise signal has a SNR of roughly 3 dB and spans from 27 GHz to 27.6 GHz. By sweeping the injection frequency, we observe multiple regions where the high phase noise signal vanishes, indicating locking of the optical modes, or partially locked, i.e presence of side bands. In these regions the noise floor is recovered as presented in Fig. 4.9 (c) in blue and red indicating locking of the optical modes. In the regime of locked beatnote we recorded the spectra, see Fig. 4.9 (d). We are clearly able to substantially change the emission spectrum depending on the injection frequency. The influence of strong RF modulation on the spectrum and on the coherence of the comb is discussed in detail in chapter 9, supporting the findings of this chapter.

By switching the operation point to the NDR, i.e. having voltage oscillations, we repeat the previous injection locking experiment. The results are shown in Fig. 4.9 (e-g). There are two main differences compared to the former: First, the injection signal shows

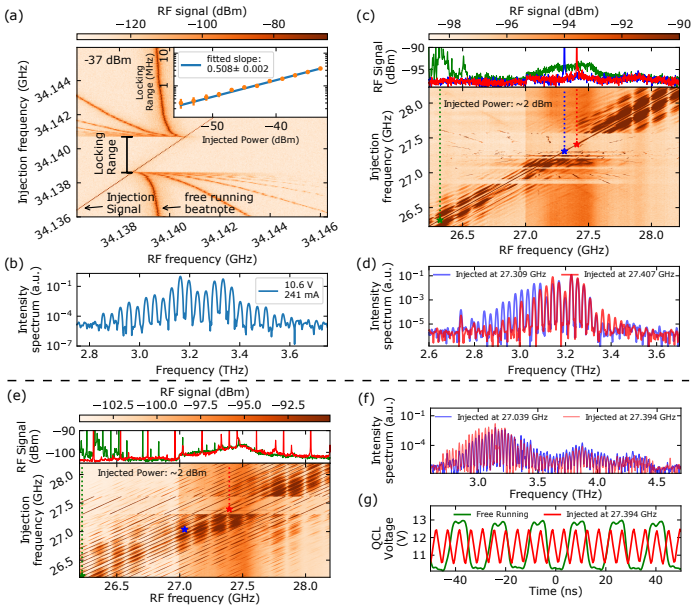

Figure 4.9 – (a) Injection locking map for -37 dBm at the QCL (1.2 mm long and 80 µm wide device, at 243 mA, 10.6 V at 20 K). Inset: Locking range for different injection powers following the square-root dependence of the Adler's equation. (b) Recorded spectra at 241 mA, 10.6 V and 20 K with injection-locked beatnote with power of -26 dBm at the device. (c) High phase noise regime below NDR of a 1.45 mm long device at 20 K, 238 mA and 10.54 V. The signal above -90 dBm is cut for visibility. The change at 27 GHz is due to the spectrum analyzer. By sweeping the injection frequency we observe locking of the modes, single curves in blue and red without any side band, indicated by reduction of the high phase noise signal in green. (d) Spectra at the two injection points marked in (c) showing that the spectral shape is changed significantly depending on the injection frequency. (e) High phase noise regime in the NDR of the same 1.45 mm device at 20 K, 186 mA and 11.50 V in voltage mode. The signal above -90 dBm is cut for visibility. The high phase noise regime stays and no entire locking is observed. (f) Spectra at the two injection points marked in (e) showing that even though the device is not locked, the spectral shape is changed. (g) The voltage oscillations of the free running (green) and injected (red) are displayed and match the corresponding side band spacing in (e). Reprint from Ref. [143].

many side modes and in the regime from 27.35 GHz to 27.65 GHz we observe a change in the side bands while keeping the high phase noise nearly unchanged. The side bands arise from the QCL voltage oscillation shown in Fig. 4.9 (g), green curve, whose main frequency component is 63 MHz, fitting to the side band spacing. Sweeping

the injection frequency further, the side band spacing changes to 216 MHz, corresponding to new a voltage oscillation (red curve of Fig. 4.9 (g)). At this point the modes are not locked to the injection, as can be seen from the unchanged high phase noise. Comparing the spectra of the two oscillating regions we observe again a change in the spectra due to the RF injection. Interestingly the changed oscillation *remains stable* when switching off the injection signal, even in the presence of FTIR feedback. Hence, multiple stable solutions of the voltage oscillation and, consequently, of the domain formation exist for the same bias point.

4.4 Conclusion

We have presented in this chapter a broadband, homogeneous THz QCL with a low threshold current. The emission bandwidth is up to roughly 1 THz with a simultaneously narrow and strong beatnote. Post analysis [7] with f_{ceo} extraction from the spectrum of this 1 THz wide spectrum indicates subcomb operation with equal f_{rep} but different f_{ceo}'s. By entering the NDR regime, lasing up to a bandwidth of 1.83 THz was observed. Such unprecedented broadband emission from a homogeneous device can be readily employed as, e. g., a bright source for FTIR spectroscopy. A reasonable agreement of measured IVs and spectral widths of the devices with NEGF simulation was found, which together with the time-resolved spectral measurements suggest domain formation inside the device. It does as well explain the origin of the observed wide emission spectrum and the self-pulsations. Finally, the low power injection locking capability of the device was demonstrated. By strong RF injection in the high phase noise regime, we observed a clear influence on both, the laser emission and the self-pulsating behavior. The strong RF modulation is further investigated in chapter 9.

As we will see in the next chapter, the same active region (AR) can be embedded into a lower loss Cu-Cu waveguide, where we see additional spectral effects.

7. The emission of subcomb was discovered after the publication of Ref. [143]. The key findings are still unchanged.

5

High Temperature THz Quantum Cascade Laser Frequency Combs

In the last two years significant temperature increase of the pulsed maximum temperature operation in THz Quantum Cascade Lasers (QCLs) was achieved [32–34] [1] and the operation with Peltier-coolers became possible. This was realized due to optimization of the active region (AR) design [34, 215, 217] and by the implementation of double-metal Cu–Cu waveguides [32, 180]. The latter was discussed before in chapter 2, where the advantage of Cu over Au is numerically predicted, see Fig. 2.7. In general, direct THz comb operation is still limited to cryogenic temperatures on the order of 20 to 40 K [39, 218] since the broad gain decreases significantly with increasing temperature and due to the continuous wave (CW) operation of comb devices. Therefore, the requirements for having a robust comb operation are as follows. A wide spectral bandwidth active region that has to feature a reasonably low threshold current density to ease CW operation over the whole dynamic range and a low-loss waveguide with eventual dispersion [17] and mode control to have only longitudinal modes excited during operation [130]. In this chapter [2], we therefore investigate the high temperature performance of THz QCLs operating in a broad frequency comb regime above 77 K, i.e. liquid nitrogen temperature, due to the fabrication of Cu–Cu double-metal waveguides of the same AR discussed in chapter 4.

1. Inoffically, the barrier of 260 K was reached this year (IRMMW conference 2021).

2. Most of the content in this chapter appeared, in some parts *verbatim*, in A. Forrer et al. "RF Injection of THz QCL Combs at 80 K Emitting over 700 GHz Spectral Bandwidth." Photonics, 7(1), 9 (2020).

The low loss Cu–Cu metal waveguide fabrication follows the procedure described in Ref. [32], where these waveguides are used in combination with a high gain two-quantum well structure to increase the maximum operating temperature of THz QCLs up to 210 K. In section 5.1, we will compare the Cu–Cu based devices to their Au–Au counterparts by comparing the temperature dependent LIV curves and evaluate the spectral evolution of such broadband Cu–Cu devices at 80 K. Section 5.2 will treat the coherence of the multimode and comb emission of these devices. Further, the comb state will be stabilized by RF injection locking and the spectral width will even be extended under strong RF injection.

5.1 Cu–Cu waveguide temperature performance: LIV and spectral evolution

The AR employed is a four-quantum-well, super-diagonal structure that features a low threshold current density ($J_{thresh} = 103$ Acm^{-2} and $J_{thresh} = 157$ Acm^{-2} in CW at 20 K and 80 K, respectively), a wide gain bandwidth and a strong photon driven transport, indication of a long upper state lifetime [143]. The presented AR is fabricated into double-metal ridge waveguides, as described in chapter 2, section 2.2.1, and cleaved to the desired cavity length and indium soldered to a copper submount.

Fig. 5.1 (a) shows light-current-voltage (LIV) measurements of a 4 mm long and 86 µm wide double-metal (Cu–Cu) laser ridge as a function of the heat sink temperature both in pulsed and CW operation. Pulsed operation is observed up to 138 K while CW operation stops at 96 K for devices exhibiting a side-absorber with nickel (side-absorber: setback of the top contact on both sides with evaporated nickel as described in chapter 2. Nickel can be applied during the fabrication process or later on mounted devices. The absorbers have been shown to be instrumental for achieving regular mode spacing in double-metal THz QCLs [130].). Such values are found consistently, higher than what is measured on the same epilayer employing Au–Au waveguides. The same device, before having nickel evaporated, even showed CW operation up to 105 K with a threshold current density of 263 Acm^{-2} with the corresponding spectrum shown in the inset of Fig. 5.1 (b), confirming as well the numerical predictions of chapter 2. The pulsed THz power is detected by the Absolute THz Power Meter by *Thomas Keating Ltd* (TK) and in CW by the 3A-

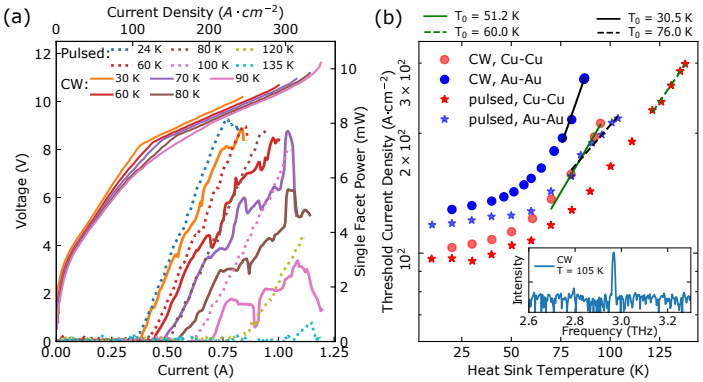

Figure 5.1 – (**a**) LIV pulsed (2 % duty cycle at 132 kHz repetition rate) and CW of a 4 mm long and 86 µm wide device. For visibility, only CW IV curves are presented. Pulsed power is detected by the Absolute THz Power Meter by *Thomas Keating Ltd* and in CW by the 3A-P-THz by *Ophir*. CW power is corrected for collection losses and atmospheric absorption in the setup by comparing it with the pulsed measurements directly in front of the cryostat. (**b**) Threshold Current Density vs Temperature of a 4 mm long and 64 µm wide Cu–Cu device and a 1.45 mm long and 65 µm wide Au-Au device. Inset: Increased CW performance of the same Cu–Cu device up to 105 K before having nickel evaporated on the top contact setback, i.e., having side-absorbers. Reprint from Ref. [144].

P-THz detector by *Ophir*. The large size TK detector allows direct detection of the unfocused beam in front of the cryostat, whereas the beam for CW detection is focused via two off-axis 90° parabolic mirrors (2″ diam., f/1). The CW powers are then corrected by the collection losses of the mirrors and atmospheric absorption.

In Fig. 5.1 (b), we compare the temperature dependence of the threshold current density both in pulsed and CW between Au–Au and Cu–Cu waveguides. The impact of the low-loss Cu-based waveguide is evident, producing an increase in T_{max} of 35 K in pulsed operation and of 10 K in CW. It has to be mentioned that the comparison is not entirely rigorous since the length of the devices are different, i.e., 1.45 mm and 4 mm for Au–Au and Cu–Cu devices, respectively, although they have nearly the same width (65 µm and 64 µm). Additionally, the temperature dependence of the threshold current can be fitted to $J_{th}(t) = J_0 \cdot exp[T/T_0]$ (in a log-scale line: only temperatures above 70 K for each measurement were considered). T_0 allows to compare different devices and is listed in

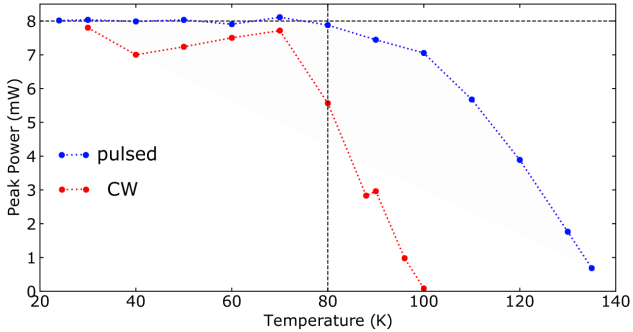

Figure 5.2 – Single facet peak power of a 4 mm long and 86 µm wide Cu–Cu device as function of temperature. The CW peak power is close to the pulsed one up to 70 K.

Fig. 5.1 (b). The increased T_0 for the Cu–Cu device compared to the Au–Au device in CW indicates an improved temperature performance.

Besides the threshold current, we also examine the maximum peak output power as a function of temperature. Pulsed and CW peak power behave very similarly, see Fig. 5.2, showing a weak temperature dependence up to 70 K with values close to 8 mW. At 80 K, we still measure 5.6 mW in CW at rollover.

Similarly, we compare in Fig. 5.3 the evolution of the maximum normalized peak output power in pulsed of an Au–Au and a Cu–Cu device. We clearly see, as for the threshold current, that the peak power of the Cu–Cu device is sustained up to 80 K whereas the Au–Au device performance already decreases after 60 K. The slope of the decreasing output power corresponds to the intrinsic temperature dependence of the AR and is nearly identical in both cases. The increased temperature performance is attributed to the improved Cu–Cu waveguide.

Inspecting again the I-V curve in Fig. 5.1, we note a very strong photon-driven transport, yielding a dynamic range that extends with temperature. This is the consequence of the low-loss waveguide combined with a diagonal active region. The maximum current flowing in the structure under laser action depends on the upper state lifetime ($J \propto \frac{1}{\tau_{up}}$) and on the optical field inside the cavity [205, 219]. When the temperature increases, the upper state lifetime decreases and the dynamic range is extended since the threshold does not

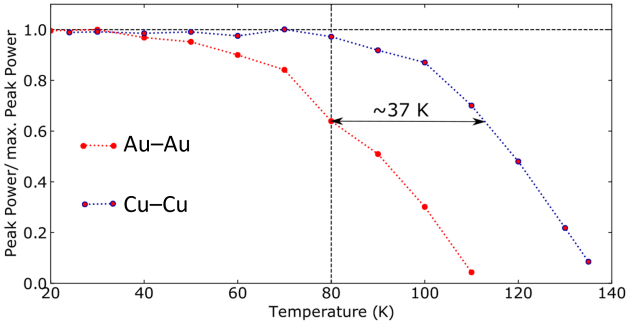

Figure 5.3 – Comparison of normalized single facet pulsed peak power of a Au–Au and a Cu–Cu device. The temperature performance is significantly improved for the Cu–Cu device.

move significantly up to 60 K.

Furthermore, the spectral emission of the same Cu–Cu laser as in Fig. 5.1 (b) at T = 80 K is reported in Fig. 5.4: broadband emission covering over 600 GHz and spectral indication of harmonic states [208, 220] (see also chapter 6) are observed. Consistently, the appearance of strong and widely spaced modes with weaker modes in between is observed as it is, for example, very pronounced at 555 mA or 690 mA in Fig. 5.4. The presented spectra reflect different states in the beatnote map, i.e., high-phase noise, single or multi beatnote regime, shown in Fig. 5.5 at T = 80 K and are discussed in the next section.

5.2 Frequency comb operation at 80 K

We saw that by embedding the AR from chapter 4 into a lower loss Cu–Cu waveguide the device performance is sustained to higher temperatures. Now we investigate the coherence properties of these Cu–Cu devices by recording the electrically detected intermode beatnote as a function of the injected current for different temperatures. In this case, the laser cavity is the same 4 mm long and 64 µm wide Cu–Cu device as in Fig. 5.1 (b). No intentional dispersion compensation schemes are implemented. The device is mounted in front of the focused FTIR port with a polytetrafluoroethylene (PTFE, Teflon) slab (transmission of $\sim$ 70%) in between to prevent saturation of the internal deuterated triglycine sulfate detector (DTGS)

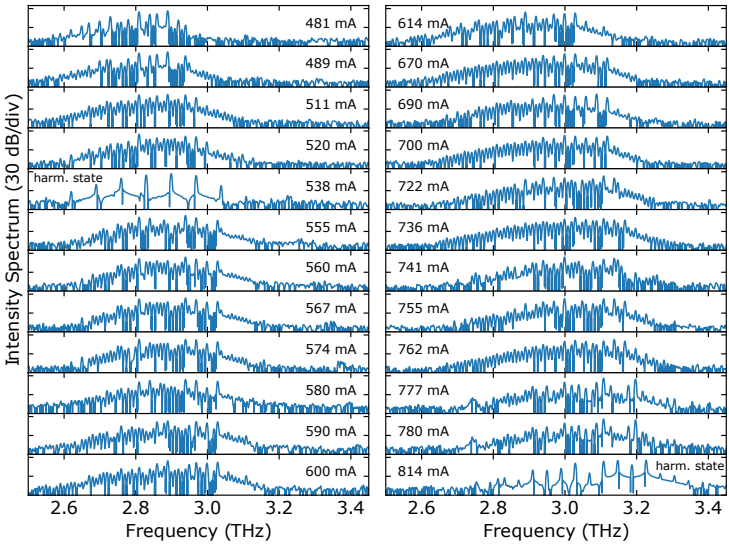

Figure 5.4 – Spectra of a 4 mm long and 64 µm wide device as a function of increasing injected currents at 80 K in CW. Reprint from Ref. [144].

detector; this also reduces the feedback. The observed effect of feedback only results in constant shifting/jitter of the beatnote frequency (self-mixing effect [41]) in the kHz range due to the constant mirror movement, but not in broadening or destabilization. This is the configuration for all the following measurements. The CW power at 20 K and 80 K at rollover is 5.2 mW and 4.0 mW for this device, respectively. As such lasers are operating in CW above 70 K, we can investigate high-temperature coherence behavior and from the data reported in Fig. 5.5, we can see that a well defined beatnote at the round trip frequency is present up to 80 K and even above (not shown). We observe that, in fact, the regions of current where only one well defined beatnote is present, indicated by the pink boxes on the left side of each beatnote map, are more extended as the temperature is increased. Such behavior is significantly different from what is observed with devices from the same epilayer processed as Au–Au ridges, see chapter 4.

A possible explanation of this phenomenon is the increased optical field inside the laser cavity combined with the fairly low repetition rate of the investigated devices. The fundamental quantity entering the master equation describing the mode coupling in mul-

timode lasers (i.e., QCLs) is the Rabi frequency written as $\Omega_R = |E_{cav}|d/\hbar$ where d is the electric dipole of the intersubband laser transition [182, 208] and $|E_{cav}|$ the electric field amplitude. If the internal optical field $|E_{cav}|$ is high, the peak of the non-linear parametric gain is detuned by $\Omega_R/2$ and then, for low repetition rates, is not directly favoring four-wave mixing-induced proliferation of nearest neighbor Fabry–Pérot modes. At the same time, we saw in chapter 2, Fig. 2.12, that longer devices have a flatter cavity mode response and that for lower temperatures, see Fig. 2.8, the losses of higher order modes are not well suppressed. This implies that many cold cavity modes are available and that the gain is sufficient for most of them to lase. This situation changes for increasing temperature where the indented losses of the sideabsorbers increase and less cold cavity modes are close to threshold. Therewith, the beatnote map shows more single and multi-beatnote behavior due to the four-wave-mixing (FWM) locking mechanism [126, 182]. Other factors to be taken into account are the relatively long upper state lifetime of the laser (surely longer than 40 ps [116] measured in our previous, less diagonal design), which would result in an intermediate behavior between amplitude modulated (AM) and frequency modulated (FM) comb regimes, and the spatial hole burning [89]. The latter is probably reduced for lower temperatures due to the particular photon-driven transport in these devices, which leads to a low differential conductance even though the low-loss subwavelength waveguides lead to higher fields.

We can also compare the LI with the corresponding beatnote map in Fig. 5.6 for different temperatures. A clear correlation between the CW output power and the appearance of high-phase noise, multi-beatnote and single beatnote is observed. The origin of this power clamping was not further investigated.

We can further control the coherence of the QCL by means of RF injection locking [111]. Fig. 5.7 (a) shows the injection locking map when an external RF synthesizer frequency is tuned through the repetition rate frequency. As we generally mount chips containing two laser ridges, as shown in Fig. 2.15 (b), the synthesizer RF output power of -10 dBm is injected through the neighboring (unbiased) laser used as an antenna, and the beatnote is measured directly on the laser bias line through a high-frequency bias-tee. The characteristic side modes as well as pulling towards the injection signal and the final locking are observed. Fig. 5.7 (b) shows a free running and injected spectrum. The injected spectrum shows a marginal change

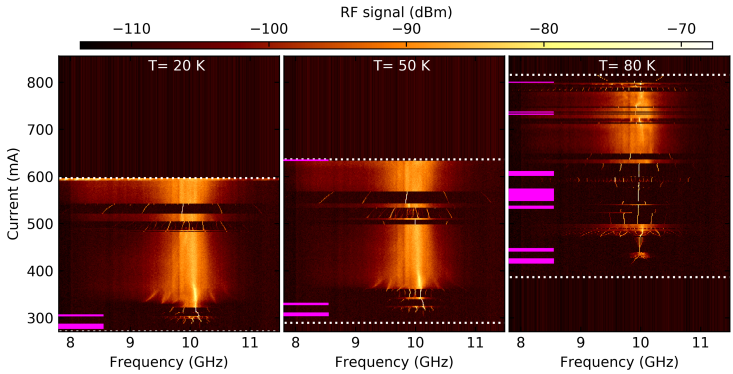

Figure 5.5 – Beatnote maps at 20 K, 50 K and 80 K of the 4 mm long and 64 µm wide Cu–Cu device. White dotted lines indicate the lasing region and the pink blocks indicate regions with a single narrow beatnote around 9.9 GHz. Reprint from Ref. [144].

for the low injection power. In Fig. 5.7 (c), we present the narrow (<2 kHz) free running beatnote as well as the lower frequency components. The beatnote has a signal-to-noise of 50 dB and, by injection, we retrieve the same noise floor at low frequencies. Unchanged low-frequency components indicate that, by injection, no destabilization of the comb state occurs. Signals around 2.4 GHz arise from pick up of WiFi signals, and below 1 GHz are spurious signals also observed below the lasing threshold. We note that weak injection locking should not change the underlying comb state on the amplitude level, and only stabilizes it, as already observed in Ref. [216] and further shown chapter 9.

In a successive series of measurements, the RF injection via the neighboring laser is replaced by direct injection on the bias line and observing the beatnote via the neighboring laser as an antenna. Using a bias-tee, this change is done under operation where the laser shows a clear single and narrow beatnote which is then picked up by the neighboring ridge (with no bias applied) with a reduced intensity. By the direct RF injection on the bias line, an increased modulation can be achieved, which results together with an increased synthesizer injection power of 30 dBm in a broadening of the spectra as shown in Fig. 5.8 (a). Under RF injection, the suppressed modes are enhanced and the spectral coverage reaches more than 700 GHz. The nominal FTIR resolution of 2.25 GHz is unable to prove the coherence. Nevertheless, by interpolating, i.e., zero-padding before

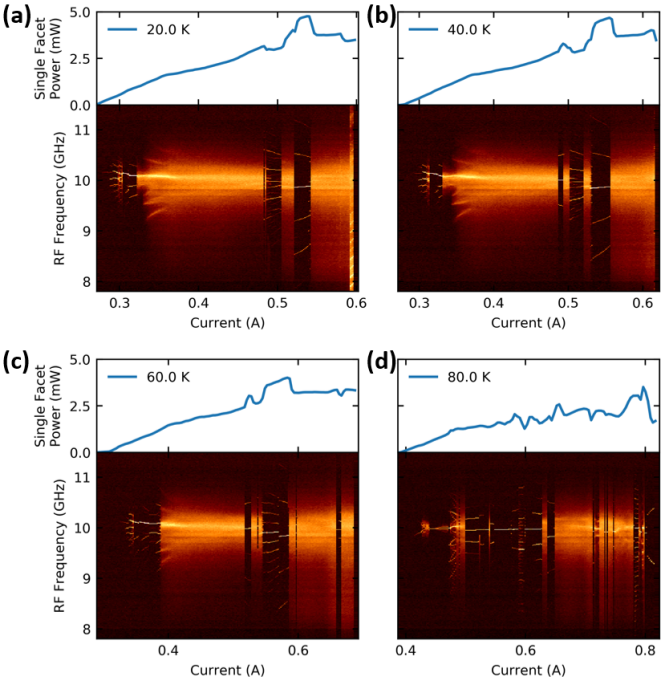

Figure 5.6 – Correlation of output power to the beatnote map for temperatures (a) T=20 K, (b) T=40 K, (c) T=60 K and (d) T=80 K.

performing the FFT, the peak position of each mode can be extrapolated. Therefore, Fig. 5.8 (b) presents the mode spacing extracted from the intensity spectrum in Fig. 5.8 (a) which agrees well with the free running beatnote and injected frequency [3]. A full proof of the coherence between all modes would need intermode beatnote spectroscopy (IBS) [11] or Shifted Wave Interference Fourier Transform (SWIFT) [17] measurements, which would require a sufficient fast THz detector not available at that time. SWIFT measurements would additionally reveal information of the FM and AM type of the comb emission. Measurements from mid-IR QCL suggest that by strong injection, the natural FM and AM comb regime goes into an AM comb regime, i.e., pulses [12, 221, 222]. These findings would also indicate that weak injection preserves the underlying

3. After the observation in chapter 9 we verified that all modes share the same f_{ceo} with the zero-padded Fourier-Transform Infrared Spectrometer (FTIR) resolution on the tens of MHz.

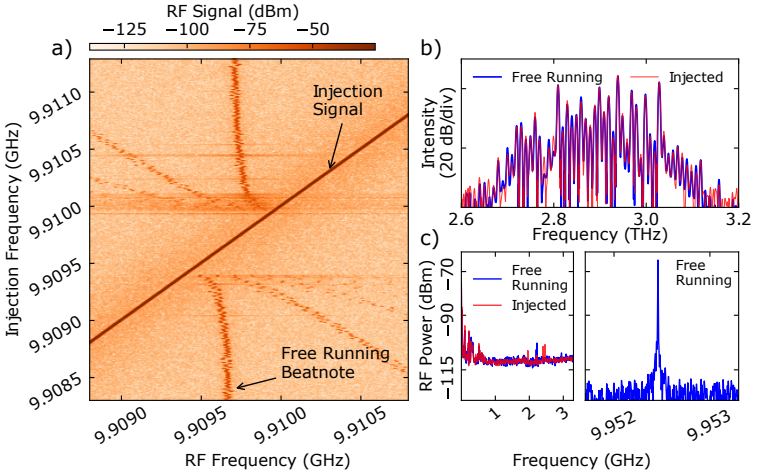

Figure 5.7 – (**a**) Low power (−10 dBm at synthesizer) injection map at 80 K (714 mA, 9.69 V) . Injection is via a neighboring laser acting as an antenna without bias applied. (**b**) Spectra of the free running and injected laser at 80 K (590 mA, 9.12 V). Minor changes are observed in the spectrum due to injection. (**c**) Low-frequency components and narrow (<2 kHz) free running BN at 80 K corresponding to the spectra in (**b**). Low-frequency components remain unchanged and suggest that injection is not destabilizing the comb state. Reprint from Ref. [144].

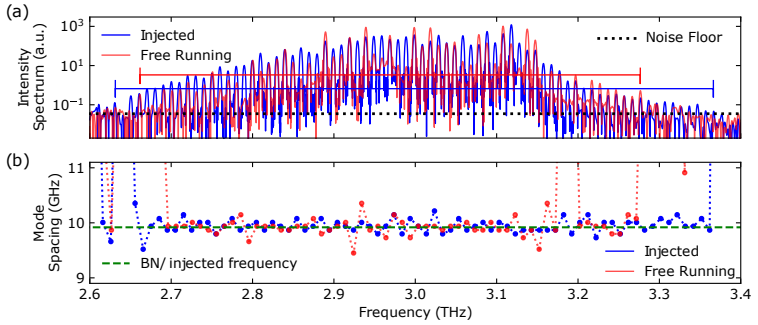

Figure 5.8 – (**a**) Free running (single beatnote regime, 714 mA) and corresponding strong injected spectra at 80 K. Significant change in the modes as well as generation of additional modes due to injection which leads to a spectral bandwidth from 600 GHz to 700 GHz. (**b**) Mode spacing extracted from (**a**) showing a quantitative agreement of the equally spaced modes. Reprint from Ref. [144].

comb state, whereas strong injection fundamentally changes the operating state. This hypothesize is investigated and confirmed in chapter 9.

5.3 Conclusions

In this chapter, we showed the impact of low-loss Cu–Cu waveguides on the THz QCL performance, allowing pulsed operation above 135 K and CW above 95 K, more than 30 K and 10 K higher than the respective Au–Au counterparts [143]. Simultaneously, an output power of roughly 8 mW in pulsed and 5.8 mW in CW at 80 K for a 4 mm long and 85 µm wide device were found. Further, free running comb operation and its injection locking at a temperature of 80 K were demonstrated. By strong RF injection, the underlying comb state at 80 K was significantly changed, resulting in an increased emission width from 600 to 700 GHz while changing the individual mode intensities. The demonstration of a stable, RF-injected comb at 80 K is significant in view of the application of such devices in dual comb experiments [223, 224].

As we saw in Fig. 5.4, these devices showed spontaneous emission on a so-called harmonic comb state. We will now further investigate these special combs in the next chapter.

6

Harmonic Frequency Combs in THz Quantum Cascade Lasers

In both chapters 4 and 5, we saw indications of harmonic comb states in the emission spectra, where the mode spacing of adjacent modes was an integer multiple of the fundamental repetition frequency f_{rep}. Also lately, harmonic frequency combs have been reported and investigated in mid-IR Quantum Cascade Lasers (QCLs) [207, 208, 220] and in active mode-locked THz QCLs [225]. Harmonic combs emitted by mid-IR QCLs were observed only after careful control of the optical feedback [131, 208, 220]. Finally, controlled generation of specific harmonic comb states was achieved by optical seeding [226] or by defect-engineered mid-IR QC ring lasers [227].

In this chapter [1], we will present results on robust, self-starting and pure harmonic frequency combs in double-metal Cu–Cu THz QCLs up to temperatures of 80 K. First, we will discuss multiple THz QCL devices which show at multiple bias-points self-starting and pure harmonic comb states and we will report on their experimentally observed differences with respect to mid-IR QCL harmonic combs. Successively, the coherence of the spectral modes will be examined via a self-mixing technique on the free running electrically detected beatnote. We will further demonstrate RF injection locking of the harmonic state to an RF synthesizer. And finally, the observed harmonic comb state, with an asymmetry in the spectral gain, will be theoretically discussed using a Maxwell-Bloch approach including two lower lasing states.

1. Most of the content in this chapter appeared, in some parts *verbatim*, in A. Forrer et al. "Self-starting harmonic comb emission in THz quantum cascade lasers." Appl. Phys. Lett., **118**, 131112 (2021).

6.1 Harmonic combs in THz quantum cascade lasers

The investigated THz quantum cascade active region (AR) is a homogeneous, four quantum well design based on highly diagonal transition, as we studied in chapter 5. The upper level has two transitions to two lower levels with dipole moments of $z_{ul_1} \sim 3.0$ nm and $z_{ul_2} \sim 2.1$ nm calculated with a Schroedinger-Poisson solver at 30 K. The bandstructure is shown in Fig. C.1 of the appendix C. These two transitions lead to an asymmetric gain profile, which significantly changes the theoretical predictions for harmonic comb generation compared to a symmetric gain profile and is discussed in the theoretical part and in detail in the Supplement of Ref. [228]. The asymmetry as well as the roughly one order of magnitude longer gain recovery time in THz ARs [114–116] are the main parameters different to mid-IR QCLs. The AR itself was discussed in chapter 4 and 5. The AR is embedded in a double metal gold-gold (Au–Au) [143] or low loss copper-copper (Cu–Cu) [144] waveguides featuring lossy setbacks in the top cladding [130] for transverse mode control. In the case of Au–Au waveguides in chapter 4, lasing starts in a single mode regime and evolves into the harmonic state, finally breaking into the fundamental/dense comb state. This mechanism mainly follows the observations on mid-IR QCLs [207, 208, 220]. In the case of Cu–Cu waveguide in chapter 5 we observe a different behavior: the harmonic comb does not arise gradually from a single mode but emerges spontaneously alternating with the fundamental comb or high-phase noise states. The harmonic comb state is observed at different bias-points, even much higher than the laser threshold. An example of a 4.00 mm long and 64 µm wide device exhibiting self-starting harmonic comb state from a dense state is presented in Fig. 6.1(a) for currents from 520 mA to 555 mA and from 780 mA to 814 mA, operating at 80 K and a lasing threshold of 390 mA. The presented spectra show the absolute values from the real part of the phase-corrected [189, 190] complex Fourier Transform from the zero-padded and with the Blackman-Harris window apodized interferogram (IFG) as we described in chapter 3, section 3.5. The absolute value was taken due to aesthetic reasons in the log-scaled plots. The symmetry of the IFG envelope arising from equally spaced modes and its interpretation in terms of coherence and purity of the comb state is further discussed below, in Fig. 6.2 and in appendix C.

In Fig. 6.1(b) we present the intensity spectrum of a funda-

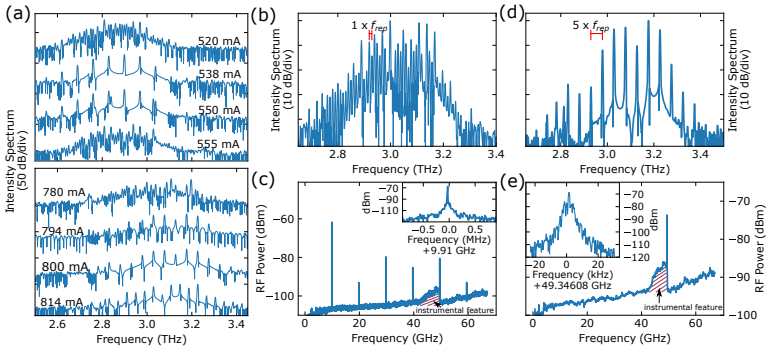

Figure 6.1 – Harmonic comb state in a 4 mm long and 64 µm wide double-metal Cu–Cu THz QCL at 80 K. (a) Transition from a dense state to a harmonic comb state and back for bias current from 520 mA to 555 mA and from a dense state to a harmonic state from 780 mA to 814 mA close to roll-over. Lasing threshold is at 390 mA. (b) Intensity spectrum with phase-correction, apodization and zero-padding applied of a fundamental comb state at 755 mA bias current. (c) Electrically detected RF spectrum on the bias corresponding to the fundamental comb state with a narrow beatnote at 9.91 GHz and its harmonics, recorded with 500 kHz RBW. The increasing noise floor and the transition at 50 GHz is an instrumental feature of the SA used. The inset shows a zoom on the fundamental BN. (d) Intensity spectrum of a harmonic comb state with phase-correction, apodization and zero-padding applied at 800 mA bias current. The modes are spaced by 5 × FSR of the cavity. (e) Electrically detected single beatnote at 49.346 GHz on the laser bias, recorded with 3 MHz RBW. The absence of other beating signals indicates the purity of the harmonic state. Inset: Zoom on the harmonic beatnote with a RBW of 300 Hz presenting a linewidth of 850 Hz with optical feedback from the FTIR. Reprint from Ref. [228].

mental comb at 755 mA bias current. The electrical beatnote at 9.91 GHz is detected over a bias-tee with 67 GHz spectrum analyzer (SA, Rohde&Schwarz, FSU67) and the RF spectrum is shown in Fig. 6.1(c). The observed linewidth is in the sub-kHz range. The harmonics of the fundamental beatnote respectively the beating of wider spaced modes are visible as well. We observe up to the 6th harmonic (59.46 GHz) of the fundamental frequency, indicating coherence at least up to the 6th mode. The observed rise of the noise floor at 50 GHz is an intrinsic feature of the SA (dashed area). The inset shows the fundamental beatnote. Fig. 6.1(d), measured on the same device, shows the harmonic comb state skipping four modes at 800 mA driving current at 80 K. Additionally to the observed THz harmonic spectrum, the intra-cavity mixing of the lasing modes spaced by 5 round trips leads to a current modulation on the bias-line which is as well detected over the bias-tee.

The single beatnote at 49.346 GHz is shown in Fig. 6.1(e) corresponding to the expected 5th harmonic of the cavity repetition rate ($49.346/5\ GHz = 9.8692$ GHz)[2]. We would like to highlight here that no other beating across the RF spectrum is observed except the one of the harmonic beatnote, indicating the purity of the harmonic state. This was further verified by investigating the RF spectra at the subharmonic frequencies with lower RWB and a lower frequency span (not shown). The inset of Fig. 6.1(e) shows the single beatnote with a linewidth of ∼850 Hz and a ∼ 45dB SNR recorded with a resolution bandwidth (RBW) of 300 Hz.

Compared to their Au–Au waveguide counterparts, the Cu–Cu waveguide features lower losses (4.4 cm^{-1} resp. 5.7 cm^{-1} at 3 THz for 150 K lattice temperature, 2D Comsol® 5.6 , mirror losses and intersubband absorption excluded) which lead to a wider dynamic range, higher maximum pumping with respect to threshold, and increased intracavity fields (estimated to be roughly 0.2 kV/cm at peak). Therefore, nonlinear effects related to four-wave mixing of laser modes become more important.

Multiple of these observed harmonic states appear for different cavity lengths and widths as well as different temperatures. Fig. 6.2(a) shows a series of IFGs with the corresponding spectra in Fig. 6.2(b) for multiple devices. Specific lengths, widths, temperatures as well as pumping levels and fundamental mode skippings are indicated in Fig. 6.2(b). The center of the envelope of the modes, in contrast to mid-IR cases, is found to be in-between two modes. This asymmetry in the envelope marks a difference in respect to what was observed in mid-IR QCL where a central, more intense mode and symmetric, less intense harmonic modes are frequently observed [208].

As mentioned above, the coherence and purity of any comb or harmonic state can be verified to a certain degree by comparing the symmetry and periodicity of the measured IFG envelope. The equidistant spacing of the modes in a fundamental or harmonic comb leads to a periodicity of the IFG envelope. This means that for a perfect interferometer all modes are in-phase for delays corresponding to a multiple of the mode spacing ($dx = c/f_{rep}$) and the measured IFG

2. The extracted fundamental beatnote frequency is actually roughly 40 MHz lower than for the fundamental comb state. This might be explained by the relatively flat cold cavity responses that we saw in chapter 2, section 2.2.2, which allows different pulling from the cold cavity modes.

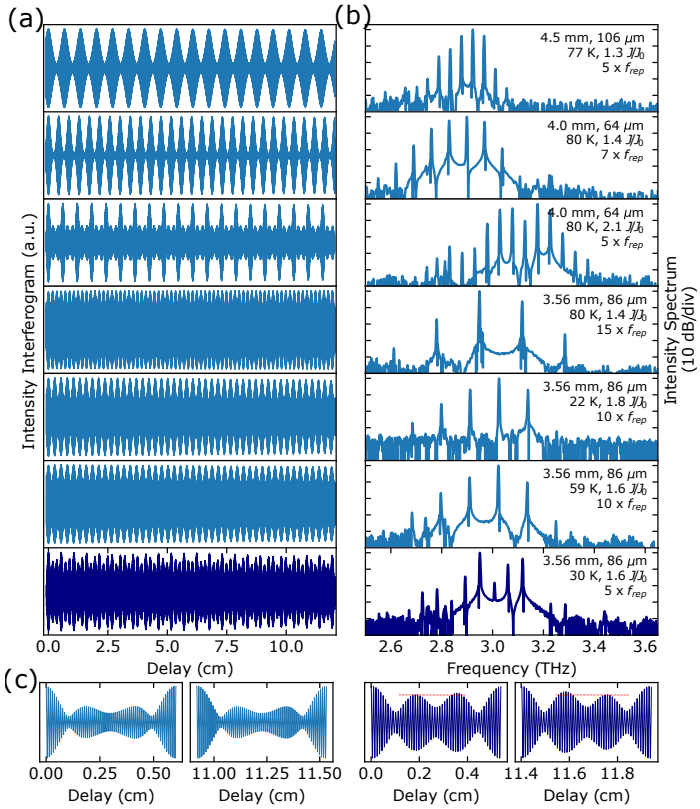

Figure 6.2 – (a) shows a series of IFGs of harmonic states (light blue) and a harmonic-like state (dark-blue). (b) presents the corresponding spectra which all show similarities to harmonic comb states. (c) compares the symmetry argument, which is a required property of the harmonic comb (as well as for fundamental combs), from the harmonic comb state (light blue) and the harmonic-like state (dark blue), where in the latter the symmetry is not preserved. Reprint from Ref. [228].

should identically repeat itself, up to a slow sinusoidal modulation with the virtual frequency f_{ceo} of the comb. For non-equidistant modes, the retardation for being in-phase is different for different mode pairs. Therefore, mode pair beatings are getting out-of-phase for increasing delay. By numerically generating IFGs similar to our case but with non-equidistant spacing we find that a linear decrease of ~ 20 MHz in the mode spacing leads to a visible asymmetry, see also appendix C. A roughly linear decrease of the mode spacing is

expected for multi-mode operation due to the GaAs dispersed cavity modes. This 20 MHz linear decrease in the mode spacing resp. 280 MHz difference between the lowest and highest frequency modes of the harmonic comb is smaller than the nominal Fourier Transform resolution of 2.5 GHz of our FTIR but is still clearly accessible. In the case of the comb in Fig. 6.1(b) with more modes this symmetry argument is even valid down to the MHz level, see appendix C. The symmetry argument is therefore a powerful and readily accessible tool for verification of pure combs on the MHz level using a simple FTIR IFG. We would like to highlight here that the same conclusion can be made in the frequency domain as we showed in chapter 3, section 3.5. But the IFG symmetry argument is straightforward and accessible by eye. The IFGs in Fig. 6.2(a) exhibit such a symmetry and a periodicity except the last one. It is important to notice that the envelope is slowly decreasing due to diffraction losses and beam divergence of any real FTIR measurement and its alignment but the symmetry within each period is conserved. The last IFG and spectrum in dark blue show an example of a harmonic-like state that is not pure. This is shown in Fig. 6.2(c) where a zoomed version of the third IFG from top of the harmonic state (light blue) and the IFG of the harmonic-like state (dark blue) around the ZPD and close to the maximum travel range of the FTIR are presented. The symmetry is preserved for the harmonic comb whereas for the harmonic-like state a clear asymmetry is observed. This IFG symmetry argument helps to identify non-pure comb states even in the presence of a single visible electrical beatnote or strong injection. Of course, the symmetry in the IFG is a required property for a comb (fundamental or harmonic) and can quantify to certain extent the coherence between the modes. The coherence should be further tested by Shifted Wave Interference Fourier Transform (SWIFT) [17], intermode beatnote spectroscopy (IBS) [11], dual comb [133] or any suitable coherence measurement [141]. Most of these techniques require fast detectors, but a much simpler approach based on self-mixing, where the QCL itself acts as a fast heterodyne detector [42], can verify to some extent the coherence of the modes additionally to electrical beatnote detection and IFG symmetry consideration and was first presented in Ref. [41] for single plasmon waveguide THz lasers [3]. The next section will therefore apply this method to a free running harmonic comb state.

3. Chapter 9 will show a SWIFT measurement performed on a harmonic comb.

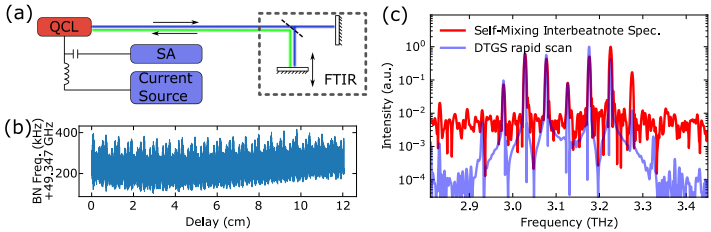

Figure 6.3 – SMIBS experiment. (a) sketches the setup where the FTIR provides a slight feedback as a function of delay and the induced beatnote frequency shift is recorded by the SA. (b) shows the uncorrected SMIBS IFG. The slow drift arises from temperature drifts. (c) compares the SMIBS spectrum with the FTIR spectrum showing the coherence of the modes. Reprint and adapted from Ref. [228].

6.2 Self-mixing intermode beatnote spectroscopy of THz quantum cascade laser frequency combs

The self-mixing coherence setup is sketched in Fig. 6.3(a) where a 4 mm long and 64 µm wide QCL is aligned to an FTIR and the electrical beatnote is detected over the bias-line. It is important to notice that double-metal THz devices are intrinsically less sensitive to feedback compared to mid-IR lasers, due to the high impedance mismatch of the double-metal waveguide that provides a high facet reflectivity. This allows the use of self-mixing techniques which are not destroying the comb state as it is observed in the mid-IR [208]. The FTIR operates in step-scan where for each step the beatnote intensity and frequency is recorded. From the single mode self-mixing theory of Lang-Kobayashi [229], a weak feedback of the optical mode itself will lead to a slight frequency shift of the optical mode frequency. In the experiment, the feedback comes from the FTIR which also filters the optical modes. In the case of a frequency comb, each mode experiences feedback at its own frequency, which will lead to its shift. Since all modes are locking coherently the shift induced to one mode will influence all other modes and their spacing and therefore the beatnote frequency has to be adjusted slightly. This allows to measure the effect of self-mixing by the frequency change of the beatnote of a laser in a comb state. A more rigorous mathematical discussion and experimental data of this concept was first presented in Ref. [41]. We will apply this SMIBS technique on a single double-metal (Au–Au) THz waveguide emitting simultaneously two unlocked combs spaced

by an octave with two independent beatnotes in chapter 7 together with the IBS technique. There, we will show that the detected self-mixing signal is sensitive to its generating comb but not to the other, indicating that indeed only coherent modes determine the beatnote shift whereas incoherent ones do not. This approach is now applied to the harmonic state presented in Fig. 6.1 and the uncorrected SMIBS IFG is shown in Fig. 6.3(b) and the SMIBS spectrum, its Fourier transform, in Fig. 6.3(c). The induced beatnote frequency change is on the order of 10^{-6} of its frequency and the slow drift arises from slight temperature changes. By comparing the SMIBS spectrum with the DC FTIR intensity spectrum we see that all observed modes are coherently locked and produce the beating signal showing the coherent harmonic comb state. It has to be noted that the SMIBS cannot fully verify the degree of coherence as it does not provide any information about the relative phases of the modes.

6.3 RF injection locking of THz quantum cascade laser frequency combs

Furthermore, RF injection locking is widely used for comb repetition rate stabilization [138, 143, 230] as we also already applied in chapter 4 and 5. In the following, we show that a THz harmonic comb displaying a strong free running narrow beatnote, as shown in Fig. 6.4(a), can be injection locked as well. The RF signal is set to a frequency roughly 600 kHz away from the beatnote. While increasing the injection power from -18 dBm at the synthesizer output up to 5 dBm typical pulling (red dashed line), appearance of side-modes (purple dashed lines) and final locking at 2 dBm is observed as presented in Fig. 6.4(b). The locking range at 2 dBm is roughly 1.2 MHz.

6.4 Theory on harmonic comb formation in THz Quantum Cascade Laser

Besides the experimental findings of harmonic combs in THz QCLs and their stabilization and coherence measurement, we developed in collaboration with Alexey Belyanin and Yongrui Wang from *Texas A&M University* a theoretical model supporting their formation and appearance. We argue that the harmonic comb regime

in our lasers is facilitated by the asymmetric gain shape created by the interplay of two optical transitions with comparable but different magnitudes of the dipole moments. This is in fact a common feature of THz QCLs with a diagonal transition design. To be specific, here we use an AR model which includes one common upper laser state and two lower laser states, (see appendix C, Fig. C.1). Following the approach similar to the one in Ref. [231], we calculate the gain, amplitudes, and phases of weak sidebands generated in the presence of a single strong lasing mode. The details of the calculations and the numerical parameters are described in the Supplement of Ref. [228]. The formalism is based on the density-matrix equations coupled to the wave equation for the EM field. Since the frequencies of the optical transitions are close to each other, around 11 and 14 meV according to bandstructure calculations, both of them contribute to the optical polarization and laser field. First, we find the field of a strong laser mode in the third-order nonlinear approximation; then we calculate the gain and eigenstates of weak side modes. At least two side modes have to be included as they are coupled through a

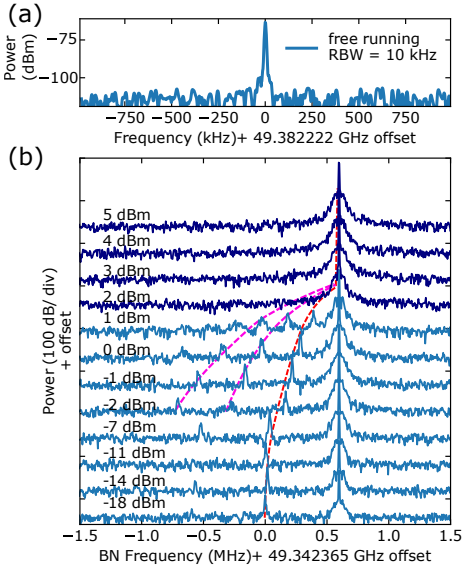

Figure 6.4 – (a) presents a free-running beatnote for the laser operating on the 5th harmonic state. (b) show the beatnote injection locking as a function of increasing RF power (from the bottom). Typical sidebands are visible and dashed lines are guides to the eye. Reprint from Ref. [228].

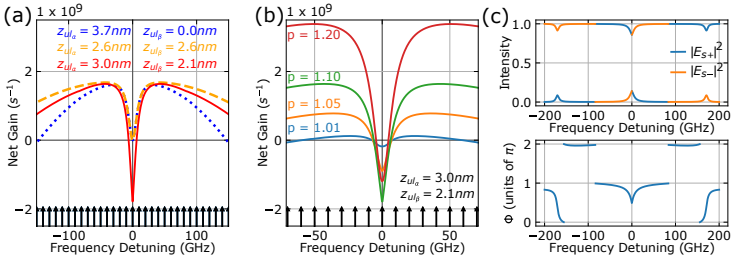

Figure 6.5 – The instability of weak side modes and their intensities and phases in the presence of a central strong lasing mode as a function of frequency detuning from the central mode for the AR. (a) The net gain at pumping level of $p = 1.10$ for a single optical transition with a dipole moment of 3.7 nm (blue dotted line), two optical transitions with equal dipole moments equal to 2.6 nm (orange dashed line), and two optical transitions with dipole moments equal to 3.0 and 2.1 nm (red line). Fabry-Pérot modes are indicated at the bottom with black arrows for a 4 mm long device. (b) The net gain for two optical transitions with dipole moments equal to 3.0 and 2.1 nm, at pumping levels of p = 1.01, 1.05, 1.10 and 1.20. Maxima are shifting to higher detunings with higher pumping rates and net losses around zero detuning decrease after 1.10 pumping level. Fabry-Pérot modes are indicated at the bottom with black arrows for a 4 mm long device. (c) The intensities and phase difference of the weak side modes at pumping level of $p = 1.10$. The gain relaxation times are $T_1 = 20$ ps and $T_2 = 0.2$ ps, and the population grating diffusion factor is $D = 100\ cm^2/s$. Horizontal lines in (a) and (b) indicate zero net gain. Reprint from Ref. [228].

strong central mode in the four-wave mixing process.

Fig. 6.5 presents the net gain, the amplitudes, and the phases of weak side modes E_{s+}, E_{s-} for three different cases: (i) only one optical transition with the dipole moment of 3.7 nm; (ii) two symmetric optical transitions with equal dipole moments equal to 2.6 nm each, and (iii) two asymmetric optical transitions with dipole moments equal to 3.0 nm and 2.1 nm. The dipole matrix elements in the first two cases are chosen so that the values of $d^2_{ul_\alpha} + d^2_{ul_\beta}$ are unchanged from the third case, and hence the total gain coefficients in all cases are similar. From Comsol simulations of the waveguide modes, we took the total cavity decay rate corresponding to the *field* propagation loss of 6.5 cm^{-1} and group velocity dispersion (GVD) of 6.35×10^4 fs^2/mm. Comparing the gain spectra in Fig. 6.5(a) one can see that for a single optical transition or two symmetric optical transitions the net gain of weak side modes is positive starting from zero detuning, which indicates that multimode lasing can start from adjacent modes favoring the dense laser spectrum. Only in the case of two asymmetric optical transitions the net gain of side

modes is negative at small frequency detunings, preventing lasing on adjacent modes and favoring the harmonic state. As is shown in the Supplement of Ref. [228] in more detail, there is an optimal range of the asymmetry ratios $d_{ul_\alpha}^2/(d_{ul_\alpha}^2 + d_{ul_\beta}^2)$ which maximizes the magnitude of the negative gain.

Figure 6.5(b) shows that the net gain of the weak side modes for two asymmetric optical transitions increases with pumping level and its peaks move to larger frequency detunings. The suppression of gain around zero frequency detuning gets stronger with increasing pumping and reaches its maximum, and then starts decreasing again as the pumping continues to increase. This indicates that the harmonic state is favored within a specific range of pumping levels.

Fig. 6.5(c) shows that in the case of two asymmetric optical transitions the phase difference between the two side modes is around π. However, the amplitudes are very different, which indicates that the laser field is not FM, it will have strong amplitude modulation. As was discussed in Ref. [231] in more detail, the AM component in the optical field makes a negative contribution to the sideband gain. It lowers the net gain to negative values at small detunings, suppressing the proliferation of neighboring modes and favoring the harmonic state. This provides a qualitative physical explanation of why the presence of two asymmetric optical transitions can support the self-starting harmonic comb. In contrast, in the case of one optical transition and two symmetric optical transitions, the two weak side modes have similar amplitudes at small frequency detunings (< 30 GHz), and their phase relations indicate FM field. At larger frequency detunings (> 50 GHz), the two side modes have different intensities, which is due to the effect of GVD. See the Supplemental of Ref. [228] for the details on these two cases.

Although not directly relevant to THz QCLs in this study, we also looked at the effect of gain recovery time T_1 on the sideband generation. As illustrated in Fig. S2 of the Supplement in Ref. [228], the main effect is that the separation between the peaks in the sideband gain increases with decreasing T_1. This is expected as the system with a shorter T_1 can support faster dynamics. The width of the negative gain region also increases, whereas the magnitude of the negative dip at zero detuning remains largely the same. This may have interesting implications for the design of mid-IR QCL ARs: the asymmetry in the gain transition introduced by design may help supporting a self-starting harmonic comb.

The results of the linear analysis of the multimode generation for two asymmetric optical transitions are qualitatively consistent with the harmonic lasing state with asymmetric sidebands observed in the experiment. The limitations of weak-sidemode approximation prevent us from making any quantitative predictions. The actual multimode lasing state will be determined by the nonlinear competition of many strong laser modes. Its modeling requires fully nonlinear space-time domain simulations which are beyond the scope of this section. Still, the presented analysis allows us to follow how the asymmetric harmonic state emerges from the coherent interplay of two optical transitions, which could be a physical mechanism behind the self-starting harmonic comb emission in THz QCLs. Obviously, more studies are needed before a complete physical picture is revealed.

6.5 Conclusion

In conclusion, we presented multiple THz QCLs operating on self-starting, pure harmonic comb states in this chapter. The electrical narrow and single beatnotes indicated the coherence of the modes and could be RF injection locked to an external RF synthesizer. The coherence was further assessed by the SMIBS spectrum, showing the equidistant spacing of the observed modes. The theoretical model, extended to including two unbalanced optical transitions in our AR design, supported qualitatively our observations of pure harmonic combs in THz QCLs.

Together with chapter 4 and 5, we saw now many different states in broadband, homogeneous THz QCLs. In the next chapter, we will investigate the formation of octave spaced combs in a monolithic, heterogeneous device. It will show the large effect of GVD in such devices and we will investigate the coherence by means of IBS.

7

Octave-spaced comb operation

In chapter 2, we saw theoretically that the dispersion of GaAs contributes significantly to the group velocity dispersion (GVD). This led in chapters 4 and 5 to observation of high-phase noise or multi-beatnote regimes and prevented comb formation for certain bias regions. In this chapter [1], we will explore a heterogeneous laser stack which includes two active region (AR) designs spaced by an octave in frequency. Each stack has a relatively narrow bandwidth of roughly 250 GHz for which comb operation should be less disturbed by the previous mentioned GVD effects. Furthermore, the resulting lasing modes of the octave-spaced THz Quantum Cascade Laser (QCL) are spectrally isolated and form two independent combs. We will present the typical performance of such devices and confirm the high GVD in GaAs-based THz QCLs in section 7.1. The comb coherence of each comb in this monolithic structure will be verified by means of self-mixing intermode beatnote spectroscopy (SMIBS) and intermode beatnote spectroscopy (IBS) in section 7.2.

Before going into the experimental results, let's revise why we are interested to investigate a device which emits coherently locked modes spaced by an octave. Up to now, full stabilization of QCLs were only achieved by referencing them to an other optical, already fully stabilized comb source [133, 140]. Only this full stabilization of the frequency comb will give access to the maximal frequency accuracy given by the linewidth of the individual comb teeth lines [185, 232]. In QCL frequency combs, one has direct access to the repetition frequency as we now saw multiple times in the previous chapters. Besides RF injection of the repetition frequency, a stabilization can also be achieved by introducing a small change on the

1. Most of the content in this chapter appeared, in some parts *verbatim*, in A. Forrer et al. "Coexisting frequency combs spaced by an octave in a monolithic quantum cascade laser." Opt. Express **26**, 23167-23177 (2018).

driving current according to the measured shift of the repetition frequency using a control loop [17, 128]. On the contrary, there is not such a direct access of f_{ceo} over the bias line in a free running laser. As briefly mentioned in chapter 1, the so-called f-2f technique [4, 53, 85], where a frequency comb spanning more than an octave is required, could provide a direct measurement of f_{ceo} and therefore the possibility to lock it to a microwave reference source. The key idea of this technique is to frequency double a low frequency mode of the frequency comb by a $\chi^{(2)}$ nonlinear medium and let it beat with the closest mode in the high frequency part of the frequency comb, leading to an RF beating signal at f_{ceo}. THz QCLs offer interesting possibilities in respect of this f-2f technique, since they can yield emission bandwidths of more than one octave [38, 39], but are not yet phase coherent over the whole spectrum. The challenge is mainly constituted by the dispersion compensation which, in fully integrated semiconductor lasers, is far from trivial. The frequency doubling could be implemented internally in a QCL thanks to the possibility of designing high second order nonlinearities, as demonstrated by Gmachl *et al.* in Ref. [233].

In this chapter, we will now explore two coexisting frequency combs spaced by one octave and simultaneously operating in the same waveguide. Only recently, two comb lasing based on heterogeneous waveguide coupling has been reported [234]. Here, we employ our 4-well active region [201] by rescaling and centering the two emission frequencies at 2.3 THz and 4.6 THz, in order to have high intensities and stable phase coherent operation independently at the octave spacing. This way of operating is different from our previous works where we achieved octave-spaced laser lines [38, 235], not in a comb regime, from the low intensity modes on the sides of the emission of a three or four stack heterogeneous laser.

7.1 Laser design and performance

With the heterogeneous QCL design we can study the simultaneous presence of two octave-spaced combs operating in a common waveguide. The alignment electric field values for the two active regions are very different, but this is not a problem for the simultaneous lasing of both stacks: what is relevant is the threshold current density, which has to be very similar for the alignment conditions of both stacks. Both structures were previously studied as homoge-

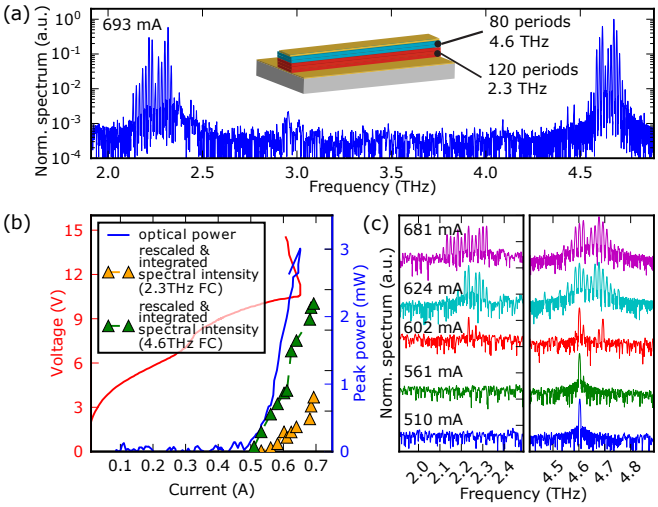

Figure 7.1 – (a) Spectrum showing the simultaneous lasing at octave-spaced frequencies in pulsed operation (5% duty cycle at 1 kHz repetition frequency at 15 K) and in the inset the schematic of the heterogeneous QCL. (b) LIV curve for a 2.4 mm long, 80 µm wide laser ridge in pulsed mode (at 120 kHz and 5% duty cycle, square wave modulated at 30 Hz at 15 K). Peak power of 3 mW is recorded. The orange and green marker show the spectral integrated intensities from (c) around the 2.3 THz and 4.6 THz frequency comb, respectively, rescaled to the peak power giving an estimate for the individual frequency comb power in the mW range. (c) Series of recorded spectra as a function of the injection current of the same device operated as in (a). The evolution shows first lasing of the 4.6 THz active regions before both active regions lase simultaneously.

neous lasers and the respective layer sequences were reported by K. Otani *et al.* in Ref. [236] and J. Lloyd-Hughe *et al.* in Ref. [237]. They are adjusted to operate in the same current density range acting mainly on the injection barrier thickness which is 5.5 nm for the 2.3 THz structure and 5.1 nm for the 4.6 THz structure. The double metal waveguide is composed of 120 repetitions of the 2.3 THz active region (sheet density $n_s^{2.3THz} = 3.6 \times 10^{10}$ cm^{-2}) and 80 repetitions of the 4.6 THz active region (sheet density $n_s^{4.6THz} = 3.3 \times 10^{10}$ cm^{-2}), for a total thickness of 13 µm. A schematic of the QCL is shown in the inset of Fig. 7.1(a).

A pulsed light-current-voltage (LIV) curve for a typical ridge device of 2.4 mm length and 80 µm width provided with metal setback and side absorbers (see Bachmann *et al.* in Ref. [130]) is shown in Fig. 7.1(b) with a peak power of 3 mW. The QCL is operated in

pulsed mode, at 120 kHz repetition frequency, 5% duty cycle and square wave modulated by 30 Hz at 15 K (detection with an *Absolute Terahertz Power Meter* by *Thomas Keating Ltd*). The markers represent the integrated spectral intensity of the 2.3 THz (orange) and 4.6 THz frequency comb (green), normalized to the LI curve; here the device was operated at 1 kHz and 5% duty cycle. This provides an estimate of the power distribution between the two frequency combs. The difference in the dynamical range between LI and rescaled integrated spectral intensity curves is due to different pulse duration settings for each kind of measurement. Fig. 7.1(c) reports the spectral evolution of the emitted radiation as a function of the injection current and Fig. 7.1(a) shows a connected spectrum at 693 mA injection current. Clear laser signal at 2.3 THz and 4.6 THz with bandwidths on the order of 300 GHz each are recorded. Unfortunately, the devices did not show simultaneous comb operation of both stacks when operated in continuous wave (CW).

To have a first indication for frequency comb emission, as we now saw many times, a beatnote should be measurable. QCLs offer the possibility to access these beatnotes directly over the bias line and detection by an RF spectrum analyzer (SA; R&S, FSW26). By scanning the current and simultaneously recording the RF spectrum, a beatnote map can be generated. Such a beatnote map is shown in Fig. 7.2 for a 2.4 mm and 80 µm wide QCL in a pulsed configuration (5 % duty cycle at 1 kHz repetition frequency) at 13.3 K. It shows first a single beatnote regime at 15.1 GHz followed by two regimes, separate by a short multi beatnote region, with two clear single beatnotes spaced by roughly 1.7 GHz. The main interest is the injection current range, where two strong and narrow beatnotes are present for the coexisting frequency combs. The assignment of the beatnotes to the frequency combs in Fig. 7.2 is discussed in the next paragraph and verified in section 7.2. The tested QCLs also emit in CW operation showing only single mode lasing or single frequency comb regimes and were therefore not studied further.

At 710 mA injection current, where two beatnotes are present in Fig. 7.2, we measure a close-up of the beatnotes over the bias-tee and record the spectrum of the QCL using a commercial FTIR (Bruker 80v, deuterated triglycine sulfate detector (DTGS) detector). The corresponding intensity spectrum is shown in Fig. 7.3(a), leaving away inter comb frequencies. Two distinct beatnotes are observed at frequencies of 16.79 GHz and 15.14 GHz as shown in Fig. 7.3(b). Free-running beatnote linewidths of tenths of kHz are

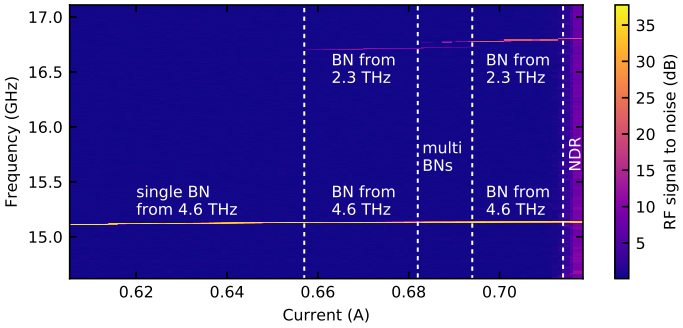

Figure 7.2 – Beatnote map from a 2.4 mm long and 80 µm wide QCL operated in pulsed (1 kHz repetition rate, 5 % duty cycle) at 13.3 K. We observe two regions where two single beatnotes at 15.1 GHz and 16.8 GHz are simultaneously present with a SNR of ∼35 dB and ∼ 20 dB, respectively¡¡. The assigning of the beatnotes was done by the simple argument of the expected f_{rep} from the frequency-dependent free spectral range of the QCL and is further addressed in the text.

observed on the SA and are further analyzed in section 7.3. The difference in the beatnote frequencies results from the high material dispersion of the GaAs which increases as the laser frequency approaches the reststrahlen band, see chapter 2, section 2.2.2. The simple model of Fabry-Pérot cavity mode spacings leads to the description of $f_{rep} \approx c/(2 \cdot n_g(\nu) \cdot L)$, where c is the speed of light, L the length of the cavity and $n_g(\nu)$ the frequency dependent group refractive index of the QCL structure. We investigate systematically, via beatnote ($f_{rep} \rightarrow n_g(\nu_c)$) and FTIR measurements (frequency comb center frequency ν_c), the mode spacing at 2.3 THz and 4.6 THz for a 2 mm long and 100 µm wide and two 2.4 mm long and 80 µm wide QCLs, where two simultaneous beatnotes are present. The assignment of the group index to the frequency comb center frequency is done due to relatively narrowband frequency combs compared to the frequency comb spacing. We report the results in Fig. 7.3(c) together with the calculated material dispersion for GaAs from the handbook of E. Palik [169] and the simulation for a QCL waveguide (*Comsol 5.0*). We see that the mode spacing is defined mainly by the expected GVD of our THz QCLs.

The results show the potential of QCLs to form frequency combs even in a very dispersive regime, here the 4.6 THz frequency comb near the reststrahlen band of GaAs. As can be seen in the inset of

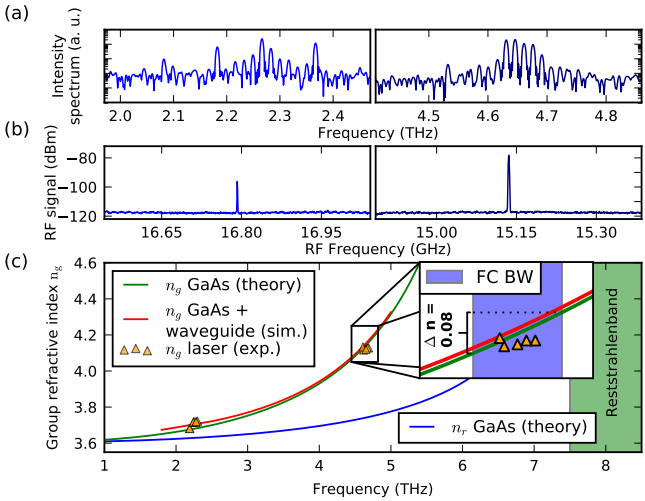

Figure 7.3 – (a) Spectrum of the two simultaneous existing frequency combs at 710 mA injection current of the beatnote map in Fig. 7.2. (b) Corresponding narrow beatnotes recorded through the bias-tee. (c) Calculated group refractive index n_g for GaAs (green) and the simulated group refractive index for the QCL waveguide (red, using *Comsol 5.0*) together with values deduced from beatnotes measurement of the two combs, using $n_g = c/(2f_{rep}L)$ for multiple devices operating in a two color comb regime. Inset: Multiple devices show lasing in a very dispersive region. The recorded frequency comb BW shows the ability of the QCL to establish a frequency comb despite the approximate 0.08 change in the group refractive index.

Fig. 7.3(c), the bulk group refractive index changes by $\Delta n \approx 0.08$ over the bandwidth of the frequency comb. Only recently QCL frequency comb formation in such a dispersive regime at 4.6 THz has been reported by Y. Yang *et al.* in Ref. [234].

7.2 Comb coherence properties

The observation of a narrow, single beatnote gives incomplete information when assessing and proving the full comb nature of the laser emission. The coherence has to be verified among all the modes which are constituting the laser spectrum because it is not a priori clear which modes contribute to the beatnote signal. Due to the absence of pulses in the QCL output in the comb regime, standard autocorrelation techniques, relying on non-linear processes allowed

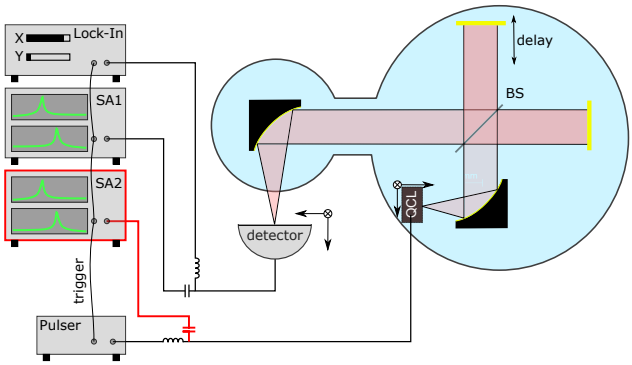

Figure 7.4 – Schematics of IBS setup. The SA on the bias line (SA2; highlighted in red) in the sketch can be used to verify the presence of two beatnotes and for detection of the self-mixing signal from the SMIBS. The laser is directly operated on a flow cryostat inside a home-made, step-scan and under vacuum FTIR (light blue area).

by high intensities, are not an option to show this coherence. To this extent, a few experimental techniques have been developed, all based on the concept of spectral filtering combined with RF beatnote detection [11, 17, 185]. Here, we employ the IBS technique using a fast THz Schottky mixer detector (*WR0.34HM, VDI Inc., 2.2 - 3.2 THz, IF out: 2 - 40 GHz, Response: 250 V/W*) coupled to a home-made step-scan FTIR. The detector allows for simultaneous recording of the RF intermode beating and the DC response to the optical THz signal as a function of delay when the appropriate triggering of the bias pulse is used. A sketch of the setup is shown in Fig. 7.4.

A 2.4 mm and 80 µm wide QCL is operated in pulsed at 10% duty cycle at 1 kHz repetition frequency at 16 K. Fig. 7.5(a) shows the simultaneously recorded intensity and intermode beatnote interferogram (at 16.79 GHz) measured by the Schottky mixer for such a measurement. The RF interferogram is deduced from the power change of the intermode beating signal in the RF spectrum for each delay step. The shape of the IBS interferogram, i.e. minimum in RF/IBS interferogram (blue) where the intensity/DC interferogram (green) peaks, qualitatively agrees with the mid-IR QCL measurement and model presented by A. Hugi *et al.* in Ref. [11], indicating the frequency-modulated (FM) operation of the QCL comb. The similarity of the intensity spectra of the two interferograms shown in Fig. 7.5(b) confirm the spectral coherence and prove the comb

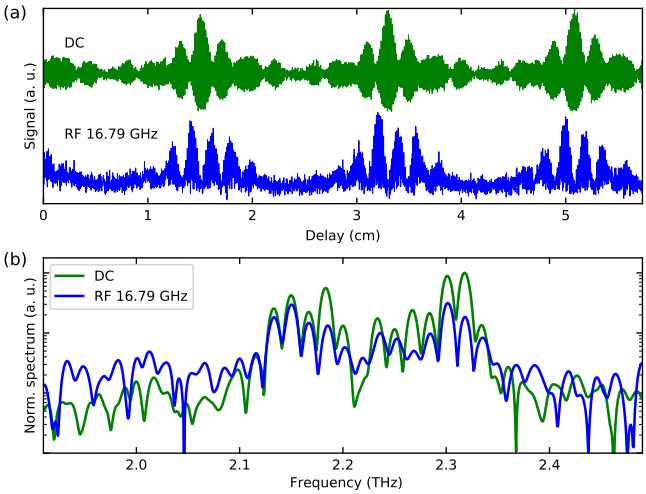

Figure 7.5 – A 2.4 mm and 80 µm wide QCL was operated at 1 kHz repetition frequency with 100 µs long pulses at 16K. (a) Interferograms recorded from the DC signal (green) and the RF signal (blue) of the Schottky detector. (b) Corresponding spectra showing the spectral coherence and confirming the comb nature around 2.3 THz.

nature for the spectral components centered around 2.3 THz [2]. At the same time, it was verified that the second beatnote at 15.14 GHz was present, indicating lasing of the 4.6 THz frequency comb.

Due to the narrow bandwidth (2.2-3.2 THz) of the antenna, which couples to the Schottky mixer, the detection of radiation around 4.6 THz is highly inefficient and inhibits IBS for the frequency comb centered at 4.6 THz. To assign the beatnote at 15.14 GHz to the 4.6 THz frequency comb we record the self-mixing signal, i.e. change in beatnote power due to back-scattered light, as the FTIR is stepping. This is slightly different than the SMIBS used in chapter 6 where we observed the beatnote frequency change. Due to the pulsed operation of the bias the beatnote frequency will drift due to heating and the SMIBS would fail where as the change in the beatnote power can still be well observed. This approach is similar to the one used by M. Wienold *et al.* in Ref. [41], where the technique was demonstrated for a single plasmon waveguide THz QCL.

2. From the intensity interferogram we see an asymmetry in the y-axis. This indicates a non-linear detector response to the light intensity and could also lead to discrepancies of the spectra in Fig. 7.5(b).

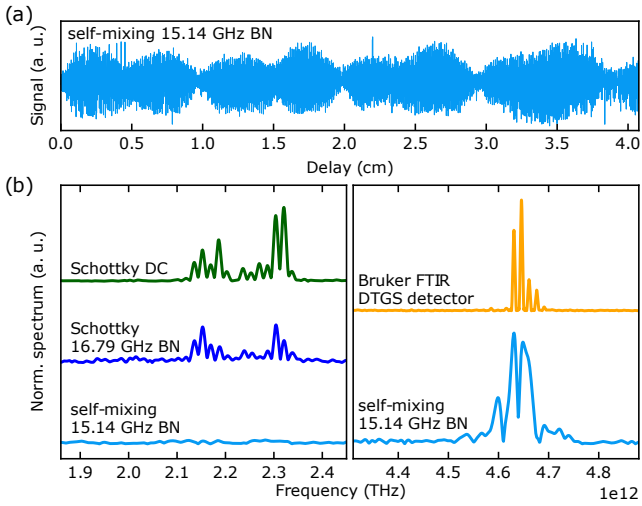

Figure 7.6 – (a) Self-mixing interferogram recorded from the 15.14 GHz beatnote in a step-scan FTIR. (b) Corresponding spectrum (azure blue) is compared to vertical displaced spectra in the two frequency comb regions. Around 2.3 THz this self-mixing spectrum is clearly not generated by the modes of the 2.3 THz frequency comb as measured by the DC (green) and RF (blue) spectrum from the Schottky measurement. Due to the lack of detection bandwidth of the Schottky, the 4.6 THz components of the self-mixing spectrum are compared to a reference measurement by a commercial FTIR (Bruker 80v, DTGS detector). Despite the low resolution of the self-mixing spectra, the origin of the 15.14 GHz beatnote from modes centered at 4.6 THz is clearly verified.

In our case we use a double metal waveguide which is inherently less prone to optical feedback with respect to the single plasmon case. In chapter 9 we will further treat these two approaches and compare them to Shifted Wave Interference Fourier Transform (SWIFT) measurements [17].

Fig. 7.4 shows the setup used for the self-mixing configuration by using one SA (highlighted in red) for the detection of the self-mixing signal of the beatnotes. This self-mixing technique together with our IBS setup allows us to directly verify the origin of the 15.14 GHz beatnote from modes centered at 4.6 THz.

In Fig. 7.6(a) we report a separate self-mixing interfrogram from the 15.14 GHz beatnote, additionally to the DC and RF interferogram in Fig. 7.5(a). The self-mixing method can also be applied for the 2.3 THz frequency comb generating the 16.79 beatnote, but suf-

fers from lower sensitivity and linearity of the detection compared to the optical RF detection by the Schottky detector and is therefore omitted from the comparison. In Fig. 7.6(b) we compare the self-mixing spectrum from the 15.14 GHz beatnote to the DC and optical 16.79 GHz RF detection and can clearly verify that, as expected, the 2.3 THz frequency comb does not generate the 15.14 GHz beatnote. Due to the lack of detection bandwidth of the Schottky detector at 4.6 THz, the 15.14 GHz beatnote self-mixing spectrum is compared to an additional spectrum recorded in a commercial FTIR (Bruker, Vertex 80v). Despite the lower resolution due to a shorter delay range and lower SNR of the self-mixing detection, the two spectra show a qualitative overlap and therefore the spectral origin of the 15.14 GHz beatnote. In summary we verified the mode coherence in the 2.3 THz comb, its beatnote generation at 16.79 GHz and the origin of the 15.14 GHz beatnote generated by the comb located at 4.6 THz. This also experimentally confirms the expected dispersion in THz QCLs.

7.3 Beatnote μs dynamics

In a second part of this chapter we investigate briefly the long-term dynamics, here in the range μs, of the beatnotes generated by the pulsed THz combs. The GHz beatnotes are extracted over a bias-tee in the bias line, RF down-mixed to 180 MHz on the lower sideband and then recorded by a fast oscilloscope (2.5 GS/s). This allows to extract low frequency drift information of the beatnotes, represented as spectrograms. These spectrograms for both down-mixed beatnotes arising from the 2.3 and 4.6 THz frequency combs as well as the down-mixed beating signal of the beatnotes for two different operation points of the same 2.4 mm long device are shown in Fig. 7.7. Fig. 7.7(a-c) shows the successively recorded down-mixed beatnotes from the 2.3 THz frequency comb, 4.6 THz frequency comb and their beating, operating at 697 mA injection current at 500 Hz repetition frequency, 100 μs long pulses at 7 K. The 15.15 GHz beatnote from the 4.6 THz frequency comb in Fig. 7.7(a) shows red and blue shifts during one pulse. The corresponding 16.79 GHz beatnote signal of the 2.3 THz frequency comb is represented in Fig. 7.7(b), showing a blue shift. The frequency difference of the two beatnotes at 1.64 GHz is also detected, due to non-linear mixing inside the QCL cavity, most probably rectification. The signal is shown in Fig. 7.7(c). In white we present the numerical

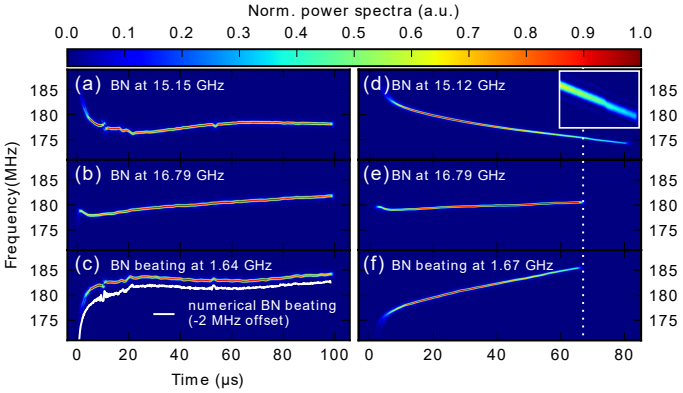

Figure 7.7 – (a) Down-mixed 15.15 GHz beatnote from a 2.4 mm device at 697 mA operated in pulsed mode at 500 Hz repetition frequency and 100 µs long pulses at 7 K. The beatnote shows red and blue shift during the same pulse. (b) Down-mixed signal from the simultaneous existing 16.79 GHz beatnote showing a blue shift. QCL operation as in (a). (c) Down-mixed signal from the beatnote beating at 1.64 GHz and the numerical beatnote beating (white) from (a) and (b), offset by -2 MHz for visibility. QCL operation as in (a) and (b). (d) New bias point. Down-mixed 15.12 GHz beatnote from the same 2.4 mm device at 668 mA operated in pulsed mode at 1 kHz repetition frequency and 80 µs long pulses at 7.7 K. The beatnote shows a red shift. Inset: Slight change of the 15.12 GHz beatnote trace when the 16.79 GHz beatnote in (e) switches off. (e) Down-mixed signal from the simultaneous existing 16.79 GHz beatnote showing a blue shift. QCL operation as in (d). The beatnote switches off after ∼67 µs (dotted white line). The slight change at this time in the time trace of the 15.12 GHz signal could indicate coupling between the beatnotes. (f) Down-mixed signal from the beatnote beating at 1.64 GHz. QCL operation as in (d) and (e). The switching-off of the 16.79 GHz beatnote is reflected in the beatnote beating.

beating of the successively recorded traces in (a) and (b), offset by -2 MHz for better visibility, verifying the beatnote beating.

In Fig. 7.7(d-f) the same measurement is repeated for a different operation point, namely 668 mA injection current at 1 kHz repetition frequency, 80 µs long pulses at 7.7 K. The 15.12 GHz beatnote is presented in (d) and shows this time a pure red shift. The 16.79 GHz beatnote in (e) shows a similar behavior as in (b), but switches off before the pulse ends. Surprisingly we see a slight change in the beatnote time trace in (d) at this time (see Fig. 7.7(d) inset). This could indicate a weak coupling of the beatnotes and is still under further investigation. Switching-off of one beatnote as observed and presented in Fig. 7.7(e) is a unique feature at this specific opera-

tion point and in most of the other investigated time-traces both beatnotes are present till the end of the pulse. In Fig. 7.7(f) we also show the beatnote beating which reflects the switching-off of the 16.79 GHz beatnote. If other processes except rectification are causing the generation of this beatnote beating, it could in principle be used to lock both beatnotes to each other by a single, much lower frequency.

In the following, we concentrate on the down-mixed signal in Fig. 7.7(d,e). The red shift of the 15.12 GHz beatnote can intuitively be understood by temperature-dependent group refractive index changes. The corresponding change in the group refractive index, which would lead to shifts on the order of 10 MHz, is estimated to be $\Delta n_g \approx \Delta f_{rep}/f_{rep} \cdot n_g = 0.0027 \Rightarrow \Delta n_r \approx 0.0006$. This corresponds to a reasonable 8 K change in temperature by assuming a temperature tuning coefficient $\beta_{tun}(K^{-1}) = \frac{1}{\lambda}\frac{d\lambda}{dT} \approx \frac{1}{n_{eff}}\frac{dn_{eff}}{dT} \approx 2 \cdot 10^{-5} K^{-1}$ [238].

Similar arguments for the beatnote at 16.79 GHz would mean a *decrease* of temperature of 2.2 K, which is unphysical. Possible reasons for the blue shift could be temperature induced changes to the individual active regions, which are spatially separate (see inset of Fig. 7.1(a)), and therefore could change the gain induced dispersion or the gain-clamping of each individual active region.

So far, we assumed the current pulse to have a perfect rectangular shape. Since a bias-tee (containing a capacitor and inductor) is used for RF extraction from the bias line, an additional component in the circuit is added. Fig. 7.8(a) shows the QCL voltage time trace recorded with a fast oscilloscope and in (b) the corresponding down-mixed beatnote time trace in a single beatnote regime of the QCL. Slight changes in the voltage reflect or cause changes in the gain and would explain the common trend of the voltage and the beatnote drift. Whether the voltage affects the gain, and therefore the beatnote, or vice versa, is not yet known, and further investigation into this peculiar behavior is out of the context of this chapter.

Due to these frequency drifts during the pulse the beatnote linewidth is broadened. Now, by numerically compensating the drift, i.e. going into the moving frame of the beatnote, the beatnote linewidth can be estimated. The procedure applies the Hilbert-transform on the measured real electrical signal $X(t)$ to estimate it's complex representation $X(t) + i \cdot Y(t) = A(t) \cdot exp[i\phi(t)]$. From the complex representation, we extract the instantaneous frequency

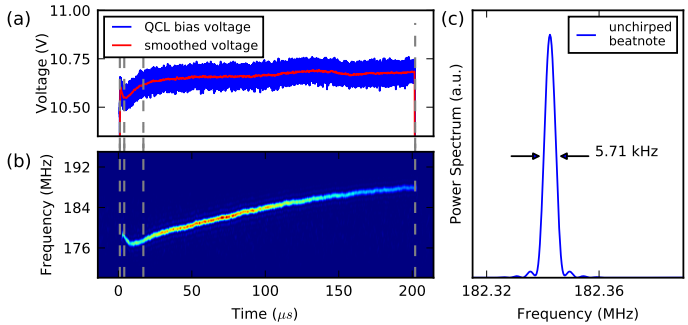

Figure 7.8 – (a) Recorded QCL bias voltage over one 200 µs long pulse. (b) Down-mixed 16.79 GHz beatnote of the same 200 µs long pulse. Some trend from the voltage shows similarities to instantaneous frequency. (c) Numerically unchirped 16.78 GHz beatnote from the 2.3 THz frequency comb which shows a narrow linewidth of 5.71 kHz.

$\nu(t)$. By multiplying now the complex representation of our signal by $exp[i2\pi(\nu_{const} - v(t))]$ we compensate the frequency drift where ν_{const} is set to 180 MHz, roughly the mean of the uncompensated signal. Mathematically we perform the following steps:

Hilbert Transform: $$X(t) \xrightarrow{\text{Hilbert Transform}} X(t) + i \cdot Y(t)$$
$$\Rightarrow X(t) + i \cdot Y(t) = A(t) \cdot e^{i\phi(t)}$$

instantaneous frequency: $$\Rightarrow \nu(t) = \frac{1}{2\pi} \cdot \frac{d\phi(t)}{dt}$$

phase corrected scope signal: $$\Rightarrow \tilde{X}(t) = A(t) \cdot e^{i\phi(t)} \cdot e^{i2\pi(\nu_{const} - \nu(t))t}$$

This approach is valid for the assumption of a single frequency signal as we have in our case. By Fourier Transforming the drift-free time signal we can extract narrow linewidths of 11 kHz for the beatnotes in Fig. 7.7(a,b) and 14.9 kHz and 17.1 kHz for the 15.14 GHz and 16.79 GHz beatnote, respectively in Fig. 7.7(d) and (e). Applying the drift compensation to the 200 µs pulse from Fig. 7.8(a) even leads to linewidth estimate of 5.71 kHz, getting close to sub-kHz widths as presented in Fig. 7.8(c).

Ideally, the devices would work on these two comb states simultaneously in CW. This would allow better investigation of the coherence and especially investigating potential second-harmonic generation (SHG) inside the waveguide. This could then further lead to beating of the SHG of the 2.3 THz located comb with the intrinsic 4.6 THz located comb, close to the situation needed for f-2f techniques.

7.4 Conclusion

We showed in this chapter the simultaneous lasing of two octave-spaced frequency combs, at 2.3 and 4.6 THz, in a monolithic QCL operated in a µs pulsed regime. By considering the cavity free spectral range of multiple devices at these two operating frequencies, taking into account the material dispersion of GaAs, we were able to predict and attribute the observed beatnotes frequencies to the 2.3 and 4.6 THz combs. This was experimentally confirmed for a 2.4 mm device by IBS, both conventionally using a Schottky diode mixer, and also using a self-mixing technique for the 4.6 THz comb. As we operated these lasers in pulsed, we also investigated the µs beatnote dynamics. Going into the moving frame of each beatnote, we estimated a beatnote linewidth of less than 15 kHz. Moreover, these time traces revealed interestingly that, while one of the two beatnotes showed the conventional thermally-induced chirp, counter intuitively, the other chirped both up and down. We speculated this to be the result of a combination of factors, including spatial thermal effects acting differently on the gain for the 2.3 and 4.6 THz, since the active regions are stacked one on top of each other. Furthermore, we observed what could be a weak coupling between the two combs, with the dynamics of one beatnote reflected on the other.

By proving that this laser can simultaneously emit a pair of combs spaced by an octave, one even being close to the Reststrahlen-band, we showed this monolithic approach to be a promising platform for further developments. With an active region tuned to lase CW and engineered for an optimized $\chi^{(2)}$, such an approach could be one step towards self-referenced f-2f combs in THz QCLs.

In addition to the limiting performance of these devices, we were also limited by the antenna bandwidth of our Schottky mixer. In the next and final chapters we will now combine our knowledge found in all previous chapters and exploit a fast, antenna coupled hot-electron

bolometer (HEB). This will allow us to access the coherence of our THz QCLs.

8

Phase and time profile of frequency combs: measurement techniques

To understand frequency comb formation in THz Quantum Cascade Lasers (QCLs) we need to gain further knowledge about the time profile and with it the phase relation between frequency comb modes. In particular, one would like to identify whether such devices tend to operate naturally in a amplitude modulated (AM) or frequency modulated (FM) way. Currently, there are several techniques to measure the phase relation of modes or the time profile of different laser sources. Today, one of the most relevant techniques in the QCL community is Shifted Wave Interference Fourier Transform (SWIFT) spectroscopy, but by far not the only one. Therefore we will first go briefly into the most common techniques in section 8.1 followed by section 8.2 where we will go through the details of SWIFT, the technique used in chapter 9.

8.1 General techniques

As many techniques were developed in the mode-locking community to characterize pulses, we will first go through these techniques followed by techniques exploited in the QCL community. The first technique to measure pulses relied on direct sampling of pulses with a fast scope and the use of a fast detector. But with the generation of even shorter pulses, this trivial technique needed to be replaced. Most common techniques from the mode-locked community now rely on the pulse to act as a gating function by itself. An excellent overview of these techniques is provided in the book of R. Trebino [106].

IAC

A still common technique for estimating pulse widths is the Interferometric Autocorrelation (IAC), also called fringe-resolved autocorrelation (FRAC), even though it does not contain the phase information of a pulse. As the name suggests it uses an interferometric delay line and the second-harmonic generation (SHG) effect which is created in a non-linear medium or directly measured by a two-photon absorption (TPA) detector. The recorded trace has a characteristic 8:1 ratio of the peak compared to the background signal that indicates isolated pulses. Certain features of the IAC trace can hint at chirped pulses or the presence of extended features such as a double pulse. But IAC does not allow to extract the phase and intensity information of a pulse. In addition, coherent artifacts can lead to an underestimation of the pulse length [239].

FROG

Since the one dimensional IAC trace does not have a unique solution, a new measurement technique had to be developed. The solution was found in the Frequency-Resolved Optical Gating (FROG) technique [240, 241], which extends in the first version the IAC by a spectrometer for the SHG signal. Therefore, the resulting measurement acquires the frequency vs. time trace, i.e. a spectrogram. The key point is that this two dimensional data set has a unique solution [106]. And by an initial guess and iterating algorithm the spectrogram is reconstructed which reveals the amplitude and phases in frequency domain and the intensity and temporal phase in time domain. It was extensively studied numerically that the intensity and phase information can also be retrieved from the spectrogram for very complex pulses [242]. There are now many different versions of FROG which depend on different nonlinear processes like polarization gate (PG), self-diffraction (SD), second-harmonic generation (SHG), and third-harmonic generation (THG), and transient grating (TG) FROG [243]. At the same time, a very compact FROG version called GRENOUILLE, a version with a reference pulse called XFROG and a single shot FROG version were developed [244]. These techniques rely on nonlinear processes which limit their application in certain frequency regions like the mid-IR or THz due to the high optical power needed or the lack of highly non-linear material in these spectral regions. A further version is the so-called

SEA TADPOLE [245] where an unknown pulse is interferometrically resolved by a spectrally overlapping reference pulse which is a linear process. Therefore, it is very sensitive, and also spatio-temporal versions were developed [246], even for single-shot measurements [247]. FROG was also used, for example, in Kerr combs which have short pulses on a quasi-constant background, i.e. not isolated pulses [248]. Additionally, FROG was shown to be able to identify coherent artifacts by comparing the experimental with the retrieved spectrogram [239]. Overall, FROG has established itself as THE method [1] in the mode-locking community, but due to limiting non-linear materials and peak powers, it is not well suited for mid-IR and THz and for the more FM-like QCLs.

SPIDER

Besides FROG there is the so-called Spectral Phase Interferometry for Direct Electric-field Reconstruction (SPIDER) technique [107] which allows to fully characterize pulses. The key idea is to split a pulse into two separate optical paths which are temporally isolated and of which one is experiencing a spectral shear. This can be achieved by broadening the pulse in a dispersive medium. The stretched pulse and the second pulse, acting as a prob pulse, are focused on a nonlinear material for SHG which then goes through a spectrometer. The resulting spectrum will show a characteristic fringing pattern. The advantage here is that the algorithm to extract the temporal intensity profile and phase is deterministic and does not rely on a converging and iterative algorithm. Nevertheless, also here SPIDER seems to be less sensitive on coherent artifacts than FROG [239] and random pulses lead to reduced fringe visibility which cannot be distinguished from misalignment of the optics. Also here, SPIDER relies on nonlinear materials. Therefore, we now saw the three most common techniques from the mode-locked community which are mostly not well suited for the mid-IR and THz. We will now go through the techniques which were applied in the QCL community.

1. The webpage of Prof. Trebino provides further illustrations and excellent material on this topic: https://frog.gatech.edu

Electro-optical sampling

The first technique which was able to show mode-locking behavior and proved comb operation in QCLs was the electro-optical sampling (EO sampling) in the THz [12]. As the name EO sampling suggests it makes use of the electro-optic effect (or Pockels effect) in a crystal. To remind, the electro-optic effect is a refractive index change induced by an electric field, which leads to a birefringence effect. In the exploited experiment, the THz field of a QCL will now induce this birefringence. The key element is an ultrafast pulse, $\tau <$ 150 fs, from a mode-locked laser which will experience this birefringence, i.e. rotation of the polarization. Since the mode-locked pulse is short compared to the THz field it will act like a delta probe of the THz field. The rotation of the short mode-locked pulse is then detected by a balanced detector and is proportional to the THz field at that point in time. To reconstruct the THz electric field, one also needs to record the repetition frequency of the mode-locked laser and the QCL comb. Since the pulse is probing one point of the THz field one also has to perform multiple shots which is in the end an averaging experiment and does not allow a single-shot experiment. As a side note, we can also work in the frequency domain where one will observe an heterodyne signal corresponding to a dual-comb experiment linked via the electro-optic effect. The drawback of EO sampling is that there is a need for a mode-locked reference laser, that both lasers need to operate in a stable comb regime and that incoherent emission cannot be identified due to the averaging.

Dual-comb measurement

Another approach to show the comb nature and reconstruct the time domain profile is to exploit a dual-comb experiment with a known reference laser [141]. The detected signal is in the final form similar to the one observed in the EO sampling but here arises from the optical beating of the two spectrally overlapping combs on a fast detector. If the reference comb is known, one can then reconstruct the unknown laser signal. This approach can also be applied at THz and in mid-IR [141]. The drawback here is as well the need for a well known reference laser and the dynamical range of the fast heterodyne detectors. Further, the approach only works if both lasers operate in a single comb regime and also here, detection of sub-combs (see section 8.2) or incoherent modes cannot be achieved.

Nonlinear optical sampling

The next technique to measure was developed quite recently and relies on the up-conversion of a mid-IR QCL with a mode-locked reference laser [150]. Also here, the mode-locked pulses are significantly shorter than the intensity profile one wants to measure and can be seen as a delta probe of the intensity. Therefore, the experiment can also be seen as an optical intensity oscilloscope. Since the mid-IR QCL and the mode-locked pulses are focused onto a nonlinear crystal, generating a SH signal, the measurement technique is an intensity- and not a field-sensitive measurement. This allows to measure the intensity profile but not it's phase.

It should be noted that the setup is very similar to the TADPOLE version of FROG expect of the frequency resolved temporal intensity measurement. This might become relevant since the above technique holds as long as the mode-locked pulse is significantly shorter than the measured pulse. And this might become relevant quite soon, since the results in Ref. [150] indicate mid-IR QCL pulses down to 630 fs. The drawback here is that incoherent components lead to a constant background, that sub-combs cannot be resolved and that this technique is available in the mid-IR but not in THz.

IBS - Intermode Beatnote Spectroscopy

All measurement techniques which we explored for QCLs up to now relied on a well known reference comb. But with the observation of FM combs in mid-IR QCLs [11] there was established a new technique called intermode beatnote spectroscopy (IBS). The method relies on a fast detector which is able to detect the optical beating which in the case of QCLs is on the order of 10 GHz. It is quite intuitive that only equidistant spaced modes are able to produce the same single and narrow beatnote. If we now observe this optical beating through an interferometric measurement one can extract from there the spectral components which produce this single and narrow beatnote. This can then be compared to the intensity spectrum do identify the spectral overlap. This method was already seen before in chapter 7. One advantage is that it clearly allows to distinguish quasi-cw operation from pulsed operation in QCLs. The drawback is that one cannot extract any phase information from this measurement. Therefore, it only shows the equidistant spacing but

not the temporal profile. If the QCL is used in a dual-comb experiment for spectroscopy, one normally does not need short pulses and the exact temporal shape is irrelevant. Therefore, the IBS is still a very useful technique, especially because it also allows to access to some part the incoherent part of the spectrum as well [11].

SMIBS - Self-Mixing Intermode Beatnote Spectroscopy

In the absence of any fast detector or reference laser there is an additional way to partially show the equidistance of spectral modes. The technique relies on optical feedback induced self-mixing [229] from an Fourier-Transform Infrared Spectrometer (FTIR) and was first presented in Ref. [41]. The idea here is that a small feedback of a mode onto itself leads to a slight change of its frequency due to the impedance matching needed at the laser facet. Since all modes in a comb are involved in the phase locking, the beatnote has to slightly adopt its frequency to satisfy locking and the self-mixing. This change of the beatnote frequency due to feedback is on the order of 200 kHz compared to the GHz ranged beatnote frequency as we saw in chapter 6, Fig. 6.3. As we will see in chapter 9, the self-mixing does shift the frequency of the beatnote and also modulates its amplitude as a function of FTIR delay. This can only be explained if the phase relation between comb modes is slightly changing or the spectral mode amplitudes change. Both indicates that a free running QCL with feedback does not fulfill exactly the definition of a comb since it should be locked. On short time scale the beatnote is narrow, indicating phase-locking, and this is sufficient for certain applications where no fully-locked comb is needed. Self-mixing intermode beatnote spectroscopy (SMIBS) shows therefore the spectral components which generate the beatnote. Further, the SMIBS obviously works only for free running combs.

By now we saw that only the techniques relying on a reference laser allow reconstructing the full temporal behavior and measuring the spectral phases of QCLs. But these techniques have limited performance to investigate noisy combs, sub-combs or any spectrally incoherent parts except to distinguish them from a perfect comb. The techniques relying on the beatnote detection can spectrally resolve the modes involved in the comb formation, but so far only evaluate the equidistant spacing of the comb modes.

In the next section we will therefore go to a method called

SWIFT which extends the IBS and will allow us to measure the phase relation between neighboring modes and therefore in theory retrieve the full spectral and temporal information of the observed combs or sub-combs.

8.2 SWIFT - Shifted Wave Interference Fourier Transform

Shifted Wave Interference Fourier Transform (SWIFT) Spectroscopy was first introduced by Burghoff et al. in Ref. [17] to show the coherence of a THz QCL comb. The concept behind SWIFT is the same as in the IBS but instate of simply measuring the optical beatnote power, the beatnote signal is additionally demodulated by a reference signal. Normally, the beatnote signal itself or a reference source to which the beatnote is locked acts as the local oscillator for the demodulation. SWIFT was then used to measure the temporal shape of THz QCLs in THz QCLs [125]. Since fast detectors in the mid-IR are more common, SWIFT was then heavily used here for phase and temporal characterization of free running, injection-locked and dispersion compensated mid-IR QCLs [88, 139, 149, 150, 216, 249]. Recently, other laser systems had been investigated for the temporal shape by means of SWIFT as well [13, 14, 250, 251]. In the following we will mathematically derive the measurement quantities of SWIFT, based mainly on Ref. [252, 253], and discuss the advantages and disadvantages of it.

Before going into mathematics, let us take a look at how a SWIFT setup typically looks like. Fig. 8.1 shows a schematic of such a SWIFT setup. The laser, here a QCL, is aligned to an FTIR. The output signal is then further focused on a slow and fast detector. This can by done simultaneously with a beam splitter, as sketched, or sequentially by switching for example from the internal (FTIR, slow) to the external (fast) detector. The latter assumes that changing the optics to focus on the other detector does not influence the comb state. The slow detector measures the standard intensity interferogram (IFG). The optical detected beatnote from the fast detector is in general further down-mixed in the RF domain by a fixed reference source. The reference beatnote, extracted from the QCL bias line or from an additional fast detector before the FTIR, is also down-mixed with the same reference source as the optical detected beatnote. This is in general needed since the beatnote frequency is on the order of some GHz and the lock-in amplifier bandwidth on

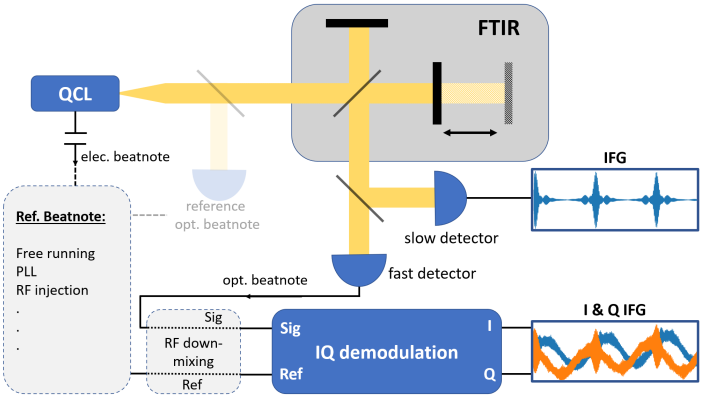

Figure 8.1 – SWIFT setup. The laser is aligned to an FTIR which output will be focused on a slow and fast detector. The signal from the slow detector corresponds to the standard intensity interferogram. The reference beatnote is extracted electrically on the laser bias line or by an additional fast detector before the FTIR. Both, the reference and optically detected beatnote, are down-mixed and IQ demodulated. The I and Q traces correspond to the SWIFT IFGs.

the order of some MHz. The IQ demodulation is then performed by a lock-in amplifier. As indicated, the reference beatnote can either be the free running beatnote itself or the signal to which it is locked, i.e. PLL or RF injection frequency. The resulting in-phase (I or X) and quadrature (Q or Y) signals as a function of the mirror delay correspond then to the two SWIFT IFGs.

Let's now jump into the mathematics. Since we measure a laser, we express its electric field by a superposition of its modes

$$E(t) = \sum_n E_n e^{i2\pi\nu_n t} \tag{8.1}$$

where $E_n \equiv E(\nu_n)$ and complex, i.e. $E_n = |E_n|e^{i\phi_n}$, and the summation is over **positive and negative**[2] n. In addition, $E_n^* = E_{-n}$ and $\nu_n^* = \nu_{-n} = -\nu_n$ to ensure a real field. By now we simply assumed that they have lasing modes given by their indexes. They do not need to be equidistant or phase-locked.

2. This means that we are **not** in a complex representation of the electric field. Therefore, in any equation followed in this section one should not simply take the real value since certain signals are complex.

Now, the intensity measured by an ideal detector of such an electric field is written as [3]

$$\begin{aligned} S(t,\tau) &= \frac{1}{2}\left(E(t)+E(t+\tau)\right)^2 \\ &= \frac{1}{2}\left(E(t)^2+E(t+\tau)^2+2E(t)E(t+\tau)\right) \\ &= \frac{1}{2}\sum_{n,m} E_n E_m^* e^{i2\pi\nu_{nm}t}\left(1+e^{i\pi\nu_{nm}\tau}+2e^{i2\pi\nu_n\tau}\right) \end{aligned} \tag{8.2}$$

with $\nu_{nm} \equiv \nu_n - \nu_m$ and m,n summation over all modes. Therefore, an ideal detector would be able to record all fast oscillations. But such detectors do not exist so we look into two cases of a slow and a fast [4] detector.

For slow detectors, the intensity as a function of delay, i.e. the IFG, will average the signal given by its bandwidth. Therefore, we write the detected intensity S_0 as

$$\begin{aligned} S_0(\tau) &= \langle S(t,\tau)\rangle \\ &= \frac{1}{2}\sum_{n,m}\langle E_n E_m^* e^{i2\pi\nu_{nm}t}\rangle\left(1+e^{i2\pi\nu_{nm}\tau}+2e^{i2\pi\nu_n\tau}\right) \end{aligned} \tag{8.3}$$

For typical slow detectors, the bandwidth is on the order of Hz or kHz. In general ν_{nm} is on the order of MHz or GHz unless $n = m$. Therefore, for slow detectors $\langle E_n E_m^* e^{i2\pi\nu_{nm}t}\rangle = 0$ for $n \neq m$ and one finds

$$\begin{aligned} S_0(\tau) &= \frac{1}{2}\sum_n \langle E_n E_n^*\rangle\left(1+1+2e^{2\pi\nu_n\tau}\right) \\ &= \sum_n \langle |E_n|^2\rangle\left(1+e^{i2\pi\nu_n\tau}\right) \end{aligned} \tag{8.4}$$

As we now also use a fast detector in our setup which bandwidth is sufficiently large to record different mode beatings there will be

3. Here we use positive delay $+\tau$ to match FTIR traveling direction different to Ref. [252].

4. but not as fast as an ideal detector.

more terms which are non-zero after averaging them, see Eq. 8.3. In SWIFT we now demodulate the signal containing many different fast oscillation frequencies with an local oscillator (LO) with frequency ν_{LO}. Therefore, we define $S_+(\tau) \equiv \langle S(t,\tau)e^{-i2\pi\nu_{LO}t}\rangle$ where now the averaging is given by the demodulator or lock-in bandwidth. It is clear that one now chooses ν_{LO} close to the mode spacing [5] ν_r. Further, $L \cdot \nu_r \approx \nu_{n,n-L}$ where L an integer value and we use a comma in the index for clarity. Typically, $L = 1$, corresponding to the beatnote frequency. For a perfect comb, one finds now that $L \cdot \nu_r = \nu_{n,n-L}$ and one can set $\nu_{LO} = L \cdot \nu_r$. $S_+(\tau)$ reads now as

$$\begin{aligned} S_{+,L}(\tau) &= \langle S(t,\tau)e^{-i2\pi\nu_{LO}t}\rangle \\ &= \frac{1}{2}\sum_n \langle E_n E^*_{n-L} e^{i2\pi(\nu_{n,n-L}-\nu_{LO})t}\rangle \\ &\qquad \cdot \left(1 + e^{i2\pi\nu_{n,n-L}\tau} + 2e^{i2\pi\nu_n\tau}\right) \end{aligned} \tag{8.5}$$

where we will write the index L for all cases expect for $L = 1$ we write 1. In general, on is only interested in the interferometric part $e^{2\pi\nu_n\tau}$ which we will denote according to [252] with $\hat{S}_0$ and $\hat{S}_+$. The interferometric parts read as [6]

$$\hat{S}_0(\tau) = \sum_n E_n E^*_n e^{i2\pi\nu_n\tau} \tag{8.6}$$

$$\hat{S}_{+,L}(\tau) = \sum_n E_n E^*_{n-L} e^{i2\pi\nu_n\tau} \tag{8.7}$$

and is denoted by $\hat{\cdot}$.

For each case $E_n E^*_n$ and $E_n E^*_{n-L}$ correspond to the Fourier amplitudes, i.e. the spectrum amplitudes.

Before we said that we measure the I and Q components in our setup which we can finally relate to S_+. We use that

$$\begin{aligned} S_{+,L}(\tau) &= \langle S(t,\tau)e^{-i2\pi\nu_{LO}t}\rangle \\ &\triangleq \langle S(t,\tau)\cos(2\pi\nu_{LO}t)\rangle - i\langle S(t,\tau)\sin(2\pi\nu_{LO}t)\rangle \end{aligned} \tag{8.8}$$

5. For multi-mode laser the round trip frequency is changing for each mode pair.

6. Also here the difference to Ref. [252] comes from the direction of delay τ.

for which one finds for the interferometric parts [7] [253]

$$\begin{aligned}\hat{S}_{I,L} &= \langle S(t,\tau)\cos(2\pi\nu_{LO}t)\rangle \\ &= \frac{1}{2}\sum_n \left(\langle E_n E^*_{n-L}\rangle + \langle E_n E^*_{n+L}\rangle\right) e^{i2\pi\nu_n\tau}\end{aligned} \tag{8.9}$$

and

$$\begin{aligned}\hat{S}_{Q,L} &= \langle S(t,\tau)\sin(2\pi\nu_{LO}t)\rangle \\ &= -\frac{i}{2}\sum_n \left(\langle E_n E^*_{n-L}\rangle - \langle E_n E^*_{n+L}\rangle\right) e^{i2\pi\nu_n\tau}\end{aligned} \tag{8.10}$$

By combining the I and Q traces one finds that

$$\hat{S}_{+,L}(\tau) \equiv \hat{S}_{I,L}(\tau) - i\hat{S}_{Q,L}(\tau) \tag{8.11}$$

$$\hat{S}_{-,L}(\tau) \equiv \hat{S}_{I,L}(\tau) + i\hat{S}_{Q,L}(\tau). \tag{8.12}$$

As typically in SWIFTS, $L = 1$ and one simply writes [8]

$$\hat{S}_+(\tau) \equiv \hat{S}_I(\tau) - i\hat{S}_Q(\tau) = \sum_n E_n E^*_{n-1} e^{i2\pi\nu_n\tau} \tag{8.13}$$

$$\hat{S}_-(\tau) \equiv \hat{S}_I(\tau) + i\hat{S}_Q(\tau) = \sum_n E_n E^*_{n+1} e^{i2\pi\nu_n\tau}. \tag{8.14}$$

SWIFT properties

As we look at the interferometric parts in Eq. 8.7, 8.9 and 8.10 we will find certain properties. For overview purpose we numerate them.

1. We highlight again that we sum over positive and negative n. One could be tempted to write the summation only over positive n. Here one should note that $\hat{S}$ is complex and

7. The same derivation can be done keeping all terms as well.
8. Also here the difference to Ref. [252] comes from the direction of delay τ.

$$\hat{S}_{+,L}(\tau) = \sum_n E_n E^*_{n-L} e^{i2\pi\nu_n\tau} \neq \sum_{n>0} E_n E^*_{n-L} e^{i2\pi\nu_n\tau} + c.c. \tag{8.15}$$

but

$$\begin{aligned}\hat{S}_{+,L}(\tau) &= \sum_n E_n E^*_{n-L} e^{i2\pi\nu_n\tau} \\ &= \sum_{n>0} E_n E^*_{n-L} e^{i2\pi\nu_n\tau} + E_{-n} E^*_{-n-L} e^{-i2\pi\nu_n\tau} \\ &= \sum_{n>0} E_n E^*_{n-L} e^{i2\pi\nu_n\tau} + E^*_n E_{n+L} e^{-i2\pi\nu_n\tau}\end{aligned} \tag{8.16}$$

with $(E_n E^*_{n-L})^* \neq E^*_n E_{n+L}$ since $E^*_{n-L} = E_{-n+L} \neq E_{-n-L}$. This means simply that the negative and positive frequency magnitudes of the Fourier Transform (FT) are **not** symmetric around zero frequency.

2. We still find a relation between the FT amplitudes $S_+(\nu_n) \equiv S^{(n)}_+$ of the positive and the negative frequencies since

$$|S^{(n)}_+| = |E_n E^*_{n-L}| \tag{8.17}$$

$$|S^{(-n+L)}_+| = |E_{-n+L} E^*_{-n}| = |E^*_{n-L} E_n| \tag{8.18}$$

$$\Rightarrow |S^{(n)}_+| = |S^{(-n+L)}_+|. \tag{8.19}$$

In other words the positive magnitudes are equal to the negative magnitudes shifted by one mode pair, i.e. $L\nu_{n,n-1}$.

3. The complex FT amplitudes $S^{(n)}_+$ contain the phase difference of this mode pair:

$$\begin{aligned}S^{(n)}_+ = E_n E^*_{n-L} &= |E_n||E^*_{n-L}| e^{i(\phi_n - \phi_{(n-L)})} \\ &\equiv |E_n||E^*_{n-L}| e^{i\Delta\phi_{n,n-L}}.\end{aligned} \tag{8.20}$$

Therefore, SWIFT measures the phase relation between mode pairs. This allows to measure the group delay $\tau_g = \frac{\partial\phi}{\partial\omega} \approx \frac{\Delta\phi}{\Delta\omega}$ as well.

Further, we find that

$$\begin{aligned} S_+^{(n)} &= |E_n||E_{n-L}^*|e^{i\Delta\phi_{n,n-L}} \\ &= |E_{-n+L}||E_{-n}^*|e^{i\Delta\phi_{-n,n+L}} = S_+^{(-n+L)}. \end{aligned} \tag{8.21}$$

We remind that due to point 2. the positive frequency is at ν_n whereas the negative frequency is at $\nu_{-n+L} = -\nu_{n-L}$.

4. In contrast to the intensity spectrum, see Eq. 8.6, the recorded **SWIFT traces are in general not symmetric** around the Zero Path Delay (ZPD) of the FTIR even though the measurements in mid-IR could suggest such case. This can be seen by rewriting Eq. 8.9 and 8.10 for positive frequencies and will find

$$\hat{S}_{I,L} = \sum_{n>0} Re\left((E_n E_{n-L}^* + E_n E_{n+L}^*)e^{i2\pi\nu_n\tau}\right) \tag{8.22}$$

$$\hat{S}_{Q,L} = \sum_{n>0} Im\left((E_n E_{n-L}^* - E_n E_{n+L}^*)e^{i2\pi\nu_n\tau}\right). \tag{8.23}$$

One could be tempted to assume that $\hat{S}_{I,L}$ corresponds to a cosine and $\hat{S}_{Q,L}$ to a sinus and therefore it should be symmetric around the ZPD. But each complex amplitude will introduce a constant phase shift $\Delta\phi_{n,n-L}$. For the case that $\Delta\phi_{n,n-L} = 0$ one actually finds that the SWIFT traces are symmetric. If the phase differences are equally spread around 2π with roughly symmetric amplitude distribution, which both imply FM with close to continuous wave (CW) emission, the traces appear to be symmetric confirming the results from mid-IR QCLs. But as we will see in chapter 9 this does not necessary hold for THz QCLs implying significantly different phase differences between mode pairs and significant AM of the measured intensity. We note that even though the symmetry is not preserved, the periodicity is. Additionally, by definition, $|\hat{S}_{+,L}|$ is symmetric and corresponds the the IBS trace.

5. One important feature of SWIFT is that we can obtain the first-order coherence g_n of the spectrum defined as

$$g_n \equiv |S_+^{(n)}|/\sqrt{S_0^{(n)} S_0^{(n-L)}} \tag{8.24}$$

where $S_+^{(n)}$ and $S_0^{(n)}$ are the Fourier coefficients, i.e. the spectrum amplitudes, of the SWIFT spectrum and intensity spectrum, respectively. $\sqrt{S_0^{(n)} S_0^{(n-L)}}$ is referred as *spectrum product*. Best results are achieved if the fast detector acts as a slow detector as well as in Ref. [17]. For the other cases one has to ensure good alignment on both detectors and avoid significant different beam paths as well. In absence of any equidistance errors or phase noise $|g_n| = 1$ and else $|g_n| < 1$.

6. Non-equidistant spacing will lead to significant loss of coherence and also to a frequency shift of the spectral components in the spectrum. This can be seen in Eq. 8.5 by replacing the explicit time by the delay and the mirror velocity v which leads to

$$E_n E_{n-L}^* e^{i2\pi(\nu_{n,n-L}-\nu_{LO})t} = E_n E_{n-L}^* e^{i2\pi(\nu_{n,n-L}-\nu_{LO})\frac{c}{2v}\tau}. \tag{8.25}$$

If the travel length τ_{max} is close to a multiple of the mode spacing we can approximate g_n by [252]

$$\begin{aligned} |g_n|^2 &= |\frac{1}{\tau_{max}} \int_0^{\tau_{max}} e^{i2\pi(\nu_{n,n-L}-\nu_{LO})\frac{c}{2v}\tau} d\tau|^2 \\ &= \mathrm{sinc}^2\left(\frac{c}{4v} 2\pi(\nu_{n,n-L}-\nu_{LO})\tau_{max}\right) \\ &= \mathrm{sinc}^2\left(\pi T(\nu_{n,n-L}-\nu_{LO})\right) \end{aligned} \tag{8.26}$$

with the total measurement time $T = 2v\tau_{max}/c$.

As a consequence, the first zero crossing of g_n occurs for equidistance error $\delta\nu = \nu_{n,n-L} - \nu_{LO} = 1/T$. The measurement time for example of the Bruker 80v with 0.075 cm^{-1} resolution in rapid scan is approximately $T = 30$ s which provides a equidistance error below 30 mHz.

But actually there is more we can extract from here: if we insert typical values for the FTIR mirror speed of 5 mm/s and assume non-equidistant mode spacing of 1 Hz we will find that this shifts the modes by 30 GHz in the spectrum which would be clearly visible. Further, non-equidistant spacing of 15 mHz would still lead to a frequency shift of 450 MHz. This means if there are individual modes which are off from equally spacing

by 15 mHz it will lead to a clearly visible asymmetry in the $|S_+(\tau)|$ IFG. [9]

7. With the previous analysis we see that the actual lock-in bandwidth, typically on the order of kHz up to MHz, will not increase the uncertainty on the equidistance. Therefore, the lock-in bandwidth is relevant for noise reduction and filtering out unwanted signal components.

8. Due to the demodulation detection, SWIFT is very sensitive on any coherent signal. At the same time, this high sensitivity does not allow SWIFT to measure any incoherent light. Therefore, only by comparison with the intensity spectrum and evaluation the coherence function one will have indications about any incoherent light component.

9. Phase noise is now the remaining source of noise in an unstable comb. As derived in Ref. [252] one can show that the integrated phase noise from $1/T$ up to the lock-in bandwidth or it's digitization Nyquist frequency, reduces the coherence function g_n. Mathematically, this is expressed as

$$|g_n|^2 = |\frac{1}{T}\int_0^T e^{i\phi(t)}dt|^2 \tag{8.27}$$

where $\phi(t)$ represents the phase noise.

This means that phase noise reduces the coherence function but the SWIFT modes are located at the correct frequency, which is not the case for equidistance errors discussed in point 6.

10. Further, we discuss the calculation of the phase difference $\Delta\phi_{n,n-L}$. Obviously, its the phase of the complex FT amplitudes $S_+^{(n)}$. Due to the Discrete Fourier Transform (DFT) the signal will consist of phase errors from the optics and wrong determination of the ZPD, which need to be corrected. This can be done in two ways.

The first method consists of rotating by the inverse phase from the intensity spectrum $S_0^{(n)}$: $\Delta\phi_{n,n-L} = argS_+^{(n)} - argS_0^{(n)}$.

9. The Doppler shift of equally spaced modes is relevant within the time one records one single IFG point. This time interval is on the order of some ms which makes the resulting shift significantly small to be discarded. At the same time one could also perform SWIFT in step-scan mode.

This does rely on accurate phase measurement from the intensity spectrum and that the intensity and SWIFT interferograms are perfectly aligned, i.e. exact same ZPD.

The second method relies on the fact that from point 3 we have $\Delta\phi_{n,n-L} = \Delta\phi_{-n,-n+L}$ whereas any phase error $\Delta\phi_{n,err}$ will be by default anti-symmetric with $\Delta\phi_{n,err} = -\Delta\phi_{-n,err}$. Since phase errors are in general slowly varying [10] we can assume $\Delta\phi_{n,err} \approx -\Delta\phi_{-n+L,err}$. Therefore, we find that

$$\begin{aligned}\Delta\phi_{n,n-L} &= \frac{1}{2} \cdot arg(S_+^{(n)} \cdot S_+^{(-n+L)}) \\ &= \frac{1}{2} \cdot (arg(S_+^{(n)}) + arg(S_+^{(-n+L)})).\end{aligned} \tag{8.28}$$

At the same time this could create a π ambiguity for certain frequencies. This can be solved by roughly selecting the ZPD and compare the negative frequency phases $arg(S^{(-n+L)})$ with the positive frequency phases $arg(S^{(n)})$. Since we selected roughly the correct ZPD, which is the main source for phase errors, we will find that these phases should be very close to each others and only differ by the small phase error. If we now have an ambiguity on the phase we will find that this spacing is increased due to the 2π phase wrapping. By simply checking if the phase difference between $arg(S^{(n)})$ and $arg(S^{(-n+L)})$ becomes smaller by adding $+2\pi$ or -2π one will detect this final π ambiguity and can correct it. In chapter 9 we implemented the second method.

11. SWIFT allows in principle to reconstruct the time domain signal from the intensity spectrum, i.e. $|E_n|$, and the cumulative sum of the phase differences $\phi_n = \phi_{n-1} + \Delta\phi_{n,n-1} \quad \forall\ n > 0$ and $\Delta\phi_{n,n-1} = 0$ for $|E_n| = 0$ or below the noise floor. This fully reconstructs the signal if all spectral modes are connected. By defining the electric field $E(t) = \sum_{\nu_n>0} E_n e^{i2\pi\nu_n t}$ one finds for the intensity

$$I(t) \equiv |E(t)|^2 \tag{8.29}$$

and for the instantaneous frequency

10. Over hundreds of GHz whereas the mode pairs are spaced by a few GHz.

$$
\begin{aligned}
f(t) &\equiv \frac{1}{2\pi} arg(E(t)) \\
&= \frac{1}{2\pi |E(t)|^2} Im\left(E^*(t)\frac{dE(t)}{dt}\right)
\end{aligned}
\tag{8.30}
$$

with the latter definition numerically more stable.

12. Finally, one should mention that SWIFT is rather difficult for low repetition rate mode-locked lasers, i.e. around 100 MHz, since one would need a very long delay line to resolve all modes. This can partially be resolved by directly analyzing the SWIFT IFG as discussed in Ref. [252]. Nevertheless, FROG or SPIDER have their advantage over SWIFT for ultra short pulses with a low repetition rate.

8.3 Conclusion

In this chapter we first reviewed briefly the IAC, FROG and SPIDER pulse characterization techniques from the mode-locked community. Even thought they can be applied in principle to mid-IR and THz QCLs, there are some practical limitations given by the need of high intensities and non-linear crystal needed to realize most of them. On the other hand, techniques such as EO sampling, dual-comb with a reference comb or a nonlinear optical sampling technique allowed to measure the temporal electric field or intensity profile of THz and mid-IR QCLs. But they also have their limitations due to the need for a well-known reference comb laser. We then briefly looked at IBS and SMIBS, two techniques relying on the beatnote detection and interferometric measurements. Both methods allowed to identify spectral regions which produce a beatnote, i.e. are equally distant spaced. At the same time they do not allow to access the fully spectral nor temporal information. We therefore went in detail into SWIFT. This technique allows to make spectral phase sensitive measurements of neighboring modes and gives access the spectral coherence of a comb or certain spectral regions. Since SWIFT is the key technique used in the next chapter we discussed it in detail.

9

Strongly RF modulated THz Quantum Cascade Lasers

In the previous chapter we examined different methods to verify the comb coherence and how to measure the phase relation of adjacent modes by means of Shifted Wave Interference Fourier Transform (SWIFT). In this chapter we will apply SWIFT to examine two broadband THz Quantum Cascade Lasers (QCLs). One device is based on an octave spanning heterogeneous design, previously examined in Ref. [38], and the other one on a homogeneous design studied in chapter 4 and 5. First, the setup and analyzing scheme will be introduced in section 9.1 followed by a first analysis of free running comb devices in section 9.2. Second, we will treat the case of RF injected THz QCLs in section 9.4. There we will see that by moderate and resonant injection the examined QCLs operate close to a frequency modulated (FM) state, whereas an increase in the RF power leads to amplitude modulated (AM) operation. In a third step in section 9.5, we will transition from RF injection locking to an RF driven system, i.e. the RF source is not only stabilizing the comb but rather dictating the operation of the device. This strong RF driving will lead to formation of sub-combs which will be investigated by means of SWIFT. Additionally, the seeding of modes which are off-resonant to the nominal fundamental repetition frequency will be investigated in section 9.6. In a fourth step, we will examine the case of a harmonic comb state by means of SWIFT in section 9.7. The final section 9.8 will bring up some open particularities of SWIFT which are experimentally observed.

9.1 Experimental configuration

Fig. 9.1 shows the experimental setup for SWIFT measurements. We employ a commercial vacuum Fourier-Transform Infrared Spectrometer (FTIR) (Bruker, Vertex 80v) and use the internal deuterated triglycine sulfate detector (DTGS) detector to record the intensity spectrum. For optical beatnote detection, a fast spiral antenna-coupled NbN hot-electron bolometer (HEB) is used [254, 255]. The precise configuration is discussed in appendix A. The fast HEB allows to experimentally observe a beatnote up to ∼33 GHz. Depending on the signal strength and frequency, an additional room temperature RF amplifier can be used at the fast detector side. The HEB is mounted on an RF optimized flow cryostat which is located in a nitrogen purge box outside the FTIR. Therefore, the optical path is extended by three additional mirrors, two TPX windows and two cold optical filters [1] and the SWIFT measurement is performed sequentially for each detector. The FTIR is operated in rapid scan [2] mode and the reference helium-neon laser (HeNe laser) is recorded by an oscilloscope to resample the I and Q interferograms (IFGs) [3]. The IQ demodulation is performed by a Spectrum Analyzer (SA) (Rohde & Schwarz, FSU 26 or FSU 65) with respect to a fixed frequency, roughly the beatnote frequency. In the following we discuss two situation for which the SWIFT measurement is applied: free running devices and RF injection or driven devices.

SWIFT setup: Free running devices

In previous SWIFT measurements in the mid-IR, the electrical beatnote from the free running QCL and the optical beatnote from the fast detector were down-mixed and fed into a lock-in amplifier [88, 138] [4]. The PLL bandwidth of lock-in amplifiers is typically on the order of 300 kHz [256–258]. This limits the measurement

1. These points can play a role during coherence analysis of SWIFT spectra. The filters block shorter wavelengths and are discussed later.

2. Constant velocity of the FTIR mirror, but slow enough that the detector bandwidth allows to assume the interference signal to be locally constant.

3. In chapter 9 we defined $\hat{S}_I$ and $\hat{S}_Q$ which we will for simplicity refer as I and Q in the following.

4. In Ref. [17] the beatnote was directly IQ demodulated to a 10 MHz reference source, to which the beatnote was phase-locked, and detected by a lock-in amplifier and is therefore not a free running experiment. The phase-locked loop (PLL) bandwidth is on the order of 350 kHz.

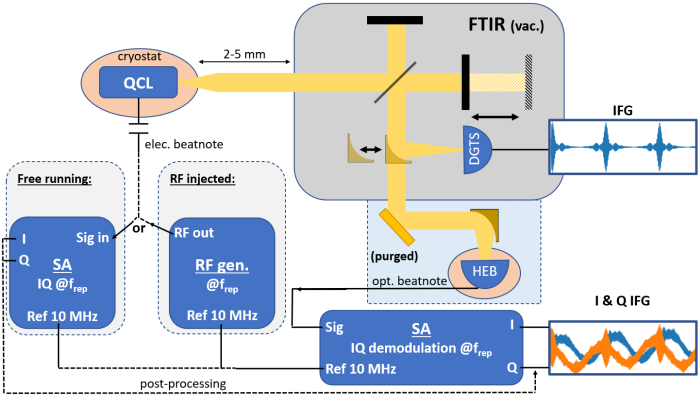

Figure 9.1 – SWIFT setup. QCL is aligned to an FTIR, high NA optics, i.e. parabolic mirrors, which records the intensity spectrum. By switching to the output port we can sequentially measure the I and Q traces of SWIFT on a fast NbN HEB. The IQ demodulation is performed either by an SA which is referenced to the RF injection generator or post-processed with respect to the free running electrical beatnote recorded on the bias-line (not connected simultaneously). Details discussed in the text.

capability of free running devices in THz since, experimentally, the beatnote is often not consistently locked by this PLL due to optical feedback. To overcome the limits of the lock-in amplifier PLL bandwidth, we chose to use two SAs to imitate a lock-in amplifier with extended bandwidth. To do so, the two SAs are referenced by the internal 10 MHz reference of one SA and the recording settings are exactly the same on both SAs. This means that both SAs record synchronously. Typically, the IQ sampling rate is set higher than 2 MSps leading to a bandwidth larger than 1.5 MHz which is sufficient for our application. It is essential that both devices use the *sampling* detector mode (see Rohde & Schwarz, FSU Manual [259]) and are triggered at the same time. The recording time is given by the scanning speed of the FTIR and is on the order of 35 s for which we fix the total recording time of the SAs to 40 s. One SA is then detecting the electrical beatnote whereas the other detects the optical beatnote from the HEB. Both have their central frequency set to a fixed frequency roughly corresponding to the free running beatnote. We can therefore go into the rotating frame of the fixed SA frequency. Both, the reference SA's and the signal SA's complex IQ vectors will now rotate in the complex plane in this rotating frame. We now want to switch into the rotating frame of the rotating ref-

erence IQ vector, which is the same thing as a lock-in amplifier is doing. Therefore, we extract the full memory of both IQ trace, i.e. $> 2 \cdot 40 \cdot 10^6$ sampling points each, and rotate each complex sample point of the reference IQ vectors back to the real axis [5]. The exact same rotation of each reference point is applied to the corresponding signal sampling point which provides us the IQ demodulated signal with respect to our reference beatnote.

It is essential to use the sampling detectors of the SAs to have synchronously sampled points with a high sampling rate. The use of any other detector setting, for example the average detector, should be avoided since it already averages the IQ sampling points, which are rotating relatively fast on the IQ circle, which would in the worst case even average to zero. Further, the full memory information is needed since the standard trace length display a subset and is limited to 100'001 sample points. Even though these subset sample points are synchronously acquired and back rotation with respect to the reference signal would work, we would discard most of the sampled points. By using the full memory, we essentially oversample the signal and after back rotation with respect to the reference signal, we can finally average the recorded signal. A well sampled intensity IFG consists in our experiment of ∼60'000 sample points whereas the IQ IFG consists of a factor 1'000 to 5'000 points more. This allows to average [6] the oversampled raw IQ IFG points, finally enhancing the signal-to-noise ratio (SNR).

By now, we showed how to record the SWIFT IQ traces by the use of two SAs of a free running THz QCL comb. Also we would like to mention that even due to the large amount of data points the data processing can be performed in a few seconds on a standard computer CPU. Due to the sequential recording of the SWIFT and intensity IFGs, the whole post-processing of the IQ traces can be done in the time of the intensity IFG measurement leading to a fast acquisition of multiple SWIFT traces.

The experimental acquisition slightly simplifies when switching to RF injection experiments, which will be discussed in the following.

5. Any other fixed vector in the IQ circle would work as well.

6. One can also filter, use a convolution with a window function with the length of this 5'000 points or any other averaging technique.

SWIFT setup: RF injected devices

In the situation of RF injected THz QCLs the beatnote is ideally locked to the RF frequency. Therefore, it is fixed in frequency and the previous SA at the QCL side is redundant. Still, the RF generator needs to be synchronized to the SA at the detector side by sharing the same 10 MHz frequency reference. The key point here is simply that the frequency set by the RF generator is exactly the same as set on the SA. The IQ detection is now in the rotating frame of the RF source and no back rotation of the IQ trace is needed. Therefore, the averaging can be performed directly by the SA, i.e. the *averaging* detector mode (see Rohde & Schwarz, FSU Manual [259]), and the extraction of the standard traces, i.e. 100'001 points which are the averaged points of the full memory, are sufficient to get the IQ traces. We note here that the SA still samples at the highest sampling rate suited for the experiment to increase the SNR but the averaging is done internally. The number of trace points is large enough to resolve the interference pattern.

Remarks on SWIFT measurements

Before discussing the measurement results from free running and RF injected devices we have to address a few experimental aspect of the exploited setup. First, as mentioned, we perform a sequential measurement of the IQ and intensity IFGs on two separate detectors. Therefore, we rely on good alignment, i.e. low divergence over the mirror traveling range, of the high NA collimated THz beam on both detectors, especially on the fast HEB for which the light passes through two additional parabolic and one elliptical mirrors. Second, the light path to the fast detector consists additionally of two TPX windows at the FTIR and the cryostat shield followed by a low pass THz filter to suppress the black body radiation of higher frequencies. Shorter wavelength radiation would influence or prevent the superconducting transition of the HEB. Those elements have a rather flat transmission, see appendix A, but still induce small etalon effects. Third, the purge box around the HEB can have certain leakage which can introduce some absorptions in the SWIFT spectrum. Fourth, the HEB detector gain and responsivity is not fully linear and depends also on the light intensity at the detector. This leads to an increased detector gain for low intensities and lower gain for high intensities produced in the interferomet-

ric measurement. The exact responsivity, still under investigation, see appendix A, for a given measurement is not corrected in the following. Fifth, for the strong injection experiment we observe a constant RF pick-up of the injected signal which limits the dynamic range of optical beatnote detection. Sixth, the THz light emitted by the QCL shortly passes through ambient air and is collected by high NA optics. Therefore, the final measured relative amplitudes will most probably differ slightly from amplitudes inside the lasing cavity. Also, the high NA used for THz QCLs could lead to slight deviation also to collection losses. Nevertheless, most effects influence mainly the amplitude but should have a marginal effect on the measured phase differences. Keeping these points in mind, we will now review the experimental findings.

9.2 Free running THz QCL SWIFT measurements

In chapter 6 and 7 we have already applied the concept of self-mixing intermode beatnote spectroscopy (SMIBS) to verify the equidistant spacing of spectral comb lines. Here, we use SWIFT to cross-check the results of intermode beatnote spectroscopy (IBS) in chapter 7 where a fast Schottky mixer was exploited. By performing a free running THz QCL SWIFT measurement, we can further discuss the free running comb operation and SMIBS.

In Fig. 9.2 we present the case of optical beatnote power as a function of the mirror delay measured in this case with a Schottky diode mixer. In this specific experiment we used an all-in vacuum FTIR except of the Schottky diode mixer which was placed outside in ambient air, see chapter 7, Fig. 7.4 [7]. The results presented in Fig. 9.2 (a) show the optical beatnote power, converted to volts for 50 Ω matching. The mirror is at a fixed position before time 0 s, only vibrating due to the stabilization by a servo loop of the stage. At time 0 s, the mirror starts moving towards the final position, reached after 12.5 s, where the mirror is stabilized again to a fixed position. The signal presented is the peak power at each time slice of a recorded spectrogram around the beatnote frequency. The investigated spectrogram shows that the beatnote changes its frequency

7. The internal optics of this FTIR in this situation consist of a parabolic mirror followed directly by the beam splitter and the two mirror arms. Therefore, the feedback of this specific experiment is increased compared to all other results and different from the setup described in Fig. 9.1.

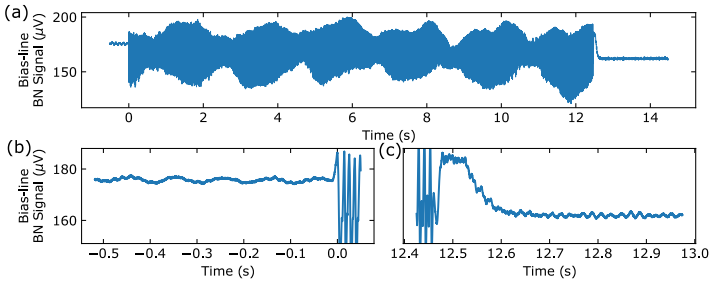

Figure 9.2 – Optical beatnote power dependence on optical feedback. (a) Optical beatnote power as a function of time. The mirror is moving between 0 and 12.5 s (4 mm/s). (b) Zoom on the beatnote power for a quasi-steady mirror position, stabilized by a servo loop. (c) Zoom on the beatnote power for a quasi-steady mirror position, stabilized by a servo loop, after the mirror movement. The final beatnote power is different from the initial one.

on the kHz level as well as amplitude during the scan, but stays narrow on the kHz level during the whole scan [8]. From this experiment we see that the beatnote power is nearly constant for fixed feedback before and after the scan, as shown by the zoom presented in Fig. 9.2 (b) and (c) (see also Ref. [134] for a feedback free setup). We note that the fixed RF power at the end differs from the one at the beginning. The small fluctuations of the beatnote power observed are attributed to temperature fluctuations and slight optical feedback introduced by the mirror servo loop. During the scan the peak power changes as a function of feedback in a periodic fashion. The same is observed for the frequency change of the beatnote (not shown here, compare chapter 6 and 7). Since the beatnote arises from the cumulative sum of the individual mode beatings and their phase relation, either the mode amplitudes or the relative phase relation between modes is altered due to the feedback. Due to the self-mixing effect, the latter might be the more relevant mechanism.

In Fig. 9.3 we employ the SWIFT setup described in Fig. 9.1 and a 4.5 mm long heterogeneous, non-RF optimized mounted THz QCL with a natural beating frequency around 8.8 GHz. The advantage of recording the IQ signal of the reference by the SA is that we store the reference beatnote power and frequency shift by default. This allows to extract the SMIBS spectrum (Fourier Transform (FT) of

8. This is in contrast to the mid-IR where feedback destabilizes the comb, i.e. broadens the beatnote. This is most probably prevented due to the high impedance interface of THz QCLs at the facets.

beatnote frequency change as function of delay) as well as the FT of the beatnote power as function of delay. The results are compared in Fig. 9.3 (a) with the intensity spectrum. The gray shaded signal is a pickup from a vibrating pump also observed below threshold operation. We see that for both cases the spectral components overlap with the intensity spectrum, agreeing with the findings in chapter 7. Interestingly, we see that the modes related to a beatnote frequency change are weighted differently to those related to beatnote amplitude change [9]. Since we record the SWIFT traces, we can compare the SWIFT spectrum to the spectrum product as shown in Fig. 9.3 (b). As we can observe, the spectrum product in black does not fully overlap with the SWIFT spectrum in red, which is also a sign for phase noise respectively self-mixing induced phase change of the neighboring modes. Since the SWIFT spectrum contains the same spectral components as the spectrum product, we can deduce that all modes are equally spaced by the (variable) beatnote frequency but not fully phase-locked [10]. Due to incoherence or phase-noise on each mode, the extraction of the phase difference as well as reconstruction of the temporal intensity profile is omitted. Nevertheless, in general we found that the SWIFT IFG has a minimum at the Zero Path Delay (ZPD) corresponding to a more FM-like output [11].

Here we want to mention that a free running THz QCL was investigated by a dual comb experiment [141] with optically rectified femto-second laser. This situation keeps the feedback fixed and it was observed that the temporal profile and phase relation between modes are drifting only slowly on the minutes scale. It also confirmed the FM nature in that case.

Due to the induced feedback on free running THz QCL combs in these experiments and it's effect on SWIFT measurements we will in the following switch to the RF injected comb state, which fixes f_{rep} but keeps f_{ceo} free running.

9. To our best knowledge there is not yet a theory which precisely predicts these spectra.

10. This means that the modes are not coherently locked over the 30 s measuring time induced by the feedback. On a short scale, they are coherently locked; otherwise there would not be a single, narrow beatnote, but this information cannot be accessed or proofed by SWIFT.

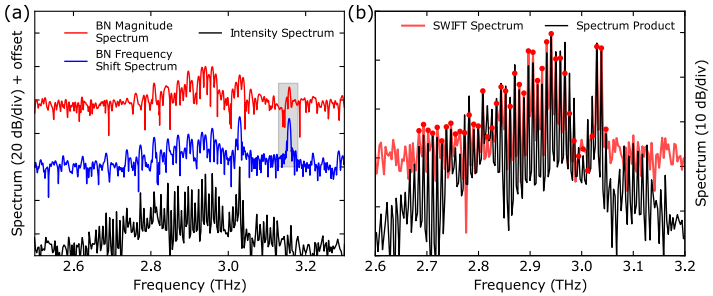

Figure 9.3 – (a) Spectra of SMIBS, i.e. the beatnote frequency shift, the beatnote power change and the intensity. The gray shaded modes are induced by vibrations from a pump. The result shows that the spectral modes in the SMIBS and from the optical beatnote power change spectrum overlap with the intensity spectrum. It also shows that the strong modes are pronounced in the SMIBS where, as from the beatnote power change, we see other modes enhanced. The beatnote frequency is 8.84 GHz and the device is operated at 74 K, 700 mA and 9.31 V. (b) SWIFT spectrum compared to the spectrum product. The coherence in the free running experiment is low as seen from the poor agreement of the mode amplitudes. However, the frequency of the modes overlaps with the spectrum product, indicating equal spacing but also the presence of high phase noise.

9.3 SWIFT data representation layout

In the following, we briefly present in Fig. 9.4 the general layout to represent SWIFT data and the extracted information. Since the shape of the SWIFT IFG around the ZPD provides already information about the AM or FM nature of the comb, we plot the intensity, I, Q and |I-iQ| IFGs in (a) whereas in (b) we show the full IFGs traces. In (c) we plot the spectrum product calculated from the intensity spectrum together with the absolute value of the SWIFT spectrum. Good overlap indicates high coherence. In the same subfigure we plot the f_{ceo}'s for each mode of the intensity spectrum extracted via zero padding. In subfigure (d) we then present the phase differences of neighboring modes obtained from the SWIFT spectrum. In (e) we can finally reconstructed the temporal intensity profile of the comb. If we observe sub-combs, with same f_{rep} but different f_{ceo} 's, we construct the temporal intensity profile for each sub-comb. We note that not the intensities but the electric fields are additive.

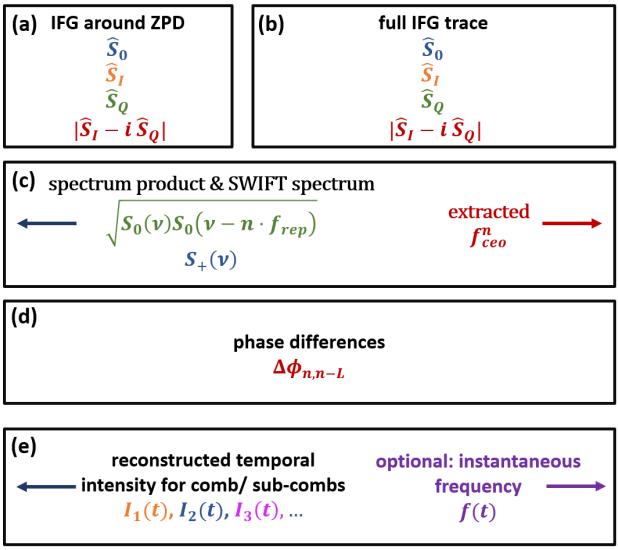

Figure 9.4 – General layout for presenting SWIFTs data. (a) and (b) show the recorded intensity and SWIFT IFGs. (c) contains the spectrum product from the intensity spectrum and the SWIFT spectrum. At the same time, the f_{ceo} for each mode in the intensity spectrum is extracted and presented as a fraction of f_{rep}. (d) shows the phase differences between neighboring modes extracted from the SWIFT spectrum. (e) shows the reconstructed temporal intensity time profile of the comb. If sub-combs are observed, the temporal profile for each sub-comb is presented. We note here that the electric field and not the intensities are additive.

9.4 Weak RF injection: from FM to AM emission

In chapter 4 and 5 we saw that the electrical beatnote can be locked to an RF synthesizer. In both cases it was observed that for certain RF powers, we call them *weak*, the locking can be described by a two oscillator model [54] given by the Adler's Equation with a locking range increasing with the RF injection power. It was also shown that for high enough RF power this locking model, based on weak injection, breaks down, and in addition to stabilizing the repetition rate we start to change the operation state and with it the spectrum, see chapter 4 and 5.

In this section we will investigate the case of weak RF injection of a heterogeneous device based on the same active region (AR) as in Ref. [38] by means of SWIFT where the spectral shape is nearly

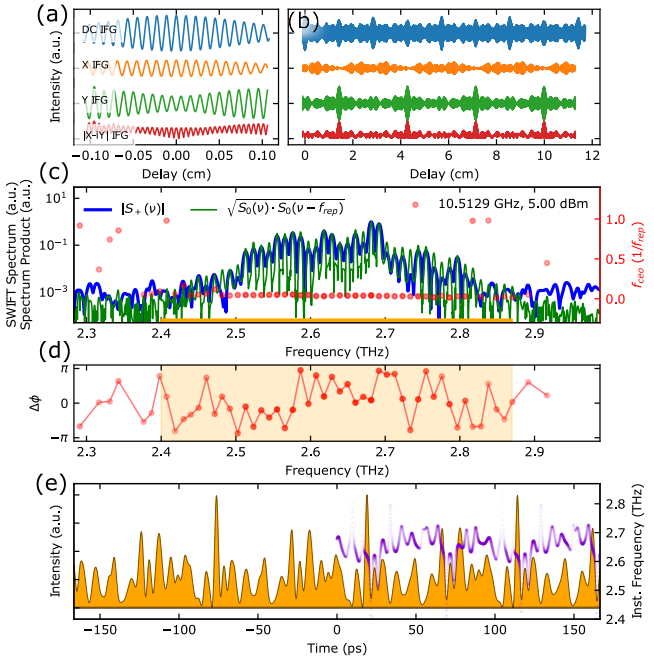

Figure 9.5 – SWIFT data of a 3.8 mm long and 86 µm wide device based on a heterogeneous AR operated at 876 mA, 9.94 V an 43 K heat sink temperature and 5 dBm RF injection power at 10.5129 GHz. (a) Zoom in on ZPD of the recorded IFGs indicating a mixture of FM and AM. (b) Full IFGs showing the preserved periodicity. (c) Comparison of SWIFT spectrum and spectrum product. Slight mismatch could arise from optical filter and insufficient purging. Red dots show the extracted f_{ceo} from the intensity spectrum. The orange bar indicates the spectral region considered for the temporal reconstruction. (d) Extracted phase differences from SWIFT spectrum. Phases are scattered around 2π and are not slowly varying. (e) Reconstructed temporal intensity profile. Clear AM is observed, but no isolated pulses are visible. The purple curve represents the calculated instantaneous frequency weighted by the intensity.

preserved. In the following we will mostly present SWIFT data in the same manner as in Fig. 9.5, as already mentioned in section 9.3.

Fig. 9.5 (a) shows a zoom on the intensity, I, Q and $|I-i\cdot Q|$ IFGs and gives a rough indication of FM or AM present in this device. Fig. 9.5 (b) presents the IFGs over the whole delay range where the symmetry indicates the coherence of a single comb state. In Fig. 9.5 (c) the SWIFT spectrum $|S_+(\nu)|$ is compared to the intensity spectrum product $\sqrt{S_0(\nu)\cdot S_0(\nu-f_{rep})}$ indicating the coherence. In the

same graph, we extract from the intensity spectrum the f_{ceo} for each mode as a fraction of f_{rep} which becomes more relevant in the next sections. Fig. 9.5 (d) shows the phase differences $\Delta\phi = \phi_n - \phi_{n-1}$ of each mode pair where the color is weighted by the mode amplitude $A^{(n)}$. We keep in mind that these phase differences are always modulo 2π. For coherent SWIFT spectra we then plot in Fig. 9.5 (e) the reconstructed temporal intensity profile. Here, the reconstruction uses the f_{ceo}'s extracted from the spectra which are by default not perfectly spaced due to the FTIR even though they are, leading to a slight error in the time profile, i.e. an asymmetry [11]. If relevant, the instantaneous frequency in purple is plotted on the same graph for times large than 0 ps for visibility reasons.

The device here is an RF optimized mounted, 3.8 mm long and 86 µm wide ridge operated at 876 mA, 9.94 V at 43 K heat sink temperature. The natural round trip frequency is around 10.5 GHz and is mounted with a PCB as shown in chapter 2, Fig. 2.15 (c), Fig. 2.16 (b) and (c). The device is injected at 10.5129 GHz with a power of 5.00 dBm at the cryostat input. From Fig. 9.5 (a) and (b) we see that we have FM-like behavior, even though no close to zero minimum is observed, and that the the intensity and $|I - i \cdot Q|$ IFGs preserve the symmetry over the delay range. In Fig. 9.5 (c), we observe partial agreement of the two spectra indicating that the locked modes are not fully coherent at higher frequencies. This is further confirmed in appendix B where we perform SWIFT on the first and second harmonic beatnotes. The phase differences in Fig. 9.5 (d) are scattered over 2π, significantly different to the mid-IR case [88, 138]. By reconstructing the temporal intensity we observe an FM-like behavior with significant AM on top. As a consequence the instantaneous frequency is here significantly different from the findings in mid-IR. i.e. the linear chirp [88].

In Fig. 9.6, the RF frequency is kept the same as in the previous case but the power is increased from 5 to 12 dBm. From the IFGs at the ZPD we observe an increase of the intensity indicating the transition towards AM. The phase differences from 2.4 to roughly 2.7 THz are closely spaced (keeping in mind the 2π modality). Only after 2.7 THz we see modes, spaced by the second harmonic, which seem to differ significantly. The temporal intensity, as expected, shows strong amplitude modulation.

11. The assumption of fixed f_{ceo}'s cannot be shown with the FTIR. Nevertheless, inspection of the low frequency components on the bias line would indicate different f_{ceo}'s by showing different beating signals.

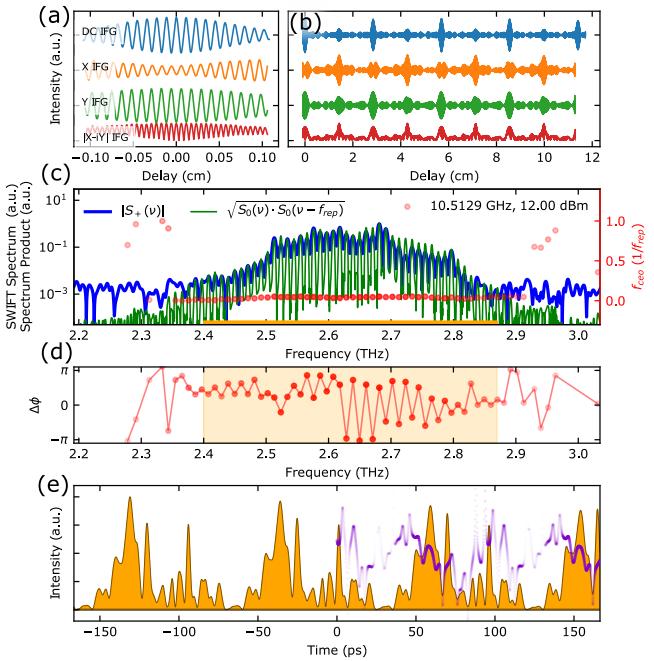

Figure 9.6 – SWIFT data of a 3.8 mm long and 86 µm wide device based on a heterogeneous AR operated at 876 mA, 9.94 V an 43 K heat sink temperature and 12 dBm RF injection power at 10.5129 GHz (compare Fig. 9.5 with 5 dBm). (a) Zoom on ZPD of the recorded IFGs indicates AM. (b) Full IFGs showing the preserved periodicity. (c) Comparison of SWIFT spectrum and spectrum product. Slight mismatch could arise from optical filter and insufficient purging. Red dots show the extracted f_{ceo} from the intensity spectrum. (d) Extracted phase differences from SWIFT spectrum. Phases are less scattered around 2π than before. (e) Reconstructed temporal intensity profile. Clear AM is observed, but no isolated pulses are observed. Purple represents the calculated instantaneous frequency weighted by the intensity.

In Fig. 9.7, the RF power is further increased to 16.00 dBm. A clear AM is identified from the IFGs around the ZPD. Again, the phases differences in this case are closely spaced from 2.4 to 2.7 THz and then start to alternate every mode pair with an indication of a linear trend on every second mode. In the temporal intensity, this leads to a long pulse, which now shows a sign of a linear chirp followed by a second pulse induced by the alternated phase differences.

In conclusion, we saw in this section that the increase of the RF power changes the FM-like output towards an AM-like output. At

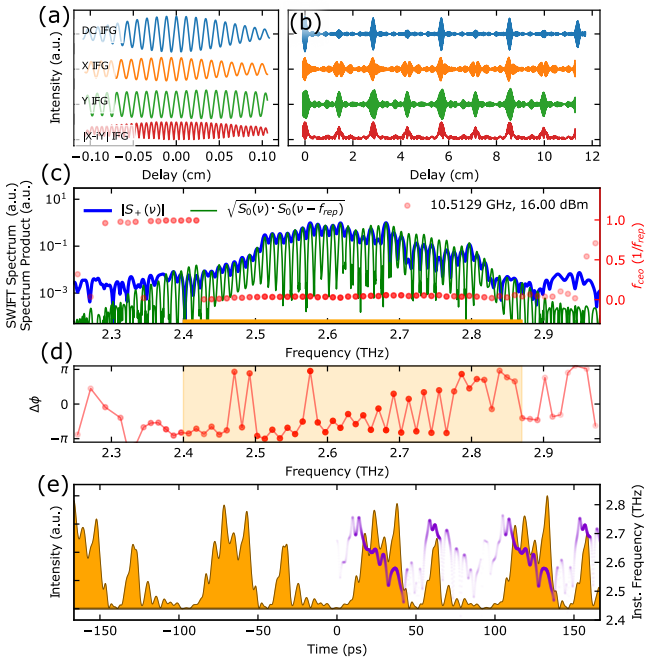

Figure 9.7 – SWIFT data of a 3.8 mm long and 86 µm wide device based on a heterogeneous AR operated at 876 mA, 9.94 V an 43 K heat sink temperature and 16 dBm RF injection power at 10.5129 GHz (compare Fig. 9.5 with 5 dBm and Fig. 9.6 with 12 dBm.). (a) Zoom in on ZPD of the recorded IFGs indicates AM. (b) Full IFGs showing the preserved periodicity. (c) Comparison of SWIFT spectrum and spectrum product. Slight mismatch could arise from optical filters and insufficient purging. Red dots show the extracted f_{ceo} from the intensity spectrum. (d) Extracted phase differences from SWIFT spectrum. (e) Reconstructed temporal intensity profile. Clear AM is observed, but no isolated pulses are observed. Purple represents the calculated instantaneous frequency weighted by the intensity. Here, the resulted instantaneous frequency reminds more to the findings in mid-IR QCLs [88].

the same time, the spectral shape is roughly constant, indicating that for these RF powers the mode amplitudes are kept constant and mainly the phase relation of different mode pairs is changing as one would expect from the weak injection locking theory of a simple oscillator [260]. In the next section, we will now examine the situation where the RF injection power is further increased, leading to significantly different findings.

9.5 From RF injection to RF driving of THz QCLs and sub-comb generation

In the previous chapters 4 and 5, we saw that by increasing the RF injection power we start to shape the spectral output and that the we can inject off-resonantly to excite different modes in the emission spectrum, see Fig. 4.9 (d) and Fig. 5.8 (a). Both devices were mounted on a semi-RF compatible way as shown in Fig. 2.15 (b) and Fig. 2.16 (a). In this section we further improve the RF injection capability by exploiting a PCB, see Fig. 2.15 (c), and using a 35 dB amplifier (saturation at 35 dBm, Mini-Circuits, ZVE-3W-183+). Therefore, the picture of weak injection does not hold anymore. These are now the states we will investigate by means of SWIFT and we will find the generation of sub-combs under this strong RF driving of homogeneous and heterogeneous THz QCLs. We note that sub-comb formation also appears for free running devices, as was actually already observed in chapter 4, Fig. 9.2 (a), but not identified at that point.

Fig. 9.8 shows the evolution of beatnote injection maps for increasing RF power of 4.5 mm long homogeneous device, in this case non-RF optimized mounted. As can be seen, the injection map for low RF powers shows a clear injection locking range, the pulling of the beatnote, and the generation of side modes in the picture of weak injection is preserved for 5 dBm and 10 dBm. By a further increase to 15 dBm and above it becomes evident that we entered a different operating regime. We also observe off-resonant locking, as is evident from Fig. 9.8 (f) at ∼8.4 GHz.

Surprisingly, the recorded intensity IFGs of these strongly RF driven devices show a clear asymmetry in the intensity envelope of the IFGs, which we saw from chapter 3 and chapter 6 should not be the case for a comb state. By investigating the intensity spectrum we find that these strongly RF driven devices tend to emit in sub-combs with the same f_{rep} but different f_{ceo}'s as discussed in more detail in the next paragraph. The observation of sub-combs also explains the asymmetry found in these IFGs.

This is investigated more closely for an other 4.5 mm long and 86 µm wide homogeneous device, which is RF optimized mounted [12] with a fundamental beatnote frequency at roughly 8.8 GHz. Fig. 9.9

12. In the following the "4.5 mm, homogeneous QCL" refers to this device.

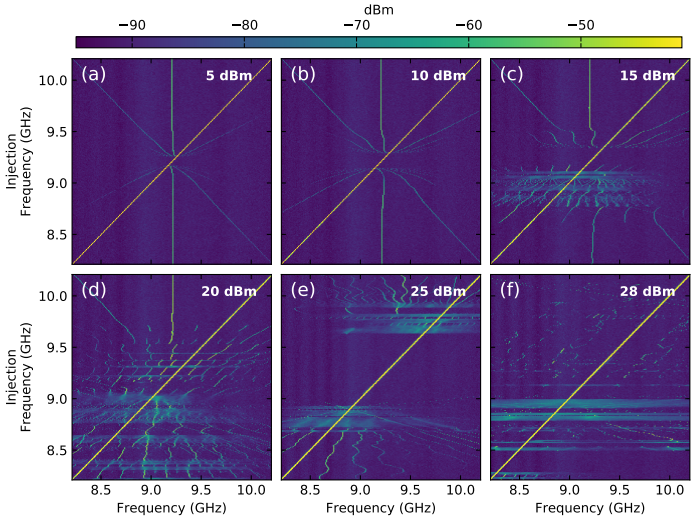

Figure 9.8 – RF injection locking maps of a non-RF optimized mounted 4.5 mm long, 86 µm wide, homogeneous device at 30 K, 552 mA and 10.3 V with a nominal beatnote frequency around 9.2 GHz for increasing RF power from 5 dBm in (a) to 28 dBm in (f). For (c)-(f) the injection deviates from the predicted weak injection theory.

(a) shows the spectra of off-resonant RF driving with 33.8 dBm at 8.373 GHz, more than 400 MHz spaced from the initial fundamental beatnote, for increasing bias voltage. The red dots represent the extracted f_{ceo}'s as a fraction of f_{rep} from the intensity spectrum. We clearly see that for increasing bias we observe sub-comb formation with equal f_{rep} but different f_{ceo}'s. We note that any f_{rep} deviating from the injection frequency on the order of 10 MHz or more would lead to a clear visible linear tilt of the extracted f_{ceo} spacings. The spectrum is also blue shifting as one would expect for increasing bias. We want to highlight here that the spectral components from 3.6 to 4.0 THz were previously only observed in a bi-stable operation point when operated in voltage mode and self-sustained domain formation oscillations occurred, see [143] and chapter 4. Therefore, the high frequency modulation lets the device operate at these higher frequencies which get even the dominant spectral components for increasing bias current which was previously not observed.

Similar behavior is observed when operated in current instead of voltage mode and keeping the bias voltage constant while increas-

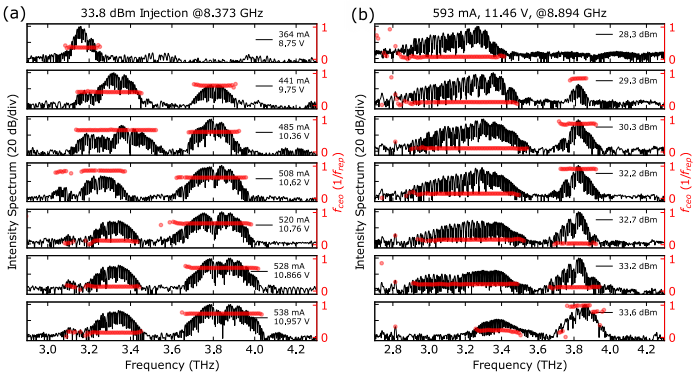

Figure 9.9 – Strong RF injection of an RF optimized mounted 4.5 mm long homogeneous device at 26 K with nominal beatnote frequency at roughly 8.8 GHz. (a) Spectral evolution for fixed RF power and frequency while increasing the bias voltage (operating voltage mode). The injection frequency is roughly 400 MHz below the nominal beatnote frequency. Red dots indicate the extracted f_{ceo} from the intensity spectrum, suggesting sub-comb generation with same f_{rep} but different f_{ceo}. (b) Spectral evolution for a fixed current of the laser while increasing the RF power from 28.3 to 33.6 dBm at roughly the nominal beatnote frequency. The RF frequency is kept constant. Also here, formation of sub-combs is observed.

ing the injection power, see Fig.9.9 (b). This time the injection frequency is chosen to be 8.894 GHz which is roughly the nominal beatnote frequency of the free running device. The injection power is set to 28.3 dBm and is increased to 33.6 dBm. During this ramping up of the RF power we see similar behavior as in Fig. 9.9 (a): the high frequency components around 3.9 THz get excited and an overall blue shift of the spectrum is observed. This can be seen as a change of the operation point on the IV due to the increasing RF power. In appendix B we provide parts of the IVs for various injection powers seeing that the prone photon driven transport of this device is changed, the threshold is lowered and the dynamical range is decreased.

The spectral analysis performed in Fig. 9.9 is very general and relies only on an FTIR and good alignment of the device. Therefore, this provides many useful information to identify a potential comb, sub-comb or high phase noise regime. Additionally, the beating of different sub-combs can be observed on the bias line if the sub-combs overlap. Such examples are shown in the appendix B. But besides the simple approach of analyzing the spectrum and the extracted

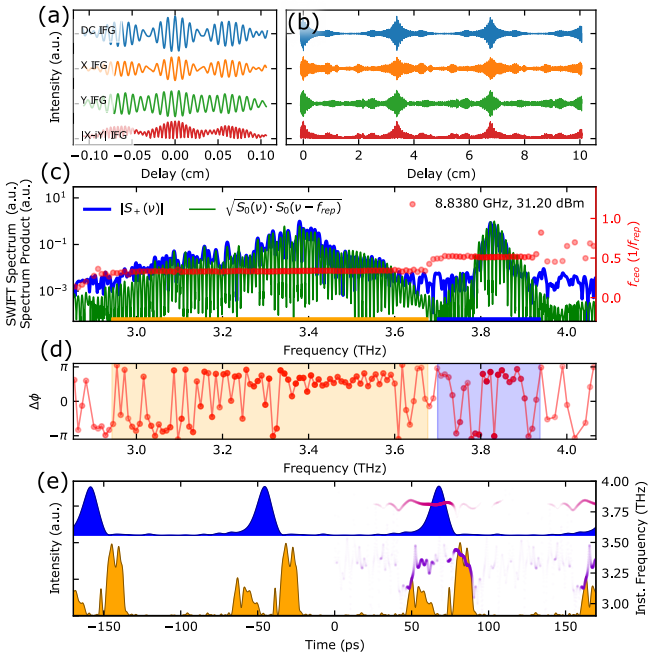

Figure 9.10 – SWIFT data of a 4.5 mm long and 86 µm wide device based on a homogeneous AR operated at 385 mA, 8.48 V, a heat sink temperature of 22.3 K and 31.20 dBm RF injection power at 8.838 GHz, around the nominal beatnote frequency. (a) Zoom on ZPD of the recorded IFGs clearly indicate AM. (b) Full IFGs showing the periodicity seems to be violated. (c) Comparison of SWIFT spectrum and spectrum product. Red dots show the extracted f_{ceo} from the intensity spectrum. It shows the emission in sub-combs which explains the asymmetry in the IFGs. (d) Extracted phase differences from SWIFT spectrum. Phases are less scattered around 2π and only at low frequency components start to scatter. (e) Reconstructed temporal intensity profile for each sub-comb. Clear AM is observed showing pulsed emission of each lobe.

f_{ceo}'s, our fast, superconducting NbN HEB allows us to fully verify the coherence and extract the phase relation between modes by SWIFT.

Fig. 9.10 represents such a SWIFT measurement on the homogeneous 4.5 mm long device. The device is injected at 8.838 GHz with 31.20 dBm at a bias of 385 mA, 8.48 V and a heat sink temperature of 22.3 K. From Fig. 9.10 (a), there is clear evidence of AM and Fig. 9.10 (b) actually presents an asymmetric intensity IFG, hardly visible. By inspecting the spectrum product and the SWIFT

spectrum in Fig. 9.10 (c), we observe a good overlap and the extraction of the f_{ceo}'s reveals a sub-comb nature. From Fig. 9.10 (d) we see the extracted phase differences which are closely spaced for the high frequency sub-comb and actually for the higher frequency part, i.e. 3.3 to 3.7 THz, of the lower frequency sub-comb [13]. From 3.17 to 3.3 THz there are some larger changes in the phase differences, while below 3.17 THz the phase differences are again closely spaced. The closely spaced phase differences, i.e. similar group delays, is reflected in the temporal intensity profile of the pulsed emission as can be seen in Fig. 9.10 (e). Reconstruction of the temporal intensity is done for each sub-comb separately since the arbitrary phase difference at the transition of two sub-combs cannot be measured by SWIFT. It reveals also the pulsed nature of each sub-comb. The sub-combs seem to be located at the two lasing regions which were also observed in chapter 4 under voltage operation.

The previous analysis was performed on a homogeneous stack. The same behavior under strong RF modulation is also observed in the heterogeneous device investigated before under weak injection in section 9.4. Fig. 9.11 shows the SWIFT results. We again observe a strong indication of AM from the IFG around the ZPD. Inspecting the full IFGs in Fig. 9.11 (b), we see clearly the dephasing due to multiple sub-combs. At the same time all sub-combs are roughly in-phase again around 11.3 cm delay. Comparing the spectrum product with the SWIFT spectrum, we observe slight deviation of low amplitude modes from the SWIFT spectrum, which is most probably induced by the nonlinearity of the detector gain. At the same time the emission groups into three sub-combs clearly visible from the f_{ceo} analysis. The spectral sub-comb regions do quite well overlap with the underlying spectral regions of the stacks in this device [38] and is currently under investigation. As is shown in the appendix B, groups of different f_{ceo} can produce a coherent beating signal defined by the difference of sub-comb f_{ceo}'s. This beating of sub-combs can potentially be locked which is under current investigation.

By further looking at the phase differences and the temporal intensity profile of each sub-comb we observe clear sign of pulsed output. Due to the different f_{ceo}'s there is an unknown phase difference, and the pulses can be shifted relatively to each other in a well-defined way. As a matter of fact, we remind the reader that

13. Remember the 2π modality and that the phase difference is directly linked to the group delay $\tau_g \approx \Delta\phi/\Delta\omega$. Therefore closely spaced phase differences indicates similar group delay.

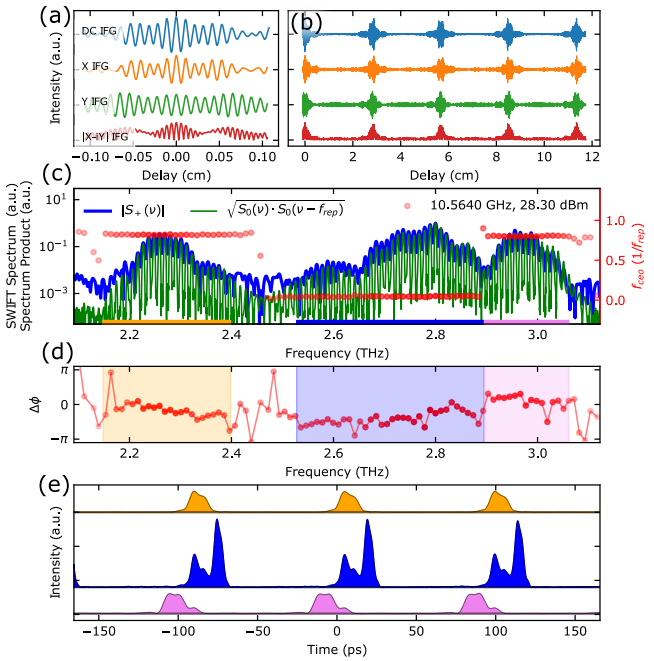

Figure 9.11 – SWIFT data of a 3.8 mm long and 86 µm wide device based on a heterogeneous AR operated at 780 mA, 9.65 V, a heat sink temperature of 42 K and 28.30 dBm RF injection power at 10.564 GHz around the nominal beatnote frequency. (a) Zoom on ZPD of the recorded IFGs clearly indicate AM. (b) Full IFGs showing the periodicity seems to be violated. (c) Comparison of SWIFT spectrum and spectrum product showing a good agreement of the coherence. Red dots show the extracted f_{ceo} from the intensity spectrum. It shows the emission of three sub-combs which explains the asymmetry in the IFGs. The sub-combs seem to spectrally overlap with each stack gain [38] of this device. (d) Extracted phase differences from SWIFT spectrum. Phases are densely spaced for each sub-comb. (e) Reconstructed temporal intensity profile for each sub-comb. Clear AM is observed showing pulsed emission of each lobe.

the total intensity is of course not the sum of the individual intensity profiles but of the underlying electrical fields. This again shows the limitations of SWIFT but also its strength: it allows spectrally resolved and local coherence measurements and does not rely on a fully coherent comb source.

By now we saw that we can RF drive THz QCLs and generate sub-comb with mode spacings defined by the injection frequency. In the next section we will now see to which extent one can vary

the RF modulation frequency and still observe coherent comb and sub-comb generation.

9.6 Off-resonant RF driving

In Fig. 9.9 we already observed that off-resonant RF modulation tends to define the mode spacing in the emission spectrum. When sweeping the RF frequency over a large range and observing through an RF circulator configuration the low frequency components (< 4 GHz), one finds that for certain injection frequencies the low frequency noise and beatings vanish [14]. This indicates that at these points the RF modulation defines the mode separation. This is also observed before on a relative large span as shown in Fig. 9.8 (f). By sweeping the frequency over even lower values [15] such indication of locking is also observed due to vanishing beating signals and high-phase noise on the low frequency region on the bias line.

Such a case is reached for the 4.5 mm long homogeneous devices when the RF frequency is tuned to 7.221 GHz, roughly 1.6 GHz lower than the fundamental free running beatnote. The corresponding SWIFT measurement is presented in Fig. 9.12. We observe AM and single, coherent comb emission. Most of the phase differences are closely spaced with some spacial mode pairs around 3.21 and 3.25 THz which seem to be at the connection point of smaller mode groups. Again, the reconstructed temporal profile confirms the AM produced by this off-resonant RF driving.

By comparing with the calculated group indexes from chapter 2 for the TM_{00}, TM_{01} and TM_{02} we would expect all of these modes to have a spacing larger than 8 GHz [16], significantly higher than observed here. Therefore, comb formation by lasing on the TM_{00} mode or purely on any higher oder mode does not explain the observations. The explanation could be that for such long devices the quality factor of the Fabry-Pérot modes decreases, as shown in Fig. 2.12 (c). Together with the higher order modes this would lead to a spectrally flattened cavity mode response. Due to the similar

14. This regions can be relatively narrow band, i.e. up to 1 MHz, and indicate locking of the modes.

15. This is expected from lasing of higher order modes which have a larger group index n_g as discussed in section 2.

16. $\Delta\nu = \frac{c}{2 \cdot 4.5mm \cdot n_g}$ with $n_{g,max} = 4.1$

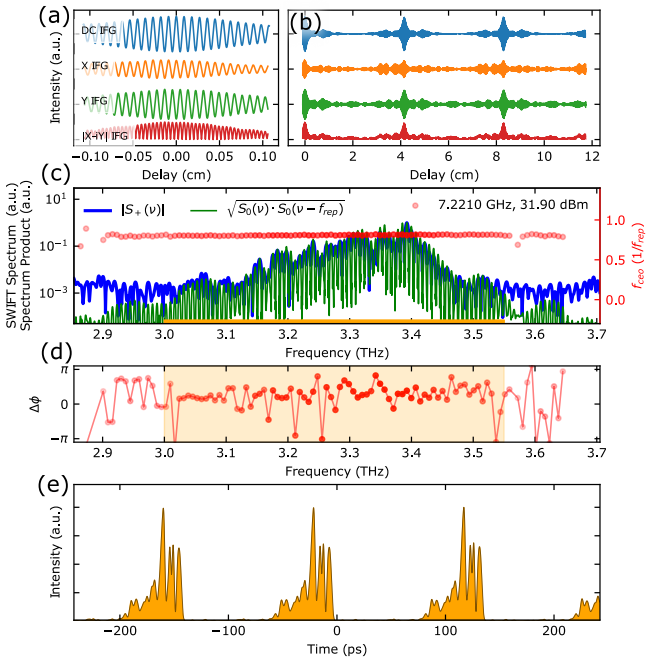

Figure 9.12 – SWIFT data of a 4.5 mm long and 86 µm wide device based on a homogeneous AR operated at 385 mA, 8.48 V, a heat sink temperature of 25.4 K and 31.90 dBm RF injection power at 7.221 GHz whereas the nominal free running beatnote frequency is around 8.8 GHz. (a) Zoom on ZPD of the recorded IFGs clearly indicate AM. (b) Full IFGs showing the periodicity. (c) Comparison of SWIFT spectrum and spectrum product. Red dots show the extracted f_{ceo} from the intensity spectrum. Single comb operation is observed here. (d) Extracted phase differences from SWIFT spectrum. Phases are densely spaced and only for transitions of subgroups of modes there seems to be a significant phase difference change. (e) Reconstructed temporal intensity profile of the comb. Clear AM is observed showing pulsed emission.

locking behavior in the optical domain, the optical locking range between neighboring modes should also depend on first order inversely on the cavity mode quality factor [54] given by $\Delta\omega_{lock} \approx \frac{2\omega_0}{Q_{cold}}\sqrt{\frac{I_{sm}}{I_m}}$ with I_{sm} the induced side mode intensity and I_m the mode intensity. In the case of strong RF modulation, instead of locking existing cavity modes, one seems to simply generate the seeded modes. This qualitative picture suggests that strong RF injection increases the side mode generation and due to the low Q-factor, and most probably the existence of higher order modes, allows the coherent locking

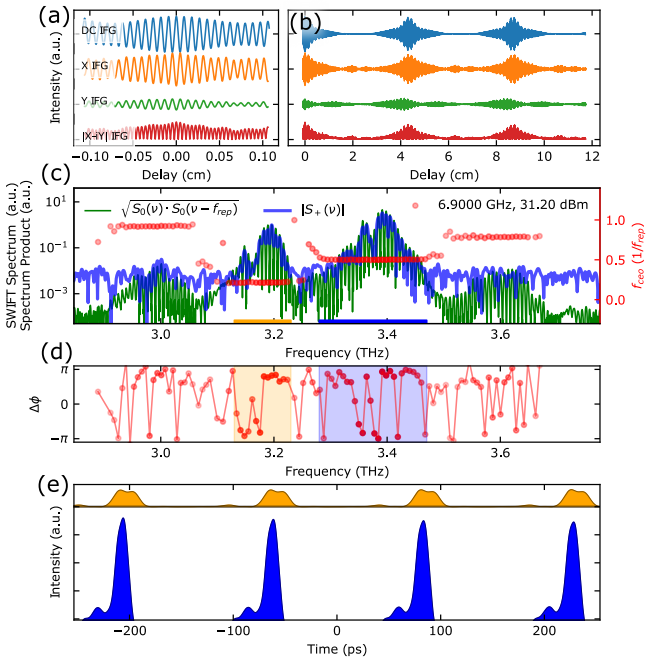

Figure 9.13 – SWIFT data of a 4.5 mm long and 86 µm wide device based on a homogeneous AR operated at 385 mA, 8.48 V, a heat sink temperature of 24.3 K and 31.20 dBm RF injection power at 6.9 GHz. The nominal beatnote frequency is around 8.8 GHz. (a) Zoom on ZPD of the recorded IFGs clearly indicate AM. (b) Full IFGs of the SWIFT traces. (c) Comparison of SWIFT spectrum and spectrum product. Red dots show the extracted f_{ceo} from the intensity spectrum. Sub-comb operation is observed here. (d) Extracted phase differences from SWIFT spectrum. Phases are strongly varying in the interval from $-\pi$ to π. (e) Reconstructed temporal intensity profile of each sub-comb. Clear AM of each sub-comb is observed showing pulsed emission.

of all modes.

Switching back to the heterogeneous device, we also observed locking of the modes to far off-resonant modulation frequencies. One result for 6.9 GHz modulation is presented in Fig. 9.13. Here we observe again the generation of sub-combs which are AM. The sub-combs seem to overlap with the underlying stack gains which seem to define the different f_{ceo}'s.

The found results might indicate that nearly all strongly injected devices will produce coherent combs or sub-combs. This is also in-

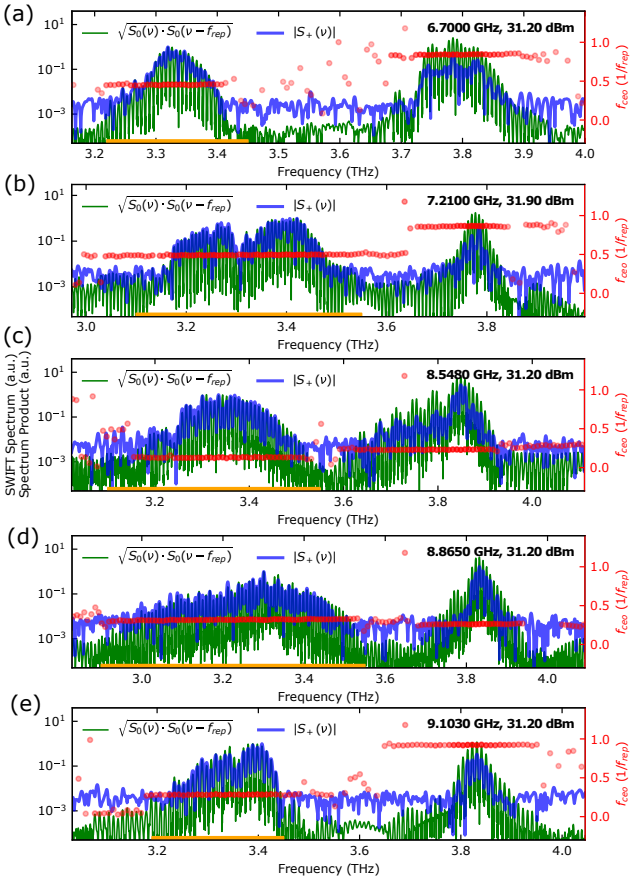

Figure 9.14 – Strong RF modulation on various RF frequencies from (a) to (e) of the 4.5 mm long homogeneous device. All spectra indicate that the modes are equally spaced but that the higher frequency lobes suffer from high-phase noise leading to a decrease in the coherence.

dicated by spectral modes and their extracted mode spacing from standard FTIR measurements, which seem to be coherently locked. But actually not all of these states lead to coherent comb or sub-comb emission. In the following we present only the spectrum product compared to the SWIFT spectrum together with the extracted f_{ceo}'s in Fig. 9.14 [17]. The 4.5 mm long homogeneous device is injected from 6.7 GHz up to 9.1 GHz and shows in the low frequency

17. All coherent modes show AM output.

spectrum lobe the coherence of the modes whereas in the high frequency lobe the modes seem to be equidistant spaced but suffer from phase noise. This shows that strong RF injection does not by default lead to coherent locking of all modes.

9.7 Harmonic comb RF injection

In chapter 6 we investigated the formation of harmonic frequency combs and showed by means of SMIBS that the modes are equally spaced. It was also shown that these harmonic states can be locked to an external RF oscillator. In this section we now confirm the coherence of a harmonic comb emitted by the heterogeneous, 3.8 mm long device under mild RF injection. The device naturally operates on the second harmonic comb state at 804 mA, 9.70 V and 28.3 K heat sink temperature. The device is injection locked with 9 dBm RF power at the harmonic frequency at 21.0033 GHz. The corresponding results are shown in Fig. 9.15. From the IFGs clear evidence of FM-like behavior is observed for this harmonic comb state. At the same time, we see that the periodicity of the IFGs is preserved. At lower injection powers, it was observed that the I and Q traces are slowly varying over the 30 s acquisition time which indicates an non-equidistant mode spacing on the mHz level. This is also slightly indicated in the SWIFT spectrum in Fig. 9.15 (c) at 2.85 THz for a single weak mode which is slightly shifted to higher frequencies. There are even more modes close to the noise floor, which may not be equidistantly spaced. Since these shifts are only a few GHz this corresponds to an f_{rep} difference of some mHz. The phase differences are scattered over 2π which supports the FM-nature and is reflected in the temporal intensity profile as well. At higher injection power, it is observed that the I and Q traces are unstable, showing that increasing RF power is not supported by this harmonic comb state.

9.8 Particularities

In chapter 8 we saw that even slight differences from equidistant mode spacing would shift the SWIFT spectrum multiple GHz in the frequency domain. Therefore, neighboring modes in the SWIFT spectrum should share the same f_{ceo}. At the same time, it is observed that the extracted f_{ceo} from the spectrum can show a linear

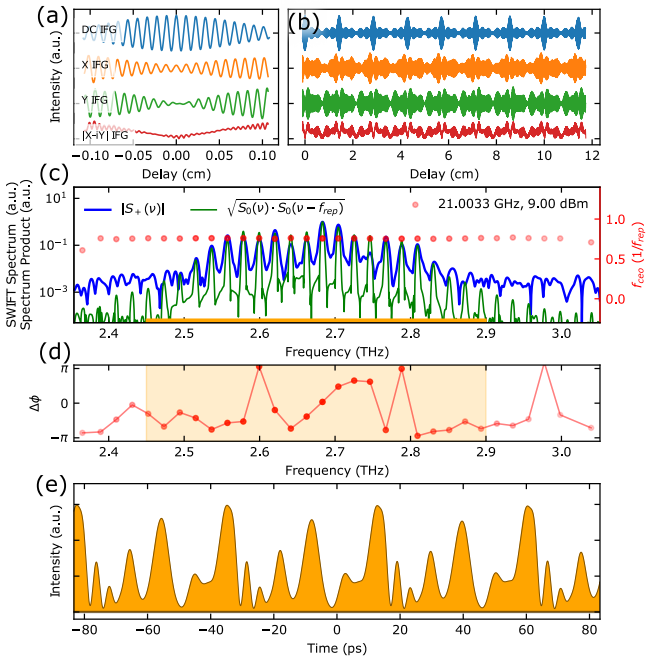

Figure 9.15 – SWIFT data of a 3.8 mm long and 86 µm wide device based on a heterogeneous AR operated at 804 mA, 9.70 V, a heat sink temperature of 28.3 K in the harmonic comb state and 9.0 dBm RF injection power at 21.0033 GHz. (a) Zoom in on ZPD of the recorded IFGs clearly indicates FM. (b) Full IFGs showing the periodicity of the IFGs. (c) Comparison of SWIFT spectrum and spectrum product showing high spectral coherence. Only at the the high frequency side there is a slight shift of a SWIFT mode which could indicate a mHz difference from the injection frequency. Red dots show the extracted f_{ceo} from the intensity spectrum. (d) Extracted phase differences from SWIFT spectrum. Phases are scattered over 2π, and there is a linear trend around the comb center. (e) Reconstructed temporal intensity profile for the harmonic comb. The FM nature is overlapped with significant additional AM of the intensity.

drift for certain injection powers and frequencies, even though the SWIFT spectrum suggests differently. This is shown as an example for the heterogeneous 3.8 mm long device in Fig. 9.16. The modes located at 2.3 THz show the expected constant f_{ceo} whereas in the spectral region from 2.5 to 3.0 THz the f_{ceo}'s drift by roughly 100 MHz per mode pair.

The observed situation is currently under investigation, but there

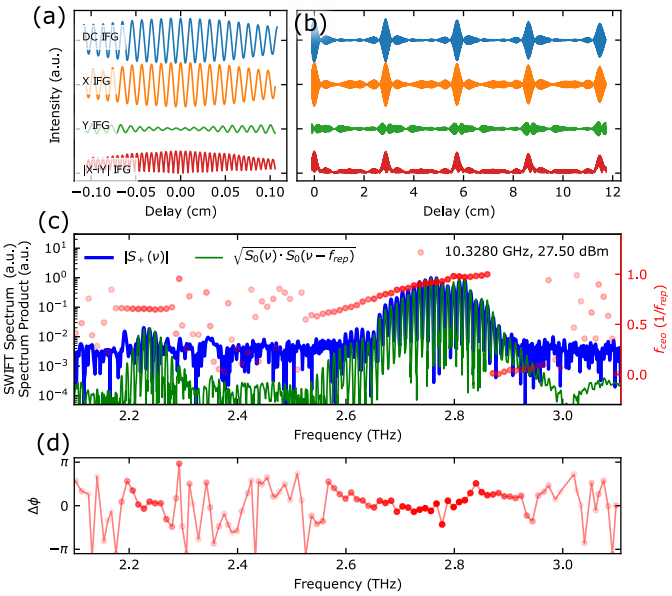

Figure 9.16 – SWIFT data of a 3.8 mm long and 86 µm wide device based on a heterogeneous AR operated at 780 mA, 9.80 V, a heat sink temperature of 42.0 K and 27.50 dBm RF injection power at 10.3280 GHz. (a) Zoom in on ZPD of the recorded IFGs clearly indicates AM. (b) Full IFGs showing the periodicity is not preserved and that the IFGs dephase. (c) Comparison of SWIFT spectrum and spectrum product exemplifies the high mutual coherence among comb lines. Red dots show the extracted f_{ceo} from the intensity spectrum. The observed drift would explain the asymmetry and dephasing of the IFGs but this would imply that the SWIFT should be sifted significantly in frequency. It might be induced by the high NA optics used in the FTIR. (d) Extracted phase differences from the SWIFT spectrum. Phases are densely spaced.

are indications that the high NA optics as well as higher order transverse modes together with the diverging QCL far field could lead to frequency errors on the measured intensity modes.

Finally, other states are observed when strongly modulating RF, which are not presented in this chapter but are in the Appendix B.

9.9 Conclusion

In this final chapter we exploited SWIFT to investigate the coherence and phase relation of free running and RF injected THz

QCLs. It was first shown that the previous results from SMIBS, showing equidistant mode spacing, are confirmed by SWIFT. At the same time, it was shown that the coherence of this free running device is reduced, which is expected from self-mixing effects induced by optical feedback.

By switching to weak RF injection we observed that the investigated heterogeneous THz QCL operates in a quasi-CW emission state with significant AM. The optical mode phase differences found differ significantly from the linear phase difference change found in mid-IR QCLs. By increasing the RF power the AM increased and signs of a linear chirp were observed.

By further increasing the RF power we saw that the weak injection theory does not hold anymore and that the locking behavior changes drastically. From standard FTIR measurements we could extract the f_{ceo}'s of each mode which indicate the formation of sub-comb with f_{rep} defined by the RF injection but different f_{ceo}'s for each sub-comb. The coherence of each sub-comb is then confirmed by SWIFT. These results are observed in both homogeneous and heterogeneous broadband THz QCLs.

It was further observed that far off-resonant injection, over 25% below the nominal cavity round trip frequency, can still lead to formation of coherent combs or sub-combs. At the same time not all RF modulation frequencies lead to fully coherent spectra.

Due to the fast HEB it was also possible to investigate the coherence of a weak injection locked harmonic comb state for the first time. FM-like emission with a significant AM contribution was observed. Increasing the RF injection power disturbed the harmonic comb state.

We also saw some particularities arising from the intensity spectrum analysis of f_{ceo}. Although the SWIFT spectrum shows the emission of coherent mode pairs, the extracted f_{ceo}'s suggested differently. This observation are most probably arising from the high NA optics and the diverging far field of THz QCLs, but are still under investigation.

As a final remark we highlight that SWIFT is the only measurement technique of all presented in chapter 8 that allows clear spectral verification of sub-comb formation, measures their phase relation and works also in the presence of incoherent spectral components.

10

Conclusion and perspectives

This thesis covered several aspects of broadband THz emission in QCLs with the main focus on frequency comb generation. We briefly saw different types of THz sources of which the QCL enables coherent, optoelectronic light emission above 1.5 THz from a compact semiconductor source with mW output power. In addition, the working principle of a QCL was described. Due to the focus on frequency combs, we defined mathematically the frequency comb and gave a historical review of frequency comb generation by mode-locked lasers and how it led to the Nobel Prize. Further, we went to the main findings and developments towards frequency comb generation in QCLs, both in the THz and mid-IR region.

In chapter 2, the general designs for QCL ARs and their growth and simulation were briefly discussed. It was followed by an detailed analysis of the double-metal waveguide which was exploited in this thesis for broadband THz emission. We saw the influence of the group velocity dispersion (GVD) on the cold cavity modes, the implementation of side absorbers and their effect on the losses and the cavity mode responses of the fundamental and higher order transverse modes. Due to the importance of RF signal extraction and injection of our devices, we analyzed and optimized our laser mounting and cryostat to increase the RF compatibility.

The standard tool to analyze the spectral content of a THz QCL is an FTIR measurement. In our opinion, it is an underestimated technique for pre-evaluating the lasing emission. We therefore showed in chapter 3 how correct data treatment allows to verify the equally spaced mode nature down to the MHz level of free running frequency comb devices. It also allowed immediately to distinguish multi-mode operation from potential comb operation. Together with the electrically detected beatnote on the bias line, this indicated already the comb coherence.

In chapter 4, we investigated the broadband emission from a homogeneous QCL device with a bandwidth of over 1.8 THz in a bi-stables regime which came with the advantage of lower threshold current compared to their heterogeneous counterparts. The bi-stable regime was further investigated experimentally and theoretically, and the results indicated domain formation inside the structure, leading to stable self-pulsation of the device. We then showed RF injection of such a laser in the stable bias regime and the influence of increased RF power on the emission state.

By fabricating lower loss Cu–Cu devices, compared to the previous Au–Au devices, we showed in chapter 5 that the performance of a homogeneous QCL is increased and extended to temperatures above 77 K. The temperature dependent multi-mode and frequency comb generation was qualitatively covered by the analysis from chapter 2 and we showed that by strong RF modulation the spectral emission is significantly broadened up to 700 GHz at a heat sink temperature of 80 K. Therefore, this chapter showed a significant improvement in THz frequency comb generation towards higher temperatures and lower threshold currents.

Chapter 6 covered the special situation in which THz QCLs naturally and self-starting operated in a pure harmonic comb state. We showed that these harmonic combs were observed in various devices and by means of SMIBS showed the equally spaced mode nature of such a harmonic comb state. As one could expect, we showed that a harmonic comb state can also be injection locked to an external RF synthesizer. To theoretically explain the pure harmonic comb formation in these devices, we provided a single-mode instability analysis based on a Maxwell-Bloch approach including two optical transition with different dipole moments. The predicated parametric net gain for two unbalanced transitions induces a net loss close to the single mode, explaining the pure nature of the harmonic comb, whereas for further detuning, a net gain at roughly the harmonic comb spacing was predicted. The found model also explained the differences in observed harmonic combs at mid-IR and THz QCLs.

In chapter 7, we briefly analyzed a QCL which emits two frequency combs, spaced by one octave, in the same monolithic device in pulsed operation. The two electrically detected beatnote frequencies of each comb reflect the enormous effect of GVD in GaAs-based THz QCLs which led to two narrow beatnotes spaced by more than 1.6 GHz. By exploiting the SMIBS technique as well the IBS, by em-

ploying a Schottky diode mixer, we showed the equidistant spacing of each comb and the spectral origin of both beatnotes.

The two techniques used in chapter 7 allowed to show equally spacing of the comb modes but only a narrow beatnote indicated the fully coherence of these states. We therefore briefly summarized common frequency comb characterization techniques in chapter 8 with a detailed description of SWIFT.

In the final chapter 9, we performed SWIFT measurements on several THz QCL states by exploiting a fast, antenna coupled, superconducting NbN HEB. The investigated devices were a homogeneous THz QCL, based on the same AR examined in chapter 4, 5 and 6, and an octave-spanning heterogeneous THz QCL based on the AR presented in Ref. [38]. The results of free running devices showed that the FTIR induced feedback reduces the coherence, but at the same time showed the equally spaced mode nature of the comb. Due to the interest and strength of fully coherent comb states we switched to RF injection locked devices. The results showed that for weak injection, the investigated heterogeneous THz QCL emits in an FM state but, contrary to mid-IR QCLs, did not show a linear chirp. For increasing RF power, we observed that the FM state changes toward an AM state with indication of a linear chirp. At the same time we saw that increased RF power leads to significant deviations from the weak injection locking theory as could be observed in the beatnote injection locking map and in the observed spectral modes. Interestingly, we observed the formation of sub-combs with same f_{rep} but different f_{ceo}'s, already indicated by FTIR measurements, which were then investigated by means of SWIFT. The SWIFT results showed that the coherence of each sub-comb. Further, this sub-comb formation was observed for resonant and far off-resonant, i.e. multiple GHz, RF modulation from the nominal repetition frequency in both the heterogeneous and homogeneous device. At the same time, all strongly RF modulated devices showed AM emission of each sub-comb, also both in heterogeneous and homogeneous devices. Even though RF injection and coherent sub-comb formation were observed for various injection frequencies, we also showed that strong RF modulation can lead to incoherent spectral content.

The experimental results in this thesis indicated the possibilities of THz frequency combs towards octave-spanning comb formation and potential integration of self-referencing techniques in QCLs. The promising approach of strong RF modulation showed that it al-

lows generation of equally spaced modes but in spectral mode groups with different f_{ceo}'s. Therefore, future work needs to address passive dispersion compensation [17, 142] and fabrication of low GVD cavities. At the same time, the influence of weak RF modulation was already investigated in mid-IR QCLs [261, 262] and appears to be closely related to the linewidth enhancement factor [263] and therefore the susceptibility. Therefore, further experimental SWIFT measurements on weak and strong RF modulated THz QCLs could reveal how the linewidth enhancement influences the comb formation. Thus, I believe that further developments will eventually lead to octave-spanning comb operation in THz QCLs.

A

Hot Electron Bolometer

In chapter 9 we used a fast, antenna-coupled NbN HEB to perform our SWIFT measurements. The general working principles of a HEB are well described for example in Ref. [255] and [254]. Here we want to point out, that it was found that the impedance of a HEB is changing as a function of bias current and detected IF frequency [255]. The HEB used in this thesis was designed and fabricated by Sara Cibella and co-workers from *Istituto di Fotonica e Nanotecnologie - CNR* in Rome. Further, here we focus on the implementation and RF performance of your specific HEB. Fig. A.1 (a) shows an scanning electron microscopy (SEM) image of the spiral antenna employed in our setup and the inset shows the HEB micro bridge. In Fig. A.1 (b) we plot the VI characteristic of the HEB as a function of heat sink temperature in our setup [1]. Fig. A.1 (c) shows a image of a mounted detector chip featuring multiple detectors. One of the detectors is wire bonded to a grounded coplanar waveguide (GCPW) whereas the image shows the prototype with a microstrip. The final version connected the middle detector and consisted of multiple short and straight wire bonds and the carrier chip was located closer to the GCPW to increase the RF performance. Fig. A.1 (d) shows the electrical connections to the detector. It was operated in current mode and passed additionally through a 20 kΩ resistor, a 1 kΩ resistor for additional current readout and a lowpass filter at room temperature. Further, a bias-tee was connected at the cryostat input to decouple the DC from the RF signal. The voltage drop over the HEB is optionally read at the bias-tee. The next generation will implement a lowpass filter and the RF decoupling directly on the cryostat to reduce Johnson noise.

1. The VI depends also on the THz power collected by the detector. Here, the THz power was on the tens ofμW level.

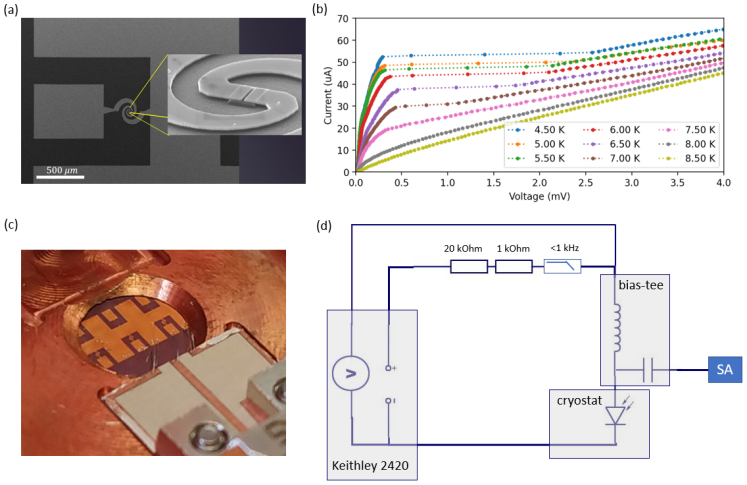

Figure A.1 – HEB. (a) SEM picture of the antenna-coupled HEB. (b) Measured VI curve of the HEB at varies temperatures showing the superconducting transition. Offset in voltage is due to the measurement setup. (c) Image of mounted HEB with first RF compatible mounting approach. (d) Biasing schema and signal extraction.

The HEB is inherently broadband and therefore the superconducting transition can be suppressed due to higher wavelength blackbody radiation. This problem is solved by placing a lowpass THz filter at the cryo shield in the cryostat. An image of the filter is shown in Fig. A.2 (a). We measured the transmission in a THz Time-Domain Spectroscopy (THz-TDS) setup (Menlo®, TeraSmart, ∼ 30μW THz power) and the result is shown in Fig. A.2 (b). The filter shows a high transmission in the THz with a slight etalon effect. Signal above 3.5 THz suffers from a low SNR of the THz-TDS setup at these frequencies. In the SWIFT experiment the filter is bent around the cylindrical cryo shield and the 2 inch THz beam is focused behind the filter. We therefore expect the etalon effects to average out in the real setup leading to a rather flat filter response.

In the FTIR setup we align the HEB to an above 50 kHz pulsed operating THz QCL due to the bias-tee cutoff frequency. In this configuration one can record a short IFG around the ZPD which corresponds to the intensity spectrum. We can tune the HEB into a bias regime where the recorded IFG shows its expected shape indicating a roughly linear operating bias point. One finds also bias regions with higher detector gain but the recorded IFGs around the

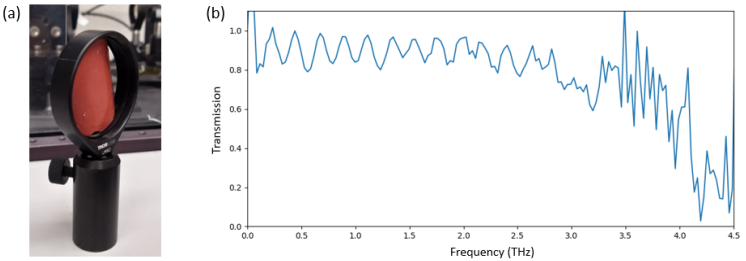

Figure A.2 – Cold filter to suppress higher wavelength light on the HEB. (a) Picture of lowpass THz filter, (d) Transmission measurement from a THz-TDS setup. The TDS bandwidth is limited to roughly 3.5 THz.

ZPD show a very nonlinear behavior. Additionally, the temperature can be tuned as well to find an optimal operating point, which does as well depend on the QCL light intensity. After alignment, the QCL can be switched into a continuous wave (CW) comb state and the beating signal can be observed.

To have an idea of the RF response of the detector, we place the THz-TDS emitter at the output of the FTIR and align the signal onto the detector, while having the QCL switched off. The THz-TDS system has a repetition rate of 100 MHz and produces all higher order harmonics on the detector. By measuring the peaks of all harmonics, we can extract frequency response function of the system. Such results are shown in Fig. A.3 and Fig. A.4 together with the VI curve at 4.5 K and 7.4 K, respectively. The frequency response functions are corrected by the S-parameters of RF cabling and PCB. From Fig. A.3 (b) we see that the frequency response at 4.5 K, normalized to the highest response for this temperature, is significantly higher close to the breaking of the superconducting transition in the IV. The peak detector signal at 100 MHz is -60 dBm. The 3 dB bandwidth is larger for very low current bias but comes with a reduced detector gain. Since we are mainly interested in a single frequency, i.e. the beatnote, we would like to increase the detector signal as much as possible which is highest for 45 μA bias current at 10 GHz. At the same time these measurements do not reveal any information about the linearity of the detector. Experimentally, detector bias points with high detector gains show a nonlinear intensity interferogram for a MHz pulsed QCL as already mentioned before. We tune the detector bias in a region where the intensity interferogram fulfills the expected symmetry properties ex-

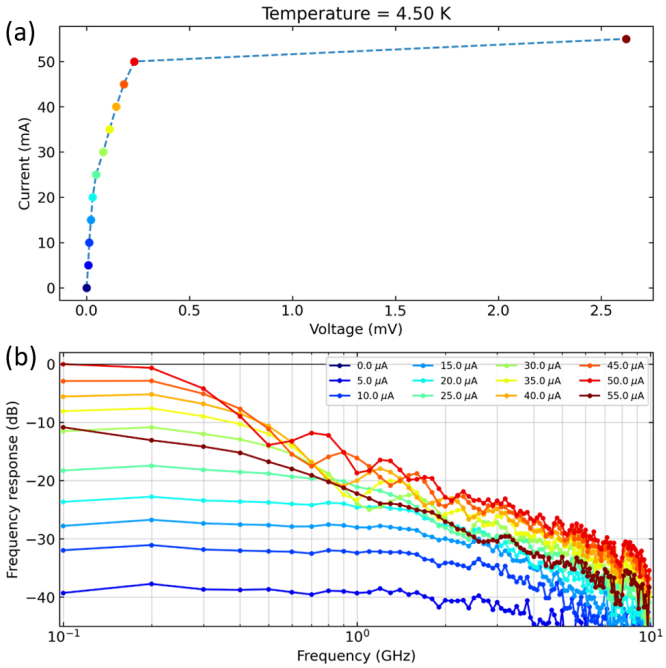

Figure A.3 – HEB response measured in a THz TDS experiment. (a) VI curve at 4.5 K. The colored triangular markers represent the different measured bias points of (b). (b) Response of HEB at different bias. Response is corrected for cryostat cable and the PCB, and normalized to the highest detector gain for constant temperature.

pected for a linear response.

Fig. A.4 shows the IV and frequency response at 7.5 K. We clearly see that the frequency response functions have an over all lower bandwidth. At the same time, the peak signal at 100 MHz is -67 dBm, roughly 7 dB lower than at 4.5 K. The response curve above 3 GHz at 2 µA bias resembles the noise floor of the detector. Therefore, we prefer to work at lower temperatures to increase the overall detector gain at all frequencies.

As we will see in appendix B, this HEB allows to record SWIFT traces at a beatnote frequency above 30 GHz due to the significantly higher output power of QCLs compared to the THz-TDS system.

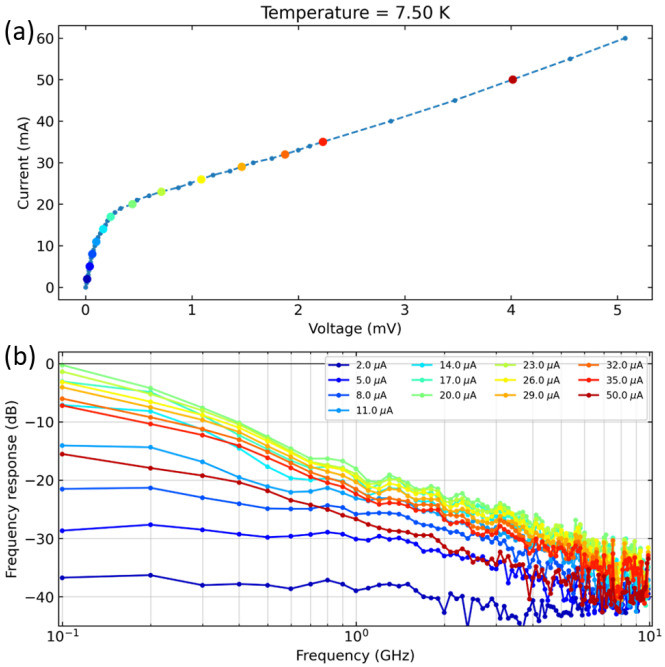

Figure A.4 – HEB response measured in a THz TDS experiment. (a) VI curve at 7.5 K. The colored triangular markers represent the different measured bias points of (b). (b) Response of HEB at different bias. Response is corrected for cryostat cable and the PCB, and normalized to the highest detector gain for constant temperature.

B

Additional strong injection and SWIFT results

B.1 RF induced LIV change

We saw that for increasing RF injection power of THz QCLs the injection locking map start to differ from the weak injection theory. This is a consequence of the RF power significantly modulating the device on its IV curve. Therefore, we call it RF driving or modulation of a QCL and not injection locking anymore. To see the influence of the injected RF signal, power measured at the cryostat input, we show in Fig. B.1 (a) a portion of the IV curve for different RF powers. The IV is recored by the Keithley, which has an additional RC lowpass filter connected. We see that the threshold current is reduced due to the increased RF power. This is again visualized in Fig. B.1 (b). Surprisingly, the photon driven transport, indicated by the slope of the IV in (a), seems to be suppressed for increased RF power.

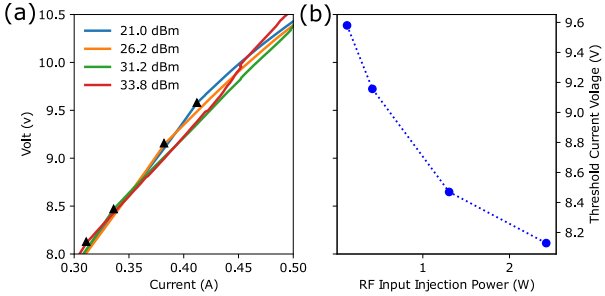

Figure B.1 – (a) shows a portion of the IV for different different RF powers. For increasing RF power the threshold current (black triangular markers) is lowered as can be seen also in (b). At the same time, increased RF power seems to suppress the photon driven transport in this device as the slope of the IV increases after the threshold compared to lower RF powers.

B.2 Sub-comb beating

In chapter 9, we saw that during strong RF driving sub-combs can be generated. They all share the same induced f_{rep} but have different f_{ceo}'s. If the sub-combs overlap, we expect to be able to observed the different f_{ceo} beating signals on the bias line. This is indeed experimentally observed and shown in Fig. B.2. The device is again the 4.5 mm long and 86 µm wide Cu–Cu laser at 26 K, at 458 mA and 10.03 V. The free running beatnote frequency is around 8.8 GHz. It was additionally RF driven at 7.638 GHz and 27 dBm RF power. In this case we observe sub-comb formation as it's shown in Fig. B.2 (b) with the extracted f_{ceo}'s. It seems that all groups of sub-comb f_{ceo}'s are spaced by nearly 2 GHz. In Fig. B.2 (d) we observe this difference in the sub-comb f_{ceo}'s at 1.92 GHz on the bias line. It needs to be mentioned that this collective beating is observed for a small power and frequency range of the RF source.

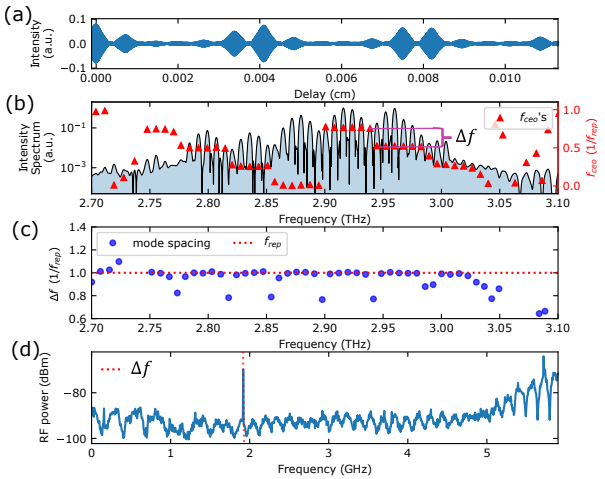

Figure B.2 – Beating of f_{ceo} sub-groups. (a) IFG of the lasing device. (b) Intensity spectrum and extracted f_{ceo}'s. (c) Extracted mode spacing matching the RF modulation frequency. (d) Beating of the sub-combs corresponding to the frequency difference of the sub-combs. Rise of RF signal above 5 GHz is due to the connected amplifier.

B.3 Subharmonic comb generation

The same state as in the previous section, but driven at 8.373 GHz at roughly 35 dBm leads to subharmonic comb generation. The result is shown in Fig. B.3. A clear symmetric IFG with the expected subharmonic comb periodicity is observed in panel (a). Fig. B.3 (b) shows the intensity spectrum and the extracted f_{ceo}'s which lie on a line at $f_{\mathrm{rep}}/2$ indicating the subharmonic comb. The extracted mode spacing in panel (c) does as well support the subharmonic comb observation. And in Fig. B.3 (d) we do also observe the subharmonic beatnote on the bias line. As in the previous section, this state can only be observed in a small range of RF frequencies and powers.

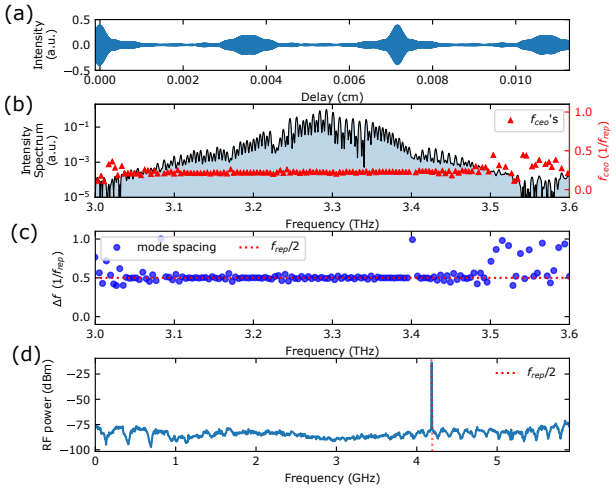

Figure B.3 – Subharmonic comb generation. (a) IFG with the expected subharmonic periodicity. (b) Intensity spectrum and the extracted f_{ceo}'s which lie on a line at $f_{\mathrm{rep}}/2$. (c) Extracted mode spacing which supports the subharmonic comb observation. (d) Electrically observed subharmonic comb beating.

B.4 f_{ceo} drift

In chapter 9, we saw that for certain SWIFT measurements we observe an unexpected behavior of the extracted f_{ceo}'s. Such a case is again shown in Fig. B.4. Even though the resulting SWIFT spectra is not extremely broad, we want to highlight here that the spectrum product shows the emission of modes over one octave. This result is encouraging to implement dispersion compensating structures into the device which might enables to RF drive such devices over an entire octave in a single comb regime. For completeness, we show the standard SWIFT figure.

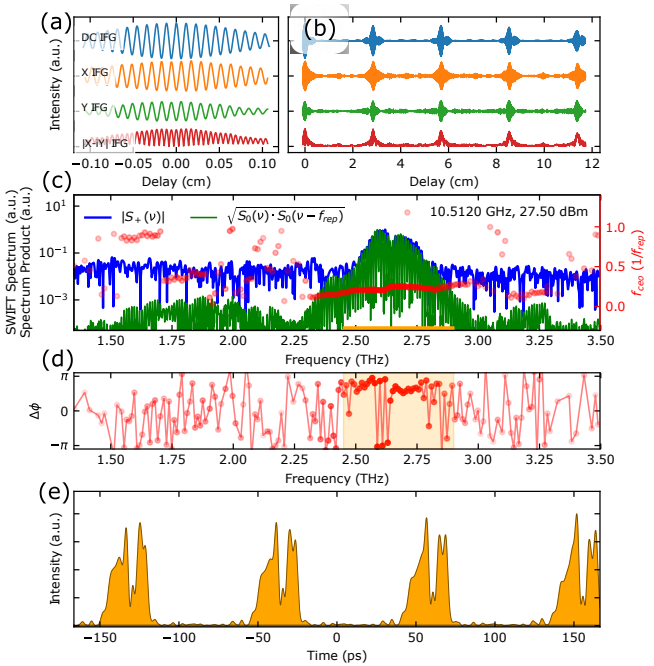

Figure B.4 – SWIFTS data of a 3.8 mm long and 86 µm wide device based on a heterogeneous AR operated at 804 mA, 9.70 V an 35.8 K heat sink temperature and 27.5 dBm RF injection power at 10.512 GHz. (a) Zoom on ZPD of the recorded IFGs indicates FM emission. (b) Full IFGs showing the dephasing due to the sub-combs. (c) Comparison of SWIFT spectrum and spectrum product. Red dots show the extracted f_{ceo} from the intensity spectrum showing high coherence. The orange bar indicates the spectral region considered for the temporal reconstruction. (d) Extracted phase differences from SWIFTS spectrum. Phases are densely spaced. (e) Reconstructed temporal intensity profile (actually not valid due to different f_{ceo}'s). Clear AM is observed, but the pulse to pulse shape is changing due to the underlying f_{ceo} drift.

B.5 Linear chirped sub-combs

Besides the general observation of flattening the phase differences of sub-combs due to strong RF modulation, we also observe for certain injection frequency a linear chirp in a sub-comb. At the same time, other sub-combs show flat phase difference relation. These results are shown in Fig. B.5.

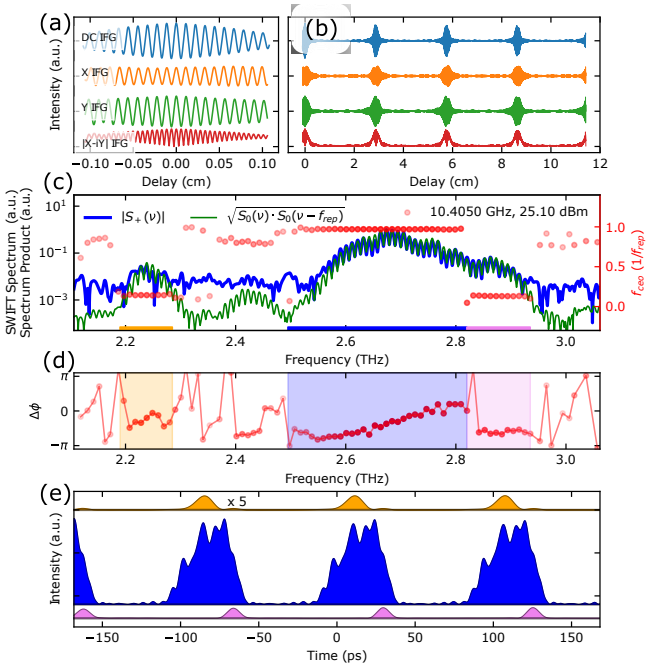

Figure B.5 – SWIFTS data of a 3.8 mm long and 86 µm wide device based on a heterogeneous AR operated at 780 mA, 9.80 V an 28.8 K heat sink temperature and 25.1 dBm RF injection power at 10.405 GHz. (a) Zoom on ZPD of the recorded IFGs indicates AM emission. (b) Full IFGs showing the dephasing due to sub-combs. (c) Comparison of SWIFT spectrum and spectrum product showing high coherence. Red dots show the extracted f_{ceo} from the intensity spectrum. (d) Extracted phase differences from SWIFTS spectrum. have lobes with flat spaced phase differences and a region which is linear chirped. (e) reconstructed temporal intensity profile for each lobe. Clear AM is observed.

B.6 SWIFT at higher harmonics

In chapter 9, we saw in Fig. 9.5 (c) that the modes could be not fully coherent at higher frequencies for weak RF injection. We now compare the phases from a fundamental beatnote SWIFT measurement at 10 dBm RF power to the phases extracted from first and second harmonic SWIFT measurements in Fig. B.6. We see, that the phase differences from the fundamental beatnote SWIFT measurement in light blue overlap well with the phase difference of the first and second harmonic SWIFT measurement in red below frequencies of 2.7 THz, panels (d) and (h). Above, the results

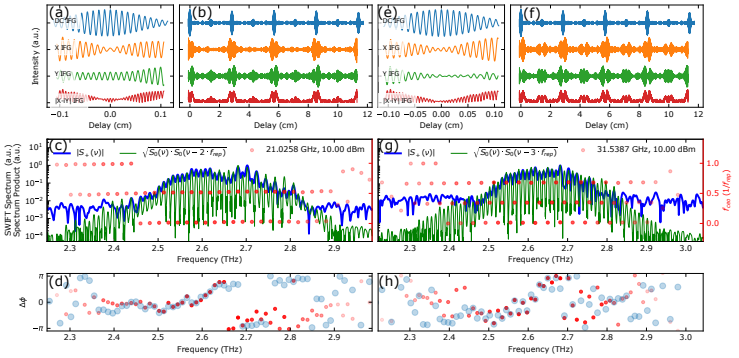

Figure B.6 – SWIFTS data of a 3.8 mm long and 86 µm wide device based on a heterogeneous AR operated at 876 mA, 9.94 V an 43 K heat sink temperature and 5 dBm RF injection power at 21.0258 GHz in (a) to (d) and 31.5387 GHz in (e) to (h). The phase differences in red are compared to the phase differences extracted from the fundamental beatnote SWIFT measurement in light blue. The results supports that the modes at higher frequencies are not fully coherent and the phase differences not well defined. Additionally, the results also show that our HEB allows to perform SWIFT measurements above 30 GHz.

show inconsistency in the extracted phase differences resembling the increased incoherence of these modes. Still, the phases are not completely off and randomly distributed. This would indicate certain amount of coherence between these modes.

Even though the resulting measurements do not show a fully coherent comb, it shows that we can perform SWIFT measurements above 30 GHz with our antenna-coupled HEB.

C

Harmonic combs

C.1 Bandstructure

The theoretical results in chapter 6 included an upper and two lower level states. Fig. C.1 shows the calculated bandstructure from a Schrödinger + Poisson solver at a lattice temperature of 150 K and 49 mV bias per period for the investigated AR.

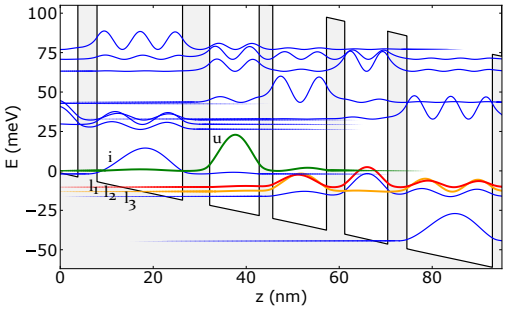

Figure C.1 – The bandstructure of our lasers at threshold bias of 49 mV per period and lattice temperature of $T_L = 150$ K from Schroedinger + Poisson solver. The layer sequence based on GaAs/$Al_{0.15}Ga_{0.85}As$ is 18.3/**5.8**/10.6/**2.9**/11.5/**3.9**/9.2/**4.1** in nm where barriers are in bold and the $2.3 \cdot 10^{16}$ cm^{-3} Si doped injection well is underlined. The sequence is repeated 151 times and grown by molecular beam epitaxy (MBE). The injection state is marked as **i**, upper lasing state as **u** and the three lower energy states as l_1, l_2 and l_3. The two lasing transitions are between the upper lasing state **u** (green) and the two lower lasing states l_1 (red) and l_2 (orange).

C.2 Interferogram envelope asymmetry

In chapter 6 we argued that from symmetry considerations of the interferogram (IFG) envelope one can verify to certain extent the coherence and especially the purity of a comb state. Here we exclude special cases like partially coherent modes and subharmonic modes for which the coherence cannot be captured fully with symmetry arguments, but are still correctly identify as non-pure comb states. In the case of a perfect comb, the modes go out-of-phase as a function of delay and after the repetition rate they all come in-phase again at the same point, up to a slow sinusoidal phase change by the frequency f_{ceo} of the comb. Nevertheless, the envelope stays periodic and symmetric for a perfect comb. Therefore, a perfectly periodic IFG envelope is created in theory. In a real FTIR one is additionally limited by diffraction losses, divergence of the beam and misalignment of the laser, which are not discussed further. By considering a non-equally spaced mode spectrum the point of being in-phase for mode pairs is different. Therefore, the IFG envelope loses its periodicity and symmetry.

Such behavior is experimentally observed as shown in Fig. C.2 for a broadband multi-mode and a comb state. In panel (a) we clearly see, that the envelope of the multi-mode laser dephases and decays whereas for the comb state it preserves its periodicity, see panel (d). By extracting the mode spacing from the intensity spectrum we see that the for the multi-mode operation we do not find the modes on a straight line whereas we see it for the comb state, see panel (c) and (f), respectively.

Further, we would like, by numerical construction of multiple IFGs, demonstrate to which extend we can identify an incoherent mode spacing or non-pure comb states by the arguments of periodic and symmetric IFGs. We construct the IFGs for the harmonic comb from Fig. 6.1(d) as well as a dense/fundamental comb from 6.1(b). The delay of 12 cm corresponds to the one of our commercial FTIR (Bruker, Vertex 80v) which has a nominal resolution of 2.5 GHz. In Fig. C.3(a) and (c) resp. Fig. C.4(a) and (c) we present the extracted intensity amplitudes of the harmonic resp. dense comb. For the same amplitudes but non-equally spaced modes ($\Delta\nu_{i,i+1} = f_{rep} - i \cdot dv$ where i the mode number) we construct the IFGs for dv = 50, 20, 1 MHz for the harmonic comb and dv = 1, 0.5, 0.1 MHz for the dense comb case and are presented in Fig. C.3

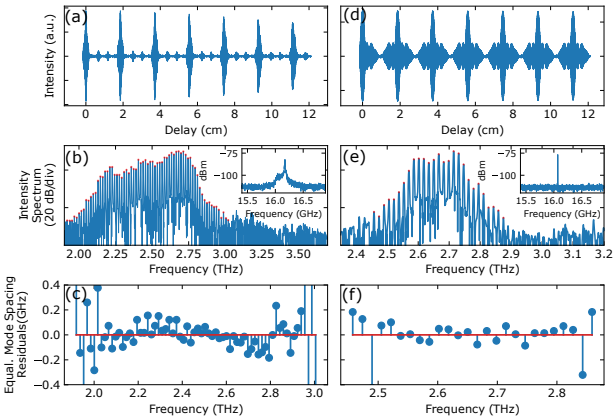

Figure C.2 – Interferogram, spectrum and extracted mode spacing from multi-mode and comb emission of a THz QCL in (a-c) and (d-f), respectively. Inset in (b) and (e) show the corresponding beating signals indicating once high phase noise and once comb operation, respectively.

(b-g) resp. Fig. C.4 (b-g). The linear decrease in the mode spacing is selected to represent the effect of GaAs dispersion for multi-mode (non-comb) lasing as experimentally observed in THz QCLs. As highlighted for both cases, a clear asymmetry is visible for the first two cases and only in the last one the asymmetry is not directly visible anymore. This means that a mode spacing difference of 240 MHz resp. 23 MHz between lowest and highest frequency mode is clearly detectable for the harmonic resp. fundamental comb state at ∼9 cm delay (nominally ∼3 GHz FTIR resolution) with no need of a fast THz detector. Of course the visibility of the asymmetry also depends on the number of modes and their relative amplitudes. Therefore, spectra with more modes and similar amplitudes will lead to more features in the IFGs which are then better visible (see small features in Fig. C.4 (c),(e)). We see that with the symmetry arguments we can identify changes in the mode spacing on the MHz range compared to the GHz nominal resolution of the FTIR. For completeness we generate for the fundamental comb interferogram for normal distributed mode spacing differences with standard deviations $\sigma = 200$, 20 and 2 MHz from the perfect spaced modes. The results are shown in Fig. C.5 and similar conclusions are drawn from symmetry considerations.

Finally, we would like to point out that the same information is in

principle contained in the intensity spectrum, but the extraction of the mode spacing is more complex and far from trivial in that case, compare to the CombFFT in chapter 3. Therefore, the analysis of the IFG envelope symmetry in the time/space domain comes very handy, does not involve any advanced mathematical methods and leads to a clear result.

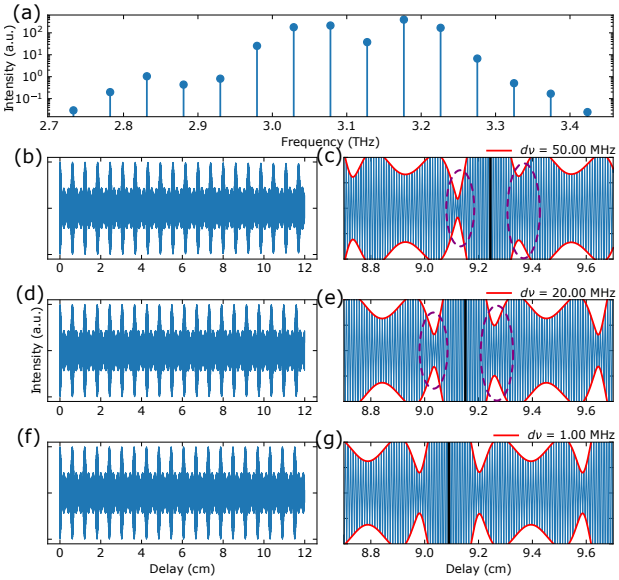

Figure C.3 – Numerically generated IFGs with varying mode spacing for the harmonic comb state presented in Fig. 1(d). (a) Extracted amplitudes from the intensity spectrum. (b)-(g) Reconstructed IFGs assuming modes spacing which linear decreases for higher frequency, i.e. $\Delta\nu_{i,i+1} = f_{rep} - i \cdot d\nu$ where i the mode number. $d\nu = 50$ MHz in (b) and (c), $d\nu = 20$ MHz in (d) and (e), and $d\nu = 1$ MHz in (f) and (g). (c), (e) and (g) zoom in on a satellite at roughly 9 cm delay. Black line indicates the mirror axis, while the dashed circle indicate the asymmetric features. The envelope (red) of the IFG is periodic for a perfect comb. Clear differences from the periodic envelope are visible in (c) and (e) and therefore identify a non-perfect mode spacing. For $d\nu = 1$ MHz the asymmetry is not detectable by eye.

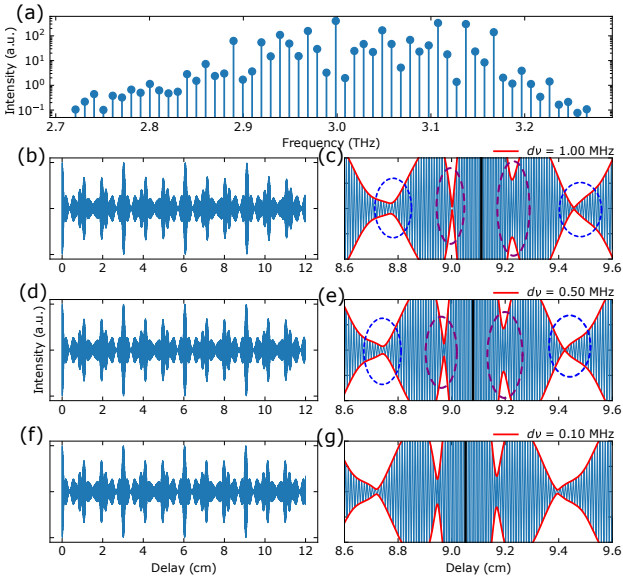

Figure C.4 – Numerically generated IFGs with varying mode spacing for the fundamental comb state presented in Fig. 1(b). (a) Extracted amplitudes from the intensity spectrum. (b)-(g) Reconstructed IFGs assuming modes spacing which linear decreases for higher frequency, i.e. $\Delta\nu_{i,i+1} = f_{rep} - i \cdot d\nu$ where i the mode number. $d\nu = 1$ MHz in (b) and (c), $d\nu = 500$ kHz in (d) and (e), and $d\nu = 100$ kHz in (f) and (g). (c), (e) and (g) zoom in on a satellite at roughly 9 cm delay. Black line indicates the mirror axis, while the dashed circle indicate the asymmetric features. The envelope (red) of the IFG is periodic for a perfect comb. Clear differences from the periodic envelope are visible in (c) and (e) and therefore identify a non-perfect mode spacing. For $d\nu = 100$ kHz the asymmetry is not clearly detectable by eye.

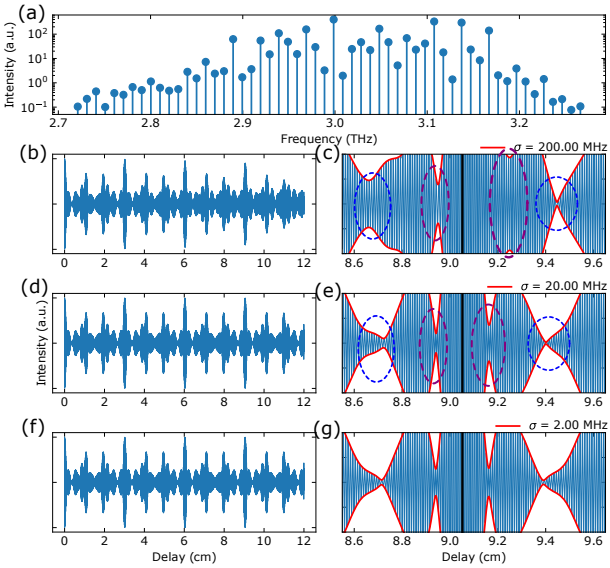

Figure C.5 – Numerically generated IFGs with varying mode spacing for the fundamental comb state presented in Fig. 1(b) with normal distributed mode spacing differences. (a) Extracted amplitudes from the intensity spectrum. (b)-(g) Reconstructed IFGs assuming modes spacing which are normal distributed around the perfect comb modes for different standard deviations σ. $\sigma = 200$ MHz in (b) and (c), $\sigma = 20$ MHz in (d) and (e), and $\sigma = 2$ MHz in (f) and (g). (c), (e) and (g) zoom in on a satellite at roughly 9 cm delay. Black line indicates the mirror axis, while the dashed circle indicate the asymmetric features. The envelope (red) of the IFG is periodic for a perfect comb. Clear differences from the periodic envelope are visible in (c) and (e) and therefore identify a non-perfect mode spacing. For $\sigma = 2$ MHz the asymmetry is not clearly detectable by eye.

D

Active region growth designs

This appendix contains all the growth designs of the relevant active region designs used throughout this work. The structures were designed and optimized by Prof. Giacomo Scalari. All samples were grown by molecular beam epitaxy (MBE) on a V80H system of VG Semicon at ETH Zürich in the joint cleanroom facility FIRST by Dr. Mattias Beck.

D.1 Homogeneous cascade design for broad emission and comb operation at 2.9 THz: EV2244

Table D.1 – Growth design of homogeneous active region EV2244 [143, 144]. The AR is designed for an emission frequency of 2.9 THz. Total thickness 10.4371µm.

Part of design	**Composition**	**Thickness [Å]**	**Doping [cm^{-3}]**
Top contact	InGaAs	200	1.00 x 10^{19}
	GaAs	400	3.80 x 10^{18}
Upper cladding	$Al_{0.15}GaAs$	100	
	GaAs	200	
	$Al_{0.15}GaAs$	58	
repeated 151 x	GaAs	106	
	$Al_{0.15}GaAs$	29	
	GaAs	115	
	$Al_{0.15}GaAs$	39	
	GaAs	92	
	$Al_{0.15}GaAs$	41	
	GaAs	183	2.30 x 10^{16}
	$Al_{0.15}GaAs$	58	
Lower cladding	GaAs	200	
	$Al_{0.15}GaAs$	100	
	GaAs	500	2.00 x 10^{18}
	$Al_{0.5}GaAs$	2000	
	GaAs	500	

D.2 Heterogeneous cascade design for broadband emission and comb operation between 1.6-3.2 THz: EV1913

Table D.2 – Growth design of active region EV1913 [38]. The design *A* is designed for an emission frequency of 2.9 THz. The design *B* is designed for an emission frequency of 2.6 THz. The design *C* is designed for an emission frequency of 2.3 THz. Total thickness 14.2535µm.

Part of design	**Composition**	**Thickness [Å]**	**Doping [cm^{-3}]**
Top contact	InGaAs	200	1.00 x 10^{19}
	GaAs	400	3.80 x 10^{18}
Upper cladding	$Al_{0.15}GaAs$	100	
	GaAs	200	
	$Al_{0.15}GaAs$	55	
Design A repeated 40 x	GaAs	110	
	$Al_{0.15}GaAs$	18	
	GaAs	115	
	$Al_{0.15}GaAs$	38	
	GaAs	94	
	$Al_{0.15}GaAs$	42	
	GaAs	184	1.70 x 10^{16}
	$Al_{0.15}GaAs$	55	
Design C repeated 40 x	GaAs	120	
	$Al_{0.15}GaAs$	18	
	GaAs	105	
	$Al_{0.15}GaAs$	38	
	GaAs	94	
	$Al_{0.15}GaAs$	42	
	GaAs	184	1.70 x 10^{16}
	$Al_{0.15}GaAs$	55	
Design B repeated 80 x	GaAs	113	
	$Al_{0.15}GaAs$	18	
	GaAs	113	
	$Al_{0.15}GaAs$	38	
	GaAs	94	
	$Al_{0.15}GaAs$	42	
	GaAs	184	1.70 x 10^{16}
	$Al_{0.15}GaAs$	55	
Design C repeated 40 x	GaAs	120	
	$Al_{0.15}GaAs$	18	

	GaAs	105	
	$Al_{0.15}GaAs$	38	
	GaAs	94	
	$Al_{0.15}GaAs$	42	
	GaAs	184	1.70×10^{16}
	$Al_{0.15}GaAs$	55	
Lower cladding	GaAs	200	
	$Al_{0.15}GaAs$	100	
	GaAs	7000	2.00×10^{18}
	$Al_{0.5}GaAs$	2000	
	GaAs	2500	

D.3 Heterogeneous cascade design for dual-color emission at 2.3 and 4.6 THz: EV2238

Table D.3 – Growth design of active region EV2238 [137]. It contains two different active region designs. The design *A* is designed for an emission frequency of 2.3 THz. The design *B* is designed for an emission frequency of 4.6 THz. Total thickness 13.0155µm.

Part of design	**Composition**	**Thickness [Å]**	**Doping [cm^{-3}]**
Top contact	InGaAs	200	1.00 x 10^{19}
	GaAs	400	3.80 x 10^{18}
Upper cladding	$Al_{0.15}GaAs$	100	
	GaAs	200	
	$Al_{0.15}GaAs$	55	
Design A repeated 120 x	GaAs	120	
	$Al_{0.15}GaAs$	18	
	GaAs	105	
	$Al_{0.15}GaAs$	38	
	GaAs	94	
	$Al_{0.15}GaAs$	42	
	GaAs	184	2.00 x 10^{16}
	$Al_{0.15}GaAs$	55	
Design B repeated 80 x	GaAs	93	
	$Al_{0.15}GaAs$	10	
	GaAs	105	
	$Al_{0.15}GaAs$	33	
	GaAs	87	
	$Al_{0.15}GaAs$	42	
	GaAs	165	2.00 x 10^{16}
	$Al_{0.15}GaAs$	51	
Lower cladding	GaAs	200	
	$Al_{0.15}GaAs$	100	
	GaAs	800	2.00 x 10^{18}
	$Al_{0.5}GaAs$	2000	
	GaAs	500	

Bibliography

[1] T. W. Hänsch, *Nobel Lecture*, https://www.nobelprize.org/prizes/physics/2005/hansch/lecture/ (visited on 08/05/2021) (see pp. 1, 9, 12).

[2] T. Udem, R. Holzwarth, and T. W. Hänsch, "Optical frequency metrology", Nature **416**, 233–237 (2002) (see pp. 1, 4).

[3] R. Holzwarth, T. Udem, T. W. Hänsch, J. C. Knight, W. J. Wadsworth, and P. S. J. Russell, "Optical Frequency Synthesizer for Precision Spectroscopy", Phys. Rev. Lett. **85**, 2264–2267 (2000) (see p. 1).

[4] S. A. Diddams, D. J. Jones, J. Ye, S. T. Cundiff, J. L. Hall, J. K. Ranka, R. S. Windeler, R. Holzwarth, T. Udem, and T. W. Hänsch, "Direct Link between Microwave and Optical Frequencies with a 300 THz Femtosecond Laser Comb", Phys. Rev. Lett. **84**, 5102–5105 (2000) (see pp. 1, 12, 130).

[5] T. Udem, J. Reichert, R. Holzwarth, and T. W. Hänsch, "Absolute Optical Frequency Measurement of the Cesium D1 Line with a Mode-Locked Laser", Phys. Rev. Lett. **82**, 3568–3571 (1999) (see pp. 1, 4).

[6] S. A. Diddams, "The evolving optical frequency comb [Invited]", J. Opt. Soc. Am. B **27**, B51 (2010) (see p. 1).

[7] G. Villares, J. Wolf, D. Kazakov, M. J. Süess, A. Hugi, M. Beck, and J. Faist, "On-chip dual-comb based on quantum cascade laser frequency combs", Appl. Phys. Lett. **107**, 251104 (2015) (see p. 1).

[8] L. A. Sterczewski, J. Westberg, and G. Wysocki, "Molecular dispersion spectroscopy based on Fabry–Perot quantum cascade lasers", Opt. Lett. **42**, 243–246 (2017) (see p. 1).

[9] J. Westberg, L. A. Sterczewski, and G. Wysocki, "Mid-infrared multiheterodyne spectroscopy with phase-locked quantum cascade lasers", Appl. Phys. Lett. **110**, 141108 (2017) (see p. 1).

[10] T. J. Kippenberg, R. Holzwarth, and S. A. Diddams, "Microresonator-Based Optical Frequency Combs", Science **332**, 555–559 (2011) (see p. 1).

[11] A. Hugi, G. Villares, S. Blaser, H. C. Liu, and J. Faist, "Mid-infrared frequency comb based on a quantum cascade laser", Nature **492**, 229–233 (2012) (see pp. 1, 5, 19–21, 85, 113, 122, 135, 149, 150, 170).

[12] S. Barbieri, M. Ravaro, P. Gellie, G. Santarelli, C. Manquest, C. Sirtori, S. P. Khanna, E. H. Linfield, and A. G. Davies, "Coherent sampling of active mode-locked terahertz quantum cascade lasers and frequency synthesis", Nature Photonics **5**, 306–313 (2011) (see pp. 1, 5, 18, 19, 87, 113, 148).

[13] L. A. Sterczewski, C. Frez, S. Forouhar, D. Burghoff, and M. Bagheri, "Frequency-modulated diode laser frequency combs at 2 μm wavelength", APL Photonics **5**, 076111 (2020) (see pp. 1, 151).

[14] J. Hillbrand, M. Beiser, A. M. Andrews, H. Detz, R. Weih, A. Schade, S. Höfling, G. Strasser, and B. Schwarz, "Picosecond pulses from a mid-infrared interband cascade laser", Optica **6**, 1334–1337 (2019) (see pp. 1, 151).

[15] J. Faist, F. Capasso, D. L. Sivco, C. Sirtori, A. L. Hutchinson, and A. Y. Cho, "Quantum Cascade Laser", Science **264**, 553–556 (1994) (see pp. 1–3).

[16] R. Köhler, A. Tredicucci, F. Beltram, H. E. Beere, E. H. Linfield, A. G. Davies, D. A. Ritchie, R. C. Iotti, and F. Rossi, "Terahertz semiconductor-heterostructure laser", Nature **417**, 156–159 (2002) (see pp. 1–3, 32).

[17] D. Burghoff, T.-Y. Kao, N. Han, C. W. I. Chan, X. Cai, Y. Yang, D. J. Hayton, J.-R. Gao, J. L. Reno, and Q. Hu, "Terahertz laser frequency combs", Nature Photonics **8**, 462–467 (2014) (see pp. 1, 5, 20–22, 33, 105, 113, 122, 130, 135, 137, 151, 158, 164, 194).

[18] D. Pavlidis, ed., *Fundamentals of Terahertz Devices and Applications*, John Wiley & Sons, Ltd, Hoboken, NJ, (2021), ISBN: 978-1-119-46073-2 978-1-119-46072-5, (see p. 2).

[19] S. S. Dhillon, M. S. Vitiello, E. H. Linfield, et al., "The 2017 terahertz science and technology roadmap", J. Phys. D: Appl. Phys. **50**, 043001 (2017) (see p. 2).

[20] G. Valušis, A. Lisauskas, H. Yuan, W. Knap, and H. G. Roskos, "Roadmap of Terahertz Imaging 2021", Sensors **21**, 4092 (2021) (see p. 2).

[21] J.-S. Rieh, "THz Applications", in *Introduction to Terahertz Electronics*, edited by J.-S. Rieh (Springer International Publishing, Cham, 2021), pp. 273–350 (see p. 2).

[22] A. Y. Pawar, D. D. Sonawane, K. B. Erande, and D. V. Derle, "Terahertz technology and its applications", Drug Invention Today **5**, 157–163 (2013) (see p. 2).

[23] L. Bosco, "THz Quantum Cascade Laser: Astrophysical Applications and High Temperature Performance", ETH Zurich, (2020), doi: 10.3929/ETHZ-B-000404798, (see pp. 2, 31, 34).

[24] J. Neu and C. A. Schmuttenmaer, "Tutorial: an introduction to terahertz time domain spectroscopy (THz-TDS)", Journal of Applied Physics **124**, 231101 (2018) (see p. 2).

[25] P. U. Jepsen, R. H. Jacobsen, and S. R. Keiding, "Generation and detection of terahertz pulses from biased semiconductor antennas", J. Opt. Soc. Am. B, JOSAB **13**, 2424–2436 (1996) (see p. 2).

[26] C. M. O'Sullivan and J. A. Murphy, *Field Guide to Terahertz Sources, Detectors, and Optics*, SPIE, 1000 20th Street, Bellingham, WA 98227-0010 USA, (2012), ISBN: 978-0-8194-9167-1, (see p. 2).

[27] S. Komiyama, "Far-Infrared Emission from Population-Inverted Hot-Carrier System in *p*-Ge", Phys. Rev. Lett. **48**, 271–274 (1982) (see p. 2).

[28] J. Faist, *Quantum Cascade Lasers*, Oxford University Press, Oxford, United Kingdom, (2013), ISBN: 978-0-19-852824-1, (see pp. 2–4, 30, 32, 42, 50, 88).

[29] C. A. Curwen, J. L. Reno, and B. S. Williams, "Terahertz quantum cascade VECSEL with watt-level output power", Applied Physics Letters **113**, 011104 (2018) (see p. 2).

[30] L. H. Li, J. X. Zhu, L. Chen, A. G. Davies, and E. H. Linfield, "The MBE growth and optimization of high performance terahertz frequency quantum cascade lasers", Opt. Express **23**, 2720–2729 (2015) (see p. 2).

[31] S. Fathololoumi, E. Dupont, C. Chan, Z. Wasilewski, Laframboise, S.R., D. Ban, A. Mátyás, C. Jirauschek, Q. Hu, and H. C. Liu, "Terahertz quantum cascade lasers operating up to ∼200 K with optimized oscillator strength and improved injection tunneling", Opt. Express **20**, 3866 (2012) (see pp. 2, 30).

[32] L. Bosco, M. Franckié, G. Scalari, M. Beck, A. Wacker, and J. Faist, "Thermoelectrically cooled THz quantum cascade laser operating up to 210 K", Appl. Phys. Lett. **115**, 010601 (2019) (see pp. 2, 25, 30, 105, 106).

[33] M. A. Kainz, M. P. Semtsiv, G. Tsianos, et al., "Thermoelectric-cooled terahertz quantum cascade lasers", Opt. Express **27**, 20688–20693 (2019) (see pp. 2, 105).

[34] A. Khalatpour, A. K. Paulsen, C. Deimert, Z. R. Wasilewski, and Q. Hu, "High-power portable terahertz laser systems", Nat. Photonics **15**, 16–20 (2021) (see pp. 2, 105).

[35] K. Fujita, M. Hitaka, A. Ito, T. Edamura, M. Yamanishi, S. Jung, and M. A. Belkin, "Terahertz generation in mid-infrared quantum cascade lasers with a dual-upper-state active region", Appl. Phys. Lett. **106**, 251104 (2015) (see p. 2).

[36] M. A. Belkin, F. Capasso, F. Xie, A. Belyanin, M. Fischer, A. Wittmann, and J. Faist, "Room temperature terahertz quantum cascade laser source based on intracavity difference-frequency generation", Appl. Phys. Lett. **92**, 201101 (2008) (see p. 2).

[37] M. A. Belkin, F. Capasso, A. Belyanin, D. L. Sivco, A. Y. Cho, D. C. Oakley, C. J. Vineis, and G. W. Turner, "Terahertz quantum-cascade-laser source based on intracavity difference-frequency generation", Nature Photon **1**, 288–292 (2007) (see pp. 2, 26).

[38] M. Rösch, G. Scalari, M. Beck, and J. Faist, "Octave-spanning semiconductor laser", Nature Photonics **9**, 42–47 (2015) (see pp. 2, 22, 33, 34, 43, 47, 70, 87, 130, 163, 172, 181, 182, 193, 217).

[39] M. Rösch, M. Beck, M. J. Süess, D. Bachmann, K. Unterrainer, J. Faist, and G. Scalari, "Heterogeneous terahertz quantum cascade lasers exceeding 1.9 THz spectral bandwidth and featuring dual comb operation", Nanophotonics **7**, 237–242 (2018) (see pp. 2, 23, 25, 75, 87, 105, 130).

[40] D. Burghoff, N. Han, F. Kapsalidis, N. Henry, M. Beck, J. Khurgin, J. Faist, and Q. Hu, "Microelectromechanical control of the state of quantum cascade laser frequency combs", Appl. Phys. Lett. **115**, 021105 (2019) (see p. 2).

[41] M. Wienold, B. Röben, L. Schrottke, and H. T. Grahn, "Evidence for frequency comb emission from a Fabry-Pérot terahertz quantum-cascade laser", Opt. Express **22**, 30410–30424 (2014) (see pp. 2, 22, 33, 110, 122, 123, 136, 150).

[42] M. Rösch, G. Scalari, G. Villares, L. Bosco, M. Beck, and J. Faist, "On-chip, self-detected terahertz dual-comb source", Appl. Phys. Lett. **108**, 171104 (2016) (see pp. 2, 122).

[43] L. Esaki and R. Tsu, "Superlattice and Negative Differential Conductivity in Semiconductors", IBM Journal of Research and Development **14**, 61–65 (1970) (see pp. 3, 92).

[44] R. F. Kazarinov and R. A. Suris, "Possibility of the amplification of electromagnetic waves in a semiconductor with a superlattice", Sov. Phys. Semicond. **5**, 707–709 (1971) (see p. 3).

[45] M. Beck, "Continuous Wave Operation of a Mid-Infrared Semiconductor Laser at Room Temperature", Science **295**, 301–305 (2002) (see p. 3).

[46] M. S. Vitiello, G. Scalari, B. Williams, and P. D. Natale, "Quantum cascade lasers: 20 years of challenges", Opt. Express **23**, 5167–5182 (2015) (see p. 3).

[47] P. Friedli, H. Sigg, B. Hinkov, A. Hugi, S. Riedi, M. Beck, and J. Faist, "Four-wave mixing in a quantum cascade laser amplifier", Appl. Phys. Lett. **102**, 222104 (2013) (see pp. 3, 20).

[48] B. Meng, M. Singleton, M. Shahmohammadi, F. Kapsalidis, R. Wang, M. Beck, and J. Faist, "Mid-infrared frequency comb from a ring quantum cascade laser", Optica **7**, 162–167 (2020) (see pp. 3, 26).

[49] M. Jaidl, N. Opačak, M. A. Kainz, et al., "Comb operation in terahertz quantum cascade ring lasers", Optica **8**, 780–787 (2021) (see pp. 3, 26).

[50] T. Udem, A. Huber, B. Gross, J. Reichert, M. Prevedelli, M. Weitz, and T. W. Hänsch, "Phase-Coherent Measurement of the Hydrogen 1S - 2S Transition Frequency with an Optical Frequency Interval Divider Chain", Phys. Rev. Lett. **79**, 2646–2649 (1997) (see p. 4).

[51] T. Udem, J. Reichert, R. Holzwarth, and T. W. Hänsch, "Accurate measurement of large optical frequency differences with a mode-locked laser", Optics Letters **24**, 881 (1999) (see pp. 4, 5, 12, 13).

[52] J. Reichert, R. Holzwarth, T. Udem, and T. W. Hänsch, "Measuring the frequency of light with mode-locked lasers", Optics Communications **172**, 59–68 (1999) (see pp. 4, 12).

[53] D. J. Jones, "Carrier-Envelope Phase Control of Femtosecond Mode-Locked Lasers and Direct Optical Frequency Synthesis", Science **288**, 635–639 (2000) (see pp. 5, 12, 130).

[54] A. E. Siegman, *Lasers*, University Science Books, (1986), ISBN: 978-0-935702-11-8, (see pp. 7, 9, 10, 13, 14, 44, 47, 48, 101, 172, 184).

[55] A. Mottaghizadeh, D. Gacemi, P. Laffaille, et al., "5-ps-long terahertz pulses from an active-mode-locked quantum cascade laser", Optica **4**, 168–171 (2017) (see p. 8).

[56] J. P. Gordon, H. J. Zeiger, and C. H. Townes, "Molecular Microwave Oscillator and New Hyperfine Structure in the Microwave Spectrum of NH_3", Phys. Rev. **95**, 282–284 (1954) (see p. 9).

[57] A. L. Schawlow and C. H. Townes, "Infrared and Optical Masers", Phys. Rev. **112**, 1940–1949 (1958) (see p. 9).

[58] T. H. Maiman, "Stimulated Optical Radiation in Ruby", Nature **187**, 493–494 (1960) (see p. 9).

[59] E. Marshall, "Gould Advances Inventor's Claim on the Laser", Science **216**, 392–395 (1982) (see p. 9).

[60] H. A. Haus, "Mode-locking of lasers", IEEE Journal of Selected Topics in Quantum Electronics **6**, 1173–1185 (2000) (see p. 9).

[61] U. Keller, "Recent developments in compact ultrafast lasers", Nature **424**, 831–838 (2003) (see pp. 9, 10, 12).

[62] L. E. Hargrove, R. L. Fork, and M. A. Pollack, "LOCKING OF He–Ne LASER MODES INDUCED BY SYNCHRONOUS INTRACAVITY MODULATION", Appl. Phys. Lett. **5**, 4–5 (1964) (see p. 9).

[63] E. Ammann, B. McMurtry, and M. Oshman, "Detailed experiments on helium-neon FM lasers", IEEE Journal of Quantum Electronics **1**, 263–272 (1965) (see pp. 9, 13).

[64] K. Gürs and R. Müller, "Breitband-modulation durch steuerung der emission eines optischen masers (Auskoppelmodulation)", Physics Letters **5**, 179–181 (1963) (see p. 9).

[65] M. DiDomenico, "Small-Signal Analysis of Internal (Coupling-Type) Modulation of Lasers", Journal of Applied Physics **35**, 2870–2876 (1964) (see p. 9).

[66] A. Yariv, "Internal Modulation in Multimode Laser Oscillators", Journal of Applied Physics **36**, 388–391 (1965) (see pp. 9, 14).

[67] O. R. Wood and S. E. Schwarz, "Passive Q-switching of a CO_2 laser", Appl. Phys. Lett. **11**, 88–89 (1967) (see p. 9).

[68] D. Kuizenga and A. Siegman, "FM and AM mode locking of the homogeneous laser - Part I: theory", IEEE Journal of Quantum Electronics **6**, 694–708 (1970) (see pp. 10, 14).

[69] A. J. DeMaria, D. A. Stetser, and H. Heynau, "Self mode-locking of lasers with saturable absorbers", Appl. Phys. Lett. **8**, 174–176 (1966) (see pp. 10, 11).

[70] E. Ippen, C. Shank, and A. Dienes, "Passive mode locking of the cw dye laser", Appl. Phys. Lett. **21**, 348–350 (1972) (see p. 10).

[71] C. V. Shank and E. P. Ippen, "Subpicosecond kilowatt pulses from a mode-locked cw dye laser", Appl. Phys. Lett. **24**, 373–375 (1974) (see p. 10).

[72] H. A. Haus, "Theory of mode locking with a fast saturable absorber", Journal of Applied Physics **46**, 3049–3058 (1975) (see p. 11).

[73] R. L. Fork, C. H. B. Cruz, P. C. Becker, and C. V. Shank, "Compression of optical pulses to six femtoseconds by using cubic phase compensation", Opt. Lett. **12**, 483–485 (1987) (see p. 11).

[74] L. F. Mollenauer and R. H. Stolen, "The soliton laser", Opt. Lett. **9**, 13–15 (1984) (see p. 11).

[75] K. Naganuma and K. Mogi, "50-fs pulse generation directly from a colliding-pulse mode-locked Ti:sapphire laser using an antiresonant ring mirror", Opt. Lett. **16**, 738–740 (1991) (see p. 11).

[76] D. E. Spence, P. N. Kean, and W. Sibbett, "60-fsec pulse generation from a self-mode-locked Ti:sapphire laser", Opt. Lett. **16**, 42–44 (1991) (see p. 11).

[77] U. Keller, G. W. 'tHooft, W. H. Knox, and J. E. Cunningham, "Femtosecond pulses from a continuously self-starting passively mode-locked Ti:sapphire laser", Opt. Lett. **16**, 1022–1024 (1991) (see p. 11).

[78] U. Keller, D. a. B. Miller, G. D. Boyd, T. H. Chiu, J. F. Ferguson, and M. T. Asom, "Solid-state low-loss intracavity saturable absorber for Nd:YLF lasers: an antiresonant semiconductor Fabry–Perot saturable absorber", Opt. Lett. **17**, 505–507 (1992) (see p. 12).

[79] U. Keller, K. Weingarten, F. Kartner, D. Kopf, B. Braun, I. Jung, R. Fluck, C. Honninger, N. Matuschek, and J. Aus der Au, "Semiconductor saturable absorber mirrors (SESAM's) for femtosecond to nanosecond pulse generation in solid-state lasers", IEEE Journal of Selected Topics in Quantum Electronics **2**, 435–453 (1996) (see p. 12).

[80] K. M. Evenson, J. S. Wells, F. R. Petersen, B. L. Danielson, G. W. Day, R. L. Barger, and J. L. Hall, "Speed of Light from Direct Frequency and Wavelength Measurements of the Methane-Stabilized Laser", Phys. Rev. Lett. **29**, 1346–1349 (1972) (see p. 12).

[81] H. Schnatz, B. Lipphardt, J. Helmcke, F. Riehle, and G. Zinner, "First Phase-Coherent Frequency Measurement of Visible Radiation", Phys. Rev. Lett. **76**, 18–21 (1996) (see p. 12).

[82] T. W. Hänsch, "High Resolution Spectroscopy of Hydrogen", in *The Hydrogen Atom*, edited by G. F. Bassani, M. Inguscio, and T. W. Hänsch (Springer Berlin Heidelberg, Berlin, Heidelberg, 1989), pp. 93–102 (see p. 12).

[83] H. R. Telle, D. Meschede, and T. W. Hänsch, "Realization of a new concept for visible frequency division: phase locking of harmonic and sum frequencies", Opt. Lett. **15**, 532 (1990) (see p. 12).

[84] J. N. Eckstein, A. I. Ferguson, and T. W. Hänsch, "High-Resolution Two-Photon Spectroscopy with Picosecond Light Pulses", Phys. Rev. Lett. **40**, 847–850 (1978) (see p. 12).

[85] H. Telle, G. Steinmeyer, A. Dunlop, J. Stenger, D. Sutter, and U. Keller, "Carrier-envelope offset phase control: a novel concept for absolute optical frequency measurement and ultrashort pulse generation", Appl Phys B **69**, 327–332 (1999) (see pp. 12, 85, 130).

[86] L. Matos, D. Kleppner, O. Kuzucu, T. R. Schibli, J. Kim, E. P. Ippen, and F. X. Kaertner, "Direct frequency comb generation from an octave-spanning, prismless Ti:sapphire laser", Opt. Lett. **29**, 1683–1685 (2004) (see p. 13).

[87] B. R. Washburn, S. A. Diddams, N. R. Newbury, J. W. Nicholson, M. F. Yan, and C. G. Jø rgensen, "Phase-locked, erbium-fiber-laser-based frequency comb in the near infrared", Opt. Lett. **29**, 250–252 (2004) (see p. 13).

[88] M. Singleton, P. Jouy, M. Beck, and J. Faist, "Evidence of linear chirp in mid-infrared quantum cascade lasers", Optica **5**, 948–953 (2018) (see pp. 13, 23, 24, 151, 164, 174, 176).

[89] N. Opačak and B. Schwarz, "Theory of Frequency-Modulated Combs in Lasers with Spatial Hole Burning, Dispersion, and Kerr Nonlinearity", Phys. Rev. Lett. **123**, 243902 (2019) (see pp. 13, 25, 47, 111).

[90] S. E. Harris and R. Targ, "FM OSCILLATION OF THE He-Ne LASER", Appl. Phys. Lett. **5**, 202–204 (1964) (see p. 13).

[91] S. E. Harris and O. P. McDuff, "Fm laser oscillation-theory", Appl. Phys. Lett. **5**, 205–206 (1964) (see pp. 13, 14).

[92] S. Harris and O. McDuff, "Theory of FM laser oscillation", IEEE Journal of Quantum Electronics **1**, 245–262 (1965) (see p. 13).

[93] C. S. Adams, G. T. Maker, and A. I. Ferguson, "FM operation of Nd: YAG lasers with standing wave and ring cavity configurations", Optics Communications **76**, 127–130 (1990) (see p. 14).

[94] P. Spencer, D. Kane, and K. Shore, "Coupled-cavity effects in FM semiconductor lasers", Journal of Lightwave Technology **17**, 1072–1078 (1999) (see p. 14).

[95] T. W. Hänsch and N. C. Wong, "Two-Photon Spectroscopy with an FM Laser", Metrologia **16**, 101–104 (1980) (see p. 14).

[96] H. Choi, L. Diehl, Z.-K. Wu, M. Giovannini, J. Faist, F. Capasso, and T. B. Norris, "Gain Recovery Dynamics and Photon-Driven Transport in Quantum Cascade Lasers", Phys. Rev. Lett. **100**, 167401 (2008) (see p. 15).

[97] R. Paiella, F. Capasso, C. Gmachl, H. Y. Hwang, D. L. Sivco, A. L. Hutchinson, A. Y. Cho, and H. C. Liu, "Monolithic active mode locking of quantum cascade lasers", Appl. Phys. Lett. **77**, 169–171 (2000) (see p. 15).

[98] R. Paiella, F. Capasso, C. Gmachl, D. L. Sivco, J. N. Baillargeon, A. L. Hutchinson, A. Y. Cho, and H. C. Liu, "Self-Mode-Locking of Quantum Cascade Lasers with Giant Ultrafast Optical Nonlinearities", Science **290**, 1739–1742 (2000) (see p. 15).

[99] A. Gordon, C. Y. Wang, L. Diehl, et al., "Multimode regimes in quantum cascade lasers: from coherent instabilities to spatial hole burning", Phys. Rev. A **77**, 053804 (2008) (see pp. 15, 17).

[100] R. Paiella, R. Martini, F. Capasso, C. Gmachl, H. Y. Hwang, D. L. Sivco, J. N. Baillargeon, A. Y. Cho, E. A. Whittaker, and H. C. Liu, "High-frequency modulation without the relaxation oscillation resonance in quantum cascade lasers", Appl. Phys. Lett. **79**, 2526–2528 (2001) (see p. 16).

[101] S. Barbieri, J. Alton, C. Baker, T. Lo, H. E. Beere, and D. Ritchie, "Imaging with THz quantum cascade lasers using a Schottky diode mixer", Opt. Express **13**, 6497 (2005) (see pp. 16, 50).

[102] A. L. Betz, R. T. Boreiko, B. S. Williams, S. Kumar, Q. Hu, and J. L. Reno, "Frequency and phase-lock control of a 3 THz quantum cascade laser", Opt. Lett. **30**, 1837–1839 (2005) (see p. 16).

[103] S. Barbieri, W. Maineult, S. S. Dhillon, C. Sirtori, J. Alton, N. Breuil, H. E. Beere, and D. A. Ritchie, "13 GHz direct modulation of terahertz quantum cascade lasers", Appl. Phys. Lett. **91**, 143510 (2007) (see pp. 16, 55, 87).

[104] P. Del'Haye, A. Schliesser, O. Arcizet, T. Wilken, R. Holzwarth, and T. J. Kippenberg, "Optical frequency comb generation from a monolithic microresonator", Nature **450**, 1214–1217 (2007) (see p. 17).

[105] C. Y. Wang, L. Kuznetsova, V. M. Gkortsas, et al., "Mode-locked pulses from mid-infrared Quantum Cascade Lasers", Opt. Express **17**, 12929–12943 (2009) (see p. 17).

[106] R. Trebino, *Frequency-Resolved Optical Gating: The Measurement of Ultrashort Laser Pulses*, Springer US, Boston, MA, (2000), ISBN: 978-1-4613-5432-1 978-1-4615-1181-6, (see pp. 17, 145, 146).

[107] C. Iaconis and I. A. Walmsley, "Spectral phase interferometry for direct electric-field reconstruction of ultrashort optical pulses", Opt. Lett. **23**, 792–794 (1998) (see pp. 17, 147).

[108] W. Maineult, L. Ding, P. Gellie, et al., "Microwave modulation of terahertz quantum cascade lasers: a transmission-line approach", Appl. Phys. Lett. **96**, 021108 (2010) (see pp. 18, 55).

[109] M. C. Wanke, E. W. Young, C. D. Nordquist, M. J. Cich, A. D. Grine, C. T. Fuller, J. L. Reno, and M. Lee, "Monolithically integrated solid-state terahertz transceivers", Nature Photon **4**, 565–569 (2010) (see pp. 18, 50).

[110] S. Barbieri, P. Gellie, G. Santarelli, L. Ding, W. Maineult, C. Sirtori, R. Colombelli, H. Beere, and D. Ritchie, "Phase-locking of a 2.7-THz quantum cascade laser to a mode-locked erbium-doped fibre laser", Nature Photonics **4**, 636–640 (2010) (see p. 18).

[111] P. Gellie, S. Barbieri, J.-F. Lampin, et al., "Injection-locking of terahertz quantum cascade lasers up to 35GHz using RF amplitude modulation", Opt. Express **18**, 20799–20816 (2010) (see pp. 18, 55, 100, 101, 111).

[112] M. Ravaro, P. Gellie, G. Santarelli, et al., "Stabilization and mode locking of terahertz quantum cascade lasers", IEEE Journal of Selected Topics in Quantum Electronics **19**, 8501011–8501011 (2013) (see p. 18).

[113] M. Ravaro, C. Manquest, C. Sirtori, S. Barbieri, G. Santarelli, K. Blary, J.-F. Lampin, S. P. Khanna, and E. H. Linfield, "Phase-locking of a 2.5 THz quantum cascade laser to a frequency comb using a GaAs photomixer", Opt. Lett. **36**, 3969–3971 (2011) (see p. 18).

[114] R. P. Green, A. Tredicucci, N. Q. Vinh, B. Murdin, C. Pidgeon, H. E. Beere, and D. A. Ritchie, "Gain recovery dynamics of a terahertz quantum cascade laser", Physical Review B **80**, 10.1103/PhysRevB.80.075303 (2009) (see pp. 18, 118).

[115] D. R. Bacon, J. R. Freeman, R. A. Mohandas, L. Li, E. H. Linfield, A. G. Davies, and P. Dean, "Gain recovery time in a terahertz quantum cascade laser", Appl. Phys. Lett. **108**, 081104 (2016) (see pp. 18, 118).

[116] C. G. Derntl, G. Scalari, D. Bachmann, M. Beck, J. Faist, K. Unterrainer, and J. Darmo, "Gain dynamics in a heterogeneous terahertz quantum cascade laser", Appl. Phys. Lett. **113**, 181102 (2018) (see pp. 18, 88, 111, 118).

[117] C. Sirtori, S. Barbieri, and R. Colombelli, "Wave engineering with THz quantum cascade lasers", Nature Photon **7**, 691–701 (2013) (see p. 19).

[118] F. Ferdous, H. Miao, D. E. Leaird, K. Srinivasan, J. Wang, L. Chen, L. T. Varghese, and A. M. Weiner, "Spectral line-by-line pulse shaping of on-chip microresonator frequency combs", Nature Photon **5**, 770–776 (2011) (see pp. 18, 23).

[119] T. Herr, K. Hartinger, J. Riemensberger, C. Y. Wang, E. Gavartin, R. Holzwarth, M. L. Gorodetsky, and T. J. Kippenberg, "Universal formation dynamics and noise of Kerr-frequency combs in microresonators", Nature Photonics **6**, 480–487 (2012) (see p. 18).

[120] P. Del'Haye, K. Beha, S. B. Papp, and S. A. Diddams, "Self-Injection Locking and Phase-Locked States in Microresonator-Based Optical Frequency Combs", Phys. Rev. Lett. **112**, 043905 (2014) (see pp. 18, 47).

[121] T. Herr, V. Brasch, J. D. Jost, C. Y. Wang, N. M. Kondratiev, M. L. Gorodetsky, and T. J. Kippenberg, "Temporal solitons in optical microresonators", Nature Photonics **8**, 145–152 (2014) (see p. 18).

[122] A. Calvar, M. I. Amanti, M. Renaudat St-Jean, S. Barbieri, A. Bismuto, E. Gini, M. Beck, J. Faist, and C. Sirtori, "High frequency modulation of mid-infrared quantum cascade lasers embedded into microstrip line", Appl. Phys. Lett. **102**, 181114 (2013) (see p. 20).

[123] J. R. Freeman, J. Maysonnave, H. E. Beere, D. A. Ritchie, J. Tignon, and S. S. Dhillon, "Electric field sampling of modelocked pulses from a quantum cascade laser", Opt. Express **21**, 16162–16169 (2013) (see p. 20).

[124] M. R. St-Jean, M. I. Amanti, A. Bernard, A. Calvar, A. Bismuto, E. Gini, M. Beck, J. Faist, H. C. Liu, and C. Sirtori, "Injection locking of mid-infrared quantum cascade laser at 14 GHz, by direct microwave modulation", Laser & Photonics Reviews **8**, 443–449 (2014) (see pp. 20, 100).

[125] D. Burghoff, Y. Yang, D. J. Hayton, J.-R. Gao, J. L. Reno, and Q. Hu, "Evaluating the coherence and time-domain profile of quantum cascade laser frequency combs", Opt. Express **23**, 1190–1202 (2015) (see pp. 21, 151).

[126] J. B. Khurgin, Y. Dikmelik, A. Hugi, and J. Faist, "Coherent frequency combs produced by self frequency modulation in quantum cascade lasers", Appl. Phys. Lett. **104**, 081118 (2014) (see pp. 21, 47, 111).

[127] P. Tzenov, D. Burghoff, Q. Hu, and C. Jirauschek, "Time domain modeling of terahertz quantum cascade lasers for frequency comb generation", Opt. Express **24**, 23232–23247 (2016) (see p. 22).

[128] G. Villares, A. Hugi, S. Blaser, and J. Faist, "Dual-comb spectroscopy based on quantum-cascade-laser frequency combs", Nat Commun **5**, 5192 (2014) (see pp. 22, 130).

[129] J. A. Fan, M. A. Belkin, F. Capasso, S. P. Khanna, M. Lachab, A. G. Davies, and E. H. Linfield, "Wide-ridge metal-metal terahertz quantum cascade lasers with high-order lateral mode suppression", Appl. Phys. Lett. **92**, 031106 (2008) (see pp. 23, 37, 47).

[130] D. Bachmann, M. Rösch, M. J. Süess, M. Beck, K. Unterrainer, J. Darmo, J. Faist, and G. Scalari, "Short pulse generation and mode control of broadband terahertz quantum cascade lasers", Optica **3**, 1087–1094 (2016) (see pp. 23, 37, 41, 47, 50, 89, 105, 106, 118, 131).

[131] H. Li, P. Laffaille, D. Gacemi, et al., "Dynamics of ultra-broadband terahertz quantum cascade lasers for comb operation", Opt. Express **23**, 33270–33294 (2015) (see pp. 23, 87, 98, 117).

[132] A. Mottaghizadeh, D. Gacemi, P. Laffaille, et al., "5-ps-long terahertz pulses from an active-mode-locked quantum cascade laser", Optica **4**, 168 (2017) (see p. 23).

[133] S. Barbieri, M. Ravaro, P. Gellie, G. Santarelli, C. Manquest, C. Sirtori, S. P. Khanna, E. H. Linfield, and A. G. Davies, "Coherent sampling of active mode-locked terahertz quantum cascade lasers and frequency synthesis", Nat Photon **5**, 306–313 (2011) (see pp. 23, 24, 122, 129).

[134] W. J. Wan, H. Li, T. Zhou, and J. C. Cao, "Homogeneous spectral spanning of terahertz semiconductor lasers with radio frequency modulation", Sci Rep **7**, 44109 (2017) (see pp. 23, 169).

[135] W. J. Wan, H. Li, and J. C. Cao, "Homogeneous spectral broadening of pulsed terahertz quantum cascade lasers by radio frequency modulation", Opt. Express **26**, 980–989 (2018) (see p. 23).

[136] Y. Bidaux, F. Kapsalidis, P. Jouy, M. Beck, and J. Faist, "Coupled-Waveguides for Dispersion Compensation in Semiconductor Lasers", Laser & Photonics Reviews **12**, 1700323 (2018) (see p. 23).

[137] A. Forrer, M. Rösch, M. Singleton, M. Beck, J. Faist, and G. Scalari, "Coexisting frequency combs spaced by an octave in a monolithic quantum cascade laser", Optics Express **26**, 23167 (2018) (see pp. 23, 219).

[138] J. Hillbrand, A. M. Andrews, H. Detz, G. Strasser, and B. Schwarz, "Coherent injection locking of quantum cascade laser frequency combs", Nature Photon **13**, 101–104 (2019) (see pp. 23, 124, 164, 174).

[139] M. Singleton, M. Beck, and J. Faist, "Pulses from a mid-infrared quantum cascade laser frequency comb using an external compressor", J. Opt. Soc. Am. B, JOSAB **36**, 1676–1683 (2019) (see pp. 24, 151).

[140] L. Consolino, M. Nafa, F. Cappelli, et al., "Fully phase-stabilized quantum cascade laser frequency comb", Nat Commun **10**, 1–7 (2019) (see pp. 24, 129).

[141] F. Cappelli, L. Consolino, G. Campo, et al., "Retrieval of phase relation and emission profile of quantum cascade laser frequency combs", Nature Photonics **13**, 562–568 (2019) (see pp. 24, 122, 148, 170).

[142] F. P. Mezzapesa, V. Pistore, K. Garrasi, L. Li, A. G. Davies, E. H. Linfield, S. Dhillon, and M. S. Vitiello, "Tunable and compact dispersion compensation of broadband THz quantum cascade laser frequency combs", Opt. Express **27**, 20231–20240 (2019) (see pp. 24, 194).

[143] A. Forrer, M. Franckié, D. Stark, T. Olariu, M. Beck, J. Faist, and G. Scalari, "Photon-Driven Broadband Emission and Frequency Comb RF Injection Locking in THz Quantum Cascade Lasers", ACS Photonics **7**, 784–791 (2020) (see pp. 25, 89–91, 93, 95, 97–100, 102, 103, 106, 115, 118, 124, 178, 216).

[144] A. Forrer, L. Bosco, M. Beck, J. Faist, and G. Scalari, "RF Injection of THz QCL Combs at 80 K Emitting over 700 GHz Spectral Bandwidth", Photonics **7**, 9 (2020) (see pp. 25, 107, 110, 112, 114, 118, 216).

[145] J. Hillbrand, N. Opačak, M. Piccardo, H. Schneider, G. Strasser, F. Capasso, and B. Schwarz, "Mode-locked short pulses from an 8 µm wavelength semiconductor laser", Nat Commun **11**, 5788 (2020) (see p. 25).

[146] C. Y. Wang, L. Kuznetsova, V. M. Gkortsas, et al., "Mode-locked pulses from mid-infrared quantum cascade lasers", Opt Express **17**, 12929–12943 (2009) (see p. 25).

[147] C. Silvestri, L. L. Columbo, M. Brambilla, and M. Gioannini, "Coherent multi-mode dynamics in a quantum cascade laser: amplitude- and frequency-modulated optical frequency combs", Opt. Express **28**, 23846–23861 (2020) (see pp. 25, 47).

[148] D. Burghoff, "Unraveling the origin of frequency modulated combs using active cavity mean-field theory", Optica **7**, 1781 (2020) (see pp. 25, 26).

[149] B. Schneider, F. Kapsalidis, M. Bertrand, M. Singleton, J. Hillbrand, M. Beck, and J. Faist, "Controlling Quantum Cascade Laser Optical Frequency Combs through Microwave Injection", Laser & Photonics Reviews, 2100242 (2021) (see pp. 25, 151).

[150] P. Täschler, M. Bertrand, B. Schneider, M. Singleton, P. Jouy, F. Kapsalidis, M. Beck, and J. Faist, "Femtosecond pulses from a mid-infrared quantum cascade laser", Nat. Photon. **15**, 919–924 (2021) (see pp. 25, 149, 151).

[151] F. Prati, M. Brambilla, M. Piccardo, L. L. Columbo, C. Silvestri, M. Gioannini, A. Gatti, L. A. Lugiato, and F. Capasso, "Soliton dynamics of ring quantum cascade lasers with injected signal", Nanophotonics **10**, 195–207 (2021) (see p. 26).

[152] L. Columbo, M. Piccardo, F. Prati, et al., "Unifying Frequency Combs in Active and Passive Cavities: temporal Solitons in Externally Driven Ring Lasers", Phys. Rev. Lett. **126**, 173903 (2021) (see p. 26).

[153] B. Meng, M. Singleton, J. Hillbrand, M. Franckié, M. Beck, and J. Faist, "Dissipative Kerr solitons in semiconductor ring lasers", Nat. Photon. **16**, 142–147 (2022) (see pp. 26, 27).

[154] Q. Lu, F. Wang, D. Wu, S. Slivken, and M. Razeghi, "Room temperature terahertz semiconductor frequency comb", Nature Communications **10**, 2403 (2019) (see p. 26).

[155] B. S. Williams, "Terahertz quantum-cascade lasers", Nat Photon **1**, 517–525 (2007) (see pp. 30, 33).

[156] G. Scalari, C. Walther, M. Fischer, R. Terazzi, H. Beere, D. Ritchie, and J. Faist, "THz and sub-THz quantum cascade lasers", Laser & Photonics Reviews **3**, 45–66 (2009) (see pp. 30, 43, 93, 94).

[157] A. Wacker, "Semiconductor superlattices: a model system for nonlinear transport", Physics Reports **357**, 1–111 (2002) (see pp. 30, 92).

[158] R. C. Iotti and F. Rossi, "Nature of Charge Transport in Quantum-Cascade Lasers", Phys. Rev. Lett. **87**, 146603 (2001) (see p. 30).

[159] R. C. Iotti, E. Ciancio, and F. Rossi, "Quantum transport theory for semiconductor nanostructures: a density-matrix formulation", Phys. Rev. B **72**, 125347 (2005) (see p. 30).

[160] F. Rossi and T. Kuhn, "Theory of ultrafast phenomena in photoexcited semiconductors", Rev. Mod. Phys. **74**, 895–950 (2002) (see p. 30).

[161] C. Jirauschek and T. Kubis, "Modeling techniques for quantum cascade lasers", Applied Physics Reviews **1**, 011307 (2014) (see p. 30).

[162] R. Terazzi and J. Faist, "A density matrix model of transport and radiation in quantum cascade lasers", New Journal of Physics **12**, 033045 (2010) (see p. 31).

[163] R. Köhler, A. Tredicucci, F. Beltram, H. E. Beere, E. H. Linfield, A. Giles Davies, and D. A. Ritchie, "High-intensity interminiband terahertz emission from chirped superlattices", Applied Physics Letters **80**, 1867–1869 (2002) (see p. 33).

[164] K. Unterrainer, R. Colombelli, C. Gmachl, F. Capasso, H. Y. Hwang, A. M. Sergent, D. L. Sivco, and A. Y. Cho, "Quantum cascade lasers with double metal-semiconductor waveguide resonators", Appl. Phys. Lett. **80**, 3060–3062 (2002) (see p. 33).

[165] B. S. Williams, S. Kumar, H. Callebaut, Q. Hu, and J. L. Reno, "Terahertz quantum-cascade laser at $\lambda \approx 100$ µm using metal waveguide for mode confinement", Appl. Phys. Lett. **83**, 2124–2126 (2003) (see p. 33).

[166] B. S. Williams, S. Kumar, Q. Hu, and J. L. Reno, "Operation of terahertz quantum-cascade lasers at 164 K in pulsed mode and at 117 K in continuous-wave mode", Opt. Express **13**, 3331–3339 (2005) (see p. 33).

[167] E. E. Orlova, J. N. Hovenier, T. O. Klaassen, et al., "Antenna Model for Wire Lasers", Phys. Rev. Lett. **96**, 173904 (2006) (see p. 33).

[168] D. Turcinkova, "Terahertz Quantum Cascade Lasers for Astronomical Applications", ETH Zurich, (2014), doi: 10.3929/ETHZ-A-010445747, (see p. 34).

[169] E. D. Palik and G. Ghosh, *Handbook of Optical Constants of Solids*, Academic Press, San Diego, (1998), ISBN: 978-0-12-544415-6, (see pp. 35, 36, 133).

[170] R. Gross, A. Marx, D. Einzel, and S. Geprägs, *Festkörperphysik: Aufgaben Und Lösungen*, De Gruyter, (2018), ISBN: 978-3-11-056613-0, (see p. 36).

[171] H. Ibach and H. Lüth, *Solid-State Physics*, Springer Berlin Heidelberg, Berlin, Heidelberg, (1996), ISBN: 978-3-642-88199-2, (see p. 36).

[172] S. Kohen, B. S. Williams, and Q. Hu, "Electromagnetic modeling of terahertz quantum cascade laser waveguides and resonators", Journal of Applied Physics **97**, 053106 (2005) (see pp. 36–38, 42, 43).

[173] M. A. Belkin, J. A. Fan, S. Hormoz, F. Capasso, S. P. Khanna, M. Lachab, A. G. Davies, and E. H. Linfield, "Terahertz quantum cascade lasers with copper metal-metal waveguides operating up to 178 K", Opt. Express **16**, 3242–3248 (2008) (see pp. 37, 38).

[174] M. Sotoodeh, A. H. Khalid, and A. A. Rezazadeh, "Empirical low-field mobility model for III–V compounds applicable in device simulation codes", Journal of Applied Physics **87**, 2890–2900 (2000) (see p. 38).

[175] M. A. Ordal, R. J. Bell, R. W. Alexander, L. L. Long, and M. R. Querry, "Optical properties of fourteen metals in the infrared and far infrared: al, Co, Cu, Au, Fe, Pb, Mo, Ni, Pd, Pt, Ag, Ti, V, and W.", Appl. Opt., AO **24**, 4493–4499 (1985) (see p. 39).

[176] M. A. Ordal, R. J. Bell, R. W. Alexander, L. L. Long, and M. R. Querry, "Optical properties of Au, Ni, and Pb at submillimeter wavelengths", Appl. Opt., AO **26**, 744–752 (1987) (see p. 39).

[177] J. R. Rumble, ed., *CRC Handbook of Chemistry and Physics*, CRC Press, Boca Raton London New York, (2021), ISBN: 978-0-367-71260-0, (see p. 39).

[178] G. K. White, S. B. Woods, and N. F. Mott, "Electrical and thermal resistivity of the transition elements at low temperatures", Philosophical Transactions of the Royal Society of London. Series A, Mathematical and Physical Sciences **251**, 273–302 (1959) (see p. 39).

[179] M. J. Weber, *Handbook of Optical Materials*, CRC Press, Boca Raton, (2003), ISBN: 978-0-8493-3512-9, (see p. 39).

[180] M. A. Belkin, J. A. Fan, S. Hormoz, F. Capasso, S. P. Khanna, M. Lachab, A. G. Davies, and E. H. Linfield, "Terahertz quantum cascade lasers with copper metal-metal waveguides operating up to 178 K", Opt. Express **16**, 3242 (2008) (see pp. 41, 105).

[181] M. Rösch, "Terahertz Quantum Cascade Laser Based Frequency Combs", ETH Zurich, (2017), doi: 10.3929/ethz-b-000171581, (see p. 42).

[182] G. Villares and J. Faist, "Quantum cascade laser combs: effects of modulation and dispersion", Opt. Express **23**, 1651–1669 (2015) (see pp. 43, 111).

[183] B. E. A. Saleh and M. C. Teich, *Fundamentals of Photonics*, John Wiley & Sons, Inc., New York, USA, (1991), ISBN: 978-0-471-83965-1 978-0-471-21374-1, (see pp. 44, 48).

[184] B. Röben, X. Lü, K. Biermann, L. Schrottke, and H. T. Grahn, "Effective group dispersion of terahertz quantum-cascade lasers", J. Phys. D: Appl. Phys. **54**, 025110 (2020) (see p. 45).

[185] J. Faist, G. Villares, G. Scalari, M. Rösch, C. Bonzon, A. Hugi, and M. Beck, "Quantum Cascade Laser Frequency Combs", Nanophotonics **5**, 10.1515/nanoph-2016-0015 (2016) (see pp. 48, 129, 135).

[186] M. Piccardo, D. Kazakov, N. A. Rubin, P. Chevalier, Y. Wang, F. Xie, K. Lascola, A. Belyanin, and F. Capasso, "Time-dependent population inversion gratings in laser frequency combs", Optica **5**, 475–478 (2018) (see pp. 50, 53).

[187] D. M. Pozar, *Microwave Engineering*, Wiley, Hoboken, NJ, (2012), ISBN: 978-0-470-63155-3, (see p. 50).

[188] P. R. Griffiths and J. A. de Haseth, *Fourier Transform Infrared Spectrometry*, John Wiley & Sons, Inc., Hoboken, NJ, USA, (2007), ISBN: 978-0-470-10631-0 978-0-471-19404-0, (see pp. 57, 58, 60, 79).

[189] L. Mertz, "Auxiliary computation for Fourier spectrometry", Infrared Physics **7**, 17–23 (1967) (see pp. 62, 118).

[190] M. L. Forman, W. H. Steel, and G. A. Vanasse, "Correction of Asymmetric Interferograms Obtained in Fourier Spectroscopy*", J. Opt. Soc. Am., JOSA **56**, 59–63 (1966) (see pp. 62, 118).

[191] C. D. Porter and D. B. Tanner, "Correction of phase errors in fourier spectroscopy", Int J Infrared Milli Waves **4**, 273–298 (1983) (see p. 62).

[192] F. Harris, "On the use of windows for harmonic analysis with the discrete Fourier transform", Proceedings of the IEEE **66**, 51–83 (1978) (see pp. 72, 82).

[193] W. W. Smith and J. M. Smith, *Handbook of Real-Time Fast Fourier Transforms: Algorithms to Product Testing*, IEEE Press, New York, (1995), ISBN: 978-0-7803-1091-9, (see p. 72).

[194] P. Maslowski, K. F. Lee, A. C. Johansson, et al., "Surpassing the path-limited resolution of Fourier-transform spectrometry with frequency combs", Phys. Rev. A **93**, 021802 (2016) (see p. 78).

[195] L. Rutkowski, P. Masłowski, A. C. Johansson, A. Khodabakhsh, and A. Foltynowicz, "Optical frequency comb Fourier transform spectroscopy with sub-nominal resolution and precision beyond the Voigt profile", Journal of Quantitative Spectroscopy and Radiative Transfer **204**, 63–73 (2018) (see p. 78).

[196] E. Baumann, F. R. Giorgetta, W. C. Swann, A. M. Zolot, I. Coddington, and N. R. Newbury, "Spectroscopy of the methane ν_3 band with an accurate midinfrared coherent dual-comb spectrometer", Phys. Rev. A **84**, 062513 (2011) (see p. 81).

[197] M. Gianella, A. Nataraj, B. Tuzson, P. Jouy, F. Kapsalidis, M. Beck, M. Mangold, A. Hugi, J. Faist, and L. Emmenegger, "High-resolution and gapless dual comb spectroscopy with current-tuned quantum cascade lasers", Opt. Express **28**, 6197 (2020) (see p. 81).

[198] H. Albrecht, "A family of cosine-sum windows for high-Resolution measurements", in 2001 IEEE International Conference on Acoustics, Speech, and Signal Processing. Proceedings (Cat. No.01CH37221), Vol. 5 (May 2001), 3081–3084 vol.5 (see p. 82).

[199] A. Nuttall, "Some windows with very good sidelobe behavior", IEEE Transactions on Acoustics, Speech, and Signal Processing **29**, 84–91 (1981) (see p. 82).

[200] K. Garrasi, F. P. Mezzapesa, L. Salemi, L. Li, L. Consolino, S. Bartalini, P. De Natale, A. G. Davies, E. H. Linfield, and M. S. Vitiello, "High Dynamic Range, Heterogeneous, Terahertz Quantum Cascade Lasers Featuring Thermally Tunable Frequency Comb Operation over a Broad Current Range", ACS Photonics **6**, 73–78 (2019) (see p. 87).

[201] M. I. Amanti, G. Scalari, R. Terazzi, M. Fischer, M. Beck, J. Faist, A. Rudra, P. Gallo, and E. Kapon, "Bound-to-continuum terahertz quantum cascade laser with a single-quantum-well phonon extraction/injection stage", New J. Phys. **11**, 125022 (2009) (see pp. 88, 130).

[202] S. Markmann, H. Nong, S. Pal, et al., "Two-dimensional coherent spectroscopy of a THz quantum cascade laser: observation of multiple harmonics", Opt. Express **25**, 21753 (2017) (see p. 88).

[203] S. Blaser, L. Diehl, M. Beck, J. Faist, U. Oesterle, J. Xu, S. Barbieri, and F. Beltram, "Characterization and modeling of quantum cascade lasers based on a photon-assisted tunneling transition", IEEE Journal of Quantum Electronics **37**, 448–455 (2001) (see pp. 88, 93).

[204] J. Faist, F. Capasso, C. Sirtori, D. L. Sivco, A. L. Hutchinson, and A. Y. Cho, "Laser action by tuning the oscillator strength", Nature **387**, 777–782 (1997) (see p. 89).

[205] G. Scalari, M. I. Amanti, C. Walther, R. Terazzi, M. Beck, and J. Faist, "Broadband THz lasing from a photon-phonon quantum cascade structure", Opt. Express **18**, 8043–8052 (2010) (see pp. 89, 108).

[206] D. O. Winge, E. Dupont, and A. Wacker, "Ignition of quantum cascade lasers in a state of oscillating electric field domains", Physical Review A **98**, 10.1103/PhysRevA.98.023834 (2018) (see pp. 90, 92, 96).

[207] D. Kazakov, M. Piccardo, Y. Wang, P. Chevalier, T. S. Mansuripur, F. Xie, C.-e. Zah, K. Lascola, A. Belyanin, and F. Capasso, "Self-starting harmonic frequency comb generation in a quantum cascade laser", Nature Photonics **11**, 789 (2017) (see pp. 90, 92, 117, 118).

[208] M. Piccardo, P. Chevalier, T. S. Mansuripur, D. Kazakov, Y. Wang, N. A. Rubin, L. Meadowcroft, A. Belyanin, and F. Capasso, "The harmonic state of quantum cascade lasers: origin, control, and prospective applications", Opt. Express **26**, 9464–9483 (2018) (see pp. 90, 92, 109, 111, 117, 118, 120, 123).

[209] M. Wienold, L. Schrottke, M. Giehler, R. Hey, and H. T. Grahn, "Nonlinear transport in quantum-cascade lasers: the role of electric-field domain formation for the laser characteristics", Journal of Applied Physics **109**, 073112 (2011) (see p. 92).

[210] S. L. Lu, L. Schrottke, S. W. Teitsworth, R. Hey, and H. T. Grahn, "Formation of Electric-Field Domains in $GaAs/Al_xGa_{1-x}As$ Quantum Cascade Laser Structures", Physical Review B **73**, 10.1103/PhysRevB.73.033311 (2006) (see p. 92).

[211] L. L. Bonilla and H. T. Grahn, "Non-linear dynamics of semiconductor superlattices", Rep. Prog. Phys. **68**, 577–683 (2005) (see p. 92).

[212] L. Esaki and L. L. Chang, "New Transport Phenomenon in a Semiconductor "Superlattice"", Phys. Rev. Lett. **33**, 495–498 (1974) (see p. 92).

[213] A. Wacker, M. Lindskog, and D. O. Winge, "Nonequilibrium Green's Function Model for Simulation of Quantum Cascade Laser Devices Under Operating Conditions", IEEE Journal of Selected Topics in Quantum Electronics **19**, 1–11 (2013) (see p. 94).

[214] M. Lindskog, J. M. Wolf, V. Trinite, V. Liverini, J. Faist, G. Maisons, M. Carras, R. Aidam, R. Ostendorf, and A. Wacker, "Comparative analysis of quantum cascade laser modeling based on density matrices and non-equilibrium Green's functions", Appl. Phys. Lett. **105**, 103106 (2014) (see p. 94).

[215] M. Franckié, L. Bosco, M. Beck, C. Bonzon, E. Mavrona, G. Scalari, A. Wacker, and J. Faist, "Two-well quantum cascade laser optimization by non-equilibrium Green's function modelling", Appl. Phys. Lett. **112**, 021104 (2018) (see pp. 94, 105).

[216] J. Hillbrand, A. M. Andrews, H. Detz, G. Strasser, and B. Schwarz, "Coherent injection locking of quantum cascade laser frequency combs", Nature Photonics **13**, 101–104 (2019) (see pp. 100, 112, 151).

[217] M. Franckié and J. Faist, "Bayesian Optimization of Terahertz Quantum Cascade Lasers", Phys. Rev. Applied **13**, 034025 (2020) (see p. 105).

[218] F. P. Mezzapesa, K. Garrasi, J. Schmidt, et al., "Terahertz Frequency Combs Exploiting an On-Chip, Solution-Processed, Graphene-Quantum Cascade Laser Coupled-Cavity", ACS Photonics **7**, 3489–3498 (2020) (see p. 105).

[219] G. Scalari, R. Terazzi, M. Giovannini, N. Hoyler, and J. Faist, "Population inversion by resonant tunneling in quantum wells", Appl. Phys. Lett. **91**, 032103 (2007) (see p. 108).

[220] T. S. Mansuripur, C. Vernet, P. Chevalier, et al., "Single-mode instability in standing-wave lasers: the quantum cascade laser as a self-pumped parametric oscillator", Phys. Rev. A **94**, 063807 (2016) (see pp. 109, 117, 118).

[221] F. Wang, H. Nong, T. Fobbe, et al., "Short Terahertz Pulse Generation from a Dispersion Compensated Modelocked Semiconductor Laser", Laser & Photonics Reviews **11**, 1700013 (2017) (see p. 113).

[222] J. Hillbrand, D. Auth, M. Piccardo, N. Opačak, E. Gornik, G. Strasser, F. Capasso, S. Breuer, and B. Schwarz, "In-Phase and Anti-Phase Synchronization in a Laser Frequency Comb", Phys. Rev. Lett. **124**, 023901 (2020) (see p. 113).

[223] Y. Yang, D. Burghoff, D. J. Hayton, J.-R. Gao, J. L. Reno, and Q. Hu, "Terahertz multiheterodyne spectroscopy using laser frequency combs", Optica **3**, 499 (2016) (see p. 115).

[224] L. A. Sterczewski, J. Westberg, Y. Yang, D. Burghoff, J. Reno, Q. Hu, and G. Wysocki, "Terahertz hyperspectral imaging with dual chip-scale combs", Optica **6**, 766–771 (2019) (see p. 115).

[225] F. Wang, V. Pistore, M. Riesch, et al., "Ultrafast response of harmonic modelocked THz lasers", Light Sci Appl **9**, 51 (2020) (see p. 117).

[226] M. Piccardo, P. Chevalier, S. Anand, Y. Wang, D. Kazakov, E. A. Mejia, F. Xie, K. Lascola, A. Belyanin, and F. Capasso, "Widely tunable harmonic frequency comb in a quantum cascade laser", Appl. Phys. Lett. **113**, 031104 (2018) (see p. 117).

[227] D. Kazakov, N. Opačak, M. Beiser, A. Belyanin, B. Schwarz, M. Piccardo, and F. Capasso, "Defect-engineered ring laser harmonic frequency combs", Optica **8**, 1277 (2021) (see p. 117).

[228] A. Forrer, Y. Wang, M. Beck, A. Belyanin, J. Faist, and G. Scalari, "Self-starting harmonic comb emission in THz quantum cascade lasers", Appl. Phys. Lett. **118**, 131112 (2021) (see pp. 118, 119, 121, 123, 125–127).

[229] R. Lang and K. Kobayashi, "External optical feedback effects on semiconductor injection laser properties", IEEE Journal of Quantum Electronics **16**, 347–355 (1980) (see pp. 123, 150).

[230] P. Gellie, J.-F. Lampin, C. Sirtori, and S. Barbieri, "RF injection-locking of terahertz quantum cascade lasers", Electron. Lett. **46**, S60 (2010) (see p. 124).

[231] Y. Wang and A. Belyanin, "Harmonic frequency combs in quantum cascade lasers: time-domain and frequency-domain theory", Phys. Rev. A **102**, 013519 (2020) (see pp. 125, 127).

[232] F. Cappelli, G. Campo, I. Galli, et al., "Frequency stability characterization of a quantum cascade laser frequency comb", Laser & Photonics Reviews **10**, 623–630 (2016) (see p. 129).

[233] C. Gmachl, A. Belyanin, D. Sivco, M. Peabody, N. Owschimikow, A. Sergent, F. Capasso, and A. Cho, "Optimized second-harmonic generation in quantum cascade lasers", IEEE Journal of Quantum Electronics **39**, 1345–1355 (2003) (see p. 130).

[234] Y. Yang, A. Paulsen, D. Burghoff, J. L. Reno, and Q. Hu, "Lateral Heterogeneous Integration of Quantum Cascade Lasers", ACS Photonics, 10.1021/acsphotonics.8b00507 (2018) (see pp. 130, 134).

[235] M. Rösch, I.-C. Benea-Chelmus, C. Bonzon, M. J. Süess, M. Beck, J. Faist, and G. Scalari, "Broadband monolithic extractor for metal-metal waveguide based terahertz quantum cascade laser frequency combs", Appl. Phys. Lett. **111**, 021106 (2017) (see p. 130).

[236] K. Ohtani, D. Turčinková, C. Bonzon, I.-C. Benea-Chelmus, M. Beck, J. Faist, M. Justen, U. U. Graf, M. Mertens, and J. Stutzki, "High performance 4.7 THz GaAs quantum cascade lasers based on four quantum wells", New J. Phys. **18**, 123004 (2016) (see p. 131).

[237] J. Lloyd-Hughes, G. Scalari, A. van Kolck, M. Fischer, M. Beck, and J. Faist, "Coupling terahertz radiation between sub-wavelength metal-metal waveguides and free space using monolithically integrated horn antennae", Opt. Express **17**, 18387–18393 (2009) (see p. 131).

[238] L. Ajili, G. Scalari, D. Hofstetter, M. Beck, J. Faist, H. Beere, G. Davies, E. Linfield, and D. Ritchie, "Continuous-wave operation of far-infrared quantum cascade lasers", Electronics Letters **38**, 1675–1676 (2002) (see p. 140).

[239] J. Ratner, G. Steinmeyer, T. C. Wong, R. Bartels, and R. Trebino, "Coherent artifact in modern pulse measurements", Opt. Lett. **37**, 2874 (2012) (see pp. 146, 147).

[240] D. Kane and R. Trebino, "Characterization of arbitrary femtosecond pulses using frequency-resolved optical gating", IEEE Journal of Quantum Electronics **29**, 571–579 (1993) (see p. 146).

[241] K. W. DeLong, R. Trebino, J. Hunter, and W. E. White, "Frequency-resolved optical gating with the use of second-harmonic generation", J. Opt. Soc. Am. B, JOSAB **11**, 2206–2215 (1994) (see p. 146).

[242] L. Xu, E. Zeek, and R. Trebino, "Simulations of frequency-resolved optical gating for measuring very complex pulses", J. Opt. Soc. Am. B **25**, A70 (2008) (see p. 146).

[243] R. Trebino, K. W. DeLong, D. N. Fittinghoff, J. N. Sweetser, M. A. Krumbügel, B. A. Richman, and D. J. Kane, "Measuring ultrashort laser pulses in the time-frequency domain using frequency-resolved optical gating", Review of Scientific Instruments **68**, 3277–3295 (1997) (see p. 146).

[244] R. Trebino, "FROG", in *Frequency-Resolved Optical Gating: the Measurement of Ultrashort Laser Pulses*, edited by R. Trebino (Springer US, Boston, MA, 2000), pp. 101–115 (see p. 146).

[245] P. Bowlan, P. Gabolde, A. Shreenath, K. McGresham, R. Trebino, and S. Akturk, "Crossed-beam spectral interferometry: a simple, high-spectral-resolution method for completely characterizing complex ultrashort pulses in real time", Opt. Express **14**, 11892 (2006) (see p. 147).

[246] P. Bowlan, U. Fuchs, R. Trebino, and U. D. Zeitner, "Measuring the spatiotemporal electric field of tightly focused ultrashort pulses with sub-micron spatial resolution", Opt. Express **16**, 13663 (2008) (see p. 147).

[247] P. Gabolde and R. Trebino, "Single-frame measurement of the complete spatiotemporal intensity and phase of ultrashort laser pulses using wavelength-multiplexed digital holography", J. Opt. Soc. Am. B **25**, A25 (2008) (see p. 147).

[248] S.-W. Huang, H. Zhou, J. Yang, J. F. McMillan, A. Matsko, M. Yu, D.-L. Kwong, L. Maleki, and C. W. Wong, "Mode-Locked Ultrashort Pulse Generation from On-Chip Normal Dispersion Microresonators", Phys. Rev. Lett. **114**, 053901 (2015) (see p. 147).

[249] F. Kapsalidis, B. Schneider, M. Singleton, M. Bertrand, E. Gini, M. Beck, and J. Faist, "Mid-infrared quantum cascade laser frequency combs with a microstrip-like line waveguide geometry", Appl. Phys. Lett. **118**, 071101 (2021) (see p. 151).

[250] C. Kriso, A. Barua, O. Mohiuddin, C. Möller, A. Ruiz-Perez, W. Stolz, M. Koch, and A. Rahimi-Iman, "Signatures of a frequency-modulated comb in a VECSEL", Optica **8**, 458–463 (2021) (see p. 151).

[251] B. Schwarz, J. Hillbrand, M. Beiser, A. M. Andrews, G. Strasser, H. Detz, A. Schade, R. Weih, and S. Höfling, "Monolithic frequency comb platform based on interband cascade lasers and detectors", Optica **6**, 890–895 (2019) (see p. 151).

[252] Z. Han, D. Ren, and D. Burghoff, "Sensitivity of SWIFT spectroscopy", Opt. Express **28**, 6002–6017 (2020) (see pp. 151, 153–155, 158, 159, 161).

[253] D. Burghoff, "Some notes on Shifted Wave Interference Fourier Transform Spectroscopy (SWIFTS)", 10.13140/RG.2.2.30934.70721 (2018) (see pp. 151, 155).

[254] I. Tretyakov, S. Ryabchun, M. Finkel, A. Maslennikova, N. Kaurova, A. Lobastova, B. Voronov, and G. Gol'tsman, "Low noise and wide bandwidth of NbN hot-electron bolometer mixers", Appl. Phys. Lett. **98**, 033507 (2011) (see pp. 164, 195).

[255] A. Shurakov, Y. Lobanov, and G. Goltsman, "Superconducting hot-electron bolometer: from the discovery of hot-electron phenomena to practical applications", Supercond. Sci. Technol. **29**, 023001 (2015) (see pp. 164, 195).

[256] Zurich Instrument, *Quad PID/PLL Controller Option — Zurich Instruments*, https://www.zhinst.com/en/products/uhf-pid-quad-pidpll-controller (visited on 09/25/2021) (see p. 164).

[257] Liquid Instruments, *Moku:Pro*, Liquid Instruments, https://www.liquidinstruments.com/products/hardware-platforms/mokupro/ (visited on 09/25/2021) (see p. 164).

[258] Standford Research Systems, *Lock-In Amplifier High Frequency - SR844*, https://www.thinksrs.com/products/SR844.htm (visited on 09/25/2021) (see p. 164).

[259] Rohde & Schwarz GmbH & Co, *R&S®FSU spectrum analyzer*, https://www.rohde-schwarz.com/us/products/test-and-measurement/signal-and-spectrum-analyzers/rs-fsu-spectrum-analyzer_63493-7993.html (visited on 09/25/2021) (see pp. 165, 167).

[260] F. Yuan, *Injection-Locking in Mixed-Mode Signal Processing*, Springer International Publishing, Cham, (2020), ISBN: 978-3-030-17362-3 978-3-030-17364-7, (see p. 176).

[261] A. Hangauer and G. Wysocki, "Gain Compression and Linewidth Enhancement Factor in Mid-IR Quantum Cascade Lasers", IEEE Journal of Selected Topics in Quantum Electronics **21**, 74–84 (2015) (see p. 194).

[262] A. Hangauer, G. Spinner, M. Nikodem, and G. Wysocki, "High frequency modulation capabilities and quasi single-sideband emission from a quantum cascade laser", Opt. Express **22**, 23439–23455 (2014) (see p. 194).

[263] N. Opačak, F. Pilat, D. Kazakov, S. D. Cin, G. Ramer, B. Lendl, F. Capasso, and B. Schwarz, "Spectrally resolved linewidth enhancement factor of a semiconductor frequency comb", Optica **8**, 1227–1230 (2021) (see p. 194).